On Anterior Cruciate Ligament Injury:
Biomechanical Studies of *In Vitro* Knee Kinematics and Bone Morphology

by

So Young Baek

A dissertation submitted in partial fulfillment
of the requirements for the degree of
Doctor of Philosophy
(Mechanical Engineering)
in the University of Michigan
2022

Doctoral Committee:

Professor James A. Ashton-Miller, Chair
Associate Professor Amanda O. Esquivel
Assistant Professor K. Alex Shorter
Professor Edward M. Wojtys

So Young Baek

soy@umich.edu

ORCiD: 0000-0003-3329-7202

© So Young Baek 2022

Acknowledgement

I am not sure I could do this dissertation without the support of many individuals during this hard and long journey. I am sincerely grateful to everyone for their support for me to finish this.

First and foremost, I would like to deeply thank my advisor, Prof. James Ashton-Miller. I will probably never forget a café near central campus where I first met and talked to him a few days after I arrived at Ann Arbor. From that day to the present, he has given kind and enthusiastic guidance and encouragement. He guided me patiently to move forward and wisely with his tremendous knowledge. He was very respectful, and I cannot express my gratitude in any words.

In addition, I am grateful to all my committee members and their valuable feedback. In the field of medicine, especially orthopedics, which was unfamiliar to me as an engineer, Dr. Edward Wojtys has shared a lot of clinical insight, and many suggestions. Prof. Amanda Esquivel gave me a lot of insightful ideas and advice for not only this dissertation and but also our IMU work together. I found many of her ideas stimulating, and I have learned a lot from her enthusiasm. I also thank Prof. Alex Shorter for his helpful comments and support to strengthen the overall dissertation.

As a member of ACL project team, I was able to make progress in research with the help of many people. I am especially grateful to Dr. Mélanie Beaulieu. She has always been a kind guide to me as a processor in the BRL, and I could never do many of my experiments without her support. I would also like to give thanks to Prof. Stephen Schlecht, Prof. Mark Banaszak

Holl, and all of the ACL team who gave much valuable feedback and answered many questions for me. I also thank Grace Carey and Mirel Ajdaroski for helping me with my experiments. Similarly, I am grateful to Conor Locke and Dr. Robert Goulet in the ORL, and Suzan Lowe and James O'Connor in the Michigan Medicine Department of Radiology for supporting me with their technical assistance. Furthermore, I cannot leave out my appreciation for the Biomechanics Research Lab members: Dr. Payam Mirshams, Dr Ali Attari, Fred Zhang, and Mariana Masteling, Over the years, we have cheered one another along as an amazing team of colleagues.

For the first time away from my family and in a language unfamiliar in a new country, I found my life as a student again was a new challenge. I started my Ph.D. in January 2018 and completed experimental testing for Chapter 2 by the time that the Covid-19 pandemic began at the end of January 2020. The pandemic led to a complete shutdown of all laboratory activities for one and half years. The pandemic meant that most of my student life had to be conducted using zoom and remote interactions. I lost the opportunity to spend time in my graduate student office with colleagues and friends, and that made life challenging. During this time, my Ann Arbor friends were a strong mental and social support. All the memories with them in my time at Ann Arbor can never be forgotten. In particularly, Carol Tucker has always been a generous and kind supporter for all my time with her. I could feel the warmth of family in Ann Arbor during the time with her and Daniela. I would like to sincerely thank Dr. Judy Dyer. She has made me strong so I wouldn't give up by mentally, advising and caring as well helping me to develop my language presentation skills during my whole Ph.D journey.

Finally, I would like to express my deep gratitude to my family in Korea and Canada. They always supported me at my side no matter what chose I made. I couldn't have done it without their insurmountable love and support.

I was able to develop from all of this support, and now I will try to be a person who returns appreciation to the people who supported me.

Preface

Chapters 2 and 3 have been written as separate manuscripts for publication. There may be some repetition of presented materials for each chapter.

Table of Contents

Acknowledgement ii

Preface............ v

List of Tables x

List of Figures xii

List of Appendices xvii

Abstract xviii

Chapter 1 : Introduction to the Dissertation Proposal............ 1

1.1 Background 1

1.2 Overall objectives and experimental approach 7

1.3 Organization of the dissertation including working hypotheses 8

1.4 References 10

Chapter 2 : A Comparison of IMU and Motion Capture Measurements of Tibiofemoral Kinematics during Simulated Pivot Landings 18

2.1 Abstract 18

2.2 Introduction 19

2.3 Materials and methods 22

2.3.1 Specimen procurement and preparation 22

2.3.2 Testing apparatus............ 23

2.3.3 Data analysis............ 25

2.4 Results 28

2.4.1 Measured peak knee angle changes............ 28

2.4.2 Comparison of the tibial and femoral angular velocity changes calculated from Certus system data with IMU data 29

2.5 Discussion 31

2.6 Conclusions 34

2.7 References 34

Chapter 3 : On the Relationship between Lateral Tibial Slope and Tibiofemoral Kinematics during Simulated Jump Landings in Male Human Cadaver Knees 38

3.1 Abstract 38

3.2 Introduction 39

3.3 Methods 41

3.3.1 Specimen procurement and preparation 41

3.3.2 Magnetic resonance imaging 42

3.3.3 Testing apparatus 44

3.3.4 Testing protocol 46

3.3.5 Statistical Analysis 47

3.4 Results 48

3.5 Discussion 52

3.6 Conclusions 54

3.7 References 54

Chapter 4 : On the Differences in Stress Distributions in the Mineralized Portion of Convex, Concave and Flat ACL Femoral Entheses. 59

4.1 Abstract 59

4.2 Introduction 60

4.3 Methods 63

4.4 Results 66

4.5 Discussion 67

4.6 Conclusions 71

4.7 References 71

Chapter 5 : On the Subchondral Bone Architecture of the Young Adult Femoral ACL Enthesis under Repetitive Submaximal Loading, and on the Regional Variations in that Architecture..... 74

5.1 Introduction 74

5.2 Methods 79

5.2.1 Sample preparation 79

5.2.2 Image scanning 80

5.2.3 Volumetric analysis 80

5.3 Results 83

5.3.1 Quantitative comparison of subchondral bone under the AM and PL fiber origins (H1) 83

5.3.2 Quantitative comparison of subchondral bone under the AM and PL fiber origins (H2) 84

5.3.3 Directionality of subchondral bone trabeculae (H3) 85

5.4 Discussion 87

5.5 Conclusions 90

5.6 References 91

Chapter 6 : General Discussion.. 95

6.1 Knee kinematics to predict and prevention ACL injury during maneuvers........................ 96

6.2 Lack of evidence for fatigue damage in the subchondral bone of the femoral ACL enthesis and evidence for regional adaptation of that subchondral bone 101

6.3 Strengths and Limitations.. 105

6.4 References 108

Chapter 7 : Conclusions.. 114

Chapter 8 : Suggestion for Future Research 116

8.1 References 118

Appendices... 120

List of Tables

Table 2-1. Demographic data of the knee specimen donors. 22

Table 2-2. Mean (SD) peak angle changes measured via Certus and IMUs, along with the corresponding Bland-Altman Bias and Limit of Agreement results calculated according to the formula in the table footnote at bottom right. 28

Table 2-3. Mean (SD) values for Bland–Altman comparisons of peak angular velocity from Certus and IMUs for the three planes. On average, the Certus measurements tended to overestimate the IMU measurements. The percentage difference (Diff [%]) is defined in the table footnote. 30

Table 3-1. Demographic data for the male donors of the seven knees. The lateral posterior tibial slopes were measured twice by the blind observer and mean (standard deviation, SD) values were calculated. As shown in the right column, the repeated measures experimental design called for increasing impact forces, with one knee randomly selected to act under low impact, and contralateral knee with relatively high impact loading. 42

Table 3-2. Results for the two linear mixed effect models: Model A for LTS and ATT, and Model B for LTS and ITR. 49

Table 4-1. The assigned model enthesial shell geometric and mechanical properties for the finite element simulations. The enthesis shell depth and thickness data were based on averaged shell geometry measured on nano CT scans of 15 femoral entheses from adult donors between 19 and 40 years (see text for details). 65

Table 4-2. Calculated distributions of tensile, compressive and shear stress values on the medial and lateral surfaces of the three model shell entheses. In each cell of the table the number in the top left corner is the stress at the proximal end, while the number in the low right corner is the stress at the distal end of the major diameter. Maximum tensile and shear stress are shown by the deep red color. The small arrow at the center of the plate indicates the direction of the ACL tension. Keys to color map values provide the calculated stress values. 66

Table 5-1. Mean [SD] values for calculated results for AM and PL subchondral bone ROIs..... 84

Table 6-1. Results for the two linear mixed effect models: Model A for MTS and ATT, and Model B for MTS and ITR. 101

Table A-1. Demographic data for the donors of the seven knee pairs in Chapter 2 122

Table A-2. Demographic data for the donors of the seven knee pairs for Chapter 3................ 123

Table A-3. Demographic data for the donors of the seven knees pairs for Chapters 5............. 124

Table A-4. Testing data for the final pivot trials of each data set for Chapter 3....................... 126

Table A-5. LTS measured by the blinded observer (Chapter 3) and the observer who conducted the testing... 127

Table A-6. Quantitative data of femoral subchondral ACL bone analyses for Chapter 5 128

Table B-1. Results for the linear mixed effect model using random intercepts........................ 129

Table B-2. Results for the linear mixed effect model for LTS measured by the observer who conducted the testing, as well as ATT and ITR... 130

List of Figures

Figure 1-1. Hierarchical structure of Type I collagen in bone, skin, and tendon. Reprinted from Chen et al. (2017) [22]. 2

Figure 2-1. Diagram of the Withrow-Oh testing apparatus [17,20] showing the locations of the fixed active marker triads along with the locations of the virtual active markers obtained by manual digitization prior to the experiment. Modified, and reproduced with permission from [Oh et al., 2011, The Journal of Bone and Joint Surgery, Inc]. 24

Figure 2-2. Three examples of the time course of the changes in knee flexion angle during simulated jump landings. Panel (a) shows measurements from the optoelectronic motion capture system, whereas panel (b) shows the calculated angles from the accelerometer and gyroscopic data from the IMUs. The peak angle change from the IMUs was calculated as the difference between the initial resting state and the maximum angle measured. 26

Figure 2-3. Bland–Altman plots comparing the measurements from the two IMUs with those of the motion capture system for measuring peak knee angle change in each direction during simulated jump landings. In this and the following figure, the different colors represent data from different knee specimens (S). 29

Figure 2-4. Bland–Altman plots showing differences, by plane, between Certus system and IMU in the angular velocity change for the tibia (top row) and the femur (bottom row). The x-axis shows the angular velocities measured via the IMUs, whereas the y-axis shows the difference in angles for each plane (left, center, and right panels). The bias was negative in the transverse plane, positive in the frontal plane, and mixed in the sagittal plane for the two bones. 31

Figure 3-1. Measured lateral posterior tibial slope for the right knee of specimen P1. (a) To define the tibial longitudinal axis, a method presented by Hudek et al.[11] was used on a sagittal-plane slice by connecting the centers of the two circles. (b) At the mediolateral center of the lateral tibial plateau, the lateral tibial slope (α) was defined as the angle between the tibial longitudinal axis (as defined in (a) and the line connecting the superior-anterior and the superior-posterior cortices of the lateral tibial plateau. 44

Figure 3-2. Diagram of Withrow-Oh testing apparatus[18,28] showing the diode physical markers ("Markers") on the load cells, and the virtual markers on tibial and femoral landmarks that were recorded using the 3D digitizing wand of the Certus system. 46

Figure 3-3. Scatter plots showing the relationship between normalized impact force and ATT (a) and ITR (b). The lines in (a) and (b) indicate the predicted effect of LTS being assumed constant at 2º, 4 º, 6 º, 8 º and 10 º in order to help interpret the effect of increasing impact force on ATT (a) and ITR (b), respectively, using the results of linear mixed model (Table 2)........................ 50

Figure 3-4. Scatter plots representing the relationship between LTS and ATT (a) and ITR (b). The three lines in (a) and (b) designate normalized impact. The vertical data scatter are the knee kinematic data for the 100 trials for a given LTS associated with each knee. The lines show the force assumed constant at 1BW, 2BW, and 3BW to help interpret the effect of LTS on ATT(a) and (ITR) (b) from the results of the linear mixed model (Table 2)... 51

Figure 4-1. (A) Posterolateral view of a left ACL femoral attachment with the anteromedial (AM) and posterolateral (PL) bundles seen after removal of the medial femoral condyle. (B) Lateral view of the generally oval perimeter of the femoral attachment marked from (A). P indicates the proximal and D indicates the distal end of the femoral condyle. Reproduced with permission from Ferretti et al. (2007) 61

Figure 4-2. (A) Plastic embedded histological section of the origin of the ACL at its femoral entheses stained with Toluidine blue stain. (B) Enlarged view of the tissue within the rectangle indicated in (A) showing part of the femoral entheses with its four tissue zones: bone; (b), calcified fibrocartilage (cf), uncalcified fibrocartilage (uf) and ligamentous tissue (l). The inset at top right in (B) shows a magnified view of the tissue within the white rectangle. Reproduced with permission from Fig. 3 in Beaulieu et al. (2015) 62

Figure 4-3. (A) Top (medial) view of the 3D elliptical finite element shell model showing the linear increase in distributed stress (see color scale for stress levels, with graphs of the tensile ACL stress and force distribution acting on transverse shell sections each having a width of 1/10 of its major diameter. P denotes the proximal end and D denotes the distal end of the enthesis shell's major axis. The yellow arrow indicates the direction of the ACL tension for knee angles near full extension. (B1) Section through the concave shell model in the y-z (coronal) plane showing the projected (attachment) scarf angle, ψ, that the ACL fibers subtend relative to the plane of the major axis of the enthesis. In this illustration, the ACL emerges from the medial (top) surface of the shell, while the lateral surface lies (below) the shell normally supported by trabecular bone (not shown). (B2) shows an x-y (transverse) plane section through the minor axis of the enthesis shell model showing the projected scarf angle, θ. Assumed values for each parameter are given in Table 1.. 64

Figure 4-4. Coronal plane section from a nano CT image of a young adult specimen shows mineralized region thickening (solid arrow heads) at the origin of the PL fibers near the distal (D) end of the enthesis when compared to the thickness at the origin of the AM fibers (open arrow heads) at its proximal (P) end. The vertical red lines delineate the borders of attachment of the AM and PL fibers. The yellow arrow shows the direction of ACL tension for a knee near full extension. 69

Figure 5-1. (a) Proximal-distal axial view of the femur (in yellow), tibia (in transparent blue) and ACL (in green) with the unloaded right knee near full extension. In this view the lateral (L) and medial (M) condyles are seen on the left and right of the image, and the yellow and blue lines are reference lines attached to the femur and tibia, respectively. b) This image shows a simulation of the knee with an internal rotation torque applied to the tibia about its longitudinal axis. The resulting strain in the ACL finite element model is shown in red as it resists axial rotation of the tibia about the center of rotation on the medial condyle (where the blue and yellow lines now cross). In terms of functional anatomy, note how the ACL is optimally located to act as a checkrein, not only to limit excessive posterior translation of the femur relative to the tibia due mainly to the patellofemoral mechanism, but also, importantly, internal tibial rotation in the knee, the last being perhaps underappreciated in the literature. (Still images reproduced from a video animation of a finite element model by Oh (2011)[37]). 75

Figure 5-2. Definition of regions of interest (ROI) for the regional analyses of subchondral bone architecture: (a) ACL attachment area was defined by an ellipse with its major axis parallel with the lateral wall of intercondylar notch (dashed line). The intercondylar notch (EF) line was assumed parallel with the major axis (AB) of the yellow ellipse denoting the enthesial attachment area. AR was defined as the length of the AM fiber attachment, while BR was defined as the length of the PL attachment area. Similarly, CD was defined as the width of the ACL attachment area, which included the AM and PL bundles. All these dimensions were taken from Ferretti et al. (2007) [19]. (b) ROI for H1 and H2: the quantitative comparison between the AM and PL fiber origins. (c) ROI for H 3: the directionalities differences of the trabecular alignments in the direction of ACL tensile loading.. 81

Figure 5-3. ROIs of the nano CT images of subchondral femoral enthesis bone. (a) Coronal plane images of the 5 m^3 cubes sectioned at the center of AM and PL area, while the colored images at right show an example of the segmentation of the cortical bone plate (Cyan) and trabecular bone (Magenta) in each volume. (b) Sagittal plane images of the 5 x 4 x 3 (depth) m^3 cuboids under the ACL attachment area; the trabecular directionalities were analyzed in each image section using an ImageJ directionality plugin. The color wheel at top right illustrates the orientation of trabeculae by color and direction. 83

Figure 5-4. Subchondral bone results beneath the AM and PL fiber origins: (a) BV/TV and (b) Ct.Th. Solid line denotes median, box: 1st – 3rd Quartile range, whiskers: 5 – 95% of data, dot: outliers, dashed line: mean) 85

Figure 5-5. Histogram showing trabecular directionalities, clockwise, by Area of interest. The inset at upper left shows the locations of each measured Area.. 86

Figure 6-1. Scatter plots for LTS measured by MRI vs PTS measured by radiograph, dotted line shows the linear regression between tibial slopes measured by MRI and radiograph................. 99

Figure 6-2. Scatter plots for the relationship between (a) measured LTS and MTS and (b) LTS and the difference between LTS and MTS. 100

Figure B-1. Scatter plots showing the relationship between normalized impact force and ATT (a-1), and LTS versus ATT (a-2). Normalized impact force versus ITR, and LTS versus ITR are shown in (b-1) and (b-2), respectively. The lines indicate the LTS being assumed constant at 2°, 4°, 6°, 8° and 10° in order to examine the effect of increasing impact force effect on ATT (a-1) and ITR (b-1), respectively. In ATT (a-2) and ITR (b-2) the normalized impact force was assumed constant at 1BW, 2BW, and 3BW in order to identify the effect of LTS on ATT. 130

Figure B-2. Power calculations for the effect of LTS on (a) ATT and (b) ITR for different sample sizes. The vertical dashed line denotes the sample size used for this study: n=13 (7 pairs of knees, each with a right and left side, one knee failing via bone fracture)............................ 131

Figure C-1. Subchondral bone plate (Ct.Th) and trabeculae (Tb.Th) morphology, as well as overall subchondral bone morphology (BV/TV and BMD) results beneath the AM, PL fiber origins. The difference between PL and AM (PL-AM) control and tested knee, and low and high impact tested knee parameters is given in the bottom row. Solid line denotes median, box: 1st – 3rd Quartile range, whiskers: 5 – 95% of data, dot: outliers, dashed line: mean) 133

Figure D-1. Sample nano CT image of Specimen P1R. A-1) Transverse plane for AM bundle, A-2) transverse plane for PL bundle, B) sagittal plane, and C) coronal plane. 134

Figure D-2. Sample nano CT image of Specimen P2R. A-1) Transverse plane for AM bundle, A-2) transverse plane for PL bundle, B) sagittal plane, and C) coronal plane 135

Figure D-3. Sample nano CT image of Specimen P3R. A-1) Transverse plane for AM bundle, A-2) transverse plane for PL bundle, B) sagittal plane, and C) coronal plane 136

Figure D-4. Sample nano CT image of Specimen P4R. A-1) Transverse plane for AM bundle, A-2) transverse plane for PL bundle, B) sagittal plane, and C) coronal plane 137

Figure D-5. Sample nano CT image of Specimen P5R. A-1) Transverse plane for AM bundle, A-2) transverse plane for PL bundle, B) sagittal plane, and C) coronal plane 138

Figure D-6. Sample nano CT image of Specimen P6R. A-1) Transverse plane for AM bundle, A-2) transverse plane for PL bundle, B) sagittal plane, and C) coronal plane 139

Figure D-7. Sample nano CT image of Specimen P7R. A-1) Transverse plane for AM bundle, A-2) transverse plane for PL bundle, B) sagittal plane, and C) coronal plane 140

Figure D-8. Sample nano CT image of Specimen P1L. A-1) Transverse plane for AM bundle, A-2) transverse plane for PL bundle, B) sagittal plane, and C) coronal plane 141

Figure D-9. Sample nano CT image of Specimen P2L. A-1) Transverse plane for AM bundle, A-2) transverse plane for PL bundle, B) sagittal plane, and C) coronal plane 142

Figure D-10. Sample nano CT image of Specimen P3L. A-1) Transverse plane for AM bundle, A-2) transverse plane for PL bundle, B) sagittal plane, and C) coronal plane 143

Figure D-11. Sample nano CT image of Specimen P4L. A-1) Transverse plane for AM bundle, A-2) transverse plane for PL bundle, B) sagittal plane, and C) coronal plane 144

Figure D-12. Sample nano CT image of Specimen P5L. A-1) Transverse plane for AM bundle, A-2) transverse plane for PL bundle, B) sagittal plane, and C) coronal plane 145

Figure D-13. Sample nano CT image of Specimen P6L. A-1) Transverse plane for AM bundle, A-2) transverse plane for PL bundle, B) sagittal plane, and C) coronal plane 146

Figure D-14. Sample nano CT image of Specimen P7L. A-1) Transverse plane for AM bundle, A-2) transverse plane for PL bundle, B) sagittal plane, and C) coronal plane 147

Figure D-15. Sample nano CT image of Specimen S1R. A-1) Transverse plane for AM bundle, A-2) transverse plane for PL bundle, B) sagittal plane, and C) coronal plane 148

Figure D-16. Sample nano CT image of Specimen S2R. A-1) Transverse plane for AM bundle, A-2) transverse plane for PL bundle, B) sagittal plane, and C) coronal plane 149

Figure D-17. Sample nano CT image of Specimen S3R. A-1) Transverse plane for AM bundle, A-2) transverse plane for PL bundle, B) sagittal plane, and C) coronal plane 150

Figure D-18. Sample nano CT image of Specimen S4R. A-1) Transverse plane for AM bundle, A-2) transverse plane for PL bundle, B) sagittal plane, and C) coronal plane 151

Figure D-19. Sample nano CT image of Specimen S5R. A-1) Transverse plane for AM bundle, A-2) transverse plane for PL bundle, B) sagittal plane, and C) coronal plane 152

Figure D-20. Sample nano CT image of Specimen S6R. A-1) Transverse plane for AM bundle, A-2) transverse plane for PL bundle, B) sagittal plane, and C) coronal plane 153

Figure D-21. Sample nano CT image of Specimen S7R. A-1) Transverse plane for AM bundle, A-2) transverse plane for PL bundle, B) sagittal plane, and C) coronal plane 154

Figure D-22. Sample nano CT image of Specimen S1L. A-1) Transverse plane for AM bundle, A-2) transverse plane for PL bundle, B) sagittal plane, and C) coronal plane 155

Figure D-23. Sample nano CT image of Specimen S2L. A-1) Transverse plane for AM bundle, A-2) transverse plane for PL bundle, B) sagittal plane, and C) coronal plane 156

Figure D-24. Sample nano CT image of Specimen S3L. A-1) Transverse plane for AM bundle, A-2) transverse plane for PL bundle, B) sagittal plane, and C) coronal plane 157

Figure D-25. Sample nano CT image of Specimen S4L. A-1) Transverse plane for AM bundle, A-2) transverse plane for PL bundle, B) sagittal plane, and C) coronal plane 158

Figure D-26. Sample nano CT image of Specimen S5L. A-1) Transverse plane for AM bundle, A-2) transverse plane for PL bundle, B) sagittal plane, and C) coronal plane 159

Figure D-27. Sample nano CT image of Specimen S6L. A-1) Transverse plane for AM bundle, A-2) transverse plane for PL bundle, B) sagittal plane, and C) coronal plane 160

Figure D-28. Sample nano CT image of Specimen S7L. A-1) Transverse plane for AM bundle, A-2) transverse plane for PL bundle, B) sagittal plane, and C) coronal plane 161

Figure E. Directionality density for Specimens. Figure 5-1-(c) shows the location of measured area (ROI) 162

List of Appendices

Appendix A : Comprehensive Datasets for the Dissertation 121

Appendix B : The Results for LTS Measured by the Observer who Conducted the Testing in relation to Chapter 3 as the Secondary Analysis 129

Appendix C : Measured Morphometric of the Subchondral Bone of the Femoral Enthesis (Chapter 5- Aim 1).. 133

Appendix D : Nano CT Images of Sections through the ACL Femoral Enthesis from all Specimens (Chapter 5 - Aim 2). 134

Appendix E : Collection of Directionality Density Plots of All Specimens (Chapter 5 - Aim 3) 162

Abstract

The anterior cruciate ligament (ACL) is an important kinematic constraint connecting the femur to the tibia to ensure normal knee function. It acts as a checkrein to limit the forward shear and internal rotation of the tibia with respect to the femur caused by internal and external forces during activities of daily living. The ACL is particularly stressed during the large rapid loads associated with using one foot to land a jump, make a sudden stop or turn during sports like basketball, soccer, football, volleyball, and skiing as evidenced by the more than 200,000 ACL ruptures each year in the U.S in active people and athletes. Better identification of the risk factors is needed in order to prevent them, as well as the unfortunate chronic knee osteoarthritis than inevitably begins within the decade in half the cases no matter how they are treated. The present work builds on recent findings from our laboratory that at least some ACL injuries may be related to localized material fatigue of the ligament near its origin from the femur under repetitive loading.

The goal of this dissertation was to investigate how knee kinematics and certain bone morphologies may contribute to the mechanism of ACL injury.

Young adult cadaveric knees were subjected to *in vitro* mechanical testing with a custom testing apparatus that simulated pivot landings by applying large impulsive simultaneous knee compression, a flexion moment and an internal tibial torque. The 3-D kinetics and muscle forces were recorded, and tibiofemoral kinematics were measured using a motion capture system during these landings. The measured knee joint movements were used to test the hypotheses that (1) the tibiofemoral kinematics obtained from the laboratory motion capture system and wearable inertial measurement units are comparable (**Chapter 2**), and (2) a lateral tibial slope measured from 3T

MR imaging correlated significantly with the anterior tibial translation and internal tibial rotation (which have previously been shown to be directly proportional to ACL strains during pivot landings) (**Chapter 3**). To better understand why localized fatigue may accumulate near the ACL femoral enthesis, (3) a finite element model of the subchondral bone and calcified cartilage shell at its femoral enthesis was developed to determine the effect of three common shell profiles (concave, flat, convex) to predict the distribution of large tensile and shear stresses on the structure **(Chapter 4)**. Then, using 3D nano CT scans through the subchondral bone of the ACL femoral enthesis, we tested the hypotheses that (4-a) sub-maximal repetitive knee loading cause the fatigue damage in the bone underlying femoral enthesis (4-b) the thickness of the subchondral bone in the most highly stressed region is consistently thicker than elsewhere, and (4-c) lifetime activities cause regions with larger predicted tensile stresses to correlate with the trabecular alignment of a tensile arcade under the femoral subchondral plate (**Chapter 5**).

It was concluded that under strenuous, highly dynamic, repetitive pivot landings (a) the wearable IMUs did not reliably measure tibiofemoral motions in all three planes, even in the absence of soft tissue motion artifact; (b) that athletes with large lateral tibial slope will experience greater anterior tibial translation and internal tibial rotation than those with more moderate slope in jump landings. Furthermore, it was also concluded that as evidence of bony adaptation due to Wolff's law, (c) the concave enthesis help to reduce the peak tensile and shear stresses in the subchondral shell: and (d) in contrast to previous work on the ligament itself, no overt signs of subchondral bone fatigue damage were visible on the nano CT scans at 20 μm resolution of the femoral enthesis following repetitive submaximal ACL loading. However, the subchondral bone resisting ACL tensile loading of the heavily loaded PL fibers is significantly thicker than elsewhere in the entheses, and there is evidence that the trabecular bone immediately under the AM fibers of the ACL aligned to the direction of ACL loading of tension as given Wolff's law.

Chapter 1: Introduction to the Dissertation Proposal

1.1 Background

What is the role of the ACL? The anterior cruciate ligament (ACL) connects the distal femur to the proximal tibia to help provide stability at the knee joint[28]. This includes resisting forward shear and external rotation of the femur on the tibia during physical activities[18,45]. The ACL is often described as having a 'two-bundle' morphology, comprised of anteromedial (AM) and posterolateral (PL) bundles, in order to share the loads on the ACL[24,30,50]. In terms of functional anatomy, the longer AM fiber bundle primarily resists forward tibial shear, while the shorter PL fiber primarily resists internal tibial rotation[2,24,50,60,86]. The PL bundle elongates more than the AM bundle during weight-bearing with a knee almost fully extended[40]. The location where the PL fibers are arise from the femur causes the fiber to be shortened by rotating toward the insertion onto the tibia as the knee is flexed[38]. This could be the reason why more than 40% of partial ACL tears occur in isolated PL fibers[71]; these partial tears can induce functionally unstable of the knee and eventually lead to ACL failure[54] either by a frank ACL rupture or a failure to restrict forward translation of the tibia to less than 3 mm on an "anterior drawer" test in the clinic[18].

What is the composition of the ACL? The major component of ACL is Type 1 collagen which can self-assemble into hierarchical structures from fibril-forming collagen molecues[59]. This hierarchical level of collagen organization starts at the nanometer scale with collagen molecules assembling to collagen fibrils at the micrometer scale, then into fibers which then forms ligament bundles at the macro-hierarchical structures (Figure 1-1)[22]. Thus, the heterogeneity of structure and composition at the molecular lever contributes to the mechanical strength of the ACL[23].

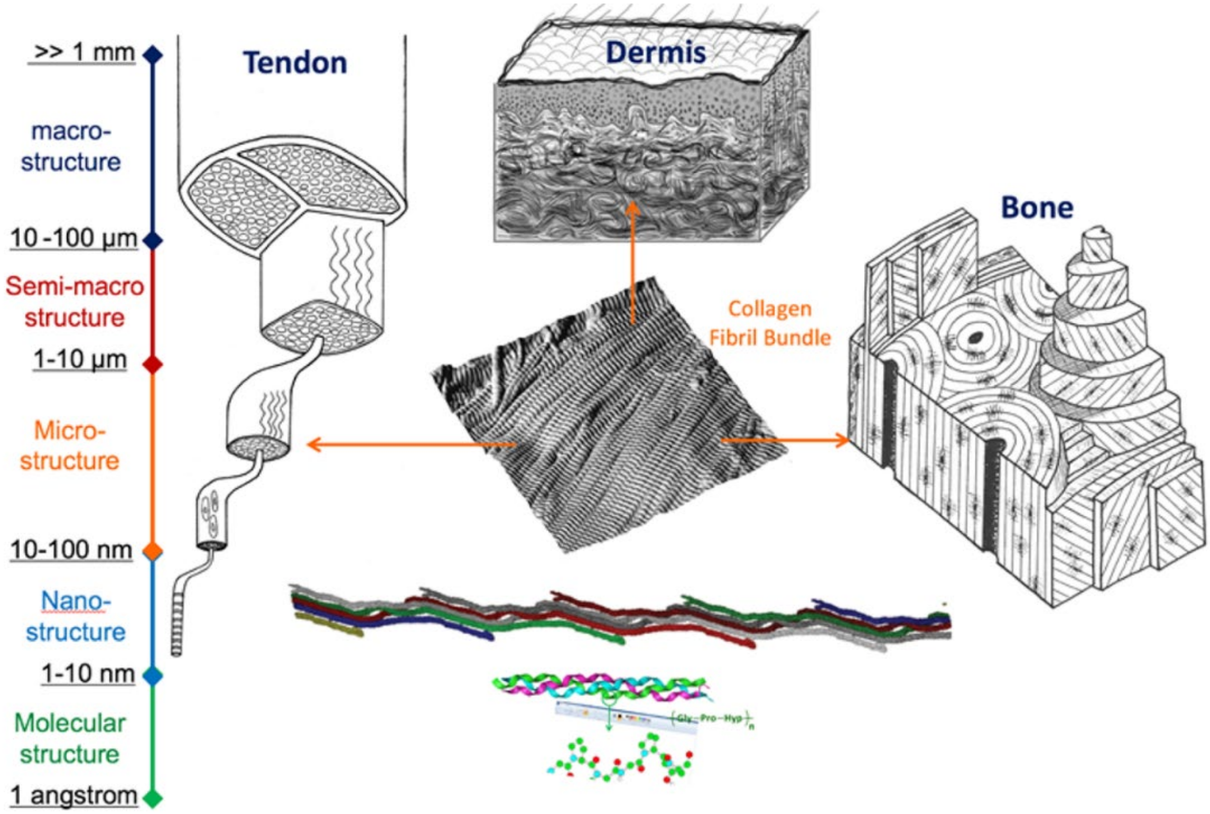

Figure 1-1. Hierarchical structure of Type I collagen in bone, skin, and tendon. Reprinted from Chen et al. (2017) [22]**.**

<u>What is known about how the ACL attaches to bone at each end of the ligament via the entheses?</u> The enthesis is the attachment site where the ligament attaches to bone. It is a dynamic area that distributes loads applied to the enthesis during movements[10]. This insertion has a complex and heterogeneous structure and composition in four zones: ligament (L), uncalcified fibrocartilage (UF), calcified fibrocartilage (CF), and bone (B)[10] (Figure 4-1). The composition and structure of the enthesis are determined by the history of the force experienced throughout its lifetime[31].

How common are ACL injuries? Approximately 200,000 anterior cruciate ligament (ACL) ruptures occur annually in the U.S.[32,53]. These are especially seen in athletes who participate in sports such as basketball, football, gymnastics, lacrosse, and soccer which have been shown to have a high risk for ACL injury[37]. Indeed over half, 65 %, of ligamentous problems during sports are ACL or ACL-related injuries[16].

Non-Contact Injuries: Video analyses have shown that ACL injuries are most often of the “non-contact” variety, meaning they occur primarily without direct contact[15,57] with another player or object; they occur during a dynamic foot plant from a jump landing, a sudden change in direction, abrupt stop, or dynamic valgus [65,75,77].Three-quarters of ACL injuries are of the non-contact type even in the high contact sports like football[15]. Therefore, identifying and detecting the history of movements or loadings causing ACL injuries is essential to better preventing ACL injury. For example, although video analysis[43,57,75,77] has been used to try to better understand tibiofemoral kinematics leading to injury, wearable sensors[9,26,63,66] offer the potential to make better measurements of the injurious tibial femoral motions because of the higher sampling frequencies available (i.e., >100 Hz) than the standard 30 or 60 fps video that has mostly been used to date. However, both suffer from measurement artefacts caused by soft tissue motion relative to the underlyin bones.

Wearable sensors to predict and/or prevent injury. Over the past 10 years wearable sensors have become more and more widespread for monitoring and recording athletic movements and physical activities. One of the commonly used wearable sensors is the inertial measurement unit (IMU) which has the advantage of being small, light, and easily attachable to different body segments[16,37,39]. Each IMU consists of a tri-axial linear accelerometer, tri-axial rate gyroscopes that measure angular velocity, and a triaxial magnetometers to measure the orientation of the gyro relative to the gravity vector[78]. However, research is needed to fill an existing knowledge gap as to whether wearable sensors can be used to accurately measure the highly dynamic tibiofemoral kinematics that have already been recorded using static gold standard laboratory motion capture (mocap) equipment and shown to positively correlate with ACL strain and failure (Chapter 2).

What are the known risk factors for ACL injury? Non-contact injury risk factors are known to include environmental, hormonal, neuromechanical factors, and anatomical factors[33,52]. Environment (extrinsic) risk factors include the type of shoe, the type of playing surface (natural or artificial grass surface, hard floor, etc.), interaction with the shoe and playing surface, and protective equipment. Hormonal, neuromechanical, and anatomical factors are considered intrinsic and have been extensively investigated. For example, female hormones, estrogen levels, influence the metabolic[48,83], compositional changes, and structural properties[85] of the ACL as well as muscle stiffness[8,58]. Neuromechanical factors can be divided into three groups: movement patterns (e.g., knee flexion, varus moment, tibial anterior shear, or pivot landings[13,19,20,82]), muscle activation patterns, and muscle stiffness. Lastly, anatomical factors include knee joint morphology (e.g., lateral posterior tibial slope (LTS)[11,12], femoral alpha angle,[5,32] ACL cross-sectional area[33,70] and femoral intercondylar notch size and shape [42,44,72,74]), lower-extremity alignment[62,67], and body mass index (BMI)[73]. Despite the extensive studies, ACL injuries continue to occur at a high rate, especially in children, so a better understanding of the ACL injury mechanism is needed to prevent future ACL injuries and their sequelae.

What role does repetitive loading play in ACL injury? In training for a sport, repeated maneuver is essential for athletes to develop skills and performances. However, the intensity and frequency of the loading cycles can lead the human ACL to fail under higher loading magnitudes and/or increased the number of loading cycles[47]. Recent studies from our laboratory suggest that the ACL can be progressively weakened due to an accumulation of material fatigue damage[23] caused when the rate of fatigue damage accumulation exceeds the rate at which biological processes repair the collagen-based tissue [22].

Known sex differences in knee morphology in ACL injury risk. The four types of risk factors described above also generally contribute to sex differences. Female athletes often experience higher rates of ACL injury than male athletes, ranging from two to eight times higher depending on the age and sport[1,4,37,61]. Many studies of sex differences have focused on whether the differences in knee morphology (anatomic factors) could account for the sex difference in ACL injuries[36,46]. For example, a smaller notch-width index[3,39,68], smaller medial tibial depth[34,35], greater lateral tibial slope (LTS) [35,51,76] and a smaller ACL size (volume and cross-sectional area)[3,21,27] are known sex differences and have been associated with increased ACL injury risk. In addition, a steeper LTS has been shown to not only increase the risk for ACL rupture but also increase ACL strain during knee loading[14,17,76,79], thereby suggesting a causal relationship. However, the relationship between LTS and the resulting tibiofemoral kinematics in the form of anterior-posterior tibial translation (ATT) and internal tibial rotation (ITR) during a dynamic foot plant is poorly understood (Chapter 3).

Where is most vulnerable region to ACL injury? Clinically, most ruptures occur in the proximal third of the ACL near its origin at the femoral enthesis[81]. A quantitative analysis which reveal the significant differences in fibrocartilage quantity and ligament attachment angle between the femoral and tibial enthesis of the ACL[7] may explain the difference injury rates in the ACL, but as we shall see later much still remains unknown. In a recent paper, progression of the ligament fatigue damage was exhibited more at the proximal region of the ACL fibers compared than midsubstance of distal regions of the ACL[41], and the accumulated damage to collagen fibrils and fibers at the ACL femoral enthesis was found as the evidence of ACL fatigue failure[23]. During knee joint movement, tensional and torsional forces are applied to the ACL, and the stress would be transferred to the bone. However, any fatigue evidence in the subchondral bone of ACL femoral enthesis is not known. Therefore, we hypothesized that repetitive knee loading would cause fatigue damage in the subchondral bone beneath ACL femoral enthesis (Chapter 5)

What is known about the morphology and osseous landmarks of femoral attachment of the ACL? In general, the ACL femoral attachment is elliptically shaped[25,55] on the medial aspect of the posterior lateral femoral condylar . The existence of a vascularized fibrous surface membrane over the ACL makes the shape of ACL femoral attachment area looks broader and oval with fan-like extensions anteriorly and posteriorly, but after the removal of the fibrous surface membrane, the ACL attachment area appears like a narrower ellipse (Figure 4-2-B) [29]. From the ACL femoral enthesis, the type 1 collagen fibers narrow in the ribbon-like collagenous body of the ACL (Figure 4-2-A)[29,69] to pass through the enthesis that marks the boundary between bone and ligament. Recently, the fiber angle of attachment at the ACL as it arises from lateral femoral epicondyle was quantified[7], and six different cross sectional profile of human femoral entheses were identified from the shape of their tidemarks: concave, convex and a combination of the two[6].

Bone adaptation in ACL injury. The shape and architecture of bones are highly adaptive to the history and direction of mechanical strain in the bone, as described by Wolff's law[84]. In what follows, for simplicity, we will consider the ACL to be comprised of two bundles, an AM and a PL fiber bundle, even if in fact there can be a smooth transition between the two regions. A finite element analysis of the effect of the shape of the femoral enthesis on ACL fiber suggested that the shorter PL fiber bundle of the ACL is more highly strained than the longer AM fiber bundle because of the scarf attachment angle[49]. When sectioned perpendicular to the major axis of the ellipse on the ACL attachment area, the most distal regions of femoral entheses were all found to have a concave profile, whereas the proximal sections were mostly convex[6]. As mentioned earlier, the AM and PL bundles play different roles as well as different functional anatomy[24,50,86], and this could be the reason why PL fibers are more often torn than the AM fibers[71]. From these studies, we hypothesized that the different shape of femoral enthesis (a flat enthesis (as a control), a concave enthesis and a convex enthesis) can affect the distribution of tensile and shear under ACL tension (Chapter 4). It is not known whether the structural failure initiates in the fibers of the ACL or in the subchondral femoral bone where those fibers attach to the ACL. One can speculate that the femoral bone underneath the origin of the PL fibers may be more vulnerable under ACL tensile stress than the bone under the origin of the AM fibers, since strain is larger there[49] and stress fractures in bone are a well-known problem under repetitive loading (i.e., shin splints)[64]. Furthermore, given Wolff's law, we hypothesized that the subchondral trabecular bone of the enthesis may exhibit a tensile arcade aligned with the tensile fiber loads, and that the bone underneath the origin of the PL bundle must be structurally more substantial (thicker and possibly denser) than the bone under AM bundle in order to reduce the applied stress. (Chapter 5).

1.2 Overall objectives and experimental approach

The objective of this dissertation is to better understand the factors leading to ACL injury under dynamic impulsive loading of the human knee known to cause ACL failure. Particular attention will be paid to the detailed ACL bone morphologies (femoral enthesis and lateral tibial slope), tibiofemoral kinematics, and any evidence of fatigue damage in the femoral subchondral enthesial bone that increase the risk of ACL injury.

This dissertation utilized a custom *in vitro* knee loading apparatus developed by Thomas Withrow[80] and refined by Youkeun Oh[56] in their doctoral dissertations to simulate a 3-D impulsive landing applying a combination of knee compression, flexion, and internal tibial torque with realistic muscle forces. This is the worst-case loading scenario for the ACL (see Background section above). Tibiofemoral kinematics were measured from a laboratory gold standard optoelectronic motion capture system as well as IMUs in order to better understand the ACL injury mechanism during impulsive knee loading known to be risk for the ACL. To better investigate knee morphological factors, we utilized 3T MR images of each knee joint along with nanoCT images of the bone beneath the femoral entheses. The lateral tibial slope, a key risk factor (see Introduction), was measured from MR images in order to determine its relationship to knee kinematics in the experimental knee loading model. A simple finite element model of femoral enthesis was developed to understand the bony morphology, and the microscopic anatomical characteristics of the femoral enthesis subchondral bone were evaluated using nanoCT to understand how donor life history of applied stress affected the structure of the subchondral bone architecture because of Wolff's law and whether repetitive loading increased the risk of fatigue damage of ACL femoral subchondral enthesial bone.

1.3 Organization of the dissertation including working hypotheses

The dissertation consists of eight chapters. Chapters 2 - 4 represent full-length manuscripts published or submitted to peer-reviewed journals.

<u>*Chapter 2 (Published in Sensors, 2022):*</u> We tested the hypothesis that the Certus optoelectronic motion capture system and wearable IMUs provide comparable measurements of the 3D changes in tibial-femoral angle and angular velocity during simulated unipedal jump landings. A Bland-Altman analysis was used to calculate the limits of agreement between the wearable IMU measurements and those from a Certus lab-based motion capture system. For knee angle changes, the IMU data were compared with the gold-standard Certus data, while the tibial

and femoral angular velocities derived from the Certus system were compared with the gold standard IMU rate gyroscope data. This study has provided the opportunity to assess the best possible dynamic performance of the APDM IMU and Certus motion capture systems, in the absence of soft tissue artifacts by eliminating the usual noise generated due to soft tissue vibration. The results suggest that these IMUs could not reliably measure these rapid peak 3D tibiofemoral angle changes, while the reliability of the Certus measurements of peak tibiofemoral angle velocity changes depended on both the plane of measurement and velocity magnitude.

Chapter 3 (Submitted to OJSM, 2022). The hypothesis was tested that an increased lateral posterior tibial slope (LTS), a known risk factor for ACL injury, correlates with increasing anterior tibial translation (ATT) and internal tibial rotation (ITR) during a range of strenuous simulated pivot landings in young male adult knees *in vitro*. The results show that a steeper LTS was associated with increased ATT and ITR, with ITR increasing at least 2.5 times more than ATT. This helps to explain the mechanism by which a large lateral tibial slope increases the risk of ACL injury. Since ACL strain is known to be proportional to ATT and ITR, athletes with larger LTS likely repeatedly load their ACLs more than those with lower slopes.

Chapter 4. Finite element models were used to examine the effect that a flat enthesis (as a control), a concave enthesis and a convex enthesis had on the distribution of tensile, compressive and shear stress on the top and bottom surfaces of an enthesial shell to determine which shape reduced peak stress the most and to find the locations of peak tensile and shear stress which could be likely locations for fatigue failure to initiate. The results shown that a concave profile is advantageous because it exhibited the lowest tensile and shear stress concentrations of the three profiles. The maximum tensile stress located at the proximal end of the enthesis, and the peak shear stress was located lateral to the distal end of the concave enthesis.

Chapter 5. We investigated the enthesial subchondral bone structural characteristics reinforcing the femoral ACL enthesis to address fatigue damage in the subchondral bone. We tested the hypothesis that the bone under the PL bundle of the ACL enthesis is denser and thicker with a higher bone fraction and cortical bone thickness than under AM bundle because it has to carry greater shear strain. Furthermore, we also tested the hypothesis that subchondral trabecular bone under the AM fibers aligns with the known direction of ACL tension near full knee extension. The results suggest that the bone immediately under the femoral ACL origin adapts to a lifetime of loading history in a manner consistent with Wolff's law, but not suggest any evidence of fatigue damage in the subchondral bone under the femoral ACL enthesis at the 20 μm.

Chapter 6. This is a General Discussion of Chapters 2-5 results within the context of what is already known in the literature.

Chapter 7. Conclusions

Chapter 8. Suggestions for Future Research

Appendices: Appendix A provides the comprehensive datasets from Chapter 2-5 of this dissertation. Appendix B contains the results for LTS measured by the same observer in relation to Chapter 3 (as a secondary analysis). Appendix C provides the calculated results as fatigue evidence on the subchondral bone (Chapter 5- Aim 1). Appendix D and E comprise a collection of nano-CT images of the segmented subchondral bone underneath the AM and PL bundles (Chapter 5 - Aim 2) and statistical plots for the trabecular directionalities for the ACL in 14 pairs (28 knees) of young adult specimens (Chapter 5 - Aim 3).

1.4 References

1. Agel J, Arendt EA, Bershadsky B. Anterior cruciate ligament injury in national collegiate athletic association basketball and soccer: A 13-year review. *Am J Sports Med*.

2005;33(4):524–530. doi:10.1177/0363546504269937

2. Amis AA. The functions of the fibre bundles of the anterior cruciate ligament in anterior drawer, rotational laxity and the pivot shift. *Knee Surgery, Sport Traumatol Arthrosc*. 2012;20(4):613–620. doi:10.1007/s00167-011-1864-7

3. Anderson AF, Dome DC, Gautam S, Awh MH, Rennirt GW. Correlation of anthropometric measurements, strength, anterior cruciate ligament size, and intercondylar notch characteristics to sex differences in anterior cruciate ligament tear rates. *Am J Sports Med*. 2001;29(1):58–66. doi:10.1177/03635465010290011501

4. Arendt E, Dick R. Knee injury patterns among men and women in collegiate basketball and soccer: NCAA data and review of literature. *Am J Sports Med*. 1995;23(6):694–701.

5. Barnum MS, Boyd ED, Vacek P, Slauterbeck JR, Beynnon BD. Association of geometric characteristics of knee anatomy (alpha angle and intercondylar notch type) with noncontact ACL injury. *Am J Sports Med*. 2021;49(10):2624–2630. doi:10.1177/03635465211023750

6. Beaulieu ML, Carey GE, Schlecht SH, Wojtys EM, Ashton-Miller JA. On the heterogeneity of the femoral enthesis of the human ACL: microscopic anatomy and clinical implications. *J Exp Orthop*. 2016;3(1). doi:10.1186/s40634-016-0050-8

7. Beaulieu ML, Carey GE, Schlecht SH, Wojtys EM, Ashton-Miller JA. Quantitative comparison of the microscopic anatomy of the human ACL femoral and tibial entheses. *J Orthop Res*. 2015;33(12):1811–1817. doi:10.1002/jor.22966

8. Bell DR, Blackburn JT, Norcorss MF, et al. Estrogen and muscle stiffness have a negative relationship in females. *Knee Surgery, Sport Traumatol Arthrosc*. 2012;20(2):361–367. doi:10.1007/s00167-011-1577-y

9. Bell KM, Onyeukwu C, McClincy MP, et al. Verification of a portable motion tracking system for remote management of physical rehabilitation of the knee. *Sensors (Switzerland)*. 2019;19(5). doi:10.3390/s19051021

10. Benjamin M, Toumi H, Ralphs JR, Bydder G, Best TM, Milz S. Where tendons and ligaments meet bone: Attachment sites ('entheses') in relation to exercise and/or mechanical load. *J Anat*. 2006;208(4):471–490. doi:10.1111/j.1469-7580.2006.00540.x

11. Bernhardson AS, Aman ZS, Dornan GJ, et al. Tibial slope and its effect on force in anterior cruciate ligament grafts: Anterior cruciate ligament force increases linearly as posterior tibial slope increases. *Am J Sports Med*. 2019;47(2):296–302. doi:10.1177/0363546518820302

12. Bernhardson AS, DePhillipo NN, Daney BT, Kennedy MI, Aman ZS, LaPrade RF. Posterior tibial slope and risk of posterior cruciate ligament injury. *Am J Sports Med*. 2019;47(2):312–317. doi:10.1177/0363546518819176

13. Besier TF, Lloyd DG, Cochrane JL, Ackland TR. External loading of the knee joint during running and cutting maneuvers. *Med Sci Sports Exerc*. 2001;33(7):1168–1175.

doi:10.1097/00005768-200107000-00014

14. Beynnon B, Yu J, Huston D, et al. A sagittal plane model of the knee and cruciate ligaments with application of a sensitivity analysis. *J Biomech Eng*. 1996;118(2):227–239. doi:10.1115/1.2795965

15. Boden BP, Sheehan FT, Torg JS, Hewett TE. Non-contact ACL injuries: Mechanisms and risk factors. *Am Acad Orthop Surg*. 2010;18(9):520–527.

16. Bollen S. Epidemiology of knee injuries: Diagnosis and triage. *Br J Sports Med*. 2000;34(3):227–228. doi:10.1136/bjsm.34.3.227

17. Brandon ML, Haynes PT, Bonamo JR, Flynn MII, Barrett GR, Sherman MF. The association between posterior-inferior tibial slope and anterior cruciate ligament insufficiency. *Arthrosc - J Arthrosc Relat Surg*. 2006;22(8):894–899. doi:10.1016/j.arthro.2006.04.098

18. Butler DL, Noyes FR, Grood ES. Ligamentous restraints to anterior-posterior drawer in the human knee. A biomechanical study. *J Bone Jt Surg - Ser A*. 1980;62(2):259–270. doi:10.2106/00004623-198062020-00013

19. Chappell JD, Herman DC, Knight BS, Kirkendall DT, Garrett WE, Yu B. Effect of fatigue on knee kinetics and kinematics in stop-jump tasks. *Am J Sports Med*. 2005;33(7):1022–1029. doi:10.1177/0363546504273047

20. Chappell JD, Yu B, Kirkendall DT, Garrett WE. A comparison of knee kinetics between male and female recreational athletes in stop-jump tasks. *Am J Sports Med*. 2002;30(2):261–267. doi:10.1177/03635465020300021901

21. Chaudhari AMW, Zelman EA, Flanigan DC, Kaeding CC, Nagaraja HN. Anterior cruciate ligament–Injured subjects have smaller anterior cruciate ligaments than matched controls: A magnetic resonance imaging study. *Am J Sports Med*. 2009;37(7):1282–1287. doi:10.1177/0363546509332256

22. Chen J, Ahn T, Colón-Bernal ID, Kim J, Banaszak Holl MM. The Relationship of Collagen Structural and Compositional Heterogeneity to Tissue Mechanical Properties: A Chemical Perspective. *ACS Nano*. 2017;11(11):10665–10671. doi:10.1021/acsnano.7b06826

23. Chen J, Kim J, Shao W, et al. An anterior cruciate ligament failure mechanism. *Am J Sports Med*. 2019;47(9):2067–2076. doi:10.1177/0363546519854450

24. Christel PS, Akgun U, Yasar T, Karahan M, Demirel B. The contribution of each anterior cruciate ligament bundle to the Lachman test. *J Bone Joint Surg Br*. 2012;94-B(1):68–74. doi:10.1302/0301-620x.94b1.26562

25. Colombet P, Robinson J, Christel P, et al. Morphology of Anterior Cruciate Ligament Attachments for Anatomic Reconstruction: A Cadaveric Dissection and Radiographic Study. *Arthrosc - J Arthrosc Relat Surg*. 2006;22(9):984–992. doi:10.1016/j.arthro.2006.04.102

26. Dahl KD, Dunford KM, Wilson SA, Turnbull TL, Tashman S. Wearable sensor validation of sports-related movements for the lower extremity and trunk. *Med Eng Phys*. 2020;84:144–150. doi:10.1016/j.medengphy.2020.08.001

27. Dienst M, Schneider G, Altmeyer K, et al. Correlation of intercondylar notch cross sections to the ACL size: A high resolution MR tomographic in vivo analysis. *Arch Orthop Trauma Surg*. 2007;127(4):253–260. doi:10.1007/s00402-006-0177-7

28. Duthon VB, Barea C, Abrassart S, Fasel JH, Fritschy D, Ménétrey J. Anatomy of the anterior cruciate ligament. *Knee Surgery, Sport Traumatol Arthrosc*. 2006;14(3):204–213. doi:10.1007/s00167-005-0679-9

29. Ferretti M, Ekdahl M, Shen W, Fu FH. Osseous landmarks of the femoral attachment of the anterior cruciate ligament: An anatomic study. *Arthrosc - J Arthrosc Relat Surg*. 2007;23(11):1218–1225. doi:10.1016/j.arthro.2007.09.008

30. Furman W, Marshall J, Girgis F. The anterior cruciate ligament, A functional analysis based on postmortem studies. *J Bone Jt Surg Am*. 1976;2(58):179–185.

31. Gao J, Messner K. Quantitative comparison of soft tissue-bone interface at chondral ligament insertions in the rabbit knee joint. *J Anat*. 1996;188 (Pt 2:367–373.

32. Griffin LY, Agel J, Albohm MJ, et al. Noncontact anterior cruciate ligament injuries: Risk factors and prevention strategies. *J Am Acad Orthop Surg*. 2000;8(3):141–150. doi:10.5435/00124635-200005000-00001

33. Griffin LY, Albohm MJ, Arendt EA, et al. Understanding and preventing noncontact anterior cruciate ligament injuries: A review of the Hunt Valley II Meeting, January 2005. *Am J Sports Med*. 2006;34(9):1512–1532. doi:10.1177/0363546506286866

34. Hashemi J, Chandrashekar N, Gill B, et al. The geometry of the tibial plateau and its influence on the biomechanics of the tibiofemoral joint. *J Bone Jt Surg - Ser A*. 2008;90(12):2724–2734. doi:10.2106/JBJS.G.01358

35. Hashemi J, Chandrashekar N, Mansouri H, et al. Shallow medial tibial plateau and steep medial and lateral tibial slopes: New risk factors for anterior cruciate ligament injuries. *Am J Sports Med*. 2010;38(1):54–62. doi:10.1177/0363546509349055

36. Hewett TE, Myer GD, Ford KR. Anterior cruciate ligament injuries in female athletes: Part 1, mechanisms and risk factors. *Am J Sports Med*. 2006;34(2):299–311. doi:10.1177/0363546505284183

37. Hootman JM, Dick R, Agel J. Epidemiology of collegiate injuries for 15 sports: Summary and recommendations for injury prevention initiatives. *J Athl Train*. 2007;42(2):311–319.

38. Hosseini A, Gill TJ, Li G. In vivo anterior cruciate ligament elongation in response to axial tibial loads. *J Orthop Sci*. 2009;14(3):298–306. doi:doi:10.1007/s00776-009-1325-z.

39. Ireland ML, Ballantyne BT, Little K, McClay IS. A radiographic analysis of the relationship between the size and shape of the intercondylar notch and anterior cruciate

ligament injury. *Knee Surgery, Sport Traumatol Arthrosc*. 2001;9(4):200–205. doi:10.1007/s001670100197

40. Katouda M, Soejima T, Kanazawa T, Tabuchi K, Yamaki K, Nagata K. Relationship between thickness of the anteromedial bundle and thickness of the posterolateral bundle in the normal ACL. *Knee Surgery, Sport Traumatol Arthrosc*. 2011;19(8):1293–1298. doi:10.1007/s00167-011-1417-0

41. Kim J, Baek SY, Schlecht SH, et al. Anterior cruciate ligament microfatigue damage detected by collagen autofluorescence in situ. *J Exp Orthop*. 2022;9(1). doi:10.1186/s40634-022-00507-6

42. Kızılgöz V, Sivrioğlu AK, Ulusoy GR, Aydın H, Karayol SS, Menderes U. Analysis of the risk factors for anterior cruciate ligament injury: an investigation of structural tendencies. *Clin Imaging*. 2018;50(October 2017):20–30. doi:10.1016/j.clinimag.2017.12.004

43. Krosshaug T, Nakamae A, Boden BP, et al. Mechanisms of anterior cruciate ligament injury in basketball: Video analysis of 39 cases. *Am J Sports Med*. 2007;35(3):359–367. doi:10.1177/0363546506293899

44. Kumar Panigrahi T, Das A, Mohanty T, Samanta S, Kumar Mohapatra S. Study of relationship of posterior tibial slope in anterior cruciate ligament injury. *J Orthop*. 2020;21(June):487–490. doi:10.1016/j.jor.2020.08.032

45. Lipke JM, Janecki CJ, Nelson CL, et al. The role of incompetence of the anterior cruciate and lateral ligaments in anterolateral and anteromedial instability. A biomechanical study of cadaver knees. *J Bone Jt Surg - Ser A*. 1981;63(6):954–960. doi:10.2106/00004623-198163060-00013

46. Lipps DB, Oh YK, Ashton-Miller JA, Wojtys EM. Morphologic characteristics help explain the gender difference in peak anterior cruciate ligament strain during a simulated pivot landing. *Am J Sports Med*. 2012;40(1):32–40. doi:10.1177/0363546511422325

47. Lipps DB, Wojtys EM, Ashton-Miller JA. Anterior cruciate ligament fatigue failures in knees subjected to repeated simulated pivot landings. *Am J Sports Med*. 2013;41(5):1058–1066. doi:10.1177/0363546513477836

48. Liu, Stephen; Al-Shaikh, Raad; Panossian, Vahe; Finerman, Gerald; Lane J. Affects the cellular metabolism of the anterior cruciate ligament estrogen explanation Injury. *Am J Sports Med*. 1997;25(5):704–709.

49. Luetkemeyer CM, Marchi BC, Ashton-Miller JA, Arruda EM. Femoral entheseal shape and attachment angle as potential risk factors for anterior cruciate ligament injury. *J Mech Behav Biomed Mater*. 2018;88(August):313–321. doi:10.1016/j.jmbbm.2018.08.045

50. Markolf KL, Park S, Jackson SR, McAllister DR. Contributions of the posterolateral bundle of the anterior cruciate ligament to anterior-posterior knee laxity and ligament forces. *Arthrosc - J Arthrosc Relat Surg*. 2008;24(7):805–809.

doi:10.1016/j.arthro.2008.02.012

51. McLean SG, Oh YK, Palmer ML, et al. The relationship between anterior tibial acceleration, tibial slope, and ACL strain during a simulated jump landing task. *J Bone Jt Surg - Ser A*. 2011;93(14):1310–1317. doi:10.2106/JBJS.J.00259

52. Murphy DF, Connolly DAJ, Beynnon BD. Risk factors for lower extremity injury: A review of the literature. *Br J Sports Med*. 2003;37(1):13–29. doi:10.1136/bjsm.37.1.13

53. Musahl V, Karlsson J. Anterior cruciate ligament tear. *N Engl J Med*. 2019;380(24):2341–2348. doi:10.1056/NEJMcp1805931

54. Noyes FR, Mooar LA, Moorman CT, McGinniss GH. Partial tears of the anterior cruciate ligament. Progression to complete ligament deficiency. *J Bone Jt Surg - Ser B*. 1989;71(5):825–833. doi:10.1302/0301-620x.71b5.2584255

55. Odensten M, Gillquist J. Functional anatomy of the anterior cruciate ligament and a rationale for reconstruction. *J Bone Jt Surg - Ser A*. 1985;67(2):257–262. doi:10.2106/00004623-198567020-00012

56. Oh YK. ON THE MECHANISMS OF NON-CONTACT ACL INJURY DURING A SIMULATED JUMP LANDING: EXPERIMENTAL AND THEORETICAL ANALYSES. *Univ Michigan*. Published online 2011(e)ko .

57. Olsen OE, Myklebust G, Engebretsen L, Bahr R. Injury mechanisms for anterior cruciate ligament injuries in team handball: A systematic video analysis. *Am J Sports Med*. 2004;32(4):1002–1012. doi:10.1177/0363546503261724

58. Park SK, Stefanyshyn DJ, Loitz-Ramage B, Hart DA, Ronsky JL. Changing hormone levels during the menstrual cycle affect knee laxity and stiffness in healthy female subjects. *Am J Sports Med*. 2009;37(3):588–598. doi:10.1177/0363546508326713

59. Petersen W, Tillmann B. Structure and vascularization of the cruciate ligaments of the human knee joint. *Anat Embryol (Berl)*. 1999;200(3):325–334. doi:10.1007/s004290050283

60. Petersen W, Zantop T. Partial rupture of the anterior cruciate ligament. *Arthroscopy*. 2006;22(11):1143–1145. doi:10.1016/j.arthro.2006.08.017

61. Prodromos CC, Han Y, Rogowski J, Joyce B, Shi K. A meta-analysis of the Incidence of Anterior Cruciate Ligament Tears as a Function of Gender, Sport, and a Knee Injury-Reduction Regimen. *Arthrosc - J Arthrosc Relat Surg*. 2007;23(12):1320–1325. doi:10.1016/j.arthro.2007.07.003

62. Purevsuren T, Kim K, Nha KW, Kim YH. Evaluation of compressive and shear joint forces on medial and lateral compartments in knee joint during walking before and after medial open-wedge high tibial osteotomy. *Int J Precis Eng Manuf*. 2016;17(10):1365–1370. doi:10.1007/s12541-016-0162-1

63. Roell M, Mahler H, Lienhard J, Gehring D, Gollhofer A, Roecker K. Validation of

wearable sensors during team sport-specific movements in indoor environments. *Sensors (Switzerland)*. 2019;19(16):1–13. doi:10.3390/s19163458

64. Romani WA, Gieck JH, Perrin DH, Saliba EN, Kahler DM. Mechanisms and management of stress fractures in physically active persons. *J Athl Train*. 2002;37(3):306–314.

65. Schilaty N, Bates N, Krych A, Hewett T. How anterior cruciate ligament injury was averted during Knee collapse in a NBA point guard. *Ann Musculoskelet Med*. 2017;1(1):008–012. doi:10.17352/amm.000002

66. Schmidt M, Jaitner T, Nolte K, Rheinländer C, Wille S, Wehn N. A wearable inertial sensor unit for jump diagnosis in multiple athletes. In: *icSPORTS 2014 - Proceedings of the 2nd International Congress on Sports Sciences Research and Technology Support*. ; 2014:216–220. doi:10.5220/0005145902160220

67. Sharma L, Song J, Felson DT, Cahue S, Shamiyeh E, Dunlop DD. The role of knee alignment in disease progression and functional decline in knee osteoarthritis. *J Am Med Assoc*. 2001;286(2):188–195. doi:10.1001/jama.286.2.188

68. Shelbourne KD, Davis TJ, Klootwyk TE. The relationship between intercondylar notch width of the femur and the incidence of anterior cruciate ligament tears: A prospective study. *Am J Sports Med*. 1998;26(3):402–408. doi:10.1177/03635465980260031001

69. Śmigielski R, Zdanowicz U, Drwięga M, Ciszek B, Ciszkowska-Łysoń B, Siebold R. Ribbon like appearance of the midsubstance fibres of the anterior cruciate ligament close to its femoral insertion site: a cadaveric study including 111 knees. *Knee Surgery, Sport Traumatol Arthrosc*. 2015;23(11):3143–3150. doi:10.1007/s00167-014-3146-7

70. Smith HC, Vacek P, Johnson RJ, et al. Risk factors for anterior cruciate ligament injury: A review of the literature - part 1: Neuromuscular and anatomic risk. *Sports Health*. 2012;4(1):69–78. doi:10.1177/1941738111428281

71. Sonnery-Cottet B, Barth J, Graveleau N, Fournier Y, Hager JP, Chambat P. Arthroscopic identification of isolated tear of the posterolateral bundle of the anterior cruciate ligament. *Arthrosc - J Arthrosc Relat Surg*. 2009;25(7):728–732. doi:10.1016/j.arthro.2008.12.018

72. Souryal TO, Freeman TR, Daniel DM. Intercondylar notch size and anterior cruciate ligament injuries in athletes. A prospective study. *Am J Sports Med*. 1993;21(4):535–539. doi:10.1177/036354659302100410

73. Uhorchak JM, Scoville CR, Williams GN, Arciero RA, St. Pierre P, Taylor DC. Risk factors associated with noncontact injury of the anterior cruciate ligament. A prospective four-year evaluation of 859 west point cadets. *Am J Sports Med*. 2003;31(6):831–842. doi:10.1177/03635465030310061801

74. Vasta S, Andrade R, Pereira R, et al. Bone morphology and morphometry of the lateral femoral condyle is a risk factor for ACL injury. *Knee Surgery, Sport Traumatol Arthrosc*. 2018;26(9):2817–2825. doi:10.1007/s00167-017-4761-x

75. Della Villa F, Tosarelli F, Ferrari R, et al. Systematic video analysis of anterior cruciate

ligament injuries in professional male rugby players: Pattern, injury mechanism, and biomechanics in 57 consecutive cases. *Orthop J Sport Med*. 2021;9(11):1–11. doi:10.1177/23259671211048182

76. Waiwaiole A, Gurbani A, Motamedi K, et al. Relationship of ACL injury and posterior tibial slope with patient age, sex, and race. *Orthop J Sport Med*. 2016;4(11):1–5. doi:10.1177/2325967116672852

77. Waldén M, Krosshaug T, Bjørneboe J, Andersen TE, Faul O, Hägglund M. Three distinct mechanisms predominate in noncontact anterior cruciate ligament injuries in male professional football players: A systematic video analysis of 39 cases. *Br J Sports Med*. 2015;49(22):1452–1460. doi:10.1136/bjsports-2014-094573

78. Watanabe T, Saito H. Tests of wireless wearable sensor system in joint angle measurement of lower limbs. *Proc Annu Int Conf IEEE Eng Med Biol Soc EMBS*. Published online 2011(e)ko :5469–5472. doi:10.1109/IEMBS.2011.6091395

79. Webb JM, Salmon LJ, Leclerc E, Pinczewski LA, Roe JP. Posterior tibial slope and further anterior cruciate ligament injuries in the anterior cruciate ligament-reconstructed patient. *Am J Sports Med*. 2013;41(12):2800–2804. doi:10.1177/0363546513503288

80. Withrow TJ. Anterior Cruciate Ligament Strain: an investigaton of muscular and positional constraints in a cadaveric impact model. *Univ Michigan*. Published online 2005(e)ko .

81. Wojtys EM, Beaulieu ML, Ashton-Miller JA. New perspectives on ACL injury: On the role of repetitive sub-maximal knee loading in causing ACL fatigue failure. *J Orthop Res*. 2016;34(12):2059–2068. doi:10.1002/jor.23441

82. Wojtys EM, Huston LJ. Neuromuscular performance in normal and anterior cruciate ligament-deficient lower extremities. *Am J Sports Med*. 1994;22(1):89–104. doi:10.1177/036354659402200116

83. Wojtys EM, Huston LJ, Boynton MD, Spindler KP, Lindenfeld TN. The effect of the menstrual cycle on anterior cruciate ligament injuries in women as determined by hormone levels. *Am J Sports Med*. 2002;30(2):182–188. doi:10.1177/03635465020300020601

84. Wolff J. Das gesetz der transformation der knochen. *DMW-Deutsche Medizinische Wochenschrift*. 1892;19(47):1222–1224.

85. Woodhouse E, Schmale GA, Simonian P, Tencer A, Huber P, Seidel K. Reproductive hormone effects on strength of the rat anterior cruciate ligament. *Knee Surgery, Sport Traumatol Arthrosc*. 2007;15(4):453–460. doi:10.1007/s00167-006-0237-0

86. Zantop T, Herbort M, Raschke MJ, Fu FH, Petersen W. The role of the anteromedial and posterolateral bundles of the anterior cruciate ligament in anterior tibial translation and internal rotation. *Am J Sports Med*. 2007;35(2):223–227. doi:10.1177/0363546506294571

Chapter 2: A Comparison of IMU and Motion Capture Measurements of Tibiofemoral Kinematics during Simulated Pivot Landings

This chapter is published MDPI Sensors, and should be referred as:

Baek, S.Y.; Ajdaroski, M.; Shahshahani, P.M.; Beaulieu, M.L.; Esquivel, A.O.; Ashton-Miller, J.A. A Comparison of Inertial Measurement Unit and Motion Capture Measurements of Tibiofemoral Kinematics during Simulated Pivot Landings. Sensors *2022,* 22*, 4433. https://doi.org/10.3390/s22124433*

2.1 Abstract

Injuries are often associated with rapid body segment movements. We compared Certus motion capture and APDM inertial measurement unit (IMU) measurements of tibiofemoral angle and angular velocity changes during simulated pivot landings (i.e., ~70 ms peak) of nine cadaver knees dissected free of skin, subcutaneous fat, and muscle. Data from a total of 852 trials were compared using the Bland–Altman limits of agreement (LoAs): the Certus system was considered the gold standard measure for the angle change measurements, whereas the IMU was considered the gold standard for angular velocity changes. The results show that, although the mean peak IMU knee joint angle changes were slightly underestimated (2.1° for flexion, 0.2° for internal rotation, and 3.0° for valgus), the LoAs were large, ranging from 35.9% to 49.8%. In the case of the angular velocity changes, Certus had acceptable accuracy in the sagittal plane, with LoAs of ±54.9°/s and ±32.5°/s for the tibia and femur. For these rapid motions, we conclude that, even in the absence of soft tissues, the IMUs could not reliably measure these peak 3D knee angle changes; Certus measurements of peak tibiofemoral angular velocity changes depended on both the magnitude of the velocity and the plane of measurement.

2.2 Introduction

There are approximately 200,000 anterior cruciate ligament (ACL) ruptures in the United States every year [19]. Impulsive 3D knee loads on the order of three to four times the body weight (BW) have been shown to cause ACL fatigue failure *in vitro* during repeated simulated jump landings; these combined a knee flexion moment with an in-ternal tibial rotation moment and axial compression due to gravitational, inertial, and trans-knee muscle forces [17,21]. This type of 3D loading causes both transitory internal rotation of the tibia relative to the femur as well as a forward translation of the tibial plateau relative to the femoral condyle due to the patellofemoral mechanism, both of which are known to significantly increase ACL strain during a landing or cut [5,14,15,21]. If one defines these as “high ACL strain” (‘HAS’) loading cycles, one might be able to track the number of these HAS cycles imposed weekly by an athlete during practice and thereby limit the number and severity of HAS loading cycles before damage ac-cumulates to the point of ACL failure due to material fatigue [35].

Traditionally, laboratory-based optoelectronic motion capture systems have employed skin markers to measure the relative 3D motions between the shank and the thigh during the athletic maneuvers associated with ACL injuries. Inertial measurement units (IMU), on the other hand, are not constrained to a laboratory setting and can also be worn simultaneously by multiple individuals. Each IMU consists of a tri-axial linear accelerometer, tri-axial rate gyroscopes that measure angular velocity, and a triaxial magnetometer to measure the orientation of the gyro [31]. The IMU is usually attached directly to the skin or via a Velcro or elastic strap or garment around the body segment [6,8]. IMUs have been incorporated into many wearable sensor systems in order to track joint kinematics during gait analysis, sports, and rehabilitation activi-ties[6,24,26] because they have the advantage of being small, light, and easily attachable to different body segments. It is possible that they could also be used to identify and count HAS loading cycles, but they would first have to be demonstrated to have acceptable accuracy and reproducibility in the field during impulsive loading maneuvers.

In terms of accuracy and repeatability, motion capture systems and IMUs have been used to validate one another's results [24,36]. In particular, a motion capture system lends itself to measuring joint angles because it collects location data of markers via line of sight [18]. Angular velocities and accelerations calculated from these data are de-rived by mathematical differentiation, which is a process that introduces noise on the signal. On the other hand, because an IMU contains three orthogonal rate gyroscopes, it has the potential to directly measure angular velocities, and only a single differentiation or integration step is required to obtain acceleration and position data, respectively. Therefore, motion capture systems and IMUs each have their strengths and weaknesses.

During dynamic tasks such as a jump landing, it is well known that the skin, as well as the underlying subcutaneous fat and muscle, will vibrate after ground contact due to their mass and viscoelastic coupling to the underlying bone. When the IMU or marker is fastened directly to the skin, this vibration leads to a soft tissue motion arti-fact that degrades the kinematic recordings of what are meant to represent motions of the underlying bone [3,11]. Several authors have employed active or passive skin markers tracked by motion capture systems to evaluate the accuracy of measuring joint angles or joint angular velocities [8,10,36]. There have also been studies with magnetic resonance imaging (MRI) [25] and X-ray fluoroscopy measurements [11] of the kinematics of the underlying bone to remove the effect from soft tissue, but stereoradiography requires a static setup of the X-ray sources in the laboratory, is invasive and unethical for use on children or adolescents, and is completely impractical for use in the field.

There are published comparisons of quasistatic IMU outputs with known changes in angles measured, for example, by a coordinate measuring system [29]. However, we are not aware of studies that have compared IMU measurements of 3D changes in the knee angle or body segment angular velocity with those made with a motion capture system during a dynamic activity such as a jump landing. Moreover, none appear to have been made in the absence of a soft tissue artifact. However, such measurements can provide a baseline for knowing the conditions under which the IMU and motion capture systems can provide reliable data. If one removes the soft tissue, for example, cadaver experiments provide just such an opportunity to compare the IMU measurement of 3D knee angle changes with those measured using a standard motion capture system. Likewise, one can make a similar comparison of 3D tibial and femoral angular velocity changes measured via a pair of IMUs (which we, in this paper, consider the gold standard because of measuring angular velocity directly) with those measured by differentiating the motion analysis system angular data. Since the IMUs and marker triads can be mounted directly on the cadaveric tibia and femur with no intervening soft tissue, this setup presents the opportunity to compare the best possible 3D performance of the two measurement systems in the absence of a soft tissue artifact.

The goal of this paper was to test the null hypothesis that motion capture system and IMU measures of abrupt 3D changes in the tibial–femoral angle and angular velocity during a simulated unipedal jump landing are comparable. We tested that hypothesis using a Bland–Altman analysis to calculate the “limits of agreement” (LoAs) between the two measurement system results: the gold standard being the motion capture system displacement data and IMU angular velocity data.

2.3 Materials and methods

2.3.1 Specimen procurement and preparation

A total of nine knees were harvested from six male and three female human donors (Table 1) procured from the University of Michigan Anatomical Donation Pro-gram, as well as Anatomy Gifts Registry, Science Care, and Gift of Life Michigan. The knee specimens were double-bagged and stored in a freezer at −20 ℃, until being removed from the freezer 48 h prior to dissection and testing. Thawed knees were dissected at room temperature, leaving intact the ligamentous capsular structures and the tendons of the quadriceps, medial hamstrings, lateral hamstrings, medial gastrocnemius, and the lateral gastrocnemius muscles. Following dissection, the distal tibia/fibula and proximal femur were cut to a standard 20 cm length from the center of the knee joint (palpated on the medial meniscus). The proximal femur and distal tibia were then potted in polymethylmethacrylate cylinders ready for mounting in the testing apparatus.

Table 2-1. Demographic data of the knee specimen donors.

Specimen No.	Gender	Side	Age [yrs]	Weight [kg]	Testing condition
S1	F	L	20	86.6	3 BW 100 trials
S2	F	R	28	63.5	4 BW 100 trials
S3	F	R	30	82.1	3 BW 52 trials *
S4	M	L	39	54.4	4 BW 100 trials
S5	M	R	32	68.0	4 BW 100 trials
S6	M	R	32	88.5	3 BW 100 trials
S7	M	R	25	86.2	3 BW 100 trials
S8	M	R	31	92.5	3 BW 100 trials
S9	M	R	33	49.9	4 BW 100 trials
Total					852 trials

F: Female, M: Male, L: Left, R: Right, BW: Body Weight.
* Testing was halted due to ACL failure, defined as a 3-mm increase in cumulative anterior tibial translation.

2.3.2 Testing apparatus

Each cadaveric knee was mechanically tested using the Withrow-Oh [17,20] testing apparatus (Figure 1) that simulated repeated single leg pivot landings. In each trial, in order to achieve a high enough loading rate to properly simulate a jump landing, a known weight (W, Figure 1) was released to impact the distal end of the tibia through a viscoelastic bumper whose properties were tuned to shape the temporal history of the impact force to peak at 70 ms [20]. Five preconditioning trials were used to find the drop height and weight required to simulate a three to four times body weight peak impulsive force on that knee. The loads applied to the knee were measured using a six-axis (MC3A-1000, AMTI, Watertown, MA, USA) load cell (L, Figure 1) located in series with the distal femur, whereas the reaction loads were measured simultaneously via an identical load cell located in series with the proximal tibia: these cells monitored the 3D input forces and moments, and 3D reaction forces and moments, respectively. The knee was initially set up with 15° of flexion held there by the quadriceps pretension, which reflects the pretension in the muscle prior to landing a jump. Each specimen was subjected to a maximum of 100 loading trials or as many trials as could be completed until the ACL failed. Failure was defined as a 3 mm or more increase in cumulative anterior tibial translation. The design of the apparatus caused the dropped weight to apply, simultaneously, an impulsive compression load, a knee flexion moment, and an internal tibial torque (T, Figure 1) to the knee, combined with realistic trans-knee muscle forces (Q, G, and H, Figure 1). Clamps were attached to grasp each tendon, with only the quadriceps tendon clamp requiring cryocooling to prevent slippage; active muscle tensile elasticity was simulated by a length of 2 mm diameter woven nylon rope, and each muscle construct was pre-tensed as follows: quadriceps (Q: 180 N), hamstrings (H: 70 N each), and gastrocnemius (G: 70 N each) [33,34].

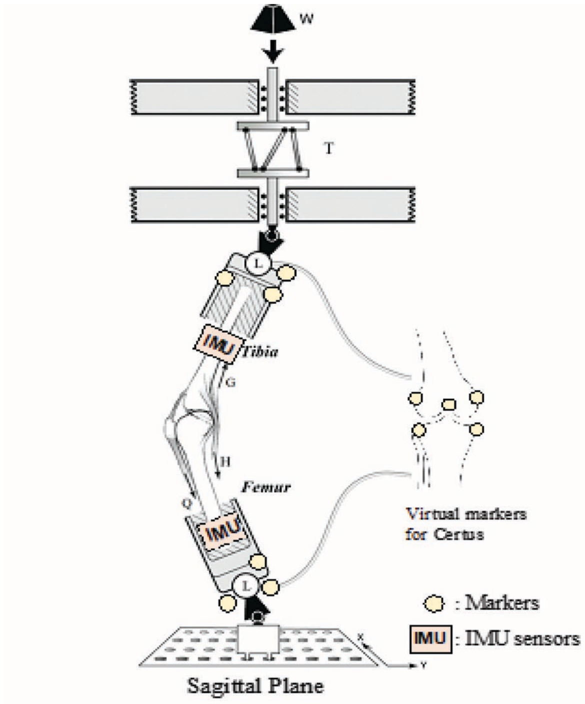

Figure 2-1. Diagram of the Withrow-Oh testing apparatus [17,20] showing the locations of the fixed active marker triads along with the locations of the virtual active markers obtained by manual digitization prior to the experiment. Modified, and reproduced with permission from [Oh et al., 2011, The Journal of Bone and Joint Surgery, Inc].

An optoelectronic imaging system (Optotrak Certus, Northern Digital Inc., Waterloo, Ontario, Canada) was used to record the 3D tibiofemoral marker triad kinematics at 400 Hz with an accuracy of 0.2 mm RMS [28]. A set of three markers ('Markers', Figure 1), affixed to a rigid body, was attached to the distal femur and proximal tibia, respectively. A 3D digitizer was used to identify standard anatomical landmarks on the knee joint ('Virtual markers', Figure 1) to calculate relative and absolute 3D tibiofemoral kinematics throughout each trial. The motion capture and load cell data were automatically synchronized by the Optotrak system.

A wearable IMU (OPAL, APDM Inc., Portland, OR, USA, Figure 1) was securely attached adjacent to the triad near the distal end of the medial tibia and the proximal end of the mid femur using tensioned Velcro straps. Linear acceleration and angular velocities were measured at 128 Hz using the two IMUs. After being set up, the knee was first fully extended for the initialization process of the two APDM OPAL units to set initial conditions and minimize the influence of drift during the angular calculations using the two IMUs. The two IMUs then provided continuously recorded data on the triaxial linear accelerations and triaxial angular velocities of each bone until the experiment ended.

Both the Optotrak system and APDM sensors have been validated in the literature for given applications [23,27,30].

2.3.3 Data analysis

A total of 852 simulated pivot jump landing trials were conducted across all nine specimens. The 3D tibial and femoral bone motions were tracked using both the Certus motion capture systems and two APDM IMUs.

2.3.3.1. Knee joint angle calculations

The 3D tibiofemoral triad marker position data from the Certus system were filtered using a 4th order Butterworth low-pass filter with 20 Hz cutoff frequency implemented using MATLAB (MATLAB_R2019b; MathWorks, Natick, MA, USA). A custom MATLAB code [20] was used to calculate relative angles and translation using the method developed by Grood and Suntay [13].

The IMU data from each trial were used to calculate the knee joint angles using the proprietary sensor fusion algorithm provided by APDM Opal to determine the orientation of the devices using the method of Watanabe et al. [2,31].

2.3.3.2. Comparison of the knee angles between the two measurement methods

The two measurement systems acquire data at different sampling rates, so linear interpolation was used to match the IMU sampling rate to that of the motion capture system. The peak angle changes from the optoelectronic motion capture system were calculated as the difference between the initial and the maximum angle measured (Figure 2a). Similarly, the peak IMU angle changes were obtained from the difference between initial resting state and the maximum values (Figure 2b) to get the peak angles during each pivot landing.

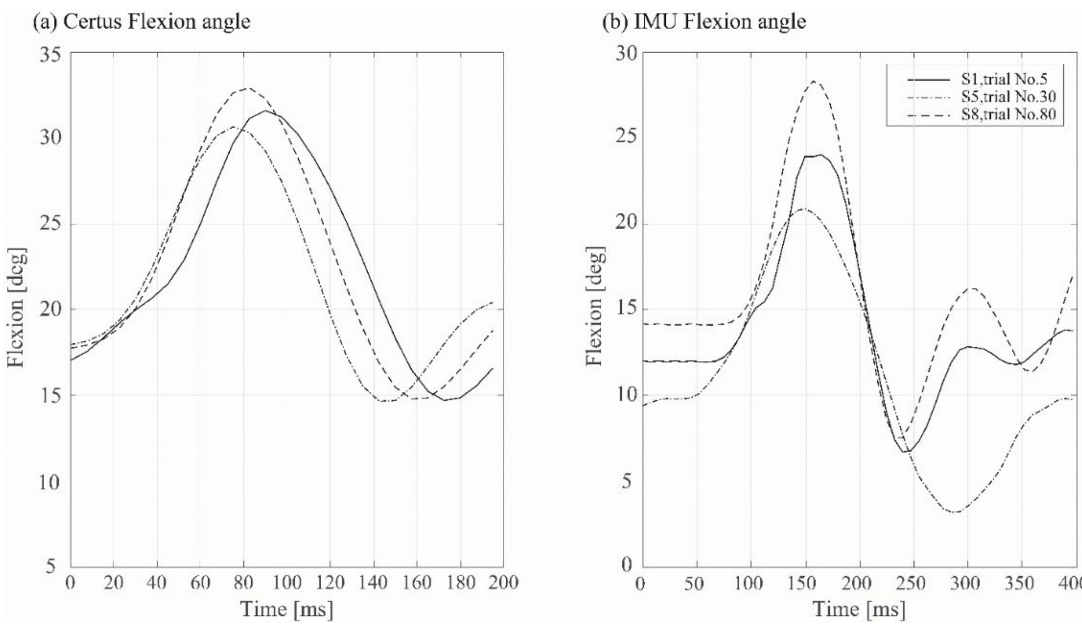

Figure 2-2. Three examples of the time course of the changes in knee flexion angle during simulated jump landings. Panel (a) shows measurements from the optoelectronic motion capture system, whereas panel (b) shows the calculated angles from the accelerometer and gyroscopic data from the IMUs. The peak angle change from the IMUs was calculated as the difference between the initial resting state and the maximum angle measured.

The difference in peak knee angle change measured with the IMUs and the motion capture systems was calculated in each plane. Bland-Altman plots were then used to assess the variation in the IMU derived peak knee angle change compared to the peak knee angle change measured using the Certus motion capture system. The mean of the difference (bias) and the 95% confidence interval (CI) of the bias (limits of agreement) were also calculated.

2.3.3.3. Peak tibial and femoral angular velocity change calculations

The three orthogonal rate gyroscopes in the wearable IMUs on the tibia and femur directly measured the time histories of the angular velocities during each impulsive loading cycle. For the Certus, the 3D angular velocities in each orthogonal plane were calculated from the 3D motions of the femur and tibia Certus marker triads sampled at 400 Hz, as described in the Section 2.3.1. The three markers on each bone were oriented in the motion capture system frontal plane, to establish a sagittal plane for the bones. These three markers on each bone allowed for the generation of unit directional vectors in each axis: anterior–posterior, medial–lateral, and proximal–distal. The temporal changes in angular rotations were then calculated in each direction using a five-point differential method and a fourth order low-pass Butterworth filter and 25 Hz calculated cut off frequency[32].

2.3.3.4. Comparison of the peak tibial and femoral angular velocity changes using the two measurement systems

Using the measured peak angular velocity changes from the wearable IMUs, we compared the measured peak bone angular velocity changes from the Certus system calculated by differentiating the angular position data over the same time span of the simulated jump landings. To compare the peak values of the bone angular velocity changes, the averaged means of all testing trials for each system and standard deviation were calculated, as well as the percent error between the peak angular velocity changes calculated from the Certus system and those measured from the IMUs. Bland–Altman plots were used to view the limits of agreement between the bone angular velocities calculated from the Certus system and compared to the IMU rate gyro-based measurements.

2.4 Results

2.4.1 Measured peak knee angle changes

Bland–Altman plots comparing IMUs versus the motion capture system for measuring the knee flexion, knee internal rotation, and knee valgus angles are shown in Figure 3. The measured peak knee angle changes from the IMUs displayed systematic bias in that they were underestimated in two of the three planes. As the peak angle change increased, the bias decreased, with internal rotation exhibiting the largest peak angle change, but only −0.18° of bias. However, the width of the limits of agreements (LoAs) band increased, with large peak angle changes (Table 2). For all three orthogonal knee angles, the standard deviation (SD) of the angular differences (IMUs-Certus) as a percentage was ~20% in all three directions; specifically, 19.8%, 25.4%, and 18.3%, respectively.

Table 2-2. Mean (SD) peak angle changes measured via Certus and IMUs, along with the corresponding Bland-Altman Bias and Limit of Agreement results calculated according to the formula in the table footnote at bottom right.

	Flexion	**Internal Rotation**	**Valgus**
Certus	13.3 (2.9)°	16.7 (2.1)°	6.6 (2.1)°
IMU	11.2 (3.2)°	16.6 (4.3)°	2.9 (1.1)°
Bias	-2.1°	-0.2°	-3.0°
LoA	(-7.2°, 3.0°)	(-8.4°, 8.1°)	(-7.6°,0.2°)
Diff [%]	-15.3% (19.8%)	-0.6% (25.4%)	-52.8% (18.3%)
Agreement Range [%]	± 38.8 %	± 49.8%	± 35.9%

Bias = $\frac{\sum(IMU - Certus)}{N}$, LoA = $Bias \pm 1.96 \times SD$,
Diff [%] = $\sum(\frac{IMU - Certus}{Certus}) \times 100/N$, Agreement Range [%] = 1.96 SD of Diff[%]

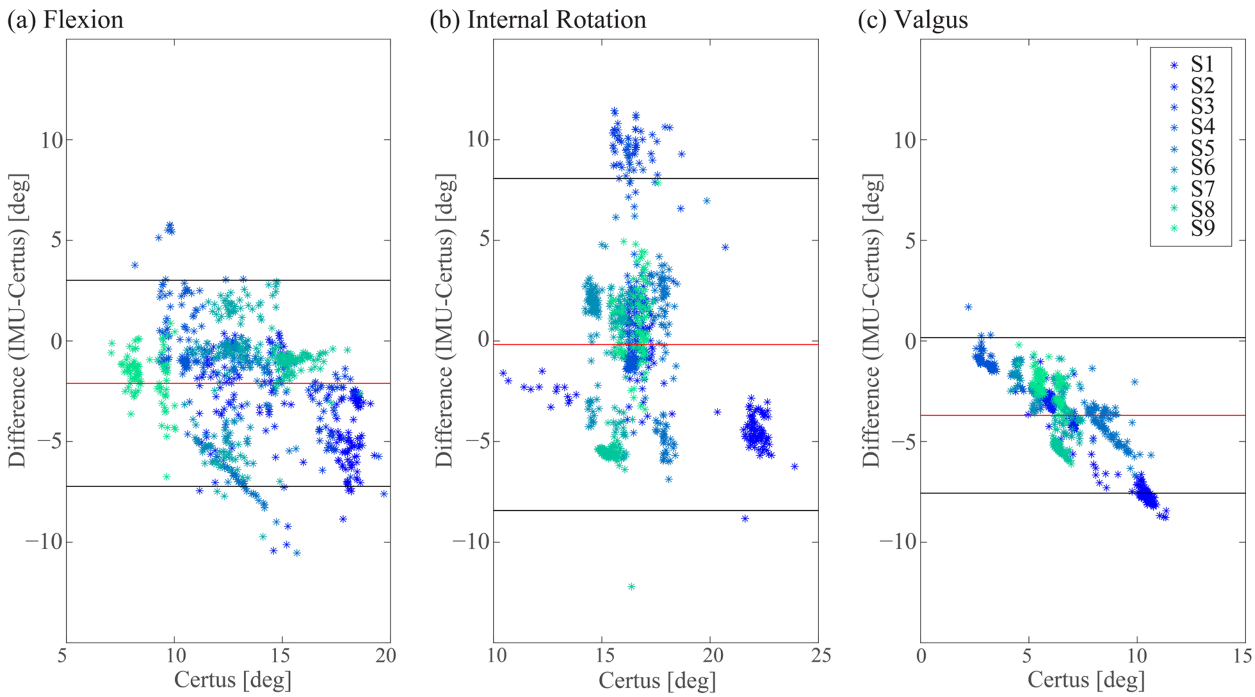

Figure 2-3. Bland–Altman plots comparing the measurements from the two IMUs with those of the motion capture system for measuring peak knee angle change in each direction during simulated jump landings. In this and the following figure, the different colors represent data from different knee specimens (S).

2.4.2 Comparison of the tibial and femoral angular velocity changes calculated from Certus system data with IMU data

The Bland–Altman plots comparing the motion capture system versus IMUs out-comes for angular velocities by plane for each bone are shown in Figure 4. The bias calculated for the femur in all directions was less than that measured for the tibia: 72.7°/s (tibia) vs. −35.8°/s (femur) in the sagittal plane, −159.1°/s (tibia) vs. 112.0°/s (femur) in the transverse plane, and 536.3°/s (tibia) vs. 100.4°/s (femur) in the frontal plane (Figure 4 and Table 3). The width of the LoA band was considerably less in the sagittal plane (54.9°/s for the tibia and −32.5°/s for the femur) than in the other planes.

The bone angular velocity changes in the transverse plane exhibited the largest magnitude (Table 3). The average of the IMU measured angular velocity changes was −832.5°/s for the tibia, and the difference in the averages measured using the IMUs and those calculated from the Certus system exhibited only an 18.9% difference, with an SD of 7.3%.

The bone angular velocity changes in the transverse plane exhibited the largest magnitude (Table 3). The average of the IMU measured angular velocity changes was −832.5 º /sec for the tibia, and the difference of the averages measured using the IMUs and those calculated from the Certus system exhibited only an 18.9% difference, with an SD of 7.3%.

Table 2-3. Mean (SD) values for Bland–Altman comparisons of peak angular velocity from Certus and IMUs for the three planes. On average, the Certus measurements tended to overestimate the IMU measurements. The percentage difference (Diff [%]) is defined in the table footnote.

	Certus [º/sec]	**IMU [º/sec]**	**Certus - IMU [º/sec]**	**LoA [º/sec]**	**Diff [%]**
			Sagittal plane		
Tibia	182.3 (32.6)	109.7 (31.5)	72.7 (28.0)	(17.8, 127.5)	75.4% (38.6%)
Femur	159.7 (33.0)	195.5 (41.7)	-35.8 (16.6)	(-68.3, -3.3)	-17.9% (6.5%)
			Transverse plane		
Tibia	673.4 (103.2)	832.5 (120.2)	-159.1 (75.9)	(-308.0, -10.3)	-18.9% (7.3%)
Femur	188.8 (45.3)	300.8 (131.6)	-112.0 (97.1)	(-302.3, 78.2)	-31.8% (17.4%)
			Frontal plane		
Tibia	684.9 (117.5)	148.6 (38.4)	536.3 (95.8)	(348.5, 724.1)	384.4% (121.6%)
Femur	191.3 (65.1)	90.9 (19.2)	100.4 (60.2)	(-17.6, 218.4)	115.5% (75.3%)

LoA denotes limits of agreement; Diff [%] = $\frac{\text{Certus–IMU}}{\text{IMU}}$. Diff [%] = $\frac{Certus–IMU}{IMU}$

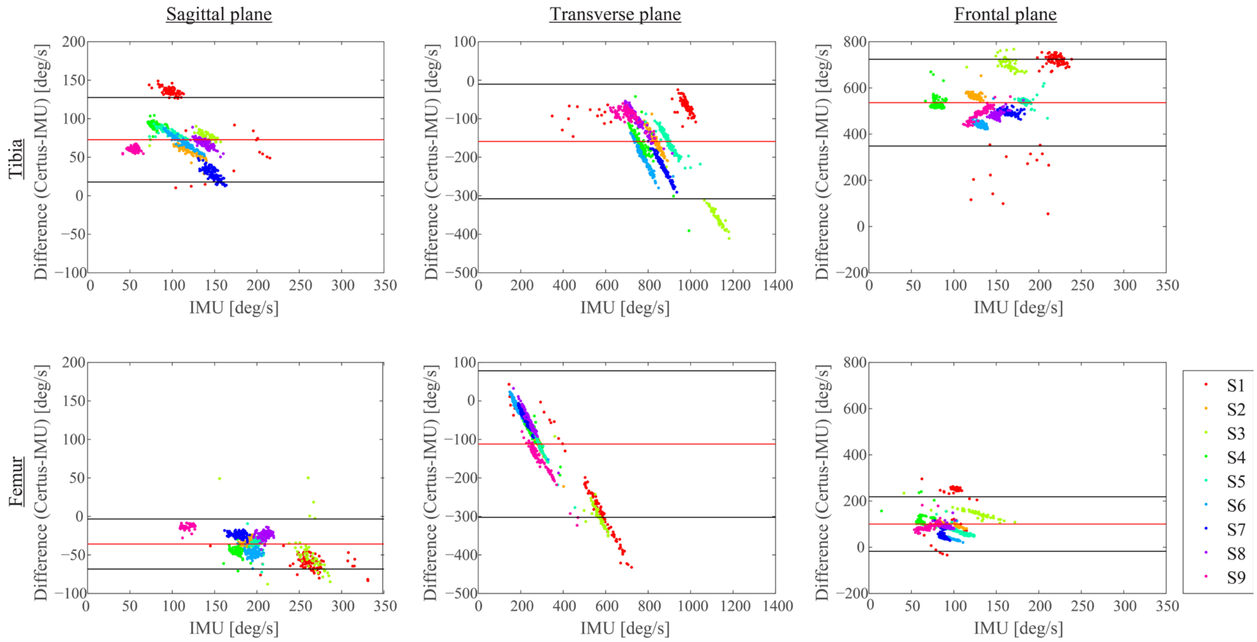

Figure 2-4. Bland–Altman plots showing differences, by plane, between Certus system and IMU in the angular velocity change for the tibia (top row) and the femur (bottom row). The x-axis shows the angular velocities measured via the IMUs, whereas the y-axis shows the difference in angles for each plane (left, center, and right panels). The bias was negative in the transverse plane, positive in the frontal plane, and mixed in the sagittal plane for the two bones.

2.5 Discussion

There are two novel aspects to this study. First, we made kinematic measurements over a time course that is characteristic of a limb landing on the ground during which time injury can result. The first peak in the foot–ground reaction force usually occurs 35–50 ms after ground contact [7,9]. However, the musculoskeletal response of the more proximal parts of the lower extremity limb, of course, lags that peak. For example, if one considers the mechanism of ACL injury [35], the magnitude of the increase in ACL strain is proportional to the change in the knee flexion angle (via the patellofemoral mechanism) and the change in the internal tibial rotation angle, which both peak ~70 ms following ground contact [20,21]. That is why we focused on calculating the change in angle and change in angular velocity over that time interval in this study. Second, we could find no studies comparing IMU and motion capture system performance measuring the kinematics of a human body segment, knee joint peak angle change, or peak bone angular velocity changes in the absence of a soft tissue motion artifact. The significance is that our experiment provides the opportunity to assess the best possible dynamic performance of the IMU and motion capture systems without the artifact caused by soft tissue vibration. Any *in vivo* measurements are certain to exhibit more variability because of noise generated by soft tissue movement artifacts.

Bland and Altman originally developed their eponymous method to compare an experimental measurement method with a standard measurement method by introducing the limits of agreement approach [4]. It has since been adopted for use by many fields [12]. The method is useful because, unlike a correlation coefficient, it quantifies any bias present, as well as the limits of agreement, within 95% of the differences for the experimental method compared to the standard method. Of course, the narrower the limits of agreement, the better the experimental method is, until the results become interchangeable with one another [22]. The peak angle changes in each orthogonal plane were slightly underestimated by the IMU measurements. Even though the bias was only −0.6% for internal rotation, which exhibited the largest peak angle change of ~16°, the peak knee angle difference between measurement methods amounted to ~±40% of the LoA (calculated from 1.96×-SD in all three orthogonal planes). This result indicates that the knee angle change calculated using these APDM IMUs and their fusion algorithm could not reliably capture the peak kinematics of the weight acceptance phase of a movement as dynamic as a unipedal pivot landing. This was true in the absence of a soft tissue artifact, so the presence of such an artifact *in vivo* would only make matters worse.

The orientation of the Certus camera relative to the lower extremity was found to affect the calculated angular velocity changes. This was because the marker triads were essentially placed in the knee parasagittal plane parallel with the frontal plane containing the three optoelectronic cameras that constitute the Certus system. This provided its best resolution, but the resolution is lower in the Certus cameras' depth plane, orthogonal to its frontal plane [28]. The Certus camera orientation therefore explains the narrow LoA band in the sagittal plane for the Certus-measured angular velocities. With the present setup, when the tibia was forced to internally rotate relative to the femur during the pivot landing, the tibial marker triad moved in the Certus camera depth plane, whereas the femoral triad moved principally in the Certus frontal plane, hence the smaller bias we found in the results for the femur than for the tibia. The exception was internal tibial rotation in the transverse plane, perhaps because it had a larger angular velocity change, 832.5 °/sec, compared to the motion in the other planes. The upshot is that the orientation of the Certus camera relative to the subject will affect the measurement accuracy of certain knee angles. However, as can be seen from the results for internal rotation, if angular velocities are sufficiently high, the camera orientation was less of an issue.

A first limitation was that the sampling frequencies of the two measurement systems were different. This could have affected the accuracy of the results because of the need for interpolation between data points when resampling data at the same rate as the second measurement system. However, the changes in angle and angular velocity were relatively smooth, so this should not have affected the results materially. A second limitation was that there will have been a slight phase difference between when the impact force acts distally on a limb and when it acts more proximally on the knee [16]. In this experiment, the order of sensed displacements would have been the tibia marker triad first (because of being closer to the point of impact), then the tibial IMU, then the femoral IMU, then the femoral marker triad. Such phase differences likely had a minor effect on our results because the angle and angular velocities of each system were calculated relative to the peak values for each trial. Finally, we employed the generic APDM software algorithm to process these data, but a custom-tuned algorithm can improve the results slightly, particularly by reducing the phase lag in the generic APDM results due to the rapid acceleration profiles [1] associated with HAS cycles. In summary, we do not believe that these limitations materially affected the overall results in comparing the two measurement systems.

2.6 Conclusions

Due to the fact that the LoAs ranged from 35.9% to 49.8% of the measured joint angle, the APDM IMUs could not reliably measure the sudden changes in joint angles that occur during simulated pivot landings, even in the absence of soft tissue artifact. Therefore, improvements to these IMUs are needed to be able to reliably measure HAS cycles *in vitro*, let alone in the presence of soft tissue *in vivo*.

Acknowledgements

We gratefully acknowledge the financial support of Public Health Service grant R01 AR054821, National Science Foundation Grant 2003434 and the technical assistance of Dr. Melanie Beaulieu during knee specimen testing.

2.7 References

1. Ajdaroski M, Ashton-Miller JA, Baek SY, Shahshahani PM, Esquivel AO. Testing a quaternion conversion method to determine human three-dimensional tibiofemoral angles

during an in vitro simulated jump landing. J Biomech Eng. 2022;144(4):1–8. doi:10.1115/1.4052496

2. Ajdaroski M, Tadakala R, Nichols L, Esquivel A. Validation of a device to measure knee joint angles for a dynamic movement. Sensors (Switzerland). 2020;20(6). doi:10.3390/s20061747

3. Akbarshahi M, Schache AG, Fernandez JW, Baker R, Banks S, Pandy MG. Non-invasive assessment of soft-tissue artifact and its effect on knee joint kinematics during functional activity. J Biomech. 2010;43(7):1292–1301. doi:10.1016/j.jbiomech.2010.01.002

4. Altman DG, Bland TM. Measurement in medicine : The analysis of method comparison studies. Statistician. 1983;32(3):307–317.

5. Beaulieu ML, Ashton-Miller JA, Wojtys EM. Loading mechanisms of the anterior cruciate ligament. Sport Biomech. 2021;00(00):1–29. doi:10.1080/14763141.2021.1916578

6. Bell KM, Onyeukwu C, McClincy MP, et al. Verification of a portable motion tracking system for remote management of physical rehabilitation of the knee. Sensors (Switzerland). 2019;19(5). doi:10.3390/s19051021

7. Cong Y, Lam WK. Effects of shear reduction shoes on joint loading, ground reaction force and free moment across different cutting angles. J Sports Sci. 2021;00(00):1–9. doi:10.1080/02640414.2021.1874716

8. Dahl KD, Dunford KM, Wilson SA, Turnbull TL, Tashman S. Wearable sensor validation of sports-related movements for the lower extremity and trunk. Med Eng Phys. 2020;84:144–150. doi:10.1016/j.medengphy.2020.08.001

9. DeGoede KM, Ashton-Miller JA. Fall arrest strategy affects peak hand impact force in a forward fall. J Biomech. 2002;35(6):843–848. doi:10.1016/S0021-9290(02)00011-8

10. Feuvrier F, Sijobert B, Azevedo C, et al. Inertial measurement unit compared to an optical motion capturing system in post-stroke individuals with foot-drop syndrome. Ann Phys Rehabil Med. 2020;63(3):195–201. doi:10.1016/j.rehab.2019.03.007

11. Garling EH, Kaptein BL, Mertens B, et al. Soft-tissue artefact assessment during step-up using fluoroscopy and skin-mounted markers. J Biomech. 2007;40(SUPPL. 1):18–24. doi:10.1016/j.jbiomech.2007.03.003

12. Giavarina D. Understanding Bland Altman analysis. Biochem Medica. 2015;25(2):141–151. doi:10.11613/BM.2015.015

13. Grood ES, Suntay WJ. A joint coordinate system for the clinical description of three-dimensional motions: Application to the knee. J Biomech Eng. 1983;105(2):136–144. doi:10.1115/1.3138397

14. Kaeding CC, Léger-St-Jean B, Magnussen RA. Epidemiology and diagnosis of anterior cruciate ligament injuries. Clin Sports Med. 2017;36(1):1–8. doi:10.1016/j.csm.2016.08.001

15. Kim HY, Ahn J, Park KY, et al. Translational movement of the tibiofemoral joint in normal gait : 3-Dimensional measurement. 2008;11(1):37–43.

16. Lee Y, Ashton-Miller JA. Age and gender effects on the proximal propagation of an impulsive force along the adult human upper extremity. Ann Biomed Eng. 2014;42(1):25–35. doi:10.1007/s10439-013-0900-9

17. Lipps DB, Wojtys EM, Ashton-Miller JA. Anterior cruciate ligament fatigue failures in knees subjected to repeated simulated pivot landings. Am J Sports Med. 2013;41(5):1058–1066. doi:10.1177/0363546513477836

18. Maletsky LP, Sun J, Morton NA. Accuracy of an optical active-marker system to track the relative motion of rigid bodies. J Biomech. 2007;40(3):682–685. doi:10.1016/j.jbiomech.2006.01.017

19. Musahl V, Karlsson J. Anterior cruciate ligament tear. N Engl J Med. 2019;380(24):2341–2348. doi:10.1056/NEJMcp1805931

20. Oh YK, Kreinbrink JL, Ashton-Miller JA, Wojtys EM. Effect of ACL transection on internal tibial rotation in an in vitro simulated pivot landing. J Bone Jt Surg - Ser A. 2011;93(4):372–380. doi:10.2106/JBJS.J.00262

21. Oh YK, Lipps DB, Ashton-Miller JA, Wojtys EM. What strains the anterior cruciate ligament during a pivot landing? Am J Sports Med. 2012;40(3):574–583. doi:10.1177/0363546511432544

22. Olofsen E, Dahan A, Borsboom G, Drummond G. Improvements in the application and reporting of advanced Bland–Altman methods of comparison. J Clin Monit Comput. 2014;29(1):127–139. doi:10.1007/s10877-014-9577-3

23. Richards JG. The measurement of human motion: A comparison of commercially available systems. Hum Mov Sci. 1999;18(5):589–602. doi:10.1016/S0167-9457(99)00023-8

24. Roell M, Mahler H, Lienhard J, Gehring D, Gollhofer A, Roecker K. Validation of wearable sensors during team sport-specific movements in indoor environments. Sensors (Switzerland). 2019;19(16):1–13. doi:10.3390/s19163458

25. Sangeux M, Marin F, Charleux F, Dürselen L, Ho Ba Tho MC. Quantification of the 3D relative movement of external marker sets vs. bones based on magnetic resonance imaging. Clin Biomech. 2006;21(9):984–991. doi:10.1016/j.clinbiomech.2006.05.006

26. Schmidt M, Jaitner T, Nolte K, Rheinländer C, Wille S, Wehn N. A wearable inertial sensor unit for jump diagnosis in multiple athletes. In: icSPORTS Rome, Italy, 24-26 Oct. 2014: :216–220. doi:10.5220/0005145902160220

27. Small CF, Bryant JT, Dwosh IL, Griffiths PM, Pichora DR, Zee B. Validation of a 3D optoelectronic motion analysis system for the wrist joint. Clin Biomech. 1996;11(8):481–483. doi:10.1016/S0268-0033(96)00042-3

28. Thompson S, Penney G, Dasgupta P, Hawkes D. Improved modelling of tool tracking errors by modelling dependent marker errors. IEEE Trans Med Imaging. 2013;32(2):165–177. doi:10.1109/TMI.2012.2216890

29. Vitali R V., Cain SM, McGinnis RS, et al. Method for estimating three-dimensional knee rotations using two inertial measurement units: Validation with a coordinate measurement machine. Sensors (Switzerland). 2017;17(9). doi:10.3390/s17091970

30. Washabaugh EP, Kalyanaraman T, Adamczyk PG, Claflin ES, Krishnan C. Validity and repeatability of inertial measurement units for measuring gait parameters. Gait Posture. 2017;55(April):87–93. doi:10.1016/j.gaitpost.2017.04.013

31. Watanabe T, Saito H. Tests of wireless wearable sensor system in joint angle measurement of lower limbs. Proc Annu Int Conf IEEE Eng Med Biol Soc EMBS. Published online 2011(e)ko :5469–5472. doi:10.1109/IEMBS.2011.6091395

32. Winter DA. Biomechanics and motor control of human movement: Fourth Edition. John wiley & Sons, Inc.; 2009. doi:10.1002/9780470549148

33. Withrow TJ, Huston LJ, Wojtys EM, Ashton-Miller JA. Effect of varying hamstring tension on anterior cruciate ligament strain during in vitro impulsive knee flexion and compression loading. J bone Jt Surg. 2008;(July 2006):815–823. doi:10.2106/JBJS.F.01352

34. Withrow TJ, Huston LJ, Wojtys EM, Ashton-Miller JA. The relatioship between quadriceps muscle force, knee flexion, and anterior cruciate ligament strain in an in vitro simulated jump landing. Am J Sports Med. 2006;34(2):269–274. doi:10.1177/0363546505280906

35. Wojtys EM, Beaulieu ML, Ashton-Miller JA. New perspectives on ACL injury: On the role of repetitive sub-maximal knee loading in causing ACL fatigue failure. J Orthop Res. 2016;34(12):2059–2068. doi:10.1002/jor.23441

36. Zügner R, Tranberg R, Timperley J, Hodgins D, Mohaddes M, Kärrholm J. Validation of inertial measurement units with optical tracking system in patients operated with total hip arthroplasty. BMC Musculoskelet Disord. 2019;20(1):1–8. doi:10.1186/s12891-019-2416-4

Chapter 3: On the Relationship between Lateral Tibial Slope and Tibiofemoral Kinematics during Simulated Jump Landings in Male Human Cadaver Knees

This chapter has been submitted for publication for OJSM.

So Young Baek, Mélanie L. Beaulieu, Edward M. Wojtys, and James A. Ashton-Miller.

3.1 Abstract

Background: It is not known mechanistically whether a steeper lateral tibial slope (LTS) leads to both an increase in anterior tibial translation (ATT) as well as internal tibial rotation (ITR) during a given jump landing.

Hypothesis/Purpose: A steeper LTS will result in increased ATT and ITR during simulated jump landings applying knee compression, flexion and internal tibial torque of increasing severity.

Study Design: A descriptive laboratory study.

Methods: Seven pairs of cadaver knees were harvested from young male adult donors [mean (SD) age: 25.71 (5.53) years, weight: 71.51(4.81) kg]. The LTS of each knee was measured by a blinded observer from 3T MR images. Two sets of 25 impact trials of ~700 N (1 BW ±10%) followed by another 2 sets of 25 trials with 1,400 N (2 BW ±10%) were applied to a randomly selected knee of each pair. Similarly, on the contralateral knee, two sets of 25 impact trials with ~1,800 N (2.5 BW ±10%) and after which two more sets of 25 trials with ~2,100N (3 BW ±10%) were applied. 3D knee kinematics, including, ATT and ITR, were measured at 400 Hz using optoelectronic motion capture. Two-factor linear mixed effect models were used to determine the relationships between LTS and ATT and ITR as impact loading increased.

Results: As LTS increased, both ATT and ITR also increased during increasingly severe landings. LTS had an increasing effect on ATT (coefficient = 0.50 ,95% CI: 0.29-0.71) relative to impact force (coefficient = 0.52, 95% CI: 0.50-0.53). Meanwhile, ITR was proportional to LTS (coefficient=1.36, 95% CI: 0.80-1.93) under increasing impact force (coefficient=0.49, 95% CI: 0.47-0.52). For steeper LTS, the increase in ITR was proportionally greater than ATT.

Conclusion: In males, a steeper LTS significantly increased both ATT and ITR during jump landings.

Clinical Relevance: A steeper LTS increases ACL strains during jump landings because of the increase in both ITR and ATT. The clinical significance of these findings should be further investigated in clinical populations.

Key Terms: ACL injury, lateral posterior tibial slope, kinematics, jump landing, anterior tibial translation, internal tibial rotation

What is known about the subject: A steeper LTS is a known morphological risk factor for non-contact injury. Exactly why this is so is not fully understood.

What this study adds to existing knowledge: This is the first evidence that a steeper LTS increases both ATT and ITR, and therefore ACL strain, in the knee during jump landings.

3.2 Introduction

Approximately 200,000 anterior cruciate ligament (ACL) ruptures occur in the United States every year[8,25] with most being non-contact injuries[29]. Video analyses have shown that many of these occur during a dynamic foot plant from a jump landing, a sudden change in direction, abrupt stop, or ‘dynamic valgus’ [32,39]. Environmental, anatomical, hormonal and neuromuscular factors[9,24] have all been considered to play a role in the injury. In terms of the anatomic factors, particular attention has been paid to individual and sex differences [1,17,35,37,41]. The most significant morphological risk factors associated with non-contact ACL injuries are an increased lateral posterior tibial slope (LTS), a larger femoral alpha angle, a smaller ACL cross-sectional area and a smaller femoral intercondylar notch[1,3,4,14,15,33,37,38,41]. In particular, a steeper LTS has been shown to not only increase the risk for ACL rupture but also increase ACL strain during knee loading[5,7], thereby suggesting a causal relationship. However, the relationship between LTS and the resulting tibiofemoral kinematics in the form of anterior-posterior tibial translation (ATT) and internal tibial rotation (ITR) during a dynamic foot plant is poorly understood.

Because the ACL acts as a kinematic constraint to excessive ATT and ITR[20,36], there is considerable orthopedic interest in normal and abnormal knee joint motion when evaluating the possibility of ACL injury. For example, attention is often focused on looking for an abnormal pivot shift during the Lachman test [13,30], a larger-than normal ATT during the anterior drawer test [13,30], and whether substantial laxity is found in ITR[36]. Experimental studies of simulated pivot landing in cadaver knees have measured the peak ACL strains in ATT and ITR as well as the effect of ACL transection[18,27,28]. But none of the studies have examined the relationship between LTS on the one hand, and the resulting ATT and ITR on the other, during an impulsive knee compression loading simulating a pivot landing. Under knee joint axial compression, the anterior patellofemoral joint reaction force component acting in the transverse plane on the LTS has two possible kinematic effects on the tibia relative to the femur causing: (a) ATT , and also (b) ITR relative to the instantaneous center of rotation near the central depression in the medial tibial plateau[19,21].

The purpose of this study was to quantify the relationship between LTS, ATT and ITR during jump landing loadings involving the application of impulsive knee compression, flexion, and internal tibial torque loading. We tested the hypothesis that a larger LTS correlates with increasing ATT and ITR during simulated pivot landings, each of which have been shown individually to increase ACL strain[18,27,28] and are therefore associated with the risk of ACL failure[18].

3.3 Methods

3.3.1 Specimen procurement and preparation

After our institutional review board "exempt and non-regulated" determination, fully de-identified unembalmed young male adult cadaver knees were procured from Anatomy Gifts Registry, Science Care, Medcure and Gift of Life [name of State withheld to blind manuscript]. Limbs were double bagged and stored in a freezer at -20ºC. Parasagittal radiographs were taken of 14 pairs of knees to estimate the LTS, from which 7 pairs were selected to provide the widest possible range of slopes in our sample. Care was taken to obtain a purely lateral view of the proximal tibia. The lateral tibial slope was measured on the radiographs as the angle between the longitudinal axis of the tibia and a line connecting the superior-anterior and the superior-posterior cortices of the tibial plateau. The longitudinal axis was estimated using a circle method presented by Hudek et al.[11] Seven pairs of young male knees [mean (SD) age: 25.71 (5.53) yrs, weight: 71.51(4.81) kg] (Table 1) were thawed at room temperature for 48 hours before dissection and MR imaging (see below for details). Thawed knees were dissected leaving intact the ligamentous capsular structures along with the tendons of the quadriceps, medial and lateral hamstrings, and medial and lateral gastrocnemius muscles. The distal tibia/fibula and proximal femur were cut 20 cm from the center of the knee joint and potted in polymethylmethacrylate cylinders ready for mounting in the testing apparatus.

Table 3-1. Demographic data for the male donors of the seven knees. The lateral posterior tibial slopes were measured twice by the blind observer and mean (standard deviation, SD) values were calculated. As shown in the right column, the repeated measures experimental design called for increasing impact forces, with one knee randomly selected to act under low impact, and contralateral knee with relatively high impact loading.

Specimen No.	Age [yrs]	Weight [kg]	Side	LTS [SD] [deg]	Testing Condition
P1	33	72.6	Right	8.5 [0.2]	2.5 BW x 50 trials*
			Left	6.0 [0.1]	1 BW x 50 trials + 2 BW x 50 trials
P2	23	72.6	Right	3.1 [0.6]	2.5 BW x 50 trials + 3 BW x 50 trials
			Left	1.8 [0.0]	1 BW x 50 trials + 2 BW x 50 trials
P3	25	69.1	Right	3.1 [0.0]	2.5 BW x 50 trials + 3 BW x 50 trials
			Left	1.1 [0.2]	1 BW x 50 trials + 2 BW x 50 trials
P4	32	64.4	Right	2.7 [2.1]	1 BW x 50 trials + 2 BW x 50 trials
			Left	7.6 [2.2]	2.5 BW x 23 trials -Tibial bone Fracture
P5	19	71.7	Right	4.8 [1.1]	1 BW x 50 trials + 2 BW x 50 trials
			Left	4.3 [0.2]	2.5 BW x 50 trials + 3 BW x 50 trials
P6	20	69.9	Right	6.2 [1.1]	1 BW x 50 trials + 2 BW x 50 trials
			Left	4.5 [0.5]	2.5 BW x 50 trials + 3 BW x 50 trials
P7	28	80.3	Right	6.2 [1.4]	1 BW x 50 trials + 2 BW x 50 trials
			Left	11.5 [0.8]	2.5 BW x 50 trials + 3 BW x 50 trials

* Due to technical error, inaccurate kinematic data were collected during the first 50 trials.

3.3.2 Magnetic resonance imaging

Prior to impact testing, T2-weighted 3D sagittal-plane MRIs were taken of the thawed cadaver knees with a 3T scanner (Philips Healthcare, Best, the Netherlands). From these images, the LTS was measured in each specimen using a method presented by Hudek et al[11] in OsiriX software (v. 3.7.1 lite, open-source). Briefly, in the sagittal plane, the longitudinal axis of the tibia was defined by a straight line connecting the center of the two circles drawn within the proximal tibia: a first circle was drawn whose lines are in contact with the anterior, posterior, and superior tibial cortex bone, and a second circle was drawn whose center is positioned on the first circle touching the anterior and posterior cortex of the tibia (Figure 1a). On the sagittal-plane slice of the mediolateral center of the lateral tibial plateau, a line was drawn connecting the superior-anterior and the superior-posterior cortices of the lateral tibial plateau (Figure 1b). The LTS was calculated as the angle between this line and a line perpendicular to the longitudinal axis of the tibia (Figure 1b). To assess measurement reliability, LTS was measured twice by an observer blinded to the results of the kinematics. The mean of the two measurements was used for analysis (Table 1). Intra- and inter-rater reliability were examined for the LTS measurements by using intraclass correlation coefficients (ICC). The primary observer and blinded observer each measured LTS twice. Intra-rater and interrater reliability were then calculated within and between the LTS measured by each observer and reported using ICCs.

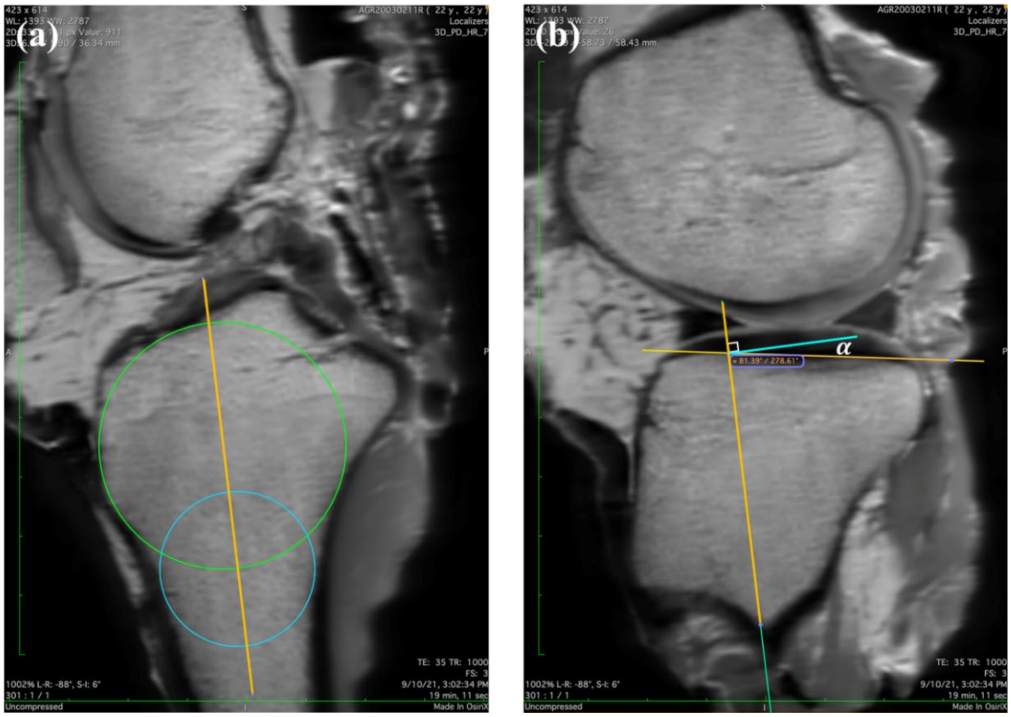

Figure 3-1. Measured lateral posterior tibial slope for the right knee of specimen P1. (a) To define the tibial longitudinal axis, a method presented by Hudek et al.[11] was used on a sagittal-plane slice by connecting the centers of the two circles. (b) At the mediolateral center of the lateral tibial plateau, the lateral tibial slope (α) was defined as the angle between the tibial longitudinal axis (as defined in (a) and the line connecting the superior-anterior and the superior-posterior cortices of the lateral tibial plateau.

3.3.3 Testing apparatus

The dissected knees were mounted in the Withrow-Oh[18,28] testing apparatus (Figure 2) in an initial configuration of 15° of knee flexion to simulate a single-leg pivot landing with 1~3 times body weight [BW]. The weight (W, Figure 2) was dropped to impact a bumper on the tibial end of the construct so as to apply the combination of an impulsive compression load and an internal tibial torque both peaking within ~70 msec via the torsional transformer mechanism (T, Figure

2). Use of the weight drop achieves a higher loading rate and larger impulsive load than a robot so as to properly match values observed *in vivo*[23]. The quadriceps, medial and lateral hamstring and medial and lateral gastrocnemius muscle forces were simulated by tensioning to the appropriate value to represent active muscle force needed to maintain 15 degrees of knee flexion prior to impact and their tensile stiffness represented by 2 mm diameter woven nylon cords elasticity[42,43] following impact. To accomplish this cryoclamps (Q, G&H, Figure 2), each with a series force transducer, were attached to each tendon, and pre-tensioned as follows: quadriceps (Q : 180 N), hamstrings (H : 70 N each), and gastrocnemius (G: 70N each). As the weight impacted the construct, the knee could flex and the tibial plateau was free to translate and internally rotate, resisted only by soft tissues and the muscle-surrogates, which could stretch under the rapidly rising knee compression, flexion moment and internal tibial torque.

Two six-axis load cells (L, Figure 2, MC3A-1000, AMTI, Watertown, MA) measured the 3D applied *input* forces and moments to the knee at the mid-tibia as well as the 3D *reaction* force and moments at the mid-femur. Impulsive forces and moments were recorded at 2 kHz, while the 3D tibiofemoral marker triad kinematics were recorded at 400 Hz with an optoelectronic imaging system (Optotrak Certus, Northern Digital Inc., Waterloo, Ontario, Canada). A triad of three markers (Figure 2) was affixed rigidly to each load cell. A 3D digitizer was used to identify anatomical landmarks on the knee joint ("virtual marker", Figure 2). From this setup, the 3D tibiofemoral kinematics were acquired. The absolute and relative 3D translation and rotation were then calculated according to Grood and Suntay[10].

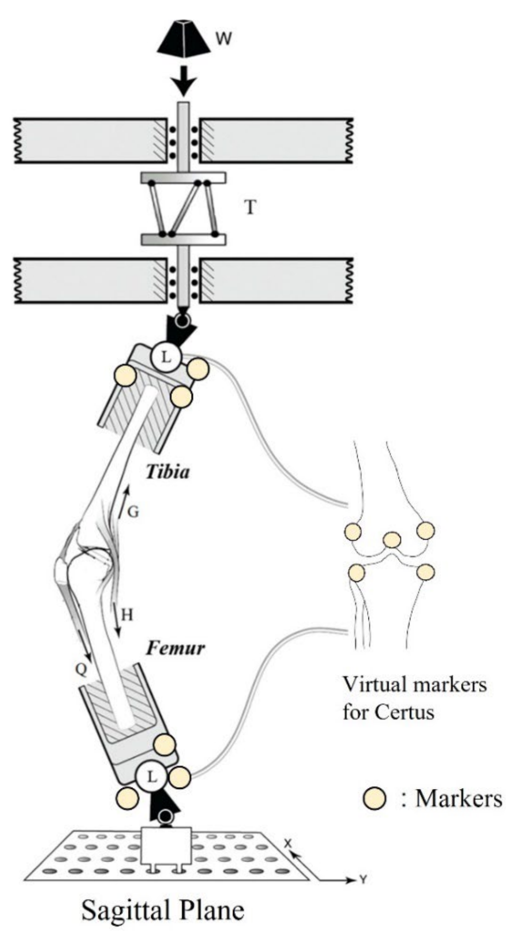

Figure 3-2. Diagram of Withrow-Oh testing apparatus[18,28] showing the diode physical markers ("Markers") on the load cells, and the virtual markers on tibial and femoral landmarks that were recorded using the 3D digitizing wand of the Certus system.

3.3.4 Testing protocol

A cross-sectional, repeated measures, experimental design was used to examine the relationship between LTS, ITR and ATT under increasing impact loading severity. It has already been shown with this apparatus that repetitive loads with a magnitude of three times BW (3*BW) or more simulating pivot landings cause the human ACL to fail due to material fatigue[18]. So we planned to repetitively load the knees with loads less than this magnitude of loading to avoid such failure. First, each specimen underwent 5 preconditioning trials to find the drop height and weight in order to simulate the target peak impulsive force on that knee (Table 1). Then the knee was subjected to a maximum of 100 loading trials, or as many trials as could be completed until the ACL failed. Repetitive loading was used because of the inherent intra and inter subject variability in the response of biological tissues to load-displacement testing[6,31]. Therefore, a randomly selected knee from each pair was tested in two sets of 25 impact trials applied with ~700 N (1 BW ±10%) after which two more sets of 25 trials were applied with ~1,400 N (2 BW ±10%).Similarly, each contralateral knee was tested with two sets of 25 impact trials with ~1,800N (2.5 BW ±10%) followed by two more sets of 25 trials with ~2,100N (3 BW±10%) in order to study how the magnitude of ATT and ITR depended on the magnitude of LTS under a range of loading magnitudes (Table 1). Between each set of 25 trials the quadriceps clamp was re-cooled using cryogenic gas to prevent slippage. Our simulated jump landing synchronized impulsive knee flexion and internal tibial moments with an impulsive axial compression force. This impulsive 3D knee impact load was shown to cause ACL fatigue failure when more than 100 trials with 3 to 4 times body weight were used[18,28]. So we employed loads of 3 BW and less in the present protocol to avoid ACL fatigue failure within 100 trials.

3.3.5 Statistical Analysis

After checking that the usual assumptions were met two, two-factor, linear mixed effect models were used to determine the simultaneous effects of LTS on ATT (designated Model A) and LTS and ITR (designated Model B) during increasing impact loading. The knee specimen (n=7) and side of the knee (right and left) were considered random effects, while the normalized impact force in BW and LTS were considered fixed effects. Random intercepts were chosen from the linear mixed model with ATT, ITR, and LTS to reflect ATT and ITR being assigned values of zero in the absence of a landing impact force, and all values under load being calculated relative to those starting values. The linear mixed models were analyzed with the *lme4* package using the open software RStudio for statistical computing (R, v. 4.1.2; Boston, MA). The underlying assumptions were found to be satisfied after checking the residuals vs fitted values and the Q-Q plots (Quantile-Quantile plot) for each model, respectively. An alpha level of $p<0.05$ was used to calculate results for both the random and fixed effects.

The *simr* package used for the power analysis suggested that the planned sample size used was acceptable. With the number of knee specimen pairs (n=7) and side of the knee (right and left), it showed a power of 100% (95% CI: 96.4 - 100) for the effects of LTS on ATT and 99.0% (95% CI: 94.6 – 100) for the effect of LTS on ITR. This seemed reasonable given our random effect size (n=13: 7 pairs of knee specimen, side of the knee (right and left), and one failed knee). Significant p values ($p<0.001$) were found for all the linear mixed model coefficients lending credence to the results.

3.4 Results

The interrater reliability of tibial slope measurements from the blind observer was excellent (ICC = 0.93). Inter-rater reliability for the agreement of measurements was also good (ICC = 0.81). A steeper LTS had a significant effect (p-value < 0.001) on both ATT and ITR as the normalized impact force (IF/BW) was increased (Table 2). As the LTS increased, the ATT was positive correlated with coefficient of 0.50 (95% CI: 0.29-0.71) independent of impact force with its coefficient of 0.52 (95% CI: 0.50-0.53). The ITR also had the positive correlation with larger coefficient of 1.36 (95% CI: 0.80-1.93) for increasing impact force (coefficient = 0.49, 95% CI: 0.47-0.52). The random term significantly affected the response with great confidence intervals not includes zero (95% CIs).

Table 3-2. Results for the two linear mixed effect models: Model A for LTS and ATT, and Model B for LTS and ITR.

	Model A: ATT ~ LTS + (IF/BW)				Model B: ITR ~ LTS + (IF/BW)			
	Coefficient	SE	t Value	P Value	Coefficient	SE	t Value	P Value
(Intercept)								
LTS	0.50	0.099	5.06	<0.001	1.36	0.26	5.11	<0.001
(IF/BW)	0.52	0.0080	64.75	<0.001	0.49	0.011	46.44	<0.001
LTS: (IF/BW)	-0.011	0.0017	-6.14	<0.001	-0.011	0.0022	-4.61	<0.001

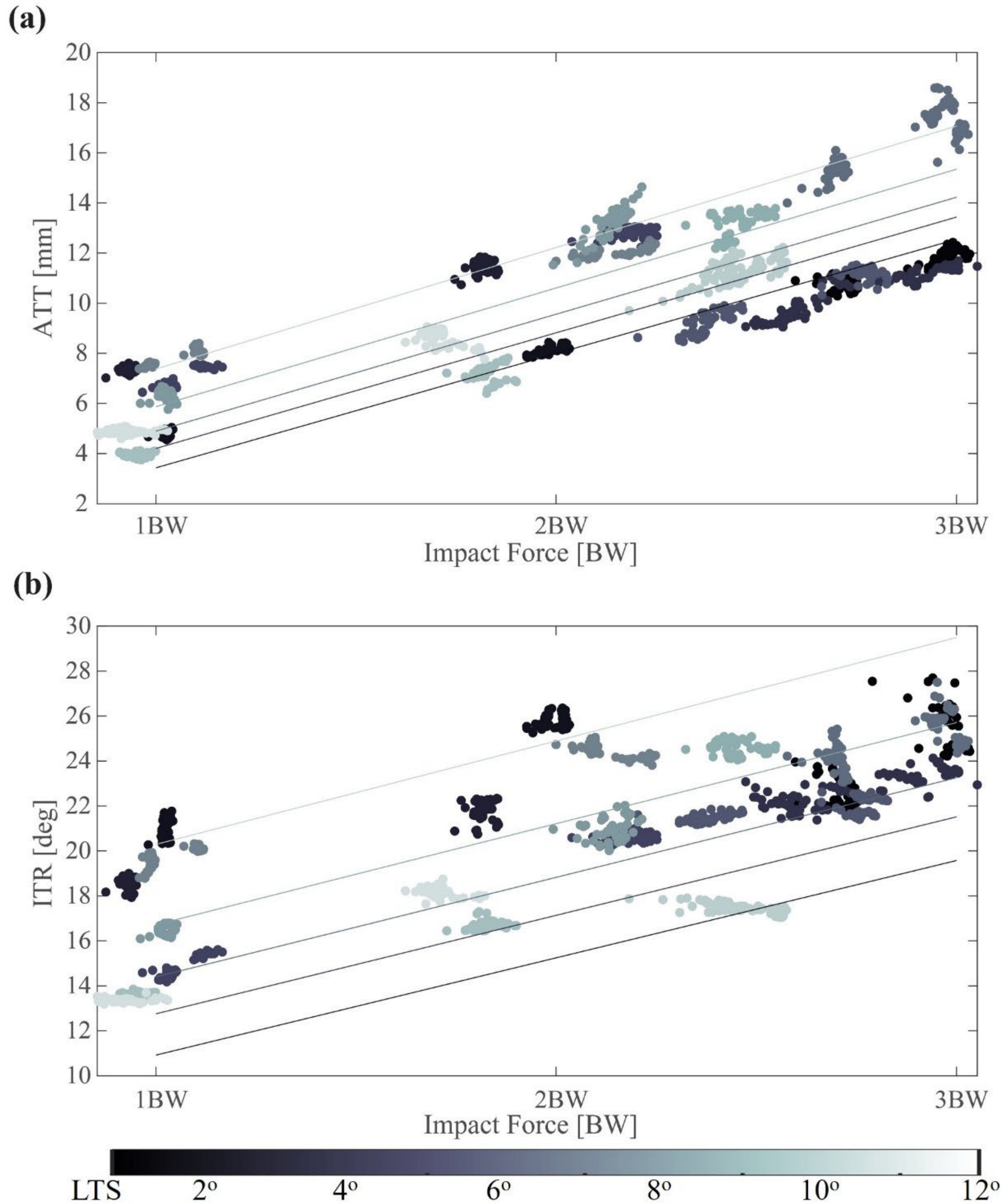

Figure 3-3. Scatter plots showing the relationship between normalized impact force and ATT (a) and ITR (b). The lines in (a) and (b) indicate the predicted effect of LTS being assumed constant at 2°, 4 °, 6 °, 8 ° and 10 ° in order to help interpret the effect of increasing impact force on ATT (a) and ITR (b), respectively, using the results of linear mixed model (Table 2).

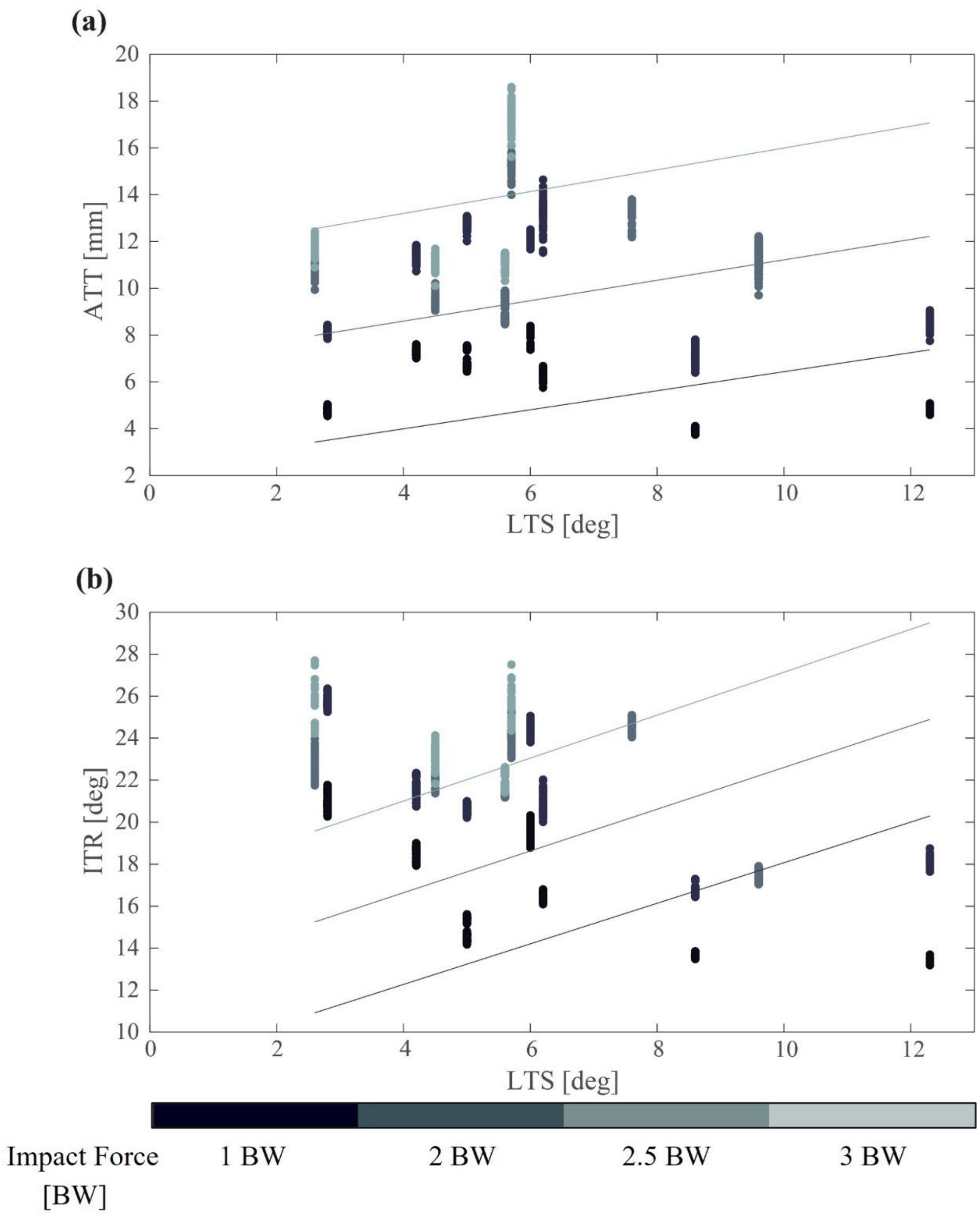

Figure 3-4. Scatter plots representing the relationship between LTS and ATT (a) and ITR (b). The three lines in (a) and (b) designate normalized impact. The vertical data scatter are the knee kinematic data for the 100 trials for a given LTS associated with each knee. The lines show the force assumed constant at 1BW, 2BW, and 3BW to help interpret the

effect of LTS on ATT(a) and (ITR) (b) from the results of the linear mixed model (Table 2).

3.5 Discussion

The present results support the primary hypothesis that knees with larger LTS are significantly associated with increased ATT and ITR in a loaded condition. Given that Oh et al. have already demonstrated that ACL strain was positively correlated with both ATT and ITR[28], the present results suggest that an athlete with a steeper LTS will systematically experience larger loads on their ACL during jump landings than the similar-sized athlete with a lower LTS performing an identical jump landing. For a given load on the ACL, the strain in the ACL will depend upon its cross-sectional area and its viscoelastic material properties. The underlying mechanism for the increase in ATT is that, under the impulsive compression loading, the LTS causes a reaction force component (equal to the inverse of the tangent of the LTS angle, see Introduction) that accelerates the tibia anteriorly relative to the femur and thereby strains the ACL[28]. Simultaneously, the LTS causes a reaction force component on the lateral tibial condyle that results in a transverse plane moment that causes the tibial plateau to pivot around an axial instantaneous center of rotation on the medial condyle[12]. Both effects will strain the ACL. Furthermore, these results are consistent with previous studies. For example, Wang et al. reported that the magnitude of ATT and ITR produced under an axial knee compression force was positively correlated with the sagittal tibial slope[40], and McLean et al. found that the greater slope of LTS was associated with anterior tibial acceleration and peak anterior knee joint reaction force which ware directly proportional to ACL strain[21,22].

Strengths of this study include the use of a simulated 3-D impulsive lower leg loading that is similar to that during a one footed pivot landing[28]. Under those conditions, the ground reaction force can reach many times body weight depending on the compliance of the shoe and ground surface[2]. The use of repetitive loading is justified because many athletic training drills for the sports most associated with ACL injuries[18,44], namely basketball, soccer, football and volleyball, require repetitions. Additionally, because only young male knees were studied, there were no confounding effects of age, osteoarthritis, trauma or sex[16,26].

Limitations of the study include the use of cadaver knees with representative muscle forces in lieu of *in vivo* experiments; accurate biplanar radiographic kinematic measures are feasible for the latter, and could be used to confirm or refute the present findings. A further limitation is that we only used male knees, because of a lack of a sufficiently large sample of young female knees to be able to study sex differences, but this could be a goal for future studies. However, tibial slope is already known to be a significant risk factor for ACL injuries in women[17,34], so the present results likely underestimate the effects that would be seen in female knees. None of the present specimens had LTS greater than 12 degrees, which would be regarded as clinically significant. Our estimates of the effect of the LTS are therefore likely underestimated relative to those that might have been seen had we been able to include knees with LTS greater than 12 degrees. Another limitation was the relatively small sample size of seven pairs of knees but the variation in LTS was sufficient to study its effect using rigorous statistical methods. The use of a range of load magnitudes (1-3BW) along with the use of repeated measures (loads) helped to counter the effect of biological tissue variability on the results. The two-factor linear mixed model used in this study lent itself for analyzing a repeated measures experimental design with a limited number of pairs of knees[23]. Lastly, we did not examine the roles of other known morphological risk factors associated with ACL injury (please see Introduction), which include the femoral alpha angle, ACL cross-sectional area and femoral intercondylar notch size, and their effect on the present outcome variables. The actual ACL injury may be caused by a combination of all risk factors. However, with the small sample size we only measured the relationship only between LTS and ATT and ITR without considering other risk factors, and the results showed that LTS increased ATT and ITR regardless of the effect of other injury factors. However, while it is possible that the femoral alpha angle and ACL cross-sectional area might correlate with LTS, it is unlikely that they or the notch size would have affected the present results qualitatively.

3.6 Conclusions

In males, a steeper LTS was associated with both increased ATT and ITR, with ITR increasing proportionally more than ATT did.

3.7 References

1. Barnum MS, Boyd ED, Vacek P, Slauterbeck JR, Beynnon BD. Association of geometric characteristics of knee anatomy (alpha angle and intercondylar notch type) with noncontact ACL injury. *Am J Sports Med*. 2021;49(10):2624–2630. doi:10.1177/03635465211023750

2. Beaulieu ML, Ashton-Miller JA, Wojtys EM. Loading mechanisms of the anterior cruciate ligament. *Sport Biomech*. 2021;00(00):1–29. doi:10.1080/14763141.2021.1916578

3. Bernhardson AS, Aman ZS, Dornan GJ, et al. Tibial slope and its effect on force in anterior cruciate ligament grafts: Anterior cruciate ligament force increases linearly as posterior tibial slope increases. *Am J Sports Med*. 2019;47(2):296–302. doi:10.1177/0363546518820302

4. Bernhardson AS, DePhillipo NN, Daney BT, Kennedy MI, Aman ZS, LaPrade RF. Posterior tibial slope and risk of posterior cruciate ligament injury. *Am J Sports Med*. 2019;47(2):312–317. doi:10.1177/0363546518819176

5. Beynnon B, Yu J, Huston D, et al. A sagittal plane model of the knee and cruciate ligaments with application of a sensitivity analysis. *J Biomech Eng*. 1996;118(2):227–239. doi:10.1115/1.2795965

6. Bradshaw EJ, Maulder PS, Keogh JWL. Biological movement variability during the sprint start: Performance enhancement or hindrance? *Sport Biomech*. 2007;6(3):246–260. doi:10.1080/14763140701489660

7. Brandon ML, Haynes PT, Bonamo JR, Flynn MII, Barrett GR, Sherman MF. The association between posterior-inferior tibial slope and anterior cruciate ligament insufficiency. *Arthrosc - J Arthrosc Relat Surg*. 2006;22(8):894–899. doi:10.1016/j.arthro.2006.04.098

8. Griffin LY, Agel J, Albohm MJ, et al. Noncontact anterior cruciate ligament injuries: Risk factors and prevention strategies. *J Am Acad Orthop Surg*. 2000;8(3):141–150. doi:10.5435/00124635-200005000-00001

9. Griffin LY, Albohm MJ, Arendt EA, et al. Understanding and preventing noncontact anterior cruciate ligament injuries: A review of the Hunt Valley II Meeting, January 2005. *Am J Sports Med*. 2006;34(9):1512–1532. doi:10.1177/0363546506286866

10. Grood ES, Suntay WJ. A joint coordinate system for the clinical description of three-dimensional motions: Application to the knee. *J Biomech Eng*. 1983;105(2):136–144. doi:10.1115/1.3138397

11. Hudek R, Schmutz S, Regenfelder F, Fuchs B, Koch PP. Novel measurement technique of the tibial slope on conventional MRI. *Clin Orthop Relat Res*. 2009;467(8):2066–2072. doi:10.1007/s11999-009-0711-3

12. Innocenti B. *Biomechanics of the knee joint*. INC; 2022. doi:10.1016/b978-0-12-824481-4.00004-4

13. Kanamori A, Woo SLY, Ma CB, et al. The forces in the anterior cruciate ligament and knee kinematics during a simulated pivot shift test: A human cadaveric study using robotic technology. *Arthroscopy*. 2000;16(6):633–639. doi:10.1053/jars.2000.7682

14. Kızılgöz V, Sivrioğlu AK, Ulusoy GR, Aydın H, Karayol SS, Menderes U. Analysis of the risk factors for anterior cruciate ligament injury: an investigation of structural tendencies. *Clin Imaging*. 2018;50(October 2017):20–30. doi:10.1016/j.clinimag.2017.12.004

15. Kumar Panigrahi T, Das A, Mohanty T, Samanta S, Kumar Mohapatra S. Study of relationship of posterior tibial slope in anterior cruciate ligament injury. *J Orthop*. 2020;21(June):487–490. doi:10.1016/j.jor.2020.08.032

16. Lang TF. The bone-muscle relationship in men and women. *J Osteoporos*. 2011;2011:1–4. doi:10.4061/2011/702735

17. Lipps DB, Oh YK, Ashton-Miller JA, Wojtys EM. Morphologic characteristics help explain the gender difference in peak anterior cruciate ligament strain during a simulated pivot landing. *Am J Sports Med*. 2012;40(1):32–40. doi:10.1177/0363546511422325

18. Lipps DB, Wojtys EM, Ashton-Miller JA. Anterior cruciate ligament fatigue failures in knees subjected to repeated simulated pivot landings. *Am J Sports Med*. 2013;41(5):1058–1066. doi:10.1177/0363546513477836

19. Loudon JK. Biomechanics and pathomechanics of the patellofemoral joint. *Int J Sports Phys Ther*. 2016;11(6):820–830.

20. Markolf KL, Burchfield DM, Shapiro MM, Shepard MF, Finerman GAM, Slauterbeck JL. Combined knee loading states that generate high anterior cruciate ligament forces. *J Orthop Res*. 1995;13(6):930–935. doi:10.1002/jor.1100130618

21. McLean SG, Lucey SM, Rohrer S, Brandon C. Knee joint anatomy predicts high-risk in vivo dynamic landing knee biomechanics. *Clin Biomech*. 2010;25(8):781–788. doi:10.1016/j.clinbiomech.2010.06.002

22. McLean SG, Oh YK, Palmer ML, et al. The relationship between anterior tibial acceleration, tibial slope, and ACL strain during a simulated jump landing task. *J Bone Jt Surg - Ser A*. 2011;93(14):1310–1317. doi:10.2106/JBJS.J.00259

23. Molenberghs G, Verbeke G. A review on linear mixed models for longitudinal data, possibly subject to dropout. *Stat Modelling*. 2001;1(4):235–269. doi:10.1191/147108201128195

24. Murphy DF, Connolly DAJ, Beynnon BD. Risk factors for lower extremity injury: A review of the literature. *Br J Sports Med*. 2003;37(1):13–29. doi:10.1136/bjsm.37.1.13

25. Musahl V, Karlsson J. Anterior cruciate ligament tear. *N Engl J Med*. 2019;380(24):2341–2348. doi:10.1056/NEJMcp1805931

26. Nieves JW, Formica C, Ruffing J, et al. Males have larger skeletal size and bone mass than females, despite comparable body size. *J Bone Miner Res*. 2005;20(3):529–535. doi:10.1359/JBMR.041005

27. Oh YK, Kreinbrink JL, Ashton-Miller JA, Wojtys EM. Effect of ACL transection on internal tibial rotation in an in vitro simulated pivot landing. *J Bone Jt Surg - Ser A*. 2011;93(4):372–380. doi:10.2106/JBJS.J.00262

28. Oh YK, Lipps DB, Ashton-Miller JA, Wojtys EM. What strains the anterior cruciate ligament during a pivot landing? *Am J Sports Med*. 2012;40(3):574–583. doi:10.1177/0363546511432544

29. Olsen OE, Myklebust G, Engebretsen L, Bahr R. Injury mechanisms for anterior cruciate ligament injuries in team handball: A systematic video analysis. *Am J Sports Med*. 2004;32(4):1002–1012. doi:10.1177/0363546503261724

30. Sakane M, Fox RJ, Woo SLY, Livesay GA, Li G, Fu FH. In situ forces in the anterior cruciate ligament and its bundles in response to anterior tibial loads. *J Orthop Res*. 1997;15(2):285–293. doi:10.1002/jor.1100150219

31. Sanders RH. Kinematics, coordination, variability, and biological noise in the prone flutter kick at different levels of a «learn-to-swim» programme. *J Sports Sci*. 2007;25(2):213–227. doi:10.1080/02640410600631025

32. Schilaty N, Bates N, Krych A, Hewett T. How anterior cruciate ligament injury was averted during Knee collapse in a NBA point guard. *Ann Musculoskelet Med*. 2017;1(1):008–012. doi:10.17352/amm.000002

33. Smith HC, Vacek P, Johnson RJ, et al. Risk factors for anterior cruciate ligament injury: A review of the literature - part 1: Neuromuscular and anatomic risk. *Sports Health*. 2012;4(1):69–78. doi:10.1177/1941738111428281

34. Sutton KM, Bullock JM. Anterior cruciate ligament rupture: Differences between males and females. *J Am Acad Orthop Surg*. 2013;21(1):41–50. doi:10.5435/JAAOS-21-01-41

35. Tat J, Crapser D, Alaqeel M, et al. A quantifiable risk factor for ACL injury: applied mathematics to model the posterolateral tibial plateau surface geometry. *Orthop J Sport Med*. 2021;9(4):1–7. doi:10.1177/2325967121998310

36. Torzilli PA, Greenberg RL, Insall J. An in vivo biomechanical evaluation of anterior-posterior motion of the knee. Roentgenographic measurement technique, stress machine, and stable population. *J Bone Joint Surg Am*. 1981;63(6):960–968.

37. Vasta S, Andrade R, Pereira R, et al. Bone morphology and morphometry of the lateral femoral condyle is a risk factor for ACL injury. *Knee Surgery, Sport Traumatol Arthrosc*. 2018;26(9):2817–2825. doi:10.1007/s00167-017-4761-x

38. Waiwaiole A, Gurbani A, Motamedi K, et al. Relationship of ACL injury and posterior tibial slope with patient age, sex, and race. *Orthop J Sport Med*. 2016;4(11):1–5. doi:10.1177/2325967116672852

39. Waldén M, Krosshaug T, Bjørneboe J, Andersen TE, Faul O, Hägglund M. Three distinct mechanisms predominate in noncontact anterior cruciate ligament injuries in male professional football players: A systematic video analysis of 39 cases. *Br J Sports Med*. 2015;49(22):1452–1460. doi:10.1136/bjsports-2014-094573

40. Wang D, Kent RN, Amirtharaj MJ, et al. Tibiofemoral kinematics during compressive loading of the ACL-intact and ACL-sectioned knee. *J Bone Jt Surg*. 2019;101(12):1085–1092. doi:10.2106/jbjs.18.00868

41. Webb JM, Salmon LJ, Leclerc E, Pinczewski LA, Roe JP. Posterior tibial slope and further anterior cruciate ligament injuries in the anterior cruciate ligament-reconstructed patient. *Am J Sports Med*. 2013;41(12):2800–2804. doi:10.1177/0363546513503288

42. Withrow TJ, Huston LJ, Wojtys EM, Ashton-Miller JA. Effect of varying hamstring tension on anterior cruciate ligament strain during in vitro impulsive knee flexion and compression loading. *J bone Jt Surg*. 2008;(July 2006):815–823. doi:10.2106/JBJS.F.01352

43. Withrow TJ, Huston LJ, Wojtys EM, Ashton-Miller JA. The relatioship between quadriceps muscle force, knee flexion, and anterior cruciate ligament strain in an in vitro simulated jump landing. *Am J Sports Med*. 2006;34(2):269–274. doi:10.1177/0363546505280906

44. Wojtys EM, Beaulieu ML, Ashton-Miller JA. New perspectives on ACL injury: On the role of repetitive sub-maximal knee loading in causing ACL fatigue failure. *J Orthop Res*. 2016;34(12):2059–2068. doi:10.1002/jor.23441

Chapter 4: On the Differences in Stress Distributions in the Mineralized Portion of Convex, Concave and Flat ACL Femoral Entheses.

4.1 Abstract

Anterior cruciate ligament (ACL) injuries usually occur proximally near the femoral enthesis. Why that is so is not understood. The thin layers of cortical bone and mineralized tissue from which the ACL collagen fibers take origin form an oval structural shell having a convex, concave and/or flat topography. The posterolateral fibers typically originate from a concave topography, while the origin of the anteromedial fibers is more variable. We hypothesized that those topographies will markedly affect the resulting shell shear, tensile and compression stress distributions for a given ACL load. So we generated three elliptical finite element shell model topographies, convex, concave and flat (as control), to which we assigned published elastic isotropic properties for cortical bone in tension, shear and compression. The results show that the maximum tensile stress was found at the proximal end of the major axis for all three enthesial topographies. The convex shell exhibited more than twice the largest tensile and shear stress in the concave shell. Likewise, at the proximal end of the shell, the areas of peak shear stress for the flat and convex entheses were considerably larger than for the concave case. The peak shear stress on the concave shell was found on its lateral surface near the distal end. We conclude that a concave enthesis helps to reduce the tensile and shear stress in the shell at the origin of the highly loaded posterolateral ACL fibers.

4.2 Introduction

While certain macroscopic tibial and femoral bone morphologies can increase the risk for non-contact anterior cruciate ligament (ACL) injury [1,22], much still remains unknown. One knowledge gap is why most injuries occur in the proximal third of the ligament near its origin at the femoral enthesis [25]. The ACL femoral enthesis has a generally oval-shaped perimeter (Figure 1)[11,20], but Benjamin noted that histological images of a cross-section showed the four layers comprising the enthesial structure which can be flat, concave or convex [5]. More recently, six different cross-sectional profiles have been identified: concave, convex and a combination of the two [2]. Let us assume for simplicity that the uncalcified cartilaginous layer of the enthesis resists none of the tensile load in the ACL fibers. That leaves the thin cortical bone and mineralized cartilage layers, together only ~2 mm thick, to anchor and resist ACL forces reaching 600~2,300 N of tension [15], or ~ x3 body weight, without failing while also resisting bending and twisting moments due to tibiofemoral kinematics [9].

At the ACL femoral enthesis the Type 1 collagen fibers originate from their fixation in its 50 - 600 um-thick mineralized region [6] to pass perpendicularly through the tidemark, the boundary between bone and ligament. From the tidemark, they turn through ~80 degrees as they pass through the ~1 mm thick layer of uncalcified cartilage (Figure 2) [3,5] before narrowing into the ribbon-like collagenous body of the ACL (Figure 1) [10,21]. An earlier finite element analysis of the effect of varying enthesial shape on ACL fiber strain near the femoral enthesis showed it to be greater with concave and lower for convex enthesial shapes, and to be particularly sensitive to the acute (or “scarf”) angle of fiber attachment [14].

In this paper we used a simple finite element model of the “bony” enthesis layers to explore how enthesial cross-sectional shape might affect the distribution of stress in the thin shell structure comprised of cortical bone and mineralized cartilage. The significance is that any tensile or shear stress concentrations could be likely points of proximal ACL failure initiation, whether under simple overload or material fatigue due to repetitive sub-maximal loading [8].

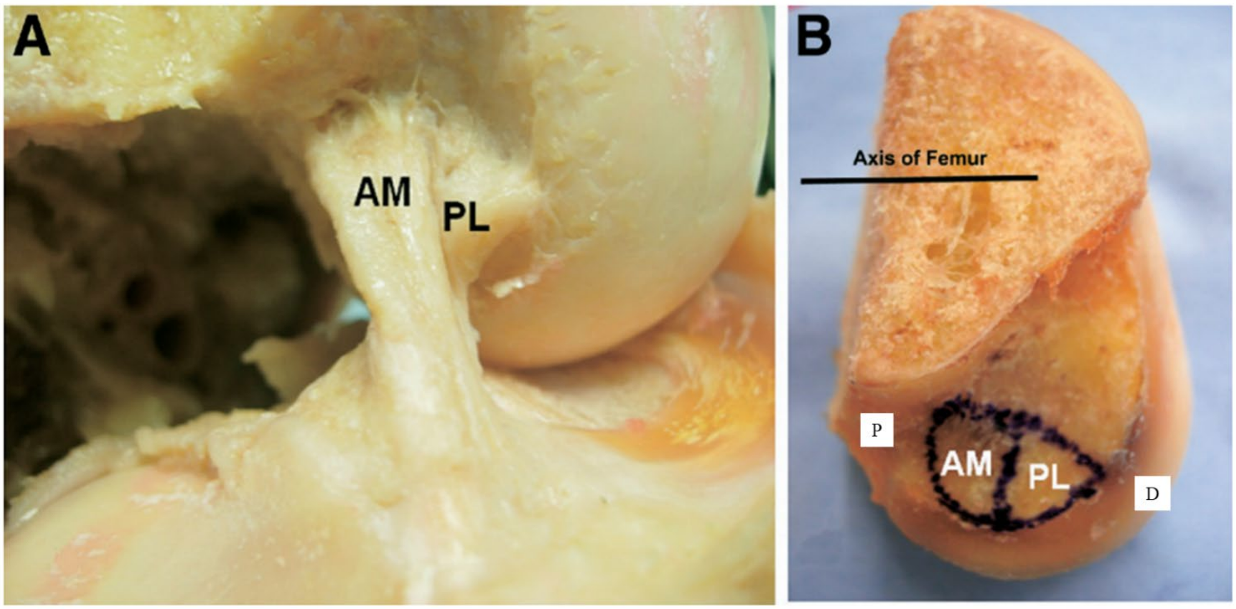

Figure 4-1. (A) Posterolateral view of a left ACL femoral attachment with the anteromedial (AM) and posterolateral (PL) bundles seen after removal of the medial femoral condyle. (B) Lateral view of the generally oval perimeter of the femoral attachment marked from (A). P indicates the proximal and D indicates the distal end of the femoral condyle. Reproduced with permission from Ferretti et al. (2007)

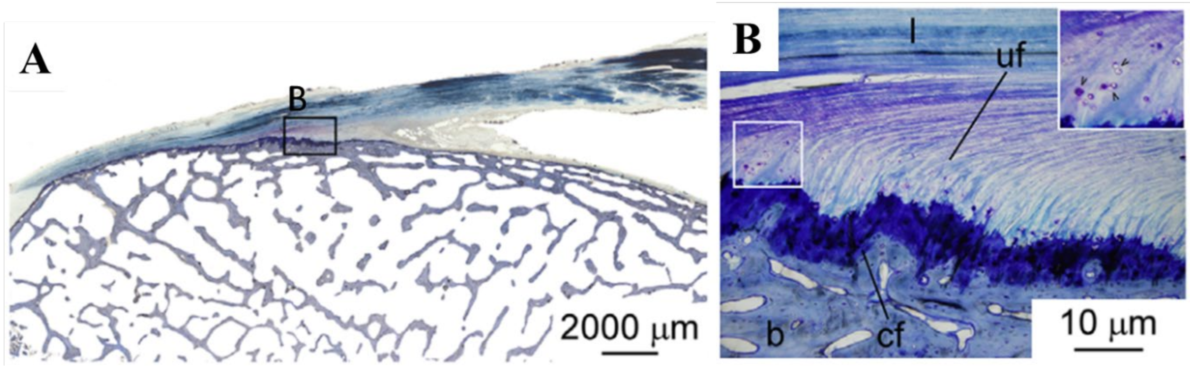

Figure 4-2. (A) Plastic embedded histological section of the origin of the ACL at its femoral entheses stained with Toluidine blue stain. (B) Enlarged view of the tissue within the rectangle indicated in (A) showing part of the femoral entheses with its four tissue zones: bone; (b), calcified fibrocartilage (cf), uncalcified fibrocartilage (uf) and ligamentous tissue (l). The inset at top right in (B) shows a magnified view of the tissue within the white rectangle. Reproduced with permission from Fig. 3 in Beaulieu et al. (2015)

An analysis of the bending of thin sheets shows that the stiffness of a sheet is dependent upon its initial transverse curvature which makes it considerably stiffer than a flat sheet [18]. Given that the magnitude of the ultimate stress of cortical bone is known to be reduced by 40% in tension, and lower by 65% in shear when compared with compression [12], one enthesial topography may reduce peak shear and tensile stresses more than the others. So we used a finite element model to study the effect that a flat enthesis (as a control), a concave enthesis and a convex enthesis had on the distribution of tensile, compressive and shear stresses on the medial (top) and lateral (bottom) surfaces of an enthesial shell to determine which shape reduced peak stresses the most. For the sake of simplicity, we neglected the tensile arcade of trabeculae that can support the mineralized shell portion of the femoral enthesis [23] but, as a check, we ran supplementary simulations to check for how much distributed elastic support in its place affected the calculated stress distributions.

4.3 Methods

Our methodological approach was to generate elliptically shaped models of the three elastic homogeneous isotropic thin shells representing the enthesial bone and mineralized region, loaded by distributed ACL fiber tension (Figure 3), using the modeling and simulation program, Inspire (v2021.2.1, Altair Engineering, Inc., Troy, MI, USA). The assumed geometry of the shell corresponded with mean measurements from our nano CT images of 15 young adult donor femoral entheses [4 female and 11 males, age: 31.8 (SD: 7.5) yrs], assuming quasilinear elastic material properties and applied ACL tensile forces (Table 1). These images were scanned using the nanotom-M (phoenix | x-ray, Baker Hughes Digital Solutions GmbH, Germany) at 20 µm resolution (80 kV, 400 µA, 500 ms exposure time, 3 ave, 1skp, 1500 images, 51 min scan time, 0.381 mm aluminum filter), and image volumes were reconstructed using datos|x reconstruction software (phoenix | x-ray, Baker Hughes Digital Solutions GmbH, Germany). The geometric measurements were made using Dragonfly™ software (v2022, ORS, Montreal, Canada). Our study used fully de-identified cadaver knees the use of which our institutional review board assigned “exempt, not regulated status”.

Given the strain results from earlier finite element simulations of ACL fiber strain across the diameter of an enthesis [14] and a range of ACL ultimate strength from 600 to 2,300 N [15], we applied a linearly increasing distributed tensile load in deciles from 10.4 ~11.5 N/mm^2 parallel to the major axis of the shell (Figure 3, Table 1). The constraints at the edge of the circular plate in the center of which the enthesis was located was assumed to be rigidly supported. For simplicity, the thicknesses of the circular cortical bone plate surrounding the elliptical enthesis and that of the shell enthesis model were assumed to be identical.

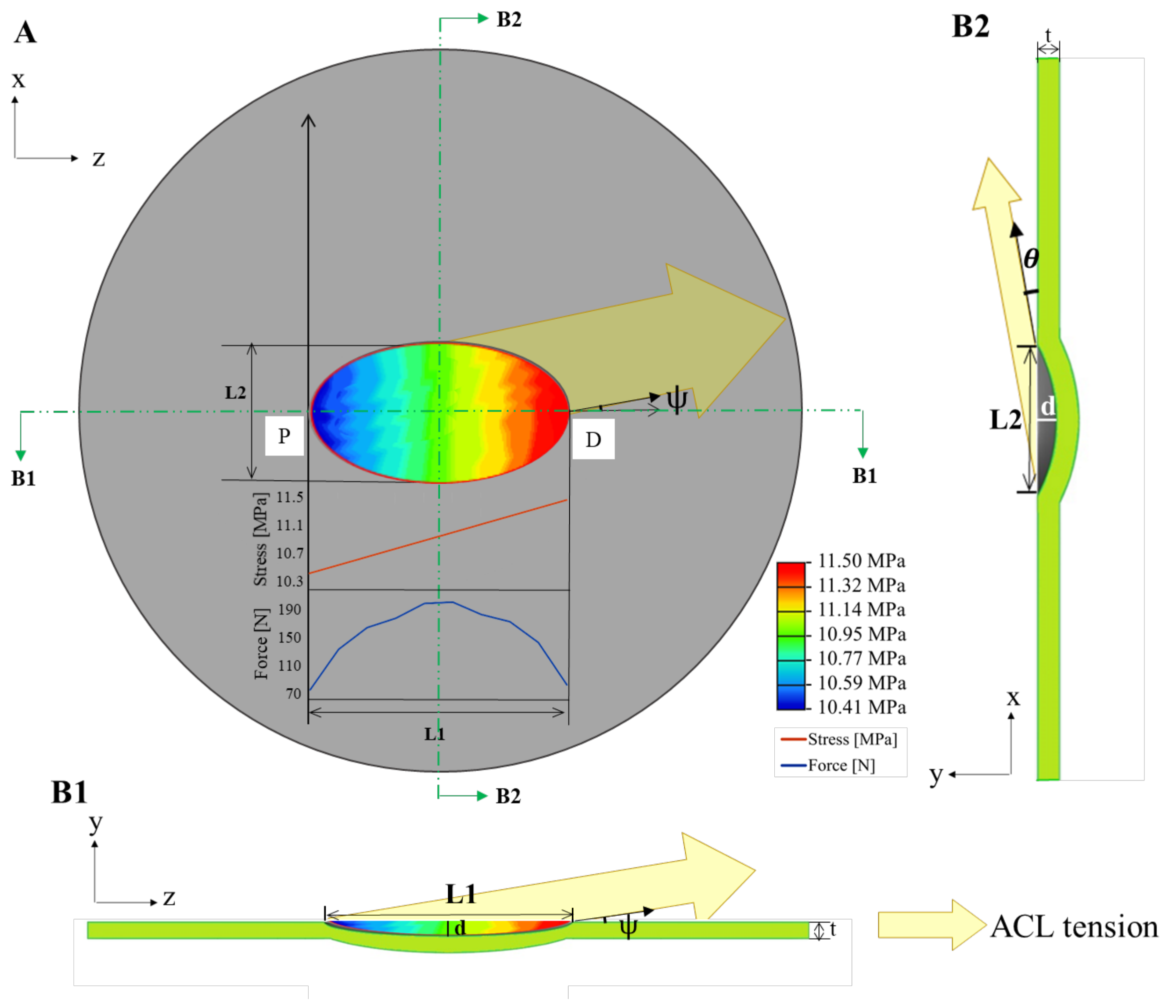

Figure 4-3. (A) Top (medial) view of the 3D elliptical finite element shell model showing the linear increase in distributed stress (see color scale for stress levels, with graphs of the tensile ACL stress and force distribution acting on transverse shell sections each having a width of 1/10 of its major diameter. P denotes the proximal end and D denotes the distal end of the enthesis shell's major axis. The yellow arrow indicates the direction of the ACL tension for knee angles near full extension. (B1) Section through the concave shell model in the y-z (coronal) plane showing the projected (attachment) scarf

angle, ψ, that the ACL fibers subtend relative to the plane of the major axis of the enthesis. In this illustration, the ACL emerges from the medial (top) surface of the shell, while the lateral surface lies (below) the shell normally supported by trabecular bone (not shown). (B2) shows an x-y (transverse) plane section through the minor axis of the enthesis shell model showing the projected scarf angle, θ. Assumed values for each parameter are given in Table 1.

Table 4-1. The assigned model enthesial shell geometric and mechanical properties for the finite element simulations. The enthesis shell depth and thickness data were based on averaged shell geometry measured on nano CT scans of 15 femoral entheses from adult donors between 19 and 40 years (see text for details).

Parameters		**Properties**	**Reference**
Enthesis dimensions	Major diameter (L1)	17.2 mm	Ferretti 2007[10]
	Minor diameter (L2)	9.8 mm	Ferretti 2007[10]
	Depth (d)	1 mm	Measured by uCT for this study
	Thickness (t)	1.2 mm	Measured by uCT for this study
ACL attachment angle (°)	Fiber attachment angle (θ) in x-y plane	24.8 °	Beaulieu 2015[4]
	Fiber attachment angle (ψ) in y-z plane	7 °	Beaulieu 2015[3]
Mineralized shell mechanical properties	Young's Modulus	17.9 GPa	Rho 1993[19] , Morgan 2018[16]
	Yield stress	114 MPa	Murphy 2016[17]
	Poisson ratio	0.3	Lai 2015[13]
	Density	170 mg/cm^3	Treece 2015[24]
ACL	Ultimate tensile strength	600~2300 N	Marieswaran 2018[15]
	Applied stress *	10.4 ~ 11.5 MPa	Based on the flat ellipse area and averaged ultimate tensile strength ± 5% (from row above)

*See text for details of stress distribution applied to the model shell

4.4 Results

The maximum tensile stress, located at the proximal end of the enthesis, was twice as large for the convex as for the concave enthesis (Table 2). The peak shear stress was located lateral to the distal end of the concave enthesis. For the flat and convex entheses the area of the maximum shear stress was considerably larger on the medial surface at the proximal end of the shells, especially in the case of the convex enthesis.

Table 4-2. Calculated distributions of tensile, compressive and shear stress values on the medial and lateral surfaces of the three model shell entheses. In each cell of the table the number in the top left corner is the stress at the proximal end, while the number in the low right corner is the stress at the distal end of the major diameter. Maximum tensile and shear stress are shown by the deep red color. The small arrow at the center of the plate indicates the direction of the ACL tension. Keys to color map values provide the calculated stress values.

	Normal Stress		Shear Stress	
	Medial Surface	Lateral Surface	Medial Surface	Lateral Surface
Concave	80.2 MPa 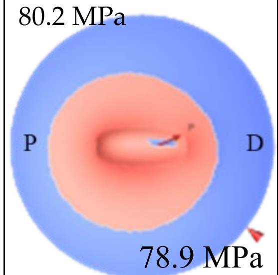 78.9 MPa	-62.0 MPa 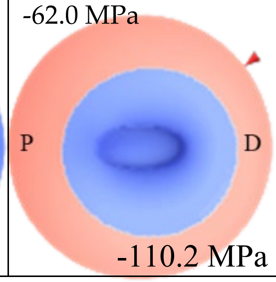 -110.2 MPa	39.9 MPa 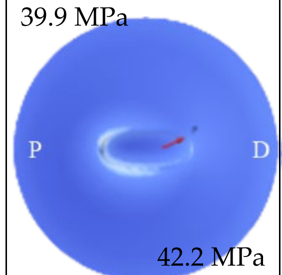 42.2 MPa	33.0 MPa 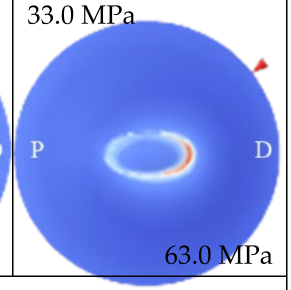 63.0 MPa
	Max tensile: 87.0 MPa Max comp.: -119.5 MPa		Max shear: 67.9 MPa	
Flat	110.3 MPa 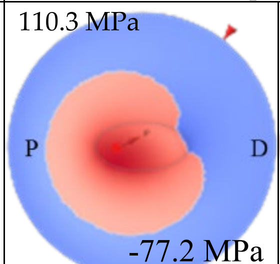 -77.2 MPa	-81.2 MPa 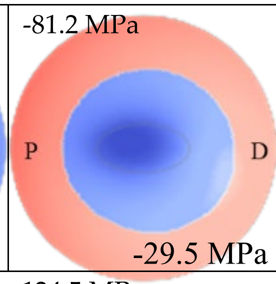 -29.5 MPa	70.4 MPa 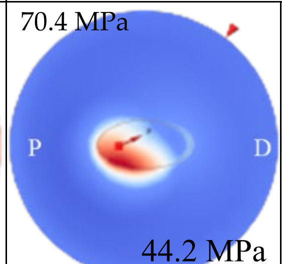 44.2 MPa	46.8 MPa 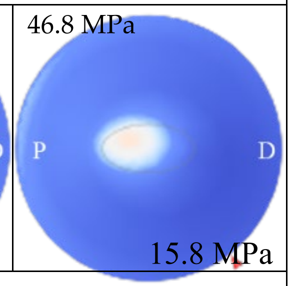 15.8 MPa
	Max tensile: 124.5 MPa Max comp.: -100.4 MPa		Max shear: 70.4 MPa	
Convex	206.4 MPa 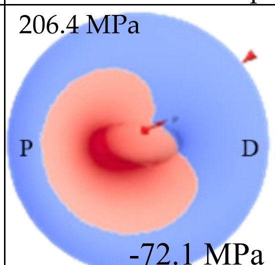 -72.1 MPa	-123.7 MPa 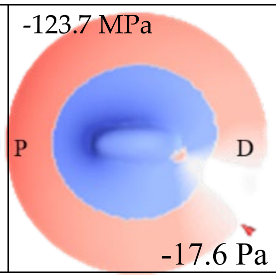 -17.6 Pa	118.7 MPa 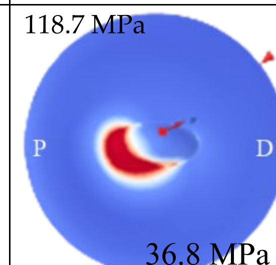 36.8 MPa	67.6 Pa 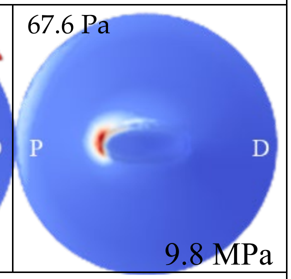 9.8 MPa
	Max tensile: 240.6 MPa Max comp.: -130.7 MPa		Max shear: 137.6 MPa	
Key to color maps	Tensile Compressive  130 MPa, 107 MPa, 84 MPa, 61 MPa, 38 MPa, 15 MPa, -8 MPa, -31 MPa, -54 MPa, -77 MPa, -100 MPa		 70 MPa, 63.1 MPa, 56.2 MPa, 49.3 MPa, 42.4 MPa, 35.5 MPa, 28.6 MPa, 21.7 MPa, 14.8 MPa, 7.8 MPa, 1.0 MPa	

4.5 Discussion

The results showed that the concave profile was advantageous because the tensile and shear stress concentrations were the lowest of the three profiles. How a concave enthesial shape develops is presently an open question. One might speculate that the type of sport played as a juvenile and adolescent could cause different enthesial shapes and trabecular morphology. For example, soccer with its sudden stops and changes in direction could load the PL bundle more than the AM bundle whereas a runner might load the PL bundle less. In one study, when entheses were sectioned normal to the major axis of the ellipse, the most distal histological regions of a series of femoral entheses, where the PL fibers originate, were all found to have a concave profile, whereas the proximal sections, where the AM fibers originate, were mostly convex [3]. We hypothesize that the existence of the concave profiles may be evidence of a longer-term bone adaptive response to reduce tensile and shear stresses. Exactly Raised regions on the medial surface of the enthesis could reflect endochondral ossification of an initially flat PL enthesis as part of a remodeling strategy to reduce strains, evidence of a repair mechanism, or possibly both. Benjamin speculated that concave entheses were due to bone localized atrophy [5], but that mechanism seems unlikely in these younger adult donors.

In earlier finite element studies of the ACL soft tissue near the femoral enthesis[14], the shorter PL fibers were predicted to be under systematically greater strain than the longer AM fibers given the acute scarf attachment angle (Figure 1). In this study, when the locations of the predicted enthesis model stress concentrations (Table 2) were compared to the morphology of nano CT cross-sections of a young adult human femoral ACL enthesis along its major axis (Figure 4), the specimen showed obvious thickening of the mineralized shell in the region of PL fiber origin. One interpretation is that thickening could be evidence of an adaptive response under Wolf's law to reduce the large shell stresses that were calculated to be present there in all the shell models.

Whether or not a uniform or linear increase in stress was applied to the shell models parallel to the major axis did not change the results qualitatively, so the stress concentrations reported here resulted mainly from the initial shell cross-sectional shapes not the assumed strain or stress distribution in the ACL fibers.

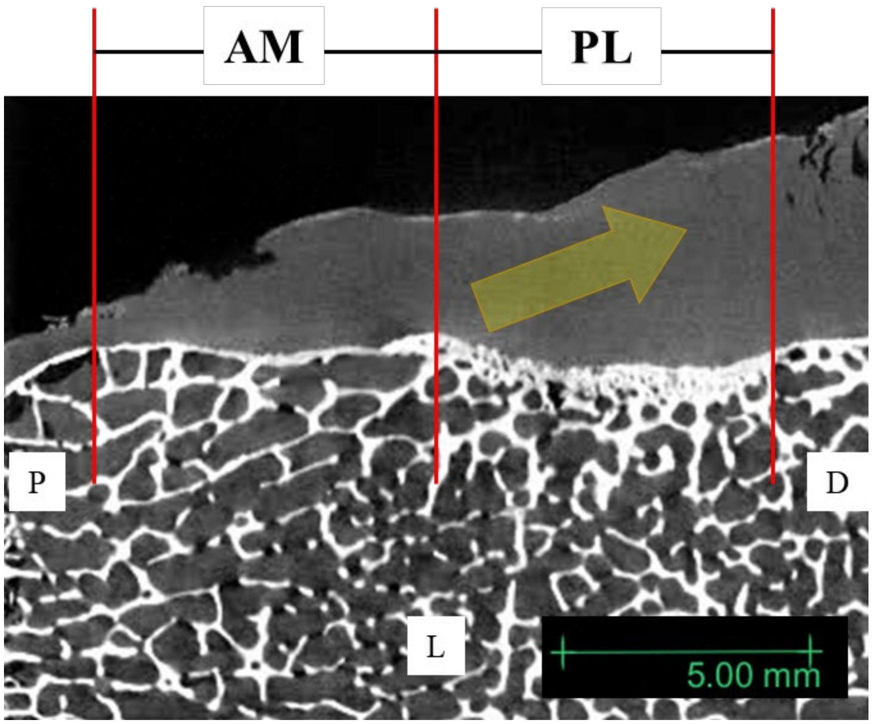

Figure 4-4. Coronal plane section from a nano CT image of a young adult specimen shows mineralized region thickening (solid arrow heads) at the origin of the PL fibers near the distal (D) end of the enthesis when compared to the thickness at the origin of the AM fibers (open arrow heads) at its proximal (P) end. The vertical red lines delineate the borders of attachment of the AM and PL fibers. The yellow arrow shows the direction of ACL tension for a knee near full extension.

Limitations of the present analysis include the simplifying assumptions of thin shell isotropy and homogeneity (see Figures 2 and 4), as well as the omission of an underlying tensile trabecular arcade [23], that would act to would stiffen the shell. As a check, we ran simulations with the model shells mounted on a homogeneous elastic layer assigned trabecular bone properties (E: 350 MPa, Poisson ratio: 0.25 [13], Density : 20 mg/cm^3 [24]): this did not change the results qualitatively for the tensile stress results. Likewise, the maximum shear stress was still located on the medial surface around the distal edge of the major enthesial axis for all three shells. The model did not include the effects of ACL fiber splay [20] which was beyond the scope of this paper. We also did not study the effect of varying ACL loading direction in the x-z plane because ACL injuries mostly happen during jump landings, pivoting, cutting or stopping abruptly with the knee near extension [7] which is where we simulated the ACL loading. We did not investigate the effect of varying the projection of the scarf angle in the y-z plane because the angle we used was the mean angle for women (Table 1). Women represent the worst case in terms of the difference in peak load applied at the ends of the major axis because men generally have a larger scarf angle (13^o)[3] and this will result in a smaller systematic difference in strain across the ACL major axis [14]. Finally, we did not include the layer of uncalcifed cartilage through which the ACL fibers bend to form the scarf angle (see Introduction). Benjamin has suggested that increases in ACL tension would tend to straighten the bend by deforming the cartilage [5] a phenomenon that was beyond the scope of this paper. Because the uncalcified cartilage was not assumed to resist ACL fiber tension in the present model, the calculated stress distributions in Table 1 represent a worst case scenario. Adding the uncalcified cartilage layer to a model shell might reduce stress values quantitatively, but it would not be expected to change the results qualitatively.

4.6 Conclusions

A flat or convex enthesis exhibits regions of high tensile and shear stress, while a concave profile is advantageous because it exhibited the lowest tensile and shear stress concentrations of the three profiles.

Acknowledgement

We thank Conor Locke for technical assistance with the nano CT imaging of the femoral enthesis specimens. We gratefully acknowledge the financial support of Public Health Service grant R01 AR054821.

4.7 References

1. Barnum MS, Boyd ED, Vacek P, Slauterbeck JR, Beynnon BD. Association of geometric characteristics of knee anatomy (alpha angle and intercondylar notch type) with noncontact ACL injury. *Am J Sports Med*. 2021;49(10):2624–2630. doi:10.1177/03635465211023750

2. Beaulieu ML, Carey GE, Schlecht SH, Wojtys EM, Ashton-Miller JA. On the heterogeneity of the femoral enthesis of the human ACL: microscopic anatomy and clinical implications. *J Exp Orthop*. 2016;3(1). doi:10.1186/s40634-016-0050-8

3. Beaulieu ML, Carey GE, Schlecht SH, Wojtys EM, Ashton-Miller JA. Quantitative comparison of the microscopic anatomy of the human ACL femoral and tibial entheses. *J Orthop Res*. 2015;33(12):1811–1817. doi:10.1002/jor.22966

4. Beaulieu ML, Wojtys EM, Ashton-Miller JA. Risk of anterior cruciate ligament fatigue failure is increased by limited internal femoral rotation during in vitro repeated pivot landings. *Am J Sports Med*. 2015;43(9):2233–2241. doi:10.1177/0363546515589164

5. Benjamin M, Kumai T, Milz S, Boszczyk B., Boszczyk A., Ralphs J. The skeletal attachment of tendons - Tendon «entheses». *Comp Biochem Physiol - A Mol Integr Physiol*. 2002;133(4):931–945.

6. Benjamin M, Toumi H, Suzuki D, Redman S, Emery P, McGonagle D. Microdamage and altered vascularity at the enthesis-bone interface provides an anatomic explanation for bone involvement in the HLA-B27-associated spondylarthritides and allied disorders. *Arthritis Rheum*. 2007;56(1):224–233. doi:10.1002/art.22290

7. Boden BP, Sheehan FT, Torg JS, Hewett TE. Non-contact ACL injuries: Mechanisms and risk factors. *Am Acad Orthop Surg*. 2010;18(9):520–527.

8. Chen J, Kim J, Shao W, et al. An anterior cruciate ligament failure mechanism. *Am J Sports Med*. 2019;47(9):2067–2076. doi:10.1177/0363546519854450

9. Cleather DJ, Goodwin JE, Bull AMJ. Hip and knee joint loading during vertical jumping and push jerking. *Clin Biomech*. 2013;28(1):98–103. doi:10.1016/j.clinbiomech.2012.10.006

10. Ferretti M, Ekdahl M, Shen W, Fu FH. Osseous landmarks of the femoral attachment of the anterior cruciate ligament: An anatomic study. *Arthrosc - J Arthrosc Relat Surg*. 2007;23(11):1218–1225. doi:10.1016/j.arthro.2007.09.008

11. Ferretti M, Levicoff EA, Macpherson TA, Moreland MS, Cohen M, Fu FH. The Fetal Anterior Cruciate Ligament: An Anatomic and Histologic Study. *Arthrosc - J Arthrosc Relat Surg*. 2007;23(3):278–283. doi:10.1016/j.arthro.2006.11.006

12. Hart NH, Nimphius S, Rantalainen T, Ireland A, Siafarikas A, Newton RU. Mechanical basis of bone strength: Influence of bone material, bone structure and muscle action. *J Musculoskelet Neuronal Interact*. 2017;17(3):114–139.

13. Lai YS, Chen WC, Huang CH, Cheng CK, Chan KK, Chang TK. The effect of graft strength on knee laxity and graft in-situ forces after posterior cruciate ligament reconstruction. *PLoS One*. 2015;10(5):1–11. doi:10.1371/journal.pone.0127293

14. Luetkemeyer CM, Marchi BC, Ashton-Miller JA, Arruda EM. Femoral entheseal shape and attachment angle as potential risk factors for anterior cruciate ligament injury. *J Mech Behav Biomed Mater*. 2018;88(August):313–321. doi:10.1016/j.jmbbm.2018.08.045

15. Marieswaran M, Jain I, Garg B, Sharma V, Kalyanasundaram D. A review on biomechanics of anterior cruciate ligament and materials for reconstruction. *Appl Bionics Biomech*. 2018;2018. doi:10.1155/2018/4657824

16. Morgan EF, Unnikrisnan GU, Hussein AI. Bone mechanical properties in healthy and diseased states. *Annu Rev Biomed Eng*. 2018;20:119–143. doi:10.1146/annurev-bioeng-062117-121139.Bone

17. Murphy W, Black J, Hastings G, arg. *Handbook of biomaterial properties*. Second. Springer; 2016. doi:10.1007/978-1-4939-3305-1_11

18. Pini V, Ruz JJ, Kosaka PM, Malvar O, Calleja M, Tamayo J. How two-dimensional bending can extraordinarily stiffen thin sheets. *Sci Rep*. 2016;6(July):1–6. doi:10.1038/srep29627

19. Rho JY, Ashman RB, Turner CH. Young's modulus of trabecular and cortical bone material: Ultrasonic and microtensile measurements. *J Biomech*. 1993;26(2):111–119. doi:10.1016/0021-9290(93)90042-D

20. Sasaki N, Ishibashi Y, Tsuda E, et al. The femoral insertion of the anterior cruciate ligament: Discrepancy between macroscopic and histological observations. *Arthrosc - J Arthrosc Relat Surg*. 2012;28(8):1135–1146. doi:10.1016/j.arthro.2011.12.021

21. Śmigielski R, Zdanowicz U, Drwięga M, Ciszek B, Ciszkowska-Łysoń B, Siebold R. Ribbon like appearance of the midsubstance fibres of the anterior cruciate ligament close to its femoral insertion site: a cadaveric study including 111 knees. *Knee Surgery, Sport Traumatol Arthrosc*. 2015;23(11):3143–3150. doi:10.1007/s00167-014-3146-7

22. Sturnick DR, Vacek PM, Desarno MJ, et al. Combined anatomic factors predicting risk of anterior cruciate ligament injury for males and females. *Am J Sports Med*. 2015;43(4):839–847. doi:10.1177/0363546514563277

23. Suzuki D, Otsubo H, Adachi T, et al. Functional adaptation of the fibrocartilage and bony trabeculae at the attachment sites of the anterior cruciate ligament. *Clin Anat*. 2020;33(7):988–996. doi:10.1002/ca.23520

24. Treece GM, Gee AH. Independent measurement of femoral cortical thickness and cortical bone density using clinical CT. *Med Image Anal*. 2015;20(1):249–264. doi:10.1016/j.media.2014.11.012

25. Wojtys EM, Beaulieu ML, Ashton-Miller JA. New perspectives on ACL injury: On the role of repetitive sub-maximal knee loading in causing ACL fatigue failure. *J Orthop Res*. 2016;34(12):2059–2068. doi:10.1002/jor.23441

Chapter 5: On the Subchondral Bone Architecture of the Young Adult Femoral ACL Enthesis under Repetitive Submaximal Loading, and on the Regional Variations in that Architecture

5.1 Introduction

Most anterior cruciate ligament (ACL) injuries occur in the proximal third of ligament near its origin at femoral enthesis[34,52]. It has been demonstrated that fatigue damage can accumulate in the Type 1 collagen of the ACL as it emerges from the bone at its femoral origin[12], but a current knowledge gap addressed in the first part of this chapter is whether fatigue damage can also accumulate in the femoral bone from which that Type 1 collagen originates.

<u>ACL anatomy:</u> The anatomy of the ACL femoral enthesis shows that the Type 1 collagen fibers emerge to pass almost at right angles through the enthesial tidemark, that is the boundary between ligament and bone, to curve and narrow into the ribbon-like collagenous body of the ACL[42]. The ACL has popularly been described as having anteromedial (AM) and posterolateral (PL) fiber bundles[14,20,32], but in reality these are arranged in a continuity of fibers across the ligament and are not necessarily divided into discrete bundles[1,25,53]. Nonetheless the two-bundle description is a useful shorthand for describing ligament function in words and will be used for convenience in this chapter. The longer AM fibers are oriented so as to primarily resist posterior shear of the tibia relative to the femur caused mainly by quadriceps tension acting via the patellofemoral mechanism[1,14,53], while the shorter PL fibers primarily resist tibial internal rotation relative to the femur[1,14,32,41,53]. An often underappreciated fact is that in a proximal–to-distal axial view of the tibial plateau, the line-of-action of the ACL acts tangentially to a radius

extending to it from the center of the medial plateau of the tibia; as a result it is well oriented to resist, marking the end range of motion, internal rotation of the tibia relative to the femur (Figure 1).

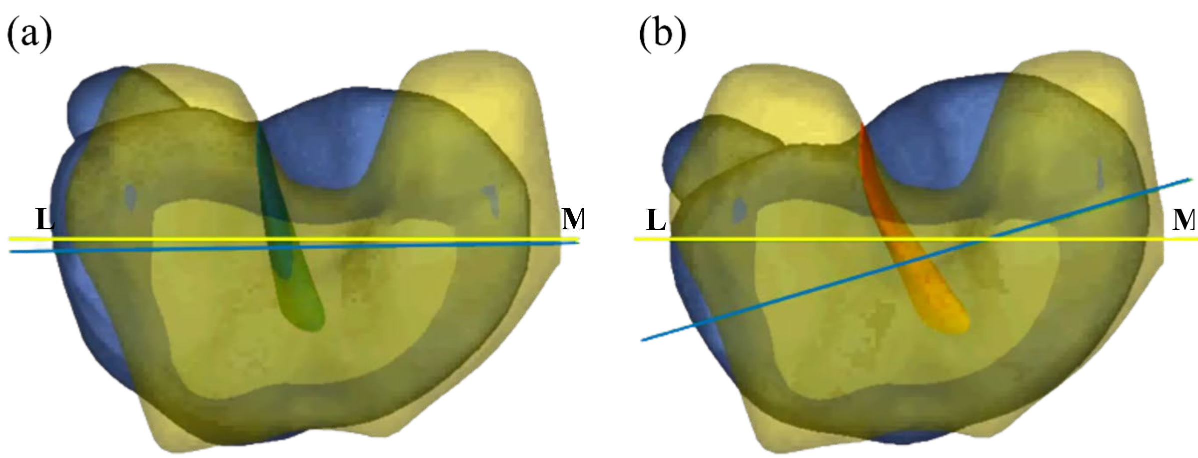

Figure 5-1. (a) Proximal-distal axial view of the femur (in yellow), tibia (in transparent blue) and ACL (in green) with the unloaded right knee near full extension. In this view the lateral (L) and medial (M) condyles are seen on the left and right of the image, and the yellow and blue lines are reference lines attached to the femur and tibia, respectively. b) This image shows a simulation of the knee with an internal rotation torque applied to the tibia about its longitudinal axis. The resulting strain in the ACL finite element model is shown in red as it resists axial rotation of the tibia about the center of rotation on the medial condyle (where the blue and yellow lines now cross). In terms of functional anatomy, note how the ACL is optimally located to act as a checkrein, not only to limit excessive posterior translation of the femur relative to the tibia due mainly to the patellofemoral mechanism, but also, importantly, internal tibial rotation in the knee, the last being perhaps underappreciated in the literature. (Still images reproduced from a video animation of a finite element model by Oh (2011)[37]).

The ACL femoral enthesis has been noted to have six different cross-sectional shapes in adults[2]. A finite element analysis examined the effect of those shapes of the femoral enthesis on ACL fiber strain and demonstrated that the origin of the PL fibers had to resist larger strain than the origin of the AM fibers whenever tension is placed on the ACL near full knee extension. This is because the PL fibers have shorter slack lengths than the AM fibers do, as a result of the scarf angle of ACL attachment at the femoral enthesis[30]. Interestingly, in a histological study, the distal-most regions of the femoral entheses, from where the PL fibers originate, were all found to have parabolic concave profiles, while the proximal section, from where the AM fibers originate, were mostly found to have a convex profile[2]. The different functional roles of the AM and PL bundles and their different strain profiles could be the reason why more than 40 % of partial ACL tears occur in the PL bundle[43], which we know to be especially strained under internal tibial rotation[38]. So, if no fatigue damage is found in the bone under the femoral enthesis in the first half of this chapter, the second half of this chapter is directed toward analyzing regional variations in the bone supporting the femoral ACL enthesis. Specifically, we wanted to establish whether the subchondral bone beneath the origin of the PL fibers exhibits architectural evidence of greater strength and stiffness under ACL tensile and torsional loading than that beneath the origin of the AM fibers as a result of bone adaptations according to Wolff's law.

<u>The four ACL femoral enthesis zones</u>: The ACL originates from femoral bone through a series of four adjacent zones: bone, calcified fibrocartilage, uncalcified fibrocartilage and finally the ligament proper[6]. These four anatomic plate-like zones, which collectively are called the enthesis, represent a systematic gradation of increasingly more flexible materials in bending and shear as the collagen fibers of the ACL emerge from the enthesis. This particular anatomical arrangement of the enthesis is thought to minimize stress concentrations and distributed forces

across the entire ACL attachment area[5]; it is also possible that the assembly serves to absorb shock when the ACL acts as a checkrein to forcibly limit the end range of two coupled tibiofemoral knee motions: namely anterior shear and internal rotation of the tibia relative to the femur[10,24].

Can the subchondral bone fatigue? The ACL is composed mainly of Type 1 collagen self-assembled into highly organized hierarchical structures having a heterogeneous composition[40]. While the anterior cruciate ligament itself can fail under a single overload, it has recently been shown that damage to collagen fibrils and fibers can accumulate in the fibrils and fibers at the femoral enthesis under repetitive sub-maximal loading[12]. However, it is not known whether fatigue damage can accumulate in the bone underlying the femoral or tibial entheses and that will be addressed in the first part of this chapter.

Subchondral bone architecture: The subchondral bone underlying the femoral enthesis has a decidedly heterogeneous structure, being divided into a subchondral cortical plate, less than a mm thick, that is supported by architectural networks of subchondral trabecular bone plates and rods[27,54]. The subchondral cortical plate provides mechanical stiffness to support the overlying articular cartilage[8,9] and resist tension in the ACL. The subchondral trabecular bone is more metabolically active than the subchondral cortical plate and there is evidence that it can adjust its architecture so as to minimize local mechanical strains according to Wolff's law[13,49]. The uncalcified cartilage, calcified cartilage and subchondral cortical and trabecular bone act as a remarkable unit to transfer substantial mechanical loads at the joint end ranges of tibial internal rotation and anterior shear motion relative to the femur[21,29].

Subchondral bone loading: Comparatively little is known about subchondral cortical bone and trabecular bone stress distributions at the femoral enthesis under ACL loading. In limiting tibiofemoral bending and twisting motions the tensile stress in the ACL alone can reach 600 ~ 2,300 N[31], or x3 body weight, before failure[15]. Obviously, such large loads place great stress and strain on the femoral and tibial entheses lying in series with it. Given Wolff's law[49], the shape and architecture of the femoral enthesial bone should adapt its architecture and shape under daily loads thereby revealing the directions of principal stress and strain. We therefore hypothesize that tensile and torsional strains on the ACL leave telltale signs in the subchondral bone structure underneath the ACL attachment area that reflect how the bone had to orient and strengthen itself under the loads on it imposed by the donor physical activity pattern.

Measures of subchondral bone fatigue damage: We sought to employ two types of measures of bone fatigue failure. A subjective measure: We visually scanned the nano CT images for signs of obvious microcracks separating one or more trabecular plate or rod leaving the two parts in close approximation but not touching[46,48,50,51]. Objective measures: These included traditional measures of bone quality with bone mechanical properties including bone volume fraction (BV/TV), bone mineral density (BMD), cortical bone thickness (Ct.Th), and trabecular bone thickness (Tb.Th) [11,22,33,39,45,47]. In theory at least these should suffice to record either the presence of voids or areas of compaction in trabecular bone of the type observed under compressive fatigue loading by Hansson et al. (1988)[23] or under tensile-compressive fatigue loading by Lin et al. (2020.)[28].

Hypotheses to be tested:

- H1, a null hypothesis, that sub-maximal repetitive knee loading known to substantially strain the ACL would not cause visible fatigue damage in the subchondral bone under the femoral enthesis.
- H2, a null hypothesis, that there would be no significant difference between at the subchondral bone under the usually more highly stressed PL bundle of the ACL enthesis and under AM bundle in BV/TV, BMD, Ct.Th, and Tb.Th.

- H3, that the trabeculae of the subchondral bone have preferred directionality, visible as an arcade, as a telltale of the most common direction of principal stress applied by the donor's activities.

5.2 Methods

5.2.1 Sample preparation

We gathered and tested fully de-identified cadaver knees under an "exempt, not regulated status" approval from the University of Michigan Institutional Review Board. Fourteen pairs of unembalmed adult human cadaver knees of similar age and weight donors (3 female and 11 male, age: 31.79 ± 7.31 years, weight: 68.89 ± 8.59 kg) were harvested from Anatomy Gifts Registry, Science Care, Medcure and Gift of Life Michigan, and frozen at - 20ºC in thick, sealed, double polyethylene bags until they were needed.

To investigate the fatigue evidence on the bone, one knee of each of seven pairs of knees was randomly reserved as an (internal) untested control knee, while the contralateral knee was used for repetitive mechanical loading under 3 times body-weight (BW). In addition, one each of the remaining seven pairs of knees was selected for 1 BW lower impact repetitive loadings, while the contralateral knee was tested with 3 BW. This mechanical testing employed the same apparatus and protocol described in Chapters 2 and 3.

After testing, the knees were refrozen double bagged and stored at -20 deg C until needed. They were then thawed in the bags at room temperature and the femoral portion of the ACL. Using a pathology bandsaw (EXAKT 312 Pathology Saw, Norderstedt, Germany) each femoral enthesis was extracted and trimmed to provide a femoral ACL subchondral bone specimen with a volume of about 1 cm^3 which had an intact ACL enthesis along with ~5 mm thick of subchondral cancellous bone. Specimens were then fixed in 10% neutral buffered formalin in a 15 ml Falcon tube for 72 hours, and once fixed were stored in 70% EtOH until the next step.

5.2.2 Image scanning

A Nonotom-M computed tomography system (phoenix | x-ray, Baker Hughes Digital Solutions GmbH, Germany) was used for making high resolution (20 µm voxel size) scans of each specimen with consistent acquisition parameters (80 kV, 400 µA, 500 ms exposure time, 1,500 images, 51 min scan time, 0.381 mm aluminum filter). Image volumes were reconstructed using datos|x reconstruction software (phoenix | x-ray, Baker Hughes Digital Solutions GmbH, Germany). The results of the reconstruction were generated via Dragonfly™ software (v2022, Object Research Systems, Montreal, Canada) to process the image analysis.

5.2.3 Volumetric analysis

Using Dragonfly, each image of femoral ACL subchondral bone specimen was reoriented with a major axis defined parallel to the nearly straight anterior border of ACL formed by the lateral intercondylar ridge emanating from the lateral wall of intercondylar notch (dashed line in Figure 1a)[19]. Based on that major axis, the ACL attachment area was then defined (yellow ellipse, Figure 1a) with the lateral bifurcate ridge and dimensions of the ACL insertion site estimated from the mean dimensions described by Ferretti et al. in who employed 16 cadaveric knees from eight adult humans[19]. The subchondral cortical plate porosities in the nano CT images are an anatomical feature associated with transfer of tissue turnover products associated with concentric layers of bone surrounding them[16].

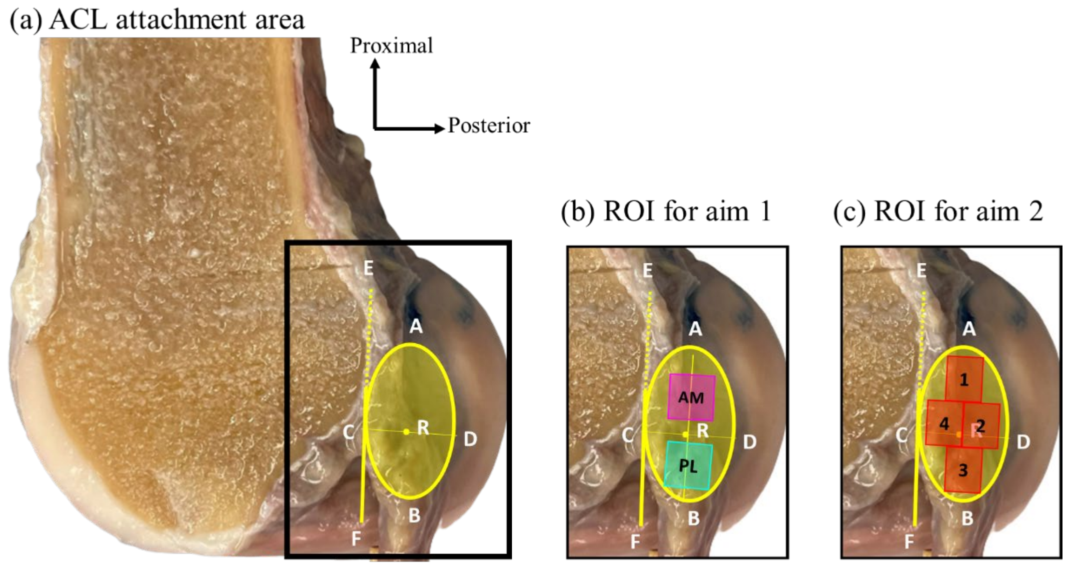

Figure 5-2. Definition of regions of interest (ROI) for the regional analyses of subchondral bone architecture: (a) ACL attachment area was defined by an ellipse with its major axis parallel with the lateral wall of intercondylar notch (dashed line). The intercondylar notch (EF) line was assumed parallel with the major axis (AB) of the yellow ellipse denoting the enthesial attachment area. AR was defined as the length of the AM fiber attachment, while BR was defined as the length of the PL attachment area. Similarly, CD was defined as the width of the ACL attachment area, which included the AM and PL bundles. All these dimensions were taken from Ferretti et al. (2007) [19]. (b) ROI for H1 and H2: the quantitative comparison between the AM and PL fiber origins. (c) ROI for H 3: the directionalities differences of the trabecular alignments in the direction of ACL tensile loading.

We tested null hypothesis that there would be no significant difference between tested and control knees, and between lower impact loads and higher impact loads tested knees in Ct.Th, Tb.Th, BV/TV, and BMD of the AM area, PL area, and difference between PL and AM areas (PL-AM), respectively. A two-sided Mann-Whitney U test was performed using MATLAB

(R2021b; MathWorks, Natick, MA, USA). Differences with alpha level of $p<0.05$ were considered statistically significant.

2) To test H2 and quantitatively compare the architecture of the trabecular between beneath the AM and PL fibers, 5 mm^3 cubes were defined and examined as ROIs centered on the AM and PL bundle attachment within the boundary of the ACL origin (Figure 1b). Dragonfly was used to calculate Ct.Th, Tb.Th, BV/TV, and BMD, and MATLAB was used for a two-sided Mann-Whitney U test. We tested the null hypotheses that there would be no significant difference in Ct.Th, Tb.Th, BV/TV, and BMD at the AM and PL sampling sites, respectively.

3) To test H3 we divided the ACL attachment area into four Areas (Figure 1b) to compare the subchondral trabecular bone orientation intensity according to the direction of ACL tensile loads. Hence a 5 (aligned with the major axis) x 4 x 3 (depth) mm^3 cuboid was identified beneath the subchondral cortical plate. Then, 150 images (directions of depth) per each area were extracted using Dragonfly™ to analyze the directionality of the trabeculae. Directionalities were calculated using ImageJ (NIH open source software) with a directionality plugin based on Fourier spectrum analysis[18]. Each image was divided into square volumes to compute their Fourier spectra, and then analyzed in polar coordinates (Figure 2b). The number of structures in each direction (^{o}) were computed to obtain the histogram required to quantify the directionality distribution.

The ROI 1 and 2 were selected to be large enough to capture substantial portion of the AM and PL enthesis with the subchondral trabeculae, but not so large that they also captured part of the large compressive arch associated with the femoral condyle[8] (Figure 5.3.(a)). (Capturing part of the large compressive arch would have compounded any differences between the AM and PL ROIs.)

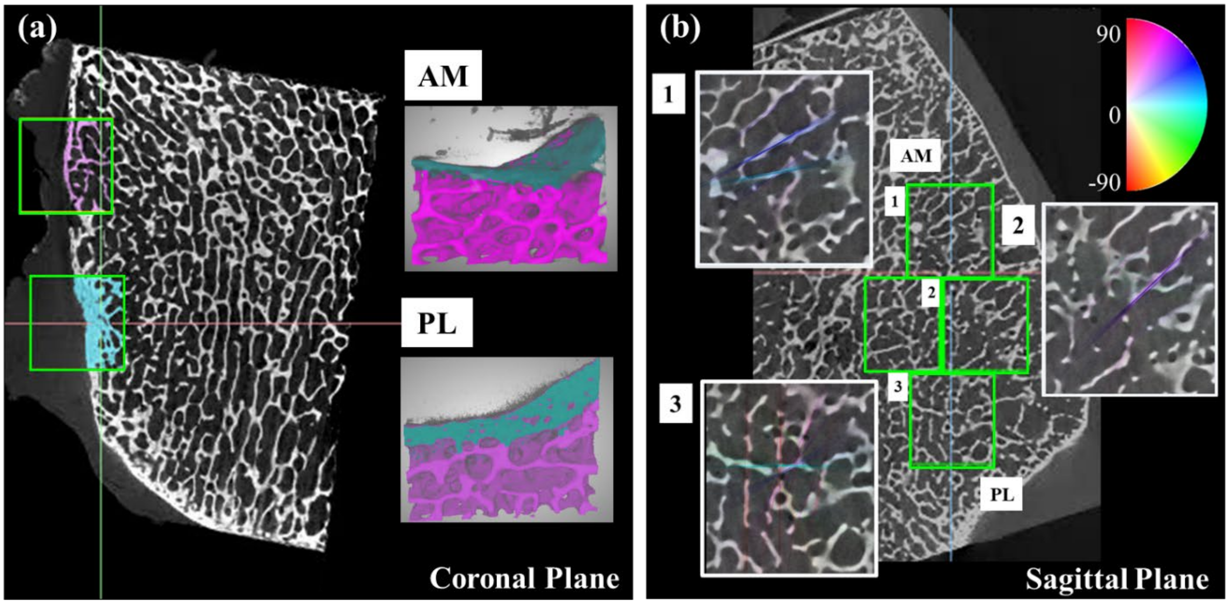

Figure 5-3. ROIs of the nano CT images of subchondral femoral enthesis bone. (a) Coronal plane images of the 5 m^3 cubes sectioned at the center of AM and PL area, while the colored images at right show an example of the segmentation of the cortical bone plate (Cyan) and trabecular bone (Magenta) in each volume. (b) Sagittal plane images of the 5 x 4 x 3 (depth) m^3 cuboids under the ACL attachment area; the trabecular directionalities were analyzed in each image section using an ImageJ directionality plugin. The color wheel at top right illustrates the orientation of trabeculae by color and direction.

5.3 Results

5.3.1 Quantitative comparison of subchondral bone under the AM and PL fiber origins (H1)

Subjectively, we did not observe obvious microcracks in trabecular plates or rods at 20 µm resolution.

Objectively, there were slightly differences in the average values between the control knees and 3 BW tested knees, as well as between the 1 BW tested knees and the 3 BW tested knees, separately (Table 1). However, the null hypotheses were supported for all factors with p>0.05: there were no significant difference between tested and control knees in Ct.Th (AM area: p =1 , PL area: p = 0.3, PL-AM: p=0.38), Tb.Th (AM area: p =1 , PL area: p =0.53 , PL-AM: p= 0.71), BV/TV (AM area: p = 0.71, PL area: p =0.46 , PL-AM: p=0.71), and BMD (AM area: p =0.38 , PL area: p =0.13 , PL-AM: p=0.23). The same was true when comparing the effect of lower impact loads with higher impact loads: Ct.Th (AM area: p =0.46 , PL area: p =0.71 , PL-AM: p=0.71), Tb.Th (AM area: p =1 , PL area: p =1 , PL-AM: p=0.31), BV/TV (AM area: p = 0.71, PL area: p =0.38 , PL-AM: p= 0.16), and BMD (AM area: p =0.1 , PL area: p =0.3 , PL-AM: p=0.38).

Table 5-1. Mean [SD] values for calculated results for AM and PL subchondral bone ROIs.

	PL				AM			
	Control knee	**Higher impact loads**	**Lower impact loads**	**Higher impact loads**	**Control knee**	**Higher impact loads**	**Lower impact loads**	**Higher impact loads**
Ct.Th [mm]	0.42 [0.080]	0.36 [0.077]	0.36 [0.075]	0.34 [0.081]	0.29 [0.072]	0.28 [0.021]	0.25 [0.069]	0.28 [0.078]
Tb.Th [mm]	0.21 [0.029]	0.20 [0.027]	0.22 [0.038]	0.22 [0.054]	0.20 [0.029]	0.20 [0.021]	0.21 [0.045]	0.22 [0.058]
BV/TV	0.49 [0.13]	0.46 [0.12]	0.42 [0.061]	0.41 [0.093]	0.34 [0.039]	0.34 [0.058]	0.35 [0.073]	0.36 [0.085]
BMD [mg/cc]	1372.3 [329.4]	1152.6 [124.2]	1208.2 [114.7]	1128.9 [41.3]	1265.0 [341.5]	1084.4 [128.6]	1159.0 [101.8]	1099.6 [43.8]

5.3.2 Quantitative comparison of subchondral bone under the AM and PL fiber origins (H2)

H2 was rejected for the bone volume fraction and cortical bone thickness in that the bone volume fraction was significantly greater under the PL than under the AM fiber origin (Figure 3a), p < 0.001 mean (SD) PL: 0.45 (0.10) vs AM: 0.35 (0.06)). In addition, the cortical bone thicknesses were significantly different under the PL and AM origins (Figure 3b), $p < 0.001$ mean (SD) PL: 0.37 (0.08) vs AM: 0.27 (0.06)). There was also a trend in the BMD ($p=0.08$ mean (SD) PL: 1215.5 (200.5) vs AM: 1152.0 (193.8)), but not in the trabecular bone thickness ($p = 0.44$, mean (SD) PL: 0.21 (0.04) vs AM: 0.21 (0.04)).

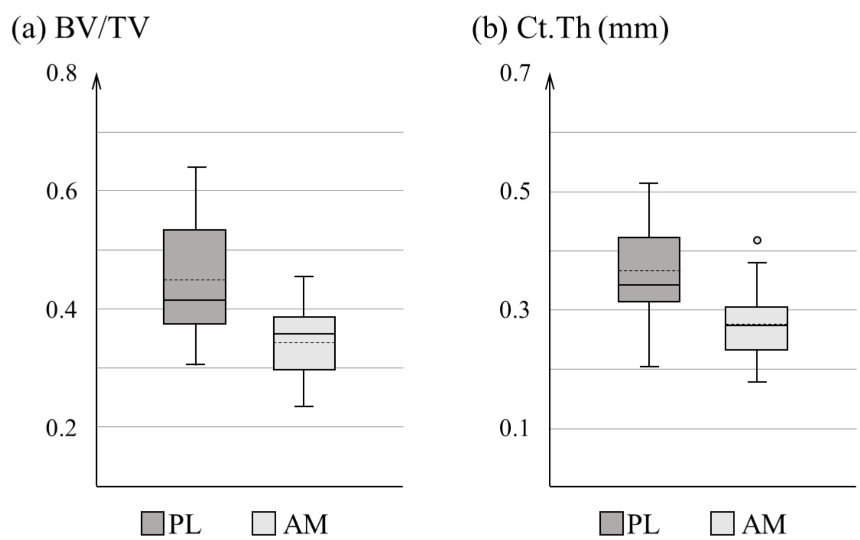

Figure 5-4. Subchondral bone results beneath the AM and PL fiber origins: (a) BV/TV and (b) Ct.Th. Solid line denotes median, box: 1st – 3rd Quartile range, whiskers: 5 – 95% of data, dot: outliers, dashed line: mean)

5.3.3 Directionality of subchondral bone trabeculae (H3)

Figure 4 shows histograms for each area's trabecular directionalities. Areas 1 and 2 under the most proximal-posterior end of the ACL attachment region exhibited left skewed histograms with orientation intensities range between 10º~ 40º: 13.3 % frequencies were in the 20º ~40º range for Area 1 and 13.6 % frequencies were in the 10º~30º range for Area 2. On the other hand, the anterior-distal areas exhibited symmetric histograms (Area 3: 12.6 % and Area 4: 12.6% within the – 10º and 10º range).

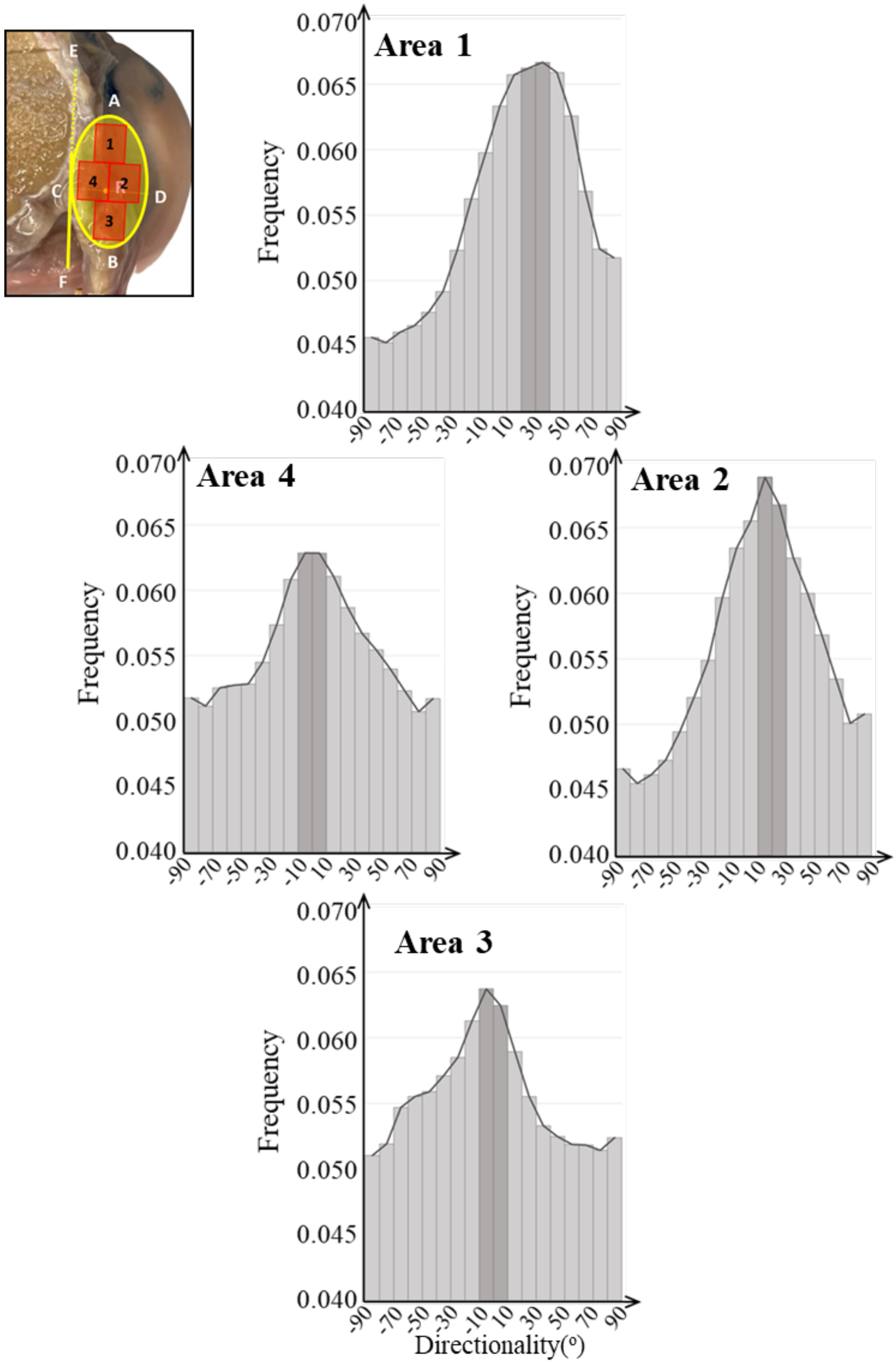

Figure 5-5. Histogram showing trabecular directionalities, clockwise, by Area of interest. The inset at upper left shows the locations of each measured Area.

5.4 Discussion

Neither our subjective visual inspection nor our quantitative nano CT measures revealed significant differences in subchondral bone architecture at any level of fatigue loading (H1). So, we conclude that, at the 20 μm resolution level of imaging resolution at least, the architecture and regional differences in bone architecture under the ACL femoral subchondral bone were unaffected by fatigue loading. It is still possible that at higher resolution, namely 2 μm or better, that such fatigue damage may still be observed. But in a specimen we rescanned at 8 μm resolution, BV/TV decreased only slightly compared than 20 μm (BV/TV: 0.42 (PL, 20 μm) vs 0.41 (PL, 8μm) and 0.39 (AM, 20 μm) vs 0.33 (AM, 8 μm).

Because our methods did not reveal fatigue evidence at the 20 μm resolution we must conclude, for the present at least, that it is the Type 1 collagen near the femoral enthesis that is most susceptible to low cycle fatigue damage accumulation under repetitive loading (see Introduction) and not the subchondral plate bone nor the subchondral trabecular bone beneath the femoral enthesis.

Damage propagation in older femoral trabeculae has been was found under compressive, torsional and combined loading at 20 μm, and microcracks were revealed through trabecular plates[50]. So, we are currently embedding all the enthesial tissues reported in this Chapter in polymethylmethacrylate and staining them with Basic Fuchsin[26] to examine them histologically under higher power magnification to double check for the presence of microcracks in the fatigued specimens (and controls). Studies in the literature of the trabeculae show that there are more susceptible to microcrack and crack propagations[35,36] under shear [17] than under tensile and compressive loading. Therefore, if we had had greater resolution than 20 μm we might have expected to see evidence of microcracks underneath PL bundle rather than the AM bundle given the results in Chapter 4.

The most interesting result in this study is the obvious thickening of the subchondral cortical ACL femoral enthesis plate beneath the origin of the PL fibers, which was accompanied by an increase in bone volume fraction there (H2). This result not only is consistent with the PL bundle fibers in the donors habitually carrying greater strain than the AM bundle fibers[30], but also is evidence of the bone's adaptive response that is consistent with Wolff's law: stiffening and strengthening of the bone to reduce peak strains. Furthermore, there were regional differences in the trabecular bone directionality under the ACL when the attachment area was divided into the four regions (H3). In Chapter 4, to better understand the stresses on the endplate under ACL tension, we ran a theoretical simulation using a simple finite element biomechanical model of an ACL attached to a uniform subchondral plate with the mean compound scarf angle of 7^{o} in the proximal-distal and 24.8 ^{o} in the anterior-posterior directions[3,4]. The maximum tensile stress was predicted to be located at the proximal-posterior end of the femoral enthesis (this is equivalent to AM Areas 1 and 2 (Figure 1c), while the distal-anterior end (the PL region, Areas 3 and 4 in Figure 1c) was under greater shear stress. This was because of scarf angle results in the shorter PL fibers undergoing systematically greater tensile strain than the AM fibers. The trabeculae in the bone under the region with greater tensile stress (i.e., Areas 1 and 2) were clearly aligned with the line of action of the ACL in a slightly flexed knee. This results also reflects Wolff's law and the need to stiffen the trabecular bone arcade there that is placed under tensile stress. The line of action of the ACL, of course, changes with the degree of knee flexion, but ACL injuries most often happen near full knee extension[7] which was why we assumed a knee flexion angle of 15^{o} in this Chapter.

Since the variables Ct.th, BV/TV, BMD, and Tb.th were not normally distributed, for Ct.th, BV/TV, and BMD were all right skewed with a peak near PL/AM ratio equal to 1 with most results larger than 1 (PL/AM ratio >1), we used a two-sided Mann-Whitney U test. The results led the hypotheses for Ct.th and BV/TV to be rejected, and the BMD result exhibited only a trend ($p = 0.008$). So we can conclude that the subchondral trabecular bone orientation was more affected by the ACL line of action and tension than was the thickness of the subchondral trabecular plate.

This study had several limitations. First, the knee donors' physical activity and disease history were unknown; this could have added variability to the results which could have obscured certain trends. Second, we assumed ACL attachment area dimensions on the nano CT images corresponded with the intercondylar ridge measurements of Ferretti et al. (2007) [19] and the subchondral plate porosities[16]. Since our donors likely differed in size, shape and lifetime physical activities, their actual attachment area may have differed slightly, but perhaps not systematically, thereby adding variability to the results. Although every effort was made to be consistent in segmenting the ROI on the nano CT images, there was also likely some variability between specimens in doing this. We used a uniform 5 mm^3 cube and a $5 \times 4 \times 3$ mm^3 cuboid as the ROI, so for narrow ACL attachment areas, we could have included regions not directly loaded by ACL tensile stress. We only tested young adult human cadaver knees (age range: 19 ~ 40 yrs), and too few women. It remains to be seen whether a similar study conducted in the knees of juveniles or adolescents during periods of rapid bone growth[44] would show similar results, and whether there a sex difference exists. Lastly, it is likely that the objective measures, BV/TV, BMD, Ct.Th, and Tb.Th., of bone quality are simply not sensitive enough to pick up microcracks of the type observed by Wu et al. (2013)[50] that did not progress completely through the trabecular plate or rod walls. That is why we are currently using an alternative, histological, method to check for the presence of them in these specimens.

5.5 Conclusions

1) At the 20 µm nano CT resolution employed for this study, none of the variables suggested any evidence of fatigue damage accumulation in the sub-chondral bone beneath the femoral ACL enthesis in knees subjected to repetitive loading. Therefore, for the present at least, we must conclude that ACL tears are unlikely to be due to an accumulation of femoral subchondral plate or bone damage under repetitive sub-maximal ACL loading.

2) The ACL femoral subchondral bone under PL fibers had significantly thicker cortical bone plates and a denser bone volume fraction in the region in which a theoretical biomechanical model (Chapter 4) has earlier demonstrated characteristically higher shear strains than in the region under the AM fibers.

3) The ACL femoral subchondral trabeculae bone in the volume 3 mm below the origin of the AM fibers, which a simple finite element model (Chapter 4) has shown carries the greatest tensile stress, exhibited a tensile arcade aligned in the direction of ACL line-of-action near full knee extension, reflecting adaptations consistent with Wolff's law.

Conflicts of interest

The authors report no conflict of interest.

Acknowledgement

We thank Conor Locke for technical assistance with the nano CT imaging of the femoral enthesis specimens. We gratefully acknowledge the financial support of Public Health Service grant R01 AR054821.

5.6 References

1. Amis AA. The functions of the fibre bundles of the anterior cruciate ligament in anterior drawer, rotational laxity and the pivot shift. *Knee Surgery, Sport Traumatol Arthrosc*. 2012;20(4):613–620. doi:10.1007/s00167-011-1864-7

2. Beaulieu ML, Carey GE, Schlecht SH, Wojtys EM, Ashton-Miller JA. On the heterogeneity of the femoral enthesis of the human ACL: microscopic anatomy and clinical implications. *J Exp Orthop*. 2016;3(1). doi:10.1186/s40634-016-0050-8

3. Beaulieu ML, Carey GE, Schlecht SH, Wojtys EM, Ashton-Miller JA. Quantitative comparison of the microscopic anatomy of the human ACL femoral and tibial entheses. *J Orthop Res*. 2015;33(12):1811–1817. doi:10.1002/jor.22966

4. Beaulieu ML, Wojtys EM, Ashton-Miller JA. Risk of anterior cruciate ligament fatigue failure is increased by limited internal femoral rotation during in vitro repeated pivot landings. *Am J Sports Med*. 2015;43(9):2233–2241. doi:10.1177/0363546515589164

5. Benjamin M, Kumai T, Milz S, Boszczyk B., Boszczyk A., Ralphs J. The skeletal attachment of tendons - Tendon «entheses». *Comp Biochem Physiol - A Mol Integr Physiol*. 2002;133(4):931–945.

6. Benjamin M, Toumi H, Ralphs JR, Bydder G, Best TM, Milz S. Where tendons and ligaments meet bone: Attachment sites ('entheses') in relation to exercise and/or mechanical load. *J Anat*. 2006;208(4):471–490. doi:10.1111/j.1469-7580.2006.00540.x

7. Boden BP, Sheehan FT, Torg JS, Hewett TE. Non-contact ACL injuries: Mechanisms and risk factors. *Am Acad Orthop Surg*. 2010;18(9):520–527.

8. Brown TD, Vrahas MS. The apparent elastic modulus of the juxtaricular subchondral bone of the femoral head. *J Orthop Res*. 1984;2(1):32–38. doi:10.1002/jor.1100020106

9. Burr DB, Gallant MA. Bone remodelling in osteoarthr. *Nat Rev Rheumatol*. 2012;130(8):665–673. doi:10.1038/nrrheum.2012.130

10. Carballo CB, Nakagawa Y, Sekiya I, Rodeo SA. Basic Science of Articular Cartilage. *Clin Sports Med*. 2017;36(3):413–425. doi:10.1016/j.csm.2017.02.001

11. Chappard D, Baslé MF, Legrand E, Audran M. Trabecular bone microarchitecture: A review. *Morphologie*. 2008;92(299):162–170. doi:10.1016/j.morpho.2008.10.003

12. Chen J, Kim J, Shao W, et al. An anterior cruciate ligament failure mechanism. *Am J Sports Med*. 2019;47(9):2067–2076. doi:10.1177/0363546519854450

13. Chen Y, Hu Y, Yu YE, et al. Subchondral trabecular rod loss and plate thickening in the development of osteoarthritis. *J Bone Miner Res*. 2018;33(2):316–327. doi:10.1002/jbmr.3313

14. Christel PS, Akgun U, Yasar T, Karahan M, Demirel B. The contribution of each anterior cruciate ligament bundle to the Lachman test. *J Bone Joint Surg Br*. 2012;94-B(1):68–74. doi:10.1302/0301-620x.94b1.26562

15. Cleather DJ, Goodwin JE, Bull AMJ. Hip and knee joint loading during vertical jumping and push jerking. *Clin Biomech*. 2013;28(1):98–103. doi:10.1016/j.clinbiomech.2012.10.006

16. Cooper DML, Kawalilak CE, Harrison K, Johnston BD, Johnston JD. Cortical bone porosity: What is it, why is it important, and how can we detect it? *Curr Osteoporos Rep*. 2016;14(5):187–

198. doi:10.1007/s11914-016-0319-y

17. Cowin 1934- SC (Stephen C. *Bone Mechanics*. CTC Press

18. Directionality. https://imagej.net/plugins/directionality

19. Ferretti M, Ekdahl M, Shen W, Fu FH. Osseous landmarks of the femoral attachment of the anterior cruciate ligament: An anatomic study. *Arthrosc - J Arthrosc Relat Surg*. 2007;23(11):1218–1225. doi:10.1016/j.arthro.2007.09.008

20. Furman W, Marshall J, Girgis F. The anterior cruciate ligament, A functional analysis based on postmortem studies. *J Bone Jt Surg Am*. 1976;2(58):179–185.

21. Goldring SR, Goldring MB. Changes in the osteochondral unit during osteoarthritis: Structure, function and cartilage bone crosstalk. *Nat Rev Rheumatol*. 2016;12(11):632–644. doi:10.1038/nrrheum.2016.148

22. Goulet RW, Goldstein SA, Ciarelli MJ, Kuhn JL, Brown MB, Feldkamp LA. The relationship between the structural and orthogonal compressive properties of trabecular bone. *J Biomech*. 1994;27(4). doi:10.1016/0021-9290(94)90014-0

23. Hansson T, Keller T, Jonson R. Fatigue fracture morphology in human lumbar motion segment. *J Spinal Disord*. 1988;1(1):33–38.

24. Jiang Y, Cai Y, Zhang W, et al. Human cartilage-derived progenitor cells from committed chondrocytes for efficient cartilage repair and regeneration. *Stem Cells Transl Med*. 2016;(5):733–744. doi:10.5966/sctm.2015-0192

25. Katouda M, Soejima T, Kanazawa T, Tabuchi K, Yamaki K, Nagata K. Relationship between thickness of the anteromedial bundle and thickness of the posterolateral bundle in the normal ACL. *Knee Surgery, Sport Traumatol Arthrosc*. 2011;19(8):1293–1298. doi:10.1007/s00167-011-1417-0

26. Lee TC, Mohsin S, Taylor D, et al. Detecting microdamage in bone. *J Anat*. 2003;203(2):161–172. doi:10.1046/j.1469-7580.2003.00211.x

27. Li B, Aspden RM. Mechanical and material properties of the subchondral bone plate from the femoral head of patients with osteoarthritis or osteoporosis. *Ann Rheum Dis*. 1997;56(4):247–254. doi:10.1136/ard.56.4.247

28. Lin X, Zhao J, Gao L, Zhang C, Gao H. Ratcheting-fatigue behavior of trabecular bone under cyclic tensile-compressive loading. *J Mech Behav Biomed Mater*. 2020;112(January):104003. doi:10.1016/j.jmbbm.2020.104003

29. Lories RJ, Luyten FP. The bone-cartilage unit in osteoarthritis. *Nat Rev Rheumatol*. 2011;197(7):43–49. doi:10.1038/nrrheum.2010.197

30. Luetkemeyer CM, Marchi BC, Ashton-Miller JA, Arruda EM. Femoral entheseal shape and attachment angle as potential risk factors for anterior cruciate ligament injury. *J Mech Behav Biomed Mater*. 2018;88(August):313–321. doi:10.1016/j.jmbbm.2018.08.045

31. Marieswaran M, Jain I, Garg B, Sharma V, Kalyanasundaram D. A review on biomechanics of anterior cruciate ligament and materials for reconstruction. *Appl Bionics Biomech*. 2018;2018. doi:10.1155/2018/4657824

32. Markolf KL, Park S, Jackson SR, McAllister DR. Contributions of the posterolateral bundle of the anterior cruciate ligament to anterior-posterior knee laxity and ligament forces. *Arthrosc - J*

Arthrosc Relat Surg. 2008;24(7):805–809. doi:10.1016/j.arthro.2008.02.012

33. Van Meer BL, Waarsing JH, van Eijsden WA, et al. Bone mineral density changes in the knee following anterior cruciate ligament rupture. *Osteoarthr Cartil*. 2014;22(1):154–161. doi:10.1016/j.joca.2013.11.005

34. Meyer EG, Baumer TG, Slade JM, Smith WE, Haut RC. Tibiofemoral contact pressures and osteochondral microtrauma during anterior cruciate ligament rupture due to excessive compressive loading and internal torque of the human knee. *Am J Sports Med*. 2008;36(10):1966–1977. doi:10.1177/0363546508318046

35. Mori S, Burr DB. Increased intracortical remodeling following fatigue damage. *Bone*. 1993;14:103–109. doi:10.3390/met7100394

36. Norman TL, Nivargikar S V., Burr DB. Resistance to crack growth in human cortical bone is greater in shear than in tension. *J Biomech*. 1996;29(8):1023–1031. doi:10.1016/0021-9290(96)00009-7

37. Oh YK. ON THE MECHANISMS OF NON-CONTACT ACL INJURY DURING A SIMULATED JUMP LANDING: EXPERIMENTAL AND THEORETICAL ANALYSES. *Univ Michigan*. Published online 2011(e)ko .

38. Oh YK, Lipps DB, Ashton-Miller JA, Wojtys EM. What strains the anterior cruciate ligament during a pivot landing? *Am J Sports Med*. 2012;40(3):574–583. doi:10.1177/0363546511432544

39. Patton DM, Ochocki DN, Martin CT, et al. State of the mineralized tissue comprising the femoral ACL enthesis in young women with an ACL failure. *J Orthop Res*. 2021;(September 2019). doi:10.1002/jor.25130

40. Petersen W, Tillmann B. Structure and vascularization of the cruciate ligaments of the human knee joint. *Anat Embryol (Berl)*. 1999;200(3):325–334. doi:10.1007/s004290050283

41. Petersen W, Zantop T. Partial rupture of the anterior cruciate ligament. *Arthroscopy*. 2006;22(11):1143–1145. doi:10.1016/j.arthro.2006.08.017

42. Śmigielski R, Zdanowicz U, Drwięga M, Ciszek B, Ciszkowska-Łysoń B, Siebold R. Ribbon like appearance of the midsubstance fibres of the anterior cruciate ligament close to its femoral insertion site: a cadaveric study including 111 knees. *Knee Surgery, Sport Traumatol Arthrosc*. 2015;23(11):3143–3150. doi:10.1007/s00167-014-3146-7

43. Sonnery-Cottet B, Barth J, Graveleau N, Fournier Y, Hager JP, Chambat P. Arthroscopic identification of isolated tear of the posterolateral bundle of the anterior cruciate ligament. *Arthrosc - J Arthrosc Relat Surg*. 2009;25(7):728–732. doi:10.1016/j.arthro.2008.12.018

44. Stagi S, Cavalli L, Iurato C, Seminara S, Brandi ML, Martino M De. Bone metabolism in children and adolescents: Main characteristics of the determinants of peak bone mass. *Clin Cases Miner Bone Metab*. 2013;10(3):172–179.

45. Stolarz M, Rajca J, Cyganik P, et al. The bone microstructure from anterior cruciate ligament footprints is similar after ligament reconstruction and does not affect long-term outcomes. *Knee Surgery, Sport Traumatol Arthrosc*. 2022;30(1):260–269. doi:10.1007/s00167-021-06493-z

46. Suzuki D, Otsubo H, Adachi T, et al. Functional adaptation of the fibrocartilage and bony trabeculae at the attachment sites of the anterior cruciate ligament. *Clin Anat*. 2020;33(7):988–996. doi:10.1002/ca.23520

47. Tie K, Wang H, Wang X, Chen L. Measurement of bone mineral density in the tunnel regions for anterior cruciate ligament reconstruction by dual-energy X-ray absorptiometry, computed tomography scan, and the immersion technique based on archimedes' principle. *Arthrosc - J Arthrosc Relat Surg*. 2012;28(10):1464–1471. doi:10.1016/j.arthro.2012.04.053

48. Turunen MJ, Le Cann S, Tudisco E, et al. Sub-trabecular strain evolution in human trabecular bone. *Sci Rep*. 2020;10(1):1–14. doi:10.1038/s41598-020-69850-x

49. Wolff J. Das gesetz der transformation der knochen. *DMW-Deutsche Medizinische Wochenschrift*. 1892;19(47):1222–1224.

50. Wu Z, LaNeve AJ, Niebur GL. In vivo microdamage is an indicator of susceptibility to initiation and propagation of microdamage in human femoral trabecular bone. *Bone*. 2013;55(1):208–215. doi:10.1016/j.bone.2013.02.019

51. Yu Q, Li Z, Li J, et al. Calcaneal fracture maps and their determinants. *J Orthop Surg Res*. 2022;17(1):1–9. doi:10.1186/s13018-022-02930-y

52. Zantop T, Brucker PU, Vidal A, Zelle BA, Fu FH. Intraarticular rupture pattern of the ACL. *Clin Orthop Relat Res*. 2007;454(454):48–53. doi:10.1097/BLO.0b013e31802ca45b

53. Zantop T, Herbort M, Raschke MJ, Fu FH, Petersen W. The role of the anteromedial and posterolateral bundles of the anterior cruciate ligament in anterior tibial translation and internal rotation. *Am J Sports Med*. 2007;35(2):223–227. doi:10.1177/0363546506294571

54. Zhu X, Chan YT, Yung PSH, Tuan RS, Jiang Y. Subchondral bone remodeling: A therapeutic target for osteoarthritis. Front Cell Dev Biol. 2021;8(January). doi:10.3389/fcell.2020.607764

Chapter 6: General Discussion

This dissertation addressed four knowledge gaps in ACL injury mechanisms pertaining to knee kinematics and bone morphologies. First, although ACL strain is known to be directly correlated with quadriceps muscle force and the 3-D external loads applied to the knee *in vitro and in silico*[62], muscle forces and loads on the ACL are not presently possible to measure in living athletes, and especially in children because they would require invasive measurements. Instead, kinematic measurements of the upper and lower leg during specific dynamic sports maneuvers, when ACL injuries are known to occur, are the gold standard. Yet unless these are based on laboratory-based biplanar cineradiographic measurements, augmented by MR reconstructions of the limb soft tissues[19], these measurements universally contain artefacts caused by movements of the skin and soft tissue relative to the underlying bones during the ground impact associated with jump landings that cause ACL injury. Likewise, second, while there have been many clinical studies of the relationship between LTS and ACL injury, we are not aware of studies that have reliably examined the correlation between LTS and tibiofemoral kinematics during a dynamic maneuver such as a jump landing because of the above soft tissue motions. Third, it is unknown whether repetitive sub-maximal loading can cause fatigue damage to accumulate in the subchondral bone beneath the ACL enthesis, as has been shown to accumulate in the most proximal part of the ligament near the femoral ACL enthesial tidemark[15]. After all bone is well known to be susceptible to accumulating fatigue damage in the case of tibial shaft stress fractures[44] and bony avulsions near tendon insertions in children[46], so it is possible that an ACL tear could initiate as fatigue damage accumulated in the subchondral bone beneath the ACL enthesis and then spread to the ligament proper across the tidemark. Lastly, fourth, if that fatigue damage accumulated in bone, it might be expected to accumulate in the "weakest" bone, namely the thinnest part of the enthesial subchondral plate or thinnest or most sparse sub-chondral trabeculae. That brings up the possibility that there could be regional differences in the subchondral plate and trabeculae triggered adaptations according to Wolff's law during an individual's life according to the physical activities they subjected their knees to. So we examined this once we found an absence of evidence for subchondral bone fatigue failure.

6.1 Knee kinematics to predict and prevention ACL injury during maneuvers

About 70% of ACL injures are of the non-contact type injuries[30] caused by foot plants during pivot landings, abrupt stops or sudden changes in direction[49,58] . These maneuvers place 3-D external dynamic loads on the knee as well as internal forces from tensed trans knee muscle forces (i.e., quadriceps, hamstrings, etc)[61,62]. Large tibiofemoral dynamic forces are incurred at the knee during these maneuvers and so understanding the tibiofemoral kinematics associated with ACL injuries is essential to understanding the mechanisms of ACL injuries. Previous work in our laboratory has examined the correlations between axial tibial torque, varus/valgus moment, quadriceps force, ACL fatigue loading history and certain tibiofemoral morphologies during repetitive sub-maximal jump landings *in vitro*[35,45,62,63].

In this dissertation we sought to understand the ACL injury mechanism a little more by measuring tibiofemoral kinematics during simulated pivot landings in the most severe ACL loading case: an internal tibial torque combined with a knee abduction moment[45] under dynamic knee compression, based on many years of previous research in our laboratory. ACL strain is known to be proportional to changes in knee flexion angle, quadriceps and hamstring tension, anterior translation and internal rotation of the tibia relative to the femur during a landing or cut[3,25,45,61,62]. Clinically, an increase in 3 mm of anterior translation of the tibia relative to the femur is associated with 85% of complete tears revealed by the anterior drawer test[13,18]. This just underlines how important an intact ACL is in acting as a checkrein in preventing excessive shear translation in the knee joint of more than a few mm under large internal and external knee forces and moments.

Traditionally motion capture systems have been used to measurement knee joint kinematics in a controlled laboratory environment. But this is not practical in outdoor settings where players are relatively much farther from the fixed cameras using visible or infrared light, thereby reducing measurement resolution. In addition, these camera systems have difficulty tracking multiple players simultaneously because other player can inadvertently block light reaching given cameras. Given the advent of better and better wearable sensors, we sought to test the reliability of wearable sensors to measure tibiofemoral kinematics when compared to the motion capture system used in Chapter 2. An IMU, of course, consists of a tri-axial linear accelerometer, tri-axial rate gyroscopes, and tri-axial magnetometer[60], and usually attached directly to the skin or around the body segment[5,17]. The significance of Chapter 2 is that our experiments essentially minimized the measurement noise usually generated by soft tissue movement artifacts so we could to assess the best possible dynamic performance of the IMU and motion capture systems. However, the results showed large LoA of ~ 40 % for all three orthogonal knee peak angle changes, so we concluded that this standard IMU and its associated data manipulation algorithms could not reliably measure these peak knee angle changes during dynamic pivot landings even in the absence of soft tissue artefacts, let alone with them. For the calculated angular velocities changes from the motion capture system, the orientation of the camera did affect the results because the parasagittal plane of the knee provided a smaller LoA when oriented parallel with the frontal plane of the camera. The custom-tuned algorithm using the QC method to reduce the phase lag in the rapid acceleration profile can improve the results slightly better than a commercial algorithm normally used for gait analysis[1]. Therefore, improved measurement techniques may be needed to measure the external forces and torques on the feet or shoes[12,16,41] as an alternative to IMUs. Based on the correlation between ACL strain and tibiofemoral kinematics, additional studies could help predict why ACL injury occurs during certain maneuvers using these improved measurement techniques.

Non-contact ACL injury risk factors are normally divided in to associations with environmental, hormonal, neuromechanical, and morphological factors (please see Introduction)[22]. We were particularly interested in the morphological risk factors that affect knee kinematics. A large femoral alpha angle, a smaller ACL cross sectional area, a smaller femoral intercondylar notch and a steeper lateral tibial slope[28,31,51,56] have a combined effect on knee joint movement and have been linked to increasing risk of ACL injuries. Because the original data stemmed from a unique longitudinal controlled study from Dr. Beynnon's University of Vermont group examining cause and effect[40], we chose to focus on LTS by examining the relationship between tibiofemoral kinematics and LTS measured via MRI. Tibial slope was defined as the angle between a tibial anatomic reference axis and a line of the posterior-inferior surface of the tibial plateau[11]. There are several methods to measure LTS, including the midpoint method[23] and the circle method[24]. We used knees whose femora and tibiae were cut mid-shaft, so we used the circle method since it is independent of proximal tibia length and is the most repeatable method[34]. To select the widest possible range of slopes, we screened the knees by measuring posterior tibial slope (PTS) with parasagittal radiograph before thawing the knees to test them. Figure 6.1 shows the association we found between PTS and LTS.

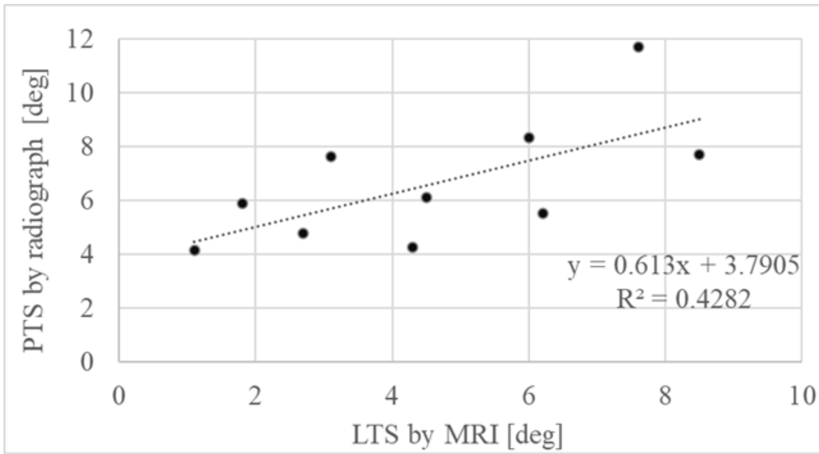

Figure 6-1. Scatter plots for LTS measured by MRI vs PTS measured by radiograph, dotted line shows the linear regression between tibial slopes measured by MRI and radiograph.

Although this result was not statistically significant with R^2=0.42 at this small group size, previous studies on the relationship between PTS by radiograph and ACL injury[55] would allow us to use PTS by radiograph as pre-measurements to select the target knees. If more samples were used to track the measurements with radiograph and MRI and the relationship between tibiofemoral kinematics, it would be more practical with radiographs, but they have the drawback that while they are cheap, they are invasive and contraindicated in children, especially.

We eliminated variability caused by anatomical or hormonal factors associated with sex by using only young male adult knee of similar age and weight[32,43], so the results may underestimate the effect in females because ACL strain is greater in females with their larger LTS than males[33]. This would need to be checked in a larger study including female knees. The results in Chapter 3 showed that a steeper LTS significantly increased both ATT and ITR during jump landings, with ITR increasing proportionally more than ATT did. These results are consistent with previous studies: the sagittal tibial slope was positively correlated with the magnitude of ATT and ITR under axial knee compressive loadings[59], and the steeper LTS was associated with anterior tibial acceleration and peak anterior knee joint reaction forces[38].

MTS is known as one of the ACL injury risk factors[29,32]. We measured MTS and compared the effect of LTS, MTS (Figure 6-2 (a)) and the differences between LTS and MTS (Figure 6-2 (b)). The correlation between LTS and MTS ($R^2 = 0.16$) was low. However, the results of the linear mixed model with MTS suggested that a steeper MTS also had a significant effect (p-value<0.001) on both ATT and ITR (Table 6.1). The results were similar to the linear mixed model using LTS in that ITR increases proportionally more than ATT. The difference between LTS and MTS was highly correlated with LTS ($R^2= 0.89$). However, the results of the linear mixed model showed that the coefficient of LTS-MTS on both ATT and ITR had large p-values (p>0.1) and was not significant.

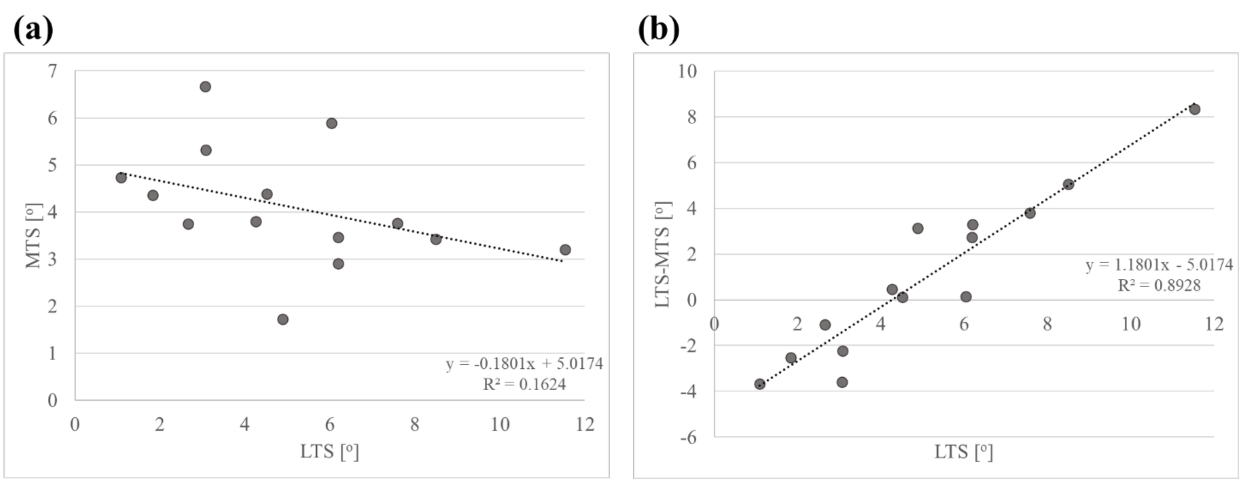

Figure 6-2. Scatter plots for the relationship between (a) measured LTS and MTS and (b) LTS and the difference between LTS and MTS.

Table 6-1. Results for the two linear mixed effect models: Model A for MTS and ATT, and Model B for MTS and ITR.

	Model A: ATT ~ MTS + (IF/BW)				Model B: ITR ~ MTS + (IF/BW)			
	Coefficient	SE	t Value	P Value	Coefficient	SE	t Value	P Value
(Intercept)								
MTS	1.68	0.20	8.47	<0.001	3.04	0.29	10.35	<0.001
(IF/BW)	0.53	0.012	43.00	<0.001	0.40	0.016	24.49	<0.001
MTS: (IF/BW)	-0.014	0.0029	-4.71	<0.001	0.013	0.0038	3.42	<0.001

Therefore, perhaps athletes with steeper LTS should limit the number of knee joint loading cycles they incur in practices by monitoring them with IMUs. This would help prevent ACL overuse injury due to too much accumulated fatigue damage in the proximal ligament in a given time period. Indeed, the monitoring of 3D knee kinematics in athletes could well be crucial for mitigating the risk of non-contact ACL injuries.

6.2 Lack of evidence for fatigue damage in the subchondral bone of the femoral ACL enthesis and evidence for regional adaptation of that subchondral bone

Damage of the Type1 collagen constituting the ACL can accumulate nearest the femoral enthesis under repetitive loadings as one possible step toward ligament fatigue failure[15,27]. But we tested an alternative hypothesis that the failure could instead start in the subchondral bone near the femoral enthesis of the ACL. So we examined the bone morphology of the subchondral bone beneath the ACL femoral enthesis both subjectively and objectively for signs of bone fatigue failure (Chapters 4 and 5).

The results of Chapter 4 and 5 showed that 1) a concave enthesial topography helps to reduce the tensile and shear stress under at the femoral enthesis, 2) there was no subjective or objective evidence of fatigue damage in the subchondral bone under ACL femoral enthesis at 20 nano CT μm resolution, 3) the subchondral bone under PL fiber had significantly thicker cortical plate thickness and denser BV/TV than AM fibers, and 4) the ACL femoral subchondral trabeculae bone in the volume 3 mm below the enthesis has a tensile arcade aligned in the direction of ACL line of action near full knee extension under the proximal posterior area (AM fibers) and the region carries greater tensile stress than does the distal anterior area (PL fibers).

The knees we tested were from young adult human cadavers (age range: 19~40 yrs) in the age range when ACL injury occur[29] after cessation of rapid bone growth[53]. Therefore, we may assume these adult knee bones had already adapted to physical stresses of activities of daily living to form the femoral enthesis subchondral plate, whether concave or convex, and any regional differences in cortical thickness and volume under the origin of the AM and PL bundles.

Although we demonstrated accumulation of low-cycle Type 1 collagen fatigue damage near the ACL femoral enthesis [15,27] using the same experimental apparatus, at 20 μm resolution at least, we were unable to either see or measure any evidence of fatigue damage accumulation in the subchondral plate or trabecular bone. The quantitative measures we used, BV/TV, Ct. Th, Tb. Th and BMD, have previously been shown to be significantly affected in the femoral ACL subchondral bone in the injured knee following ACL rupture than in healthy control knees[10,39,47]. But they were not sensitive enough to pick up any evidence of fatigue damage in the femoral subchondral bone at 20 μm resolution. In one study of small proximal femoral trabecular bone explants from old adults that were placed under compressive, torsional or combined loading, propagating damage was found at this resolution[66]. So we conclude that either the loading magnitude we used in our experiment was insufficient to cause microcracks or the 20 μm resolution was insufficient, or microcracks do not form in the subchondral bone under this type of loading. To eliminate one of these three possibilities, we are currently conducting a histological study that will enable us to use much higher resolution imaging to check for microcracks. The significance of these in the clinic would be that failure of the bone due to an accumulation of fatigue damage could be picked up on MR imaging as inflammation and then a suitable rest period would allow the injured bone to heal given the vascularity in that region.

Although we could not find any evidence of fatigue damage accumulation in the subchondral bone, the other topological and bone quality results were consistent with the previous research showing adaptations to resist large ACL tensile stresses. As described by Wolf's law, the shape and architecture of bones are highly adaptive to the history and direction of mechanical stress in the bone[64]. One histology study showed that the posterolateral entheses from 15 human knees were all found to have concave topographies, while the anteromedial entheses were mostly convex[4]. More than 40% of partial ACL tears occur in the PL fibers[52] which are subjected to larger shear strains than the AL fibers[36]. This suggests that either the PL fibers are subjected to more strain, or they are weaker than the AM fibers, or both. Our results suggest that the subchondral bone of ACL femoral enthesis adapted via Wolff's law to support ACL tensile loadings via different regional morphologies, and certain bone morphologies may be more resistant to fatigue damage accumulation and ACL tensile loads than others.

As a hard-soft tissue interface, entheses are susceptible to acute or overuse injuries in sports. These include Achilles tendinopathies, tennis and golfer's elbow, and jumper's knee, because of stress concentrations[7]. Entheses develop under mechanical influences during growth and these influences affect the regional distributions of fibrocartilage and entheseal new bone formation[6,8].

According to the simple femoral enthesis FE model (Chapter 4), the proximal-posterior region was found to be mainly under tensile stress, while the distal anterior area was mainly shear stress. This insight leads to the results of the nano CT imaging in Chapter 5. Although there was no significantly difference between the trabecular bone thickness on the AM and PL area, the directionality of subchondral trabecular bone from the images, which are parallel to the ACL femoral attachment, was higher in the proximal posterior area (AM) than the distal anterior area (PL). Suzuki et al. (2020) cut his ethesial specimens perpendicular to the ACL attachment area, and their results also showed the posterior proximal region had a greater orientation intensity of the trabecular bone. Therefore, we may say that the trabecular bone was oriented along the ACL tensile direction in three dimensions, and also say that the trabeculae adapt their directionality more than their thickness to resist the ACL tensile loading. We also assumed that the thicker and denser bone underneath PL area of the ACL femoral enthesis is required to support considerable shear stress. From these results, we can conclude that, in general, the density factors such as bone volume fraction and cortical thickness were adapted to withstand shear stress, while tensile stress affected trabecular architectural structures more than density. In the full extension of the knee position, the PL bundle experiences more elongation than AM bundle due to the scarf attachment angle[26] and this may be the reason why the subchondral bone beneath PL bundle is denser. This, given that the AM bundle primarily resists forward tibial shear, while the PL bundle shorter than AM bundle primarily resists internal tibial rotation[2,37,65].

In Chapter 4, we used the simple finite element model to identify which topology has the best resistance to ACL tension and how the stress is distributed through the model subchndral plate for an ACL attachment angle at 15° of knee flexion. However, the line of action of ACL tension changes with the knee flexion, and the most vulnerable position of the ACL to injury is near full knee extension[9]. We did not examine the effect of ACL bending or torsion on these stress distributions and trabecular supports. In addition, we did not examine possible sex differences in the elastic properties of the bone in these young adults. Mechanical properties of bone do play a role related to cracks or fracture under fatigue loading[67]. There is no significant sex difference in the overall composition of bones[48], but bone morphologies are the primary factor affecting sex differences[43]. Therefore, our model for young humans might be effected by sex differences in bone morphology. A more detailed model considering these conditions will be able to demonstrate more detailed results of how the subchondral cortical plate supports the ACL loads, where the most vulnerable regions under tensile or shear stress is, and whether to expect crack propagation under fatigue loading. Despite our simple analysis, our studies of the stress distribution on the ACL femoral subchondral cortical plate have indicated that certain bone morphologies have adapted to resist ACL tension when we pair the model with the nano CT images. This also help predict where an initiating region of bone microcrack formation might lie.

6.3 Strengths and Limitations

A strength of this dissertation is the use of healthy young human cadaver knees in the age range when most ACL injuries occur. Their age effectively eliminated the confounding effects of any age-related degeneration of the ACL or its entheses[57], but did not include adolescents with growing bones who are also at known risk for ACL injury[53]. A limitation of this dissertation was that all the experiments had to be performed *in vitro*. While we minimized the number of free-thaw cycles of the specimens, they will have slightly affected the tissue material properties because of some inevitable dehydration, although internal structures like the ACL and its entheses would be much less affected than the peripheral structures, and the effects of freeze-thaw cycles only become of concern over 10 cycles[21] which we did not approach. Even though the actions of the major knee muscles and external forces and moments were simulated prior to and during the first 100 ms of the jump landing, the biological response of the human tissues[14], the function of ankle which absorbs energy[50], and interactions between quadriceps and hamstrings could not be simulated[20,42].

In Chapters 2 and 3, the tibiofemoral kinematics were measured from repetitively loaded knees with a maximum of 100 trials or as many trials as could be completed until the ACL failed with less than 3 BW. This lower load protocol was designed to avoid ACL failure due to material fatigue[35] which occurred under same sub-maximal repetitive loading but with larger loads. Despite the wish to avoid any fatigue damage, microdamage has been observed at the loads we used in the form of an accumulation of collagen unraveling[14,27]. In Chapter 3, microdamage of ACL due to repeated loadings could have affected the results about the relationship between LTS and kinematics. So, we added the loading trials as fixed effects in the linear mixed effect models that we used. The results showed that loading trials has only 3% coefficient compared with BW and LTS with $p<0.01$. Therefore, we may say these repetitive loads did not significantly affect the results.

While our cadaver experiments utilized knees from young adult donors, unfortunately our sample included few young female knees. In Chapter 3, all 7 pairs of knees were from young men. On the one hand it can be considered a strength by eliminating variability due to sex effects such as hormonal and anatomical differences between male and female[32]. However, it is already known that female has steeper LTS[33] than male and LTS is a significant risk factor for ACL injuries in women[54]. So our results likely underestimated the effect of LTS on tibiofemoral kinematics in female knees. In addition, none of our knees had an LTS of 12 degree or more which is the clinical threshold for taking action. If we had been able to include those knees >+12 degrees, we would have observed a stronger LTS effect. In Chapter 5, we also tested young adult knees with similar ages and body weights from 3 females and 11 males. A limitation was that the donors' disease history and physical activity were unknown. Although we performed a paired test by comparing paired knees (Chapter 5, Aim 1), AM and PL region (Chapter 5, Aim 2), and 4 regions (Chapter 5, Aim 3), variability may include a sex difference which could have obscured certain trends.

Clinically, more than 3 mm of forward translation of the tibia is considered to signal an ACL rupture[13]. Many previous studies have predicted ACL injury from microscale damage to ACL strain[27,35,45]. In this research, we used tibiofemoral kinematics to examine the ACL injury mechanism because ACL strain is known to be positively correlated with ATT and ITR[45]. The measurement of tibiofemoral kinematics has the advantage of being able to be measured during exercise without disturbing the knee or ligaments to make real-time measurements. So, although we did not demonstrate high correlations between IMU and the motion capture kinematic measures, our results indicate that improved algorithms for wearable sensors during highly dynamic landings such as those studied in Chapter 2 would be worthwhile.

Despite these limitations, we believe the general trends of our main results should remain valid. This dissertation took a step closer to predicting ACL injuries from tibiofemoral kinematics of athletes in maneuvers by examining the reliability of wearable sensors during a highly dynamic maneuver, and examined why a larger LTS increases the risk for ACL injury whether under a single overload or repetitive sub-maximal loading. Furthermore, based on Wolff's law, it was demonstrated how the femoral subchondral bone appears to have adapted over the donor's life to best support its ACL enthesis under the large ACL loads that occur when it acts as a checkrein.

6.4 References

1. Ajdaroski M, Ashton-Miller JA, Baek SY, Shahshahani PM, Esquivel AO. Testing a quaternion conversion method to determine human three-dimensional tibiofemoral angles during an in vitro simulated jump landing. *J Biomech Eng*. 2022;144(4):1–8. doi:10.1115/1.4052496

2. Amis AA. The functions of the fibre bundles of the anterior cruciate ligament in anterior drawer, rotational laxity and the pivot shift. *Knee Surgery, Sport Traumatol Arthrosc*. 2012;20(4):613–620. doi:10.1007/s00167-011-1864-7

3. Beaulieu ML, Ashton-Miller JA, Wojtys EM. Loading mechanisms of the anterior cruciate ligament. *Sport Biomech*. 2021;00(00):1–29. doi:10.1080/14763141.2021.1916578

4. Beaulieu ML, Carey GE, Schlecht SH, Wojtys EM, Ashton-Miller JA. On the heterogeneity of the femoral enthesis of the human ACL: microscopic anatomy and clinical implications. *J Exp Orthop*. 2016;3(1). doi:10.1186/s40634-016-0050-8

5. Bell KM, Onyeukwu C, McClincy MP, et al. Verification of a portable motion tracking system for remote management of physical rehabilitation of the knee. *Sensors (Switzerland)*. 2019;19(5). doi:10.3390/s19051021

6. Benjamin M, Kaiser E, Milz S. Structure-function relationships in tendons: A review. *J Anat*. 2008;212(3):211–228. doi:10.1111/j.1469-7580.2008.00864.x

7. Benjamin M, Toumi H, Ralphs JR, Bydder G, Best TM, Milz S. Where tendons and ligaments meet bone: Attachment sites ('entheses') in relation to exercise and/or mechanical load. *J Anat*. 2006;208(4):471–490. doi:10.1111/j.1469-7580.2006.00540.x

8. Benjamin M, Toumi H, Suzuki D, Hayashi K, McGonagle D. Evidence for a distinctive pattern of bone formation in enthesophytes. *Ann Rheum Dis*. 2009;68(6):1003–1010. doi:10.1136/ard.2008.091074

9. Boden BP, Sheehan FT, Torg JS, Hewett TE. Non-contact ACL injuries: Mechanisms and risk factors. *Am Acad Orthop Surg*. 2010;18(9):520–527.

10. Boyd SK, Matyas JR, Wohl GR, Kantzas A, Zernicke RF. Early regional adaptation of periarticular bone mineral density after anterior cruciate ligament injury. *J Appl Physiol*. 2000;89(6):2359–2364. doi:10.1152/jappl.2000.89.6.2359

11. Brandon ML, Haynes PT, Bonamo JR, Flynn MII, Barrett GR, Sherman MF. The association between posterior-inferior tibial slope and anterior cruciate ligament insufficiency. *Arthrosc - J Arthrosc Relat Surg*. 2006;22(8):894–899. doi:10.1016/j.arthro.2006.04.098

12. Bucinskas V, Dzedzickis A, Rozene J, et al. Wearable feet pressure sensor for human gait

and falling diagnosis. *Sensors*. 2021;21(15). doi:10.3390/s21155240

13. Butler DL, Noyes FR, Grood ES. Ligamentous restraints to anterior-posterior drawer in the human knee. A biomechanical study. *J Bone Jt Surg - Ser A*. 1980;62(2):259–270. doi:10.2106/00004623-198062020-00013

14. Chen J, Ahn T, Colón-Bernal ID, Kim J, Banaszak Holl MM. The Relationship of Collagen Structural and Compositional Heterogeneity to Tissue Mechanical Properties: A Chemical Perspective. *ACS Nano*. 2017;11(11):10665–10671. doi:10.1021/acsnano.7b06826

15. Chen J, Kim J, Shao W, et al. An anterior cruciate ligament failure mechanism. *Am J Sports Med*. 2019;47(9):2067–2076. doi:10.1177/0363546519854450

16. Cong Y, Lam WK, Cheung JTM, Zhang M. In-shoe plantar tri-axial stress profiles during maximum-effort cutting maneuvers. *J Biomech*. 2014;47(16):3799–3806. doi:10.1016/j.jbiomech.2014.10.028

17. Dahl KD, Dunford KM, Wilson SA, Turnbull TL, Tashman S. Wearable sensor validation of sports-related movements for the lower extremity and trunk. *Med Eng Phys*. 2020;84:144–150. doi:10.1016/j.medengphy.2020.08.001

18. Daniel DM, Stone ML, Sachs R, Malcom L. Instrumented measurement of anterior knee laxity in patients with acute anterior cruciate ligament disruption. *Am J Sports Med*. 1985;13(6):401–407. doi:10.1177/036354658501300607

19. Englander ZA, Baldwin EL, Smith WAR, Garrett WE, Spritzer CE, DeFrate LE. In vivo anterior cruciate ligament deformation during a single-legged jump measured by magnetic resonance imaging and high-speed biplanar radiography. *Am J Sports Med*. 2019;47(13):3166–3172. doi:10.1177/0363546519876074

20. Fagenbaum R, Darling WG. Jump landing strategies in male and female college athletes and the implications of such strategies for anterior cruciate ligament injury. *Am J Sports Med*. 2003;31(2):233–240. doi:10.1177/03635465030310021301

21. Giannini S, Buda R, Di Caprio F, et al. Effects of freezing on the biomechanical and structural properties of human posterior tibial tendons. *Int Orthop*. 2008;32(2):145–151. doi:10.1007/s00264-006-0297-2

22. Griffin LY, Albohm MJ, Arendt EA, et al. Understanding and preventing noncontact anterior cruciate ligament injuries: A review of the Hunt Valley II Meeting, January 2005. *Am J Sports Med*. 2006;34(9):1512–1532. doi:10.1177/0363546506286866

23. Hashemi J, Chandrashekar N, Mansouri H, et al. Shallow medial tibial plateau and steep medial and lateral tibial slopes: New risk factors for anterior cruciate ligament injuries. *Am J Sports Med*. 2010;38(1):54–62. doi:10.1177/0363546509349055

24. Hudek R, Schmutz S, Regenfelder F, Fuchs B, Koch PP. Novel measurement technique of

the tibial slope on conventional MRI. *Clin Orthop Relat Res*. 2009;467(8):2066–2072. doi:10.1007/s11999-009-0711-3

25. Kaeding CC, Léger-St-Jean B, Magnussen RA. Epidemiology and diagnosis of anterior cruciate ligament injuries. *Clin Sports Med*. 2017;36(1):1–8. doi:10.1016/j.csm.2016.08.001

26. Katouda M, Soejima T, Kanazawa T, Tabuchi K, Yamaki K, Nagata K. Relationship between thickness of the anteromedial bundle and thickness of the posterolateral bundle in the normal ACL. *Knee Surgery, Sport Traumatol Arthrosc*. 2011;19(8):1293–1298. doi:10.1007/s00167-011-1417-0

27. Kim J, Baek SY, Schlecht SH, et al. Anterior cruciate ligament microfatigue damage detected by collagen autofluorescence in situ. *J Exp Orthop*. 2022;9(1). doi:10.1186/s40634-022-00507-6

28. Kızılgöz V, Sivrioğlu AK, Ulusoy GR, Aydın H, Karayol SS, Menderes U. Analysis of the risk factors for anterior cruciate ligament injury: an investigation of structural tendencies. *Clin Imaging*. 2018;50(October 2017):20–30. doi:10.1016/j.clinimag.2017.12.004

29. Kobayashi H, Kanamura T, Koshida S, et al. Mechanisms of the anterior cruciate ligament injury in sports activities: A twenty-year clinical research of 1,700 athletes. *J Sport Sci Med*. 2010;9(4):669–675.

30. Krosshaug T, Nakamae A, Boden BP, et al. Mechanisms of anterior cruciate ligament injury in basketball: Video analysis of 39 cases. *Am J Sports Med*. 2007;35(3):359–367. doi:10.1177/0363546506293899

31. Kumar Panigrahi T, Das A, Mohanty T, Samanta S, Kumar Mohapatra S. Study of relationship of posterior tibial slope in anterior cruciate ligament injury. *J Orthop*. 2020;21(June):487–490. doi:10.1016/j.jor.2020.08.032

32. Lang TF. The bone-muscle relationship in men and women. *J Osteoporos*. 2011;2011:1–4. doi:10.4061/2011/702735

33. Lipps DB, Oh YK, Ashton-Miller JA, Wojtys EM. Morphologic characteristics help explain the gender difference in peak anterior cruciate ligament strain during a simulated pivot landing. *Am J Sports Med*. 2012;40(1):32–40. doi:10.1177/0363546511422325

34. Lipps DB, Wilson AM, Ashton-Miller JA, Wojtys EM. Evaluation of different methods for measuring lateral tibial slope using magnetic resonance imaging. *Am J Sports Med*. 2012;40(12):2731–2736. doi:10.1177/0363546512461749

35. Lipps DB, Wojtys EM, Ashton-Miller JA. Anterior cruciate ligament fatigue failures in knees subjected to repeated simulated pivot landings. *Am J Sports Med*. 2013;41(5):1058–1066. doi:10.1177/0363546513477836

36. Luetkemeyer CM, Marchi BC, Ashton-Miller JA, Arruda EM. Femoral entheseal shape and attachment angle as potential risk factors for anterior cruciate ligament injury. *J Mech Behav Biomed Mater*. 2018;88(August):313–321. doi:10.1016/j.jmbbm.2018.08.045

37. Markolf KL, Park S, Jackson SR, McAllister DR. Contributions of the posterolateral bundle of the anterior cruciate ligament to anterior-posterior knee laxity and ligament forces. *Arthrosc - J Arthrosc Relat Surg*. 2008;24(7):805–809. doi:10.1016/j.arthro.2008.02.012

38. McLean SG, Oh YK, Palmer ML, et al. The relationship between anterior tibial acceleration, tibial slope, and ACL strain during a simulated jump landing task. *J Bone Jt Surg - Ser A*. 2011;93(14):1310–1317. doi:10.2106/JBJS.J.00259

39. Van Meer BL, Waarsing JH, van Eijsden WA, et al. Bone mineral density changes in the knee following anterior cruciate ligament rupture. *Osteoarthr Cartil*. 2014;22(1):154–161. doi:10.1016/j.joca.2013.11.005

40. Murphy DF, Connolly DAJ, Beynnon BD. Risk factors for lower extremity injury: A review of the literature. *Br J Sports Med*. 2003;37(1):13–29. doi:10.1136/bjsm.37.1.13

41. Nagano H, Begg RK. Shoe-insole technology for injury prevention in walking. *Sensors (Switzerland)*. 2018;18(5). doi:10.3390/s18051468

42. Nagano Y, Ida H, Akai M, Fukubayashi T. Gender differences in knee kinematics and muscle activity during single limb drop landing. *Knee*. 2007;14(3):218–223. doi:10.1016/j.knee.2006.11.008

43. Nieves JW, Formica C, Ruffing J, et al. Males have larger skeletal size and bone mass than females, despite comparable body size. *J Bone Miner Res*. 2005;20(3):529–535. doi:10.1359/JBMR.041005

44. O'Connor KJ. Fatigue Fracture of the Tibia. *Proc R Soc Med*. 1944;37(5):229–230. doi:10.1007/BF02974850

45. Oh YK, Lipps DB, Ashton-Miller JA, Wojtys EM. What strains the anterior cruciate ligament during a pivot landing? *Am J Sports Med*. 2012;40(3):574–583. doi:10.1177/0363546511432544

46. Orava S, Kujala U. Tendon avulsions in children and adolescents. *Tendon Inj Basic Sci Clin Med*. Published online 2005(e)ko :86–89. doi:10.1007/1-84628-050-8_10

47. Patton DM, Ochocki DN, Martin CT, et al. State of the mineralized tissue comprising the femoral ACL enthesis in young women with an ACL failure. *J Orthop Res*. 2021;(September 2019). doi:10.1002/jor.25130

48. Pietrzak WS, Woodell-may J, Mcdonald N. Assay of Bone Morphogenetic Protein-2, -4, and -7 in Human Demineralized Bone Matrix. *J Craniofac Surg*. 2006;17(1):84–90.

49. Schilaty N, Bates N, Krych A, Hewett T. How anterior cruciate ligament injury was averted during Knee collapse in a NBA point guard. *Ann Musculoskelet Med*. 2017;1(1):008–012. doi:10.17352/amm.000002

50. Self BP, Paine D. Ankle biomechanics dring four landing techniques. *Med Sci Sport Exerc*. 2001;33(8):1338–1344.

51. Smith HC, Vacek P, Johnson RJ, et al. Risk factors for anterior cruciate ligament injury: A review of the literature - part 1: Neuromuscular and anatomic risk. *Sports Health*. 2012;4(1):69–78. doi:10.1177/1941738111428281

52. Sonnery-Cottet B, Barth J, Graveleau N, Fournier Y, Hager JP, Chambat P. Arthroscopic identification of isolated tear of the posterolateral bundle of the anterior cruciate ligament. *Arthrosc - J Arthrosc Relat Surg*. 2009;25(7):728–732. doi:10.1016/j.arthro.2008.12.018

53. Stagi S, Cavalli L, Iurato C, Seminara S, Brandi ML, Martino M De. Bone metabolism in children and adolescents: Main characteristics of the determinants of peak bone mass. *Clin Cases Miner Bone Metab*. 2013;10(3):172–179.

54. Sutton KM, Bullock JM. Anterior cruciate ligament rupture: Differences between males and females. *J Am Acad Orthop Surg*. 2013;21(1):41–50. doi:10.5435/JAAOS-21-01-41

55. Todd MS, Lalliss S, Garcia ES, Deberardino TM, Cameron KL. The Relationship Between Posterior Tibial Slope and Anterior Cruciate Ligament Injuries. *Am J Sport Med Vol 38, No1*. Published online 2010(e)ko . doi:10.1177/0363546509343198

56. Vasta S, Andrade R, Pereira R, et al. Bone morphology and morphometry of the lateral femoral condyle is a risk factor for ACL injury. *Knee Surgery, Sport Traumatol Arthrosc*. 2018;26(9):2817–2825. doi:10.1007/s00167-017-4761-x

57. Villotte S, Knüsel CJ. Understanding Entheseal Changes: Definition and Life Course Changes. *Int J Osteoarchaeol*. 2013;23(2):135–146. doi:10.1002/oa.2289

58. Waldén M, Krosshaug T, Bjørneboe J, Andersen TE, Faul O, Hägglund M. Three distinct mechanisms predominate in noncontact anterior cruciate ligament injuries in male professional football players: A systematic video analysis of 39 cases. *Br J Sports Med*. 2015;49(22):1452–1460. doi:10.1136/bjsports-2014-094573

59. Wang D, Kent RN, Amirtharaj MJ, et al. Tibiofemoral kinematics during compressive loading of the ACL-intact and ACL-sectioned knee. *J Bone Jt Surg*. 2019;101(12):1085–1092. doi:10.2106/jbjs.18.00868

60. Watanabe T, Saito H. Tests of wireless wearable sensor system in joint angle measurement of lower limbs. *Proc Annu Int Conf IEEE Eng Med Biol Soc EMBS*. Published online 2011(e)ko :5469–5472. doi:10.1109/IEMBS.2011.6091395

61. Withrow TJ, Huston LJ, Wojtys EM, Ashton-Miller JA. Effect of varying hamstring tension on anterior cruciate ligament strain during in vitro impulsive knee flexion and

compression loading. *J bone Jt Surg*. 2008;(July 2006):815–823. doi:10.2106/JBJS.F.01352

62. Withrow TJ, Huston LJ, Wojtys EM, Ashton-Miller JA. The relatioship between quadriceps muscle force, knee flexion, and anterior cruciate ligament strain in an in vitro simulated jump landing. *Am J Sports Med*. 2006;34(2):269–274. doi:10.1177/0363546505280906

63. Wojtys EM, Beaulieu ML, Ashton-Miller JA. New perspectives on ACL injury: On the role of repetitive sub-maximal knee loading in causing ACL fatigue failure. *J Orthop Res*. 2016;34(12):2059–2068. doi:10.1002/jor.23441

64. Wolff J. Das gesetz der transformation der knochen. *DMW-Deutsche Medizinische Wochenschrift*. 1892;19(47):1222–1224.

65. Woodhouse E, Schmale GA, Simonian P, Tencer A, Huber P, Seidel K. Reproductive hormone effects on strength of the rat anterior cruciate ligament. *Knee Surgery, Sport Traumatol Arthrosc*. 2007;15(4):453–460. doi:10.1007/s00167-006-0237-0

66. Wu Z, LaNeve AJ, Niebur GL. In vivo microdamage is an indicator of susceptibility to initiation and propagation of microdamage in human femoral trabecular bone. *Bone*. 2013;55(1):208–215. doi:10.1016/j.bone.2013.02.019

67. Wu Z, Ovaert TC, Niebur GL. Viscoelastic properties of human cortical bone tissue depend on gender and elastic modulus. *J Orthop Res*. 2012;30(5):693–699. doi:10.1002/jor.22001

Chapter 7: Conclusions

Based on the results presented in Chapter 2 - 5 we conclude:

1) Because the LoAs ranged from 35.9 % to 49.8 % of the measured joint angles, the APDM^R IMUs could not reliably measure the sudden changes in joint angles that occur during simulated pivot landings, even in the absence of soft tissue artifacts (Chapter 2).
2) A steeper LTS was associated with greater ATT and ITR, with ITR increasing proportionally more than ATT did (Chapter 3).
3) The finite element modeling showed that a concave femoral enthesis is advantageous in reducing the peak tensile and shear stresses in that structure under ACL tension near full knee extension, the knee posture most often used in jump landings and contact the ground during sudden deceleration maneuvers (Chapter 4).
4) At 20 μm resolution, none of the nano CT variables suggested any evidence of fatigue damage in the subchondral bone plate or trabeculae beneath the femoral ACL enthesis under sub-maximal repetitive loading, but rather leads to fatigue damage accumulation in the ACL approximately 50 um distal to the femoral enthesial tidemark, as demonstrated in other papers from our group. (Chapter 5).
5) The subchondral bone at the origin of the PL bundle of the ACL femoral enthesis is denser and thicker, with a higher volume fraction and cortical bone thickness, than at the AM bundle origin. We speculate this is to resist higher shear strains under the PL bundle. (Chapter 5).

6) The subchondral trabecular bone below the origin of ACL femoral enthesis exhibited a tensile arcade aligned in the direction of ACL line of action near full knee extension. We take this as evidence of Wolff's law leading to stiffening of the structure thereby reducing bone strains (Chapter 5).

Chapter 8: Suggestion for Future Research

The ultimate goal of this research was to better understand the mechanism of ACL injury, so more ACL injuries could be predicted and prevented. The dissertation focused on knee kinematics during a simulated jump landing and how certain bone morphologies might contribute to ACL injury. There are still many questions and knowledge gaps remaining.

1) The wearable IMUs could not reliably measure tibiofemoral kinematics in all three planes under during pivot landings (Chapter 2). In a related study, a custom tuned algorithm did improve the results slightly[1]. It remains a challenge to increase the correlation between data from motion capture systems and wearable sensors. One possibility would be for the wearable sensor to continuously monitor its location relative to the underlying bone thereby removing the problematic soft tissue artifact.

2) Both ATT and ITR are positively correlated with ACL strain[10]. To take advantage of findings in Chapter 3, one might be able to use a 1T office MRI to measure LTS and alpha angle [2] in order to identify athletes who have steeper-than-normal LTS and alpha angles.

3) We identified a steeper LTS was associated with increased ATT and ITR in Chapter 3 with 7 pairs of male human knees. However, it is already known that females have a steeper LTS and it is a known risk factor for ACL injuries in women[9,12]. Therefore, studies need to be done that include females and larger sample sizes.

4) The relationship between LTS and tibiofemoral kinematics was examined in Chapter 3. However, several risk factors affect the ACL injury simultaneously including smaller notch-width index[7,8], smaller ACL cross sectional area size[5,11], smaller medial tibial depth[6], and increased femoral alpha angle[2,4]. Therefore, it would be worthwhile to examine the relationship between these anatomical factors and tibiofemoral kinematics.

5) The results of the finite element analysis in Chapter 4 showed that the concave profile of femoral enthesis has the lowest tensile and shear stress concentrations among the three profiles, and also suggested where the highest tensile and shear stress are applied to the subchondral cortical plates. However, we did not apply torsional stress to the ACL and did not add the effect of subcortical trabecular bone. Future research could investigate in detail where the stress concentrations occur under different loading conditions.

6) Regional adaptation of the subchondral bone in the femoral ACL enthesis was revealed in Chapter 5 with the cortical bone plates thickening and trabecular bone orientation in the young adult knees. Therefore, it would be interesting to know how and where in this changes occur in growing children.

7) As the results of Chapter 5 show, no evidence of fatigue damage in the subchondral bone beneath the ACL femoral enthesis was found at 20 μm resolution. Therefore, it would still be worth imaging the subchondral bone at a higher resolution and that could be done using histology and staining techniques to rule out any fatigue failures in subchondral bone. Once that is done, we will know that up to 3 times body-weight loading only causes fatigue failure on the collagen fibrils and fibers of the ligament[3] near the femoral enthesis, but not in the bone beneath it.

8.1 References

1. Ajdaroski M, Ashton-Miller JA, Baek SY, Shahshahani PM, Esquivel AO. Testing a quaternion conversion method to determine human three-dimensional tibiofemoral angles during an in vitro simulated jump landing. *J Biomech Eng*. 2022;144(4):1–8. doi:10.1115/1.4052496

2. Barnum MS, Boyd ED, Vacek P, Slauterbeck JR, Beynnon BD. Association of geometric characteristics of knee anatomy (alpha angle and intercondylar notch type) with noncontact ACL injury. *Am J Sports Med*. 2021;49(10):2624–2630. doi:10.1177/03635465211023750

3. Chen J, Kim J, Shao W, et al. An anterior cruciate ligament failure mechanism. *Am J Sports Med*. 2019;47(9):2067–2076. doi:10.1177/0363546519854450

4. Griffin LY, Agel J, Albohm MJ, et al. Noncontact anterior cruciate ligament injuries: Risk factors and prevention strategies. *J Am Acad Orthop Surg*. 2000;8(3):141–150. doi:10.5435/00124635-200005000-00001

5. Griffin LY, Albohm MJ, Arendt EA, et al. Understanding and preventing noncontact anterior cruciate ligament injuries: A review of the Hunt Valley II Meeting, January 2005. *Am J Sports Med*. 2006;34(9):1512–1532. doi:10.1177/0363546506286866

6. Hashemi J, Chandrashekar N, Gill B, et al. The geometry of the tibial plateau and its influence on the biomechanics of the tibiofemoral joint. *J Bone Jt Surg - Ser A*. 2008;90(12):2724–2734. doi:10.2106/JBJS.G.01358

7. Ireland ML, Ballantyne BT, Little K, McClay IS. A radiographic analysis of the relationship between the size and shape of the intercondylar notch and anterior cruciate ligament injury. *Knee Surgery, Sport Traumatol Arthrosc*. 2001;9(4):200–205. doi:10.1007/s001670100197

8. Kumar Panigrahi T, Das A, Mohanty T, Samanta S, Kumar Mohapatra S. Study of relationship of posterior tibial slope in anterior cruciate ligament injury. *J Orthop*. 2020;21(June):487–490. doi:10.1016/j.jor.2020.08.032

9. Lipps DB, Oh YK, Ashton-Miller JA, Wojtys EM. Morphologic characteristics help explain the gender difference in peak anterior cruciate ligament strain during a simulated pivot landing. *Am J Sports Med*. 2012;40(1):32–40. doi:10.1177/0363546511422325

10. Oh YK, Lipps DB, Ashton-Miller JA, Wojtys EM. What strains the anterior cruciate ligament during a pivot landing? *Am J Sports Med*. 2012;40(3):574–583. doi:10.1177/0363546511432544

11. Smith HC, Vacek P, Johnson RJ, et al. Risk factors for anterior cruciate ligament injury: A review of the literature - part 1: Neuromuscular and anatomic risk. *Sports Health*. 2012;4(1):69–78. doi:10.1177/1941738111428281

12. Sutton KM, Bullock JM. Anterior cruciate ligament rupture: Differences between males and females. *J Am Acad Orthop Surg*. 2013;21(1):41–50. doi:10.5435/JAAOS-21-01-41

Appendices

Appendix A: Comprehensive Datasets for the Dissertation

This Appendix includes the demographic data for donors and datasets as well as the representative data for statistical analyses for Chap 2 - 5 in this dissertation. Donor information and testing conditions for Chap 2 - 5 are shown in Table A.1-A.3. The testing data for the final pivot trials of each set for Chap 3 are shown in Table A.4. The measured LTS results from both the primary and blinded observer for Chap 3 are presented in Table A.5. Quantitative data from the femoral enthesis subchondral bone analyses for Chap 4 are presented in Table A.6.

Table A-1. Demographic data for the donors of the seven knee pairs in Chapter 2

Specimen No.	Donor ID	Source*	Gender	Side	Age [yrs]	Height [cm]	Weight [kg]	BMI [kg/m^2]	Testing condition
S1	#35588	U-M	F	L	20	165	86.6	31.8	3 BW 100 trials
S2	#40374	U-M	F	R	28	170	63.5	21.9	4 BW 100 trials
S3	#90932	U-M	F	R	30	173	82.1	27.5	3 BW 52 trials
S4	#182486	SC	M	L	39	180	54.4	16.7	4 BW 100 trials
S5	#182515	SC	M	R	32	180	68.0	20.9	4 BW 100 trials
S6	#19011797	AGR	M	R	32	180	88.5	27.2	3 BW 100 trials
S7	GOL22	GOL	M	R	25	180	86.2	26.5	3 BW 100 trials
S8	GOL21	GOL	M	R	31	175	92.5	30.1	3 BW 100 trials
S9	#91814	U-M	M	R	33	155	49.9	20.8	4 BW 100 trials

* Source

- U-M : University of Michigan Anatomical Donation Program
- AGR : Anatomy Gifts Registry
- SC : Science Care
- GOL : Gift of Life Michigan

Table A-2. Demographic data for the donors of the seven knee pairs for Chapter 3

Specimen No.	Donor ID	Source*	Age [yrs]	Height [cm]	Weight [kg]	BMI [kg/m2]	Side	Testing condition
P1	#20030211	AGR	33	160	72.6	28.3	Right	2.5 BW x 50 trials
							Left	1 BW x 50 trials + 2 BW x 50 trials
P2	#201506	SC	23	160	72.6	28.3	Right	2.5 BW x 50 trials + 3 BW x 50 trials
							Left	1 BW x 50 trials + 2 BW x 50 trials
P3	GOL29	GOL	25	152	69.1	29.8	Right	2.5 BW x 50 trials + 3 BW x 50 trials
							Left	1 BW x 50 trials + 2 BW x 50 trials
P4	#2101627	MC	32	142	64.4	32.0	Right	1 BW x 50 trials + 2 BW x 50 trials
							Left	2.5 BW x 23 trials -Tibial bone fracture
P5	#911614	MC	19	158	71.7	28.7	Right	1 BW x 50 trials + 2 BW x 50 trials
							Left	2.5 BW x 50 trials + 3 BW x 50 trials
P6	#200241	SC	20	154	69.9	29.5	Right	1 BW x 50 trials + 2 BW x 50 trials
							Left	2.5 BW x 50 trials + 3 BW x 50 trials
P7	#20030426	AGR	28	177	80.3	25.6	Right	1 BW x 50 trials + 2 BW x 50 trials
							Left	2.5 BW x 50 trials + 3 BW x 50 trials

*Source

- AGR : Anatomy Gifts Registry
- SC : Science Care
- MC : Medcure
- GOL : Gift of Life Michigan

Table A-3. Demographic data for the donors of the seven knees pairs for Chapters 5

Specimen No.	Donor ID	Source *	Gender	Age [yrs]	Height [cm]	Weight [kg]	BMI [kg/m^2]	Side	Testing condition
S1	#91635	U-M	F	40	110	49.9	41.2	Right	3 BW x 7 trials -Tibial bone fracture
								Left	Control knee
S2	#00003	U-M	F	36	122	55.3	37.2	Right	2.5 BW x 50 trials + 3 BW x 50 trials
								Left	Control knee
S3	#2101635	MC	M	39	134	60.8	33.9	Right	2.5 BW x 50 trials + 3 BW x 50 trials
								Left	Control knee
S4	#912935	MC	F	40	156	70.8	29.1	Right	Control knee
								Left	3 BW x 3 trials -Tibial bone fracture
S5	#200129177	AGR	M	37	170	77.1	26.7	Right	Control knee
								Left	2.5 BW x 50 trials + 3 BW x 50 trials
S6	#19040316	AGR	M	38	154	69.9	29.5	Right	Control knee
								Left	2.5 BW x 50 trials + 3 BW x 50 trials
S7	#93409	SC	M	35	177	80.3	25.6	Right	Control knee
								Left	2.5 BW x 50 trials + 3 BW x 50 trials
P1	#20030211	AGR	M	33	160	72.6	28.3	Right	2.5 BW x 50 trials
								Left	1 BW x 50 trials + 2 BW x 50 trials
P2	#201506	SC	M	23	160	72.6	28.3	Right	2.5 BW x 50 trials + 3 BW x 50 trials
								Left	1 BW x 50 trials + 2 BW x 50 trials
P3	GOL29	GOL	M	25	152	69.1	29.8	Right	2.5 BW x 50 trials + 3 BW x 50 trials

								Left	1 BW x 50 trials + 2 BW x 50 trials
P4	#2101627	MC	M	32	142	64.4	32.0	Right	1 BW x 50 trials + 2 BW x 50 trials
								Left	2.5 BW x 23 trials - Tibial bone fracture
P5	#911614	MC	M	19	158	71.7	28.7	Right	1 BW x 50 trials + 2 BW x 50 trials
								Left	2.5 BW x 50 trials + 3 BW x 50 trials
P6	#200241	SC	M	20	154	69.9	29.5	Right	1 BW x 50 trials + 2 BW x 50 trials
								Left	2.5 BW x 50 trials + 3 BW x 50 trials
P7	#20030426	AGR	M	28	177	80.3	25.6	Right	1 BW x 50 trials + 2 BW x 50 trials
								Left	2.5 BW x 50 trials + 3 BW x 50 trials

*Source

- U-M : University of Michigan Anatomical Donation Program
- MC : Medcure
- AGR : Anatomy Gifts Registry
- SC : Science Care
- GOL : Gift of Life Michigan

Table A-4. Testing data for the final pivot trials of each data set for Chapter 3

Specimen No.	Side	1st 25 trials			2nd 25 trials			3rd 25 trials			4th 25 trials		
		ATT [mm]	ITR[°]	IF/BW	ATT [mm]	ITR[°]	IF/BW	ATT [mm]	ITR[°]	IF/BW	ATT [mm]	ITR[°]	IF/BW
P1	Right	13.5	24.6	2.4	12.3	25.1	2.4						
	Left	8.4	20.3	1.1	7.5	18.9	1.0	12.4	24.2	2.2	11.9	24.3	2.1
P2	Right	9.1	21.3	2.3	9.6	21.5	2.4	11.4	22.5	2.8	11.2	21.9	2.7
	Left	6.5	16.8	1.0	6.6	16.8	1.0	14.6	21.4	2.2	13.4	20.4	2.1
P3	Right	10.8	22.1	2.7	10.5	22.3	2.7	12.4	26.4	3.0	12.3	24.7	3.0
	Left	5.0	21.7	1.0	4.7	20.9	1.0	8.4	26.3	2.0	8.4	26.4	2.0
P4	Right	5.0	13.4	0.9	4.8	13.5	0.9	8.8	18.3	1.7	9.0	18.4	1.7
	Left	Tibia bone fracture											
P5	Right	7.6	19.0	0.9	7.2	17.9	0.9	11.3	21.2	1.9	11.6	21.4	1.8
	Left	9.7	21.4	2.6	11.0	22.7	2.8	11.0	22.4	2.9	11.3	23.5	3.0
P6	Right	6.8	14.3	1.0	7.5	15.6	1.1	12.7	20.3	2.2	13.0	21.0	2.2
	Left	15.8	23.4	2.7	15.2	23.2	2.7	18.2	26.3	3.0	18.5	26.5	3.0
P7	Right	4.1	13.7	1.0	4.1	13.7	0.9	7.4	16.8	1.8	7.8	16.8	1.9
	Left	12.1	17.5	2.4	11.8	17.5	2.5	11.6	17.3	2.4	12.2	17.1	2.6

Table A-5. LTS measured by the blinded observer (Chapter 3) and the observer who conducted the testing

Specimen No.	Side	LTS [º] by the blinded observer			LTS [º] by the observer who conducted the testing		
		1st measured	2nd measured	mean [SD]	1st measured	2nd measured	mean [SD]
P1	Right	8.61	8.38	8.5 [0.2]	7.49	7.70	7.6 [0.1]
	Left	5.97	6.09	6.0 [0.1]	6.06	6.00	6.0 [0.0]
P2	Right	2.65	3.51	3.1 [0.6]	5.37	3.50	4.4 [1.3]
	Left	1.84	1.83	1.8 [0.0]	1.70	5.90	3.8 [3.0]
P3	Right	3.09	3.05	3.1 [0.0]	3.39	1.80	2.6 [1.1]
	Left	1.20	0.96	1.1 [0.2]	1.84	2.01	1.9 [0.1]
P4	Right	1.19	4.13	2.7 [2.1]	11.74	5.50	8.6 [4.4]
	Left	9.14	6.02	7.6 [2.2]	9.33	5.80	7.6 [2.5]
P5	Right	5.67	4.09	4.8 [1.1]	4.22	4.20	4.2 [0.0]
	Left	4.42	4.10	4.3 [0.2]	4.42	4.50	4.5 [0.1]
P6	Right	5.40	6.98	6.2 [1.1]	6.06	1.70	3.9 [3.1]
	Left	4.16	4.86	4.5 [0.5]	2.80	6.00	4.4 [2.3]
P7	Right	7.19	5.21	6.2 [1.4]	8.52	8.70	8.6 [0.1]
	Left	12.11	10.96	11.5 [0.8]	10.46	8.80	9.6 [1.2]

Table A-6. Quantitative data of femoral subchondral ACL bone analyses for Chapter 5

Specimen No.	Side	BVF		BMD [mg/cc]		Ct.th [mm]		Tb.th [mm]	
		PL	AM	PL	AM	PL	AM	PL	AM
S1	Right	0.39	0.32	954	893	0.31	0.26	0.17	0.19
	Left	0.41	0.36	1422	1379	0.37	0.35	0.20	0.17
S2	Right	0.60	0.30	1120	946	0.48	0.27	0.22	0.19
	Left	0.57	0.30	1194	1075	0.49	0.23	0.21	0.18
S3	Right	0.37	0.25	1097	1034	0.30	0.30	0.20	0.18
	Left	0.44	0.34	2065	1984	0.48	0.42	0.22	0.20
S4	Right	0.63	0.37	1170	978	0.51	0.31	0.25	0.23
	Left	0.62	0.40	1329	1215	0.44	0.29	0.21	0.22
S5	Right	0.41	0.31	1171	1102	0.33	0.22	0.20	0.21
	Left	0.54	0.42	1239	1176	0.38	0.25	0.21	0.23
S6	Right	0.30	0.28	1146	1109	0.31	0.23	0.17	0.18
	Left	0.36	0.36	1094	1125	0.35	0.30	0.17	0.18
S7	Right	0.64	0.39	1438	1228	0.42	0.28	0.24	0.25
	Left	0.35	0.36	1236	1201	0.27	0.38	0.24	0.20
P1	Right	0.42	0.39	1153	1145	0.31	0.28	0.20	0.21
	Left	0.48	0.32	1279	1182	0.34	0.24	0.20	0.20
P2	Right	0.48	0.38	1204	1157	0.39	0.27	0.25	0.22
	Left	0.53	0.37	1196	1160	0.50	0.27	0.24	0.20
P3	Right	0.31	0.27	1103	1048	0.20	0.19	0.16	0.17
	Left	0.43	0.26	1051	986	0.31	0.18	0.19	0.16
P4	Right	0.41	0.27	1262	1052	0.33	0.18	0.18	0.17
	Left	0.31	0.24	1118	1177	0.38	0.21	0.16	0.14
P5	Right	0.37	0.35	1246	1236	0.27	0.26	0.23	0.22
	Left	0.38	0.37	1075	1073	0.32	0.28	0.21	0.23
P6	Right	0.41	0.45	1062	1076	0.34	0.38	0.23	0.24
	Left	0.41	0.40	1115	1101	0.33	0.42	0.24	0.21
P7	Right	0.52	0.43	1361	1296	0.41	0.30	0.29	0.30
	Left	0.57	0.49	1134	1121	0.46	0.35	0.31	0.33

Appendix B: The Results for LTS Measured by the Observer who Conducted the Testing in relation to Chapter 3 as the Secondary Analysis

To assess measurement reliability, LTS was measured by an observer blinded to the knee testing results. As a supplementary analysis of Chapter 3, LTS was also measured by the same observer as conducted the experimental biomechanical testing (Table A.5), and the statistical analysis was also performed in the same way as in Chap 3.

Table B-1 shown the results for the linear mixed model with ATT, ITR, and LTS which were used for random intercepts to reflect ATT and ITR being assigned values of zero in the absence of a landing impact force, and all values under load being calculated relative to those starting values.

Table B-1. Results for the linear mixed effect model using random intercepts.

	Model C1. ATT ~ ITR				Model C2. ITR ~ ATT			
	Coefficient	SE	t Value	P Value	Coefficient	SE	t Value	P Value
(Intercept)	-9.10	1.47	-6.21	<0.001	11.62	0.95	12.23	<0.001
ITR (ATT)	0.94	0.061	15.34	<0.001	0.88	0.057	15.55	<0.001

Similar to the Chapter 3 results, a steeper LTS had a significant effect on ATT and ITR, respectively, as normalized impact force (IF/BW) was increased (Table B-2). The effect of LTS on ATT can be seen from its positive coefficient of 0.38 (95% CI: 0.19-0.57) independent of impact force with its coefficient of 0.46 (95% CI: 0.44-0.48). The effect of LTS on ITR is seen from its larger positive coefficient of 0.94 (95% CI: 0.51-1.36) for increasing impact force (coefficient = 0.43, 95% CI: 0.41-0.46).

Table B-2. Results for the linear mixed effect model for LTS measured by the observer who conducted the testing, as well as ATT and ITR.

	Model A. ATT ~ LTS + BW				Model B. ITR ~ LTS + BW			
	Coefficient	SE	t Value	P Value	Coefficient	SE	t Value	P Value
(Intercept)								
LTS	0.38	0.089	4.23	<0.001	0.94	0.20	4.66	<0.001
BW	0.46	0.0095	48.12	<0.001	0.43	0.013	34.66	<0.001
LTS:BW	0.0003	0.0015	2.06	0.04	0.0029	0.0019	1.49	0.14

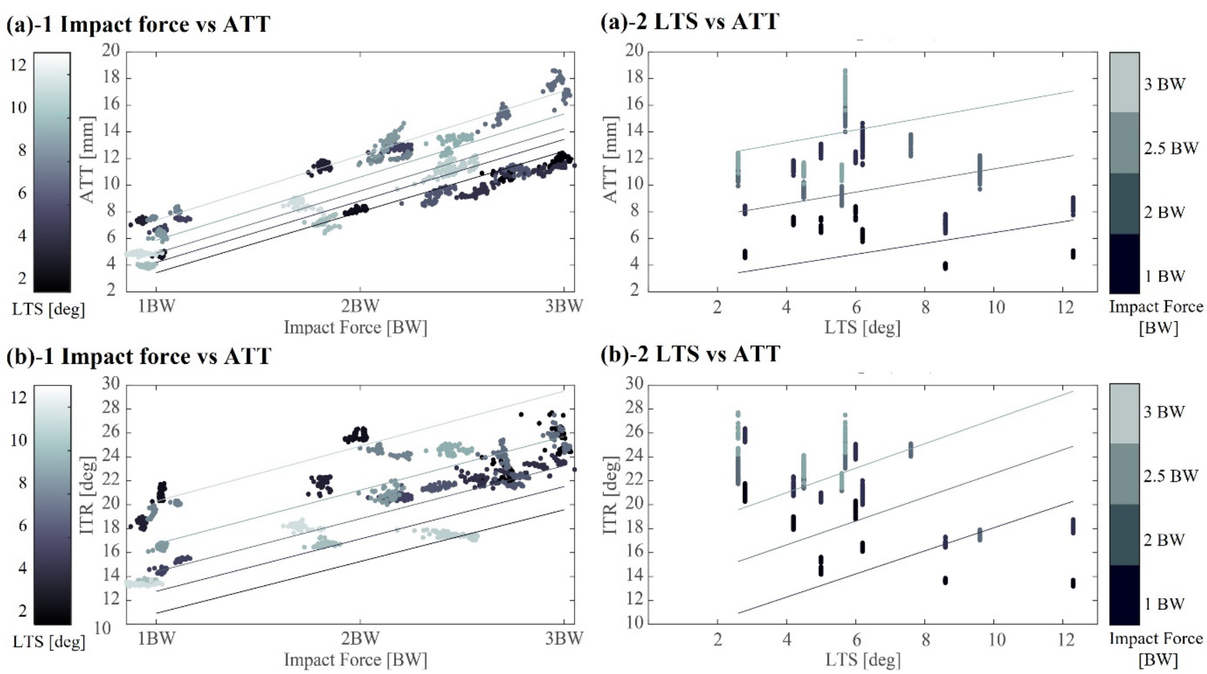

Figure B-1. Scatter plots showing the relationship between normalized impact force and ATT (a-1), and LTS versus ATT (a-2). Normalized impact force versus ITR, and LTS versus ITR are shown in (b-1) and (b-2), respectively. The lines indicate the LTS being assumed constant at 2°, 4°, 6°, 8° and 10° in order to examine the effect of increasing impact force effect on ATT (a-1) and ITR (b-1), respectively. In ATT (a-2) and ITR (b-2) the normalized impact force was assumed constant at 1BW, 2BW, and 3BW in order to identify the effect of LTS on ATT.

A power analysis was also performed to determine whether the sample size used was acceptable. With the knee specimen (n=7) and side of the knee (right and left), it showed power of 84% (95% CI: 75.32 - 90.57) for the effects of LTS on ATT (Figure B-1-a). Therefore, this analysis had over 80% power with our random effect size (n=13, 7 pairs of knee specimens), side of the knee (right and left), and one failed knee. However, the power for examining the effect of LTS on ITR (Figure B-1-b) had only 74.00% (95%CI: 64.27 - 82.26), so it was slightly underpowered with this model and sample size. Figure B-2 shows if we had used more than 10 pairs of knees, we would achieve better power for both the ATT and ITR effects. An alternative way to raise power would have been to increase the number of trials, which would increase the power to 90.00% (95% CI: 82.38 - 95.10) for ATT with same specimen number. Interestingly, the effect of impact force on ATT and ITR had 100 % power regardless of number of specimens. This was because impact force was an input variable, and ATT and ITR were outputs that were highly correlated during these simulated pivot landings.

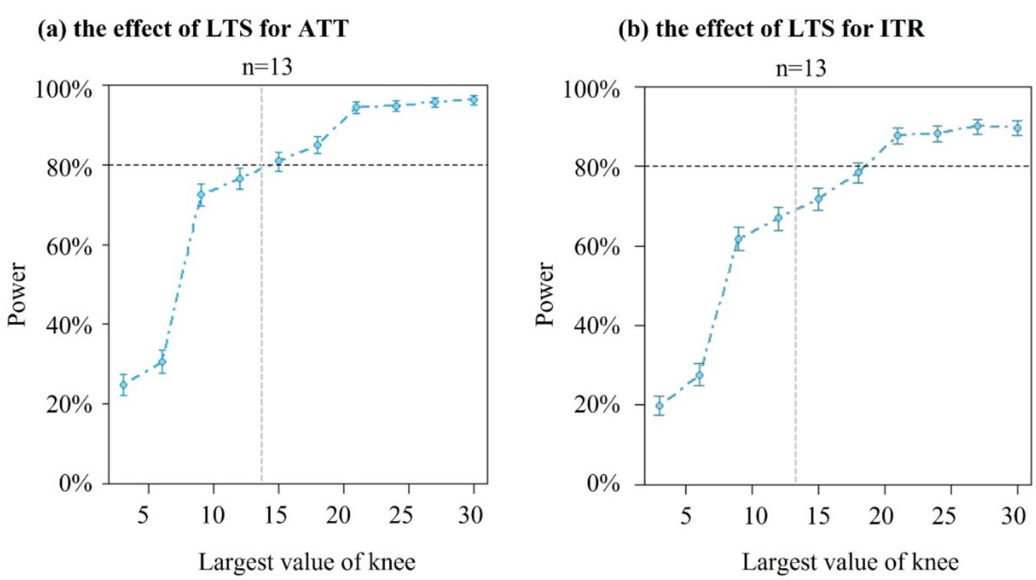

Figure B-2. Power calculations for the effect of LTS on (a) ATT and (b) ITR for different sample sizes. The vertical dashed line denotes the sample size used for this study: n=13 (7 pairs of knees, each with a right and left side, one knee failing via bone fracture).

Inter-rater reliability was examined for the LTS measurements by using intraclass correlation coefficient (ICC), and it was acceptable (ICC = 0.81) for the agreement of measurements.

Although there are numerical differences between two sets of results, the conclusion that a steeper LTS was associated with both increased ATT and ITR, with ITR increasing proportionally more than ATT did was the same.

Appendix C : Measured Morphometric of the Subchondral Bone of the Femoral Enthesis (Chapter 5- Aim 1)

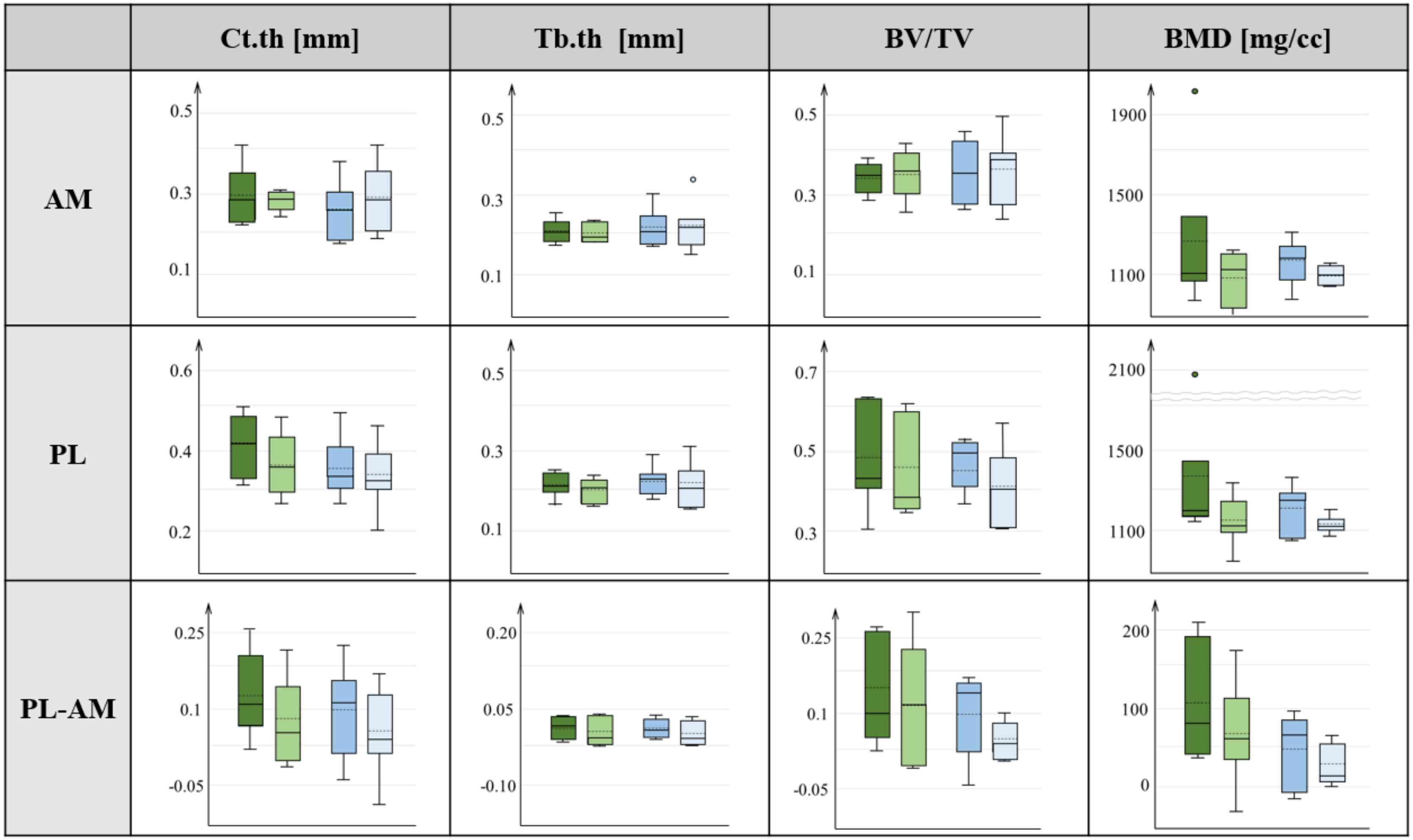

control knee tested knee (3BW)	7 pairs
tested knee (1BW) tested knee (3BW)	7 pairs

Figure C-1. Subchondral bone plate (Ct.Th) and trabeculae (Tb.Th) morphology, as well as overall subchondral bone morphology (BV/TV and BMD) results beneath the AM, PL fiber origins. The difference between PL and AM (PL-AM) control and tested knee, and low and high impact tested knee parameters is given in the bottom row. Solid line denotes median, box: 1st – 3rd Quartile range, whiskers: 5 – 95% of data, dot: outliers, dashed line: mean)

Appendix D: Nano CT Images of Sections through the ACL Femoral Enthesis from all Specimens (Chapter 5 - Aim 2).

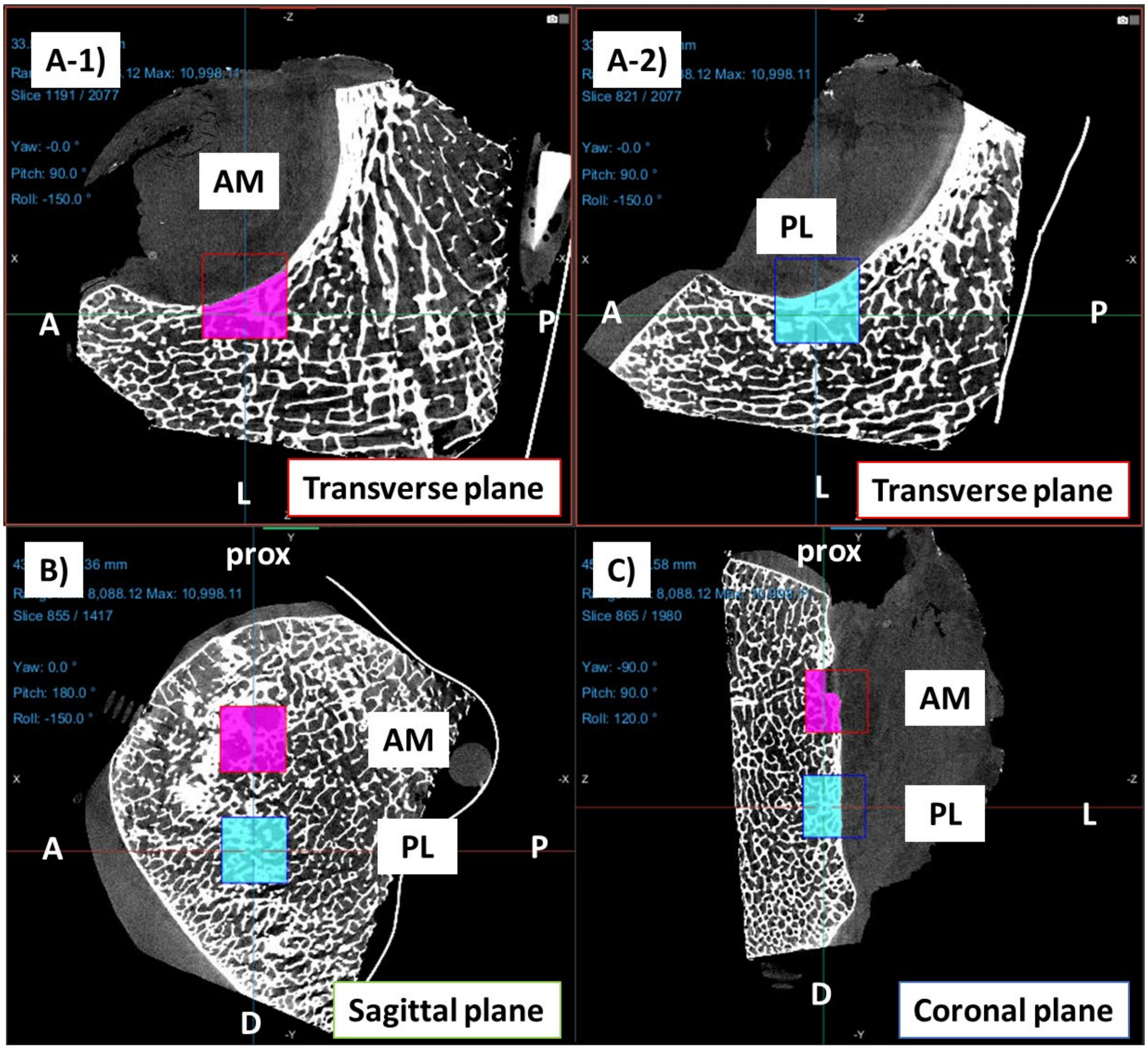

Figure D-1. Sample nano CT image of Specimen P1R. A-1) Transverse plane for AM bundle, A-2) transverse plane for PL bundle, B) sagittal plane, and C) coronal plane.

In this and following images, AM and PL denote anteromedial and posterolateral, respectively.

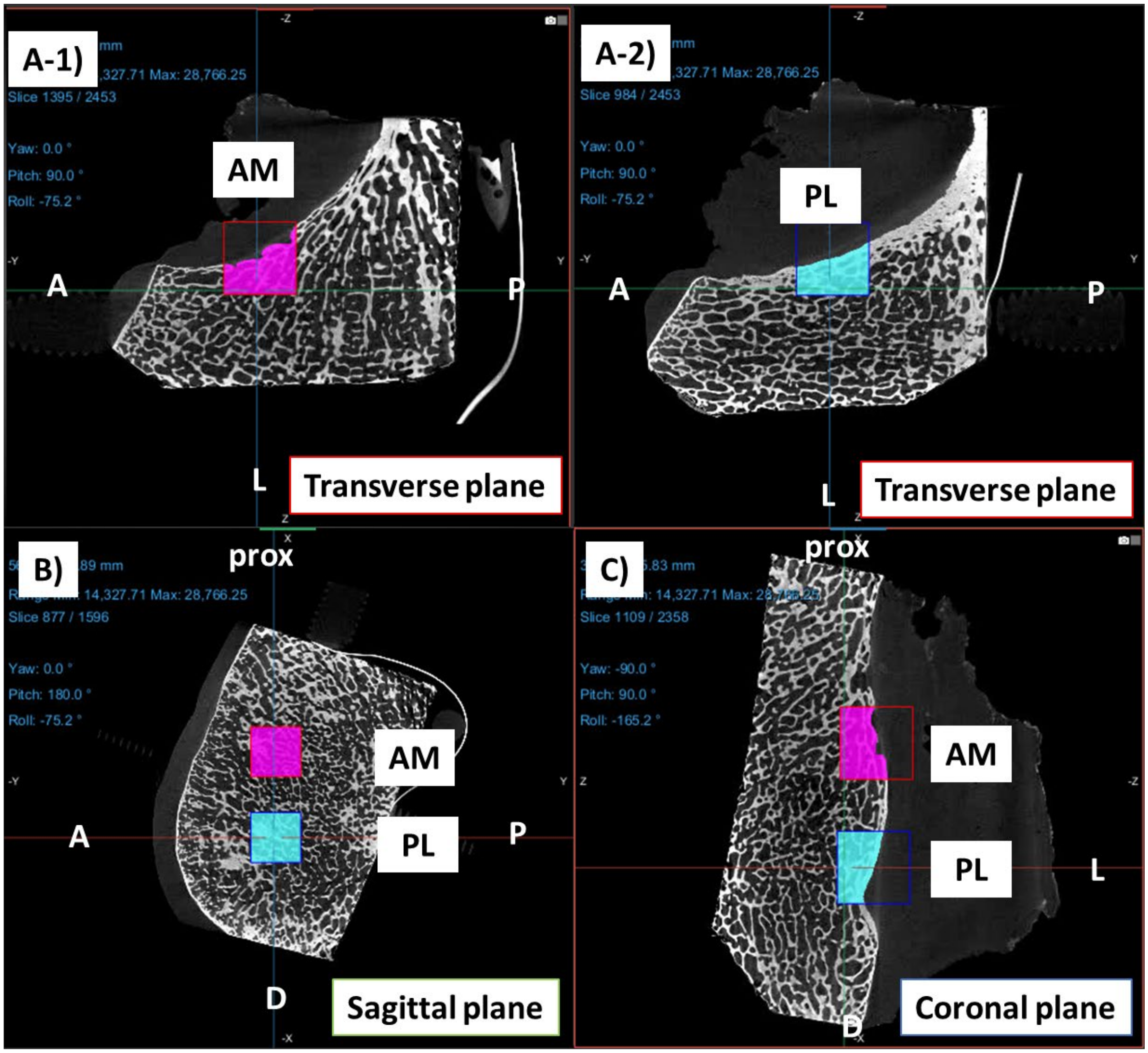

Figure D-2. Sample nano CT image of Specimen P2R. A-1) Transverse plane for AM bundle, A-2) transverse plane for PL bundle, B) sagittal plane, and C) coronal plane

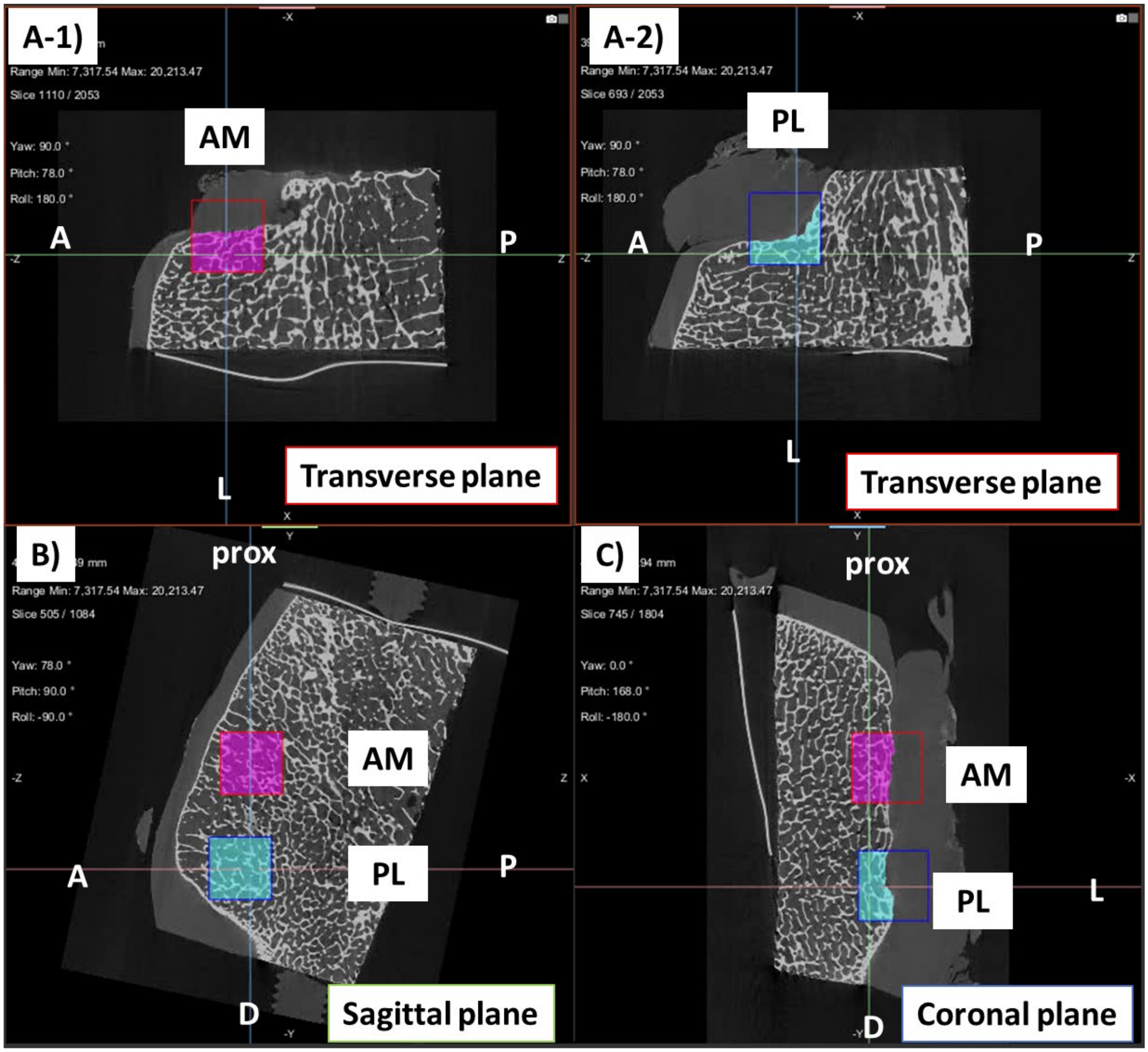

Figure D-3. Sample nano CT image of Specimen P3R. A-1) Transverse plane for AM bundle, A-2) transverse plane for PL bundle, B) sagittal plane, and C) coronal plane

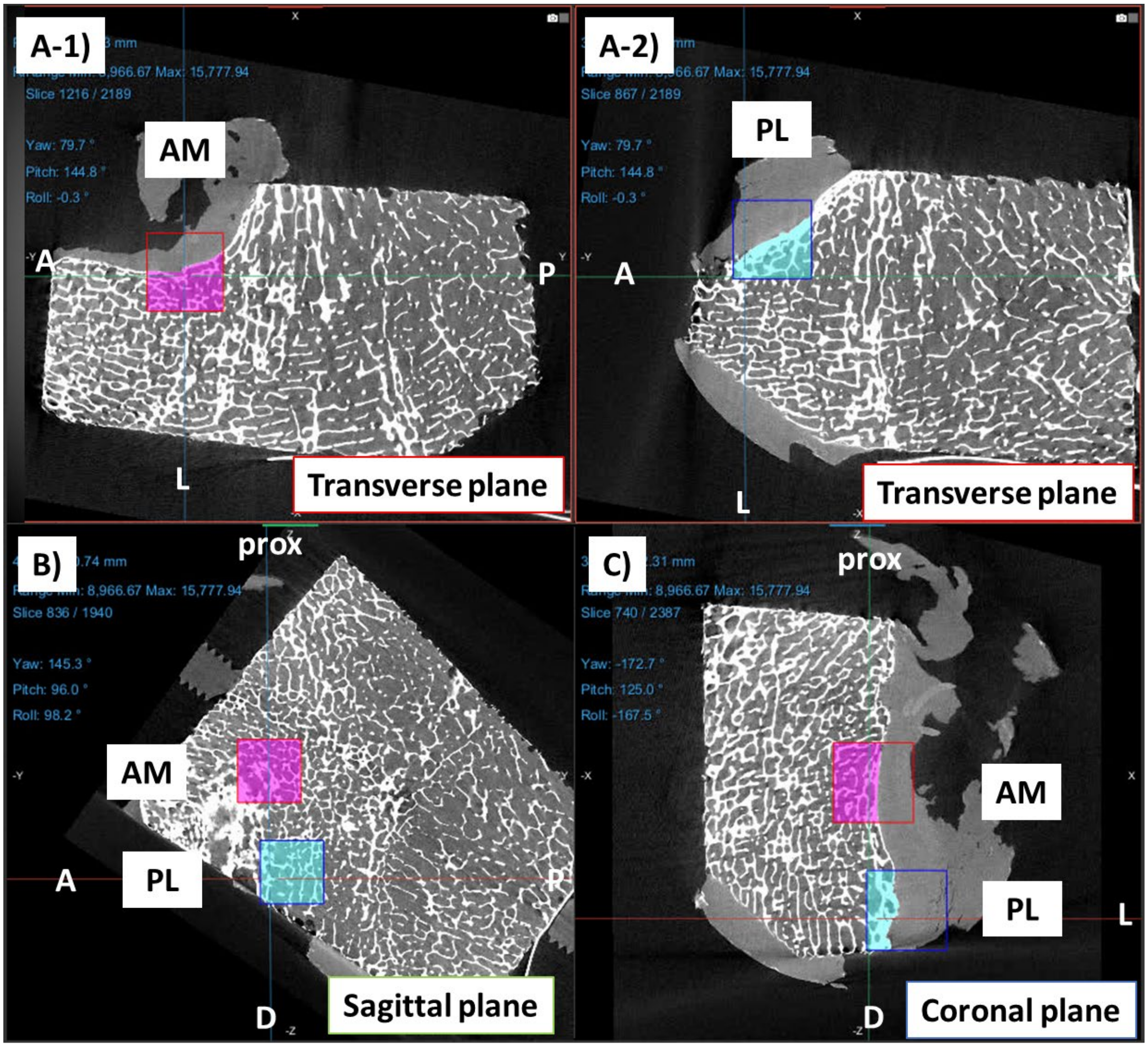

Figure D-4. Sample nano CT image of Specimen P4R. A-1) Transverse plane for AM bundle, A-2) transverse plane for PL bundle, B) sagittal plane, and C) coronal plane

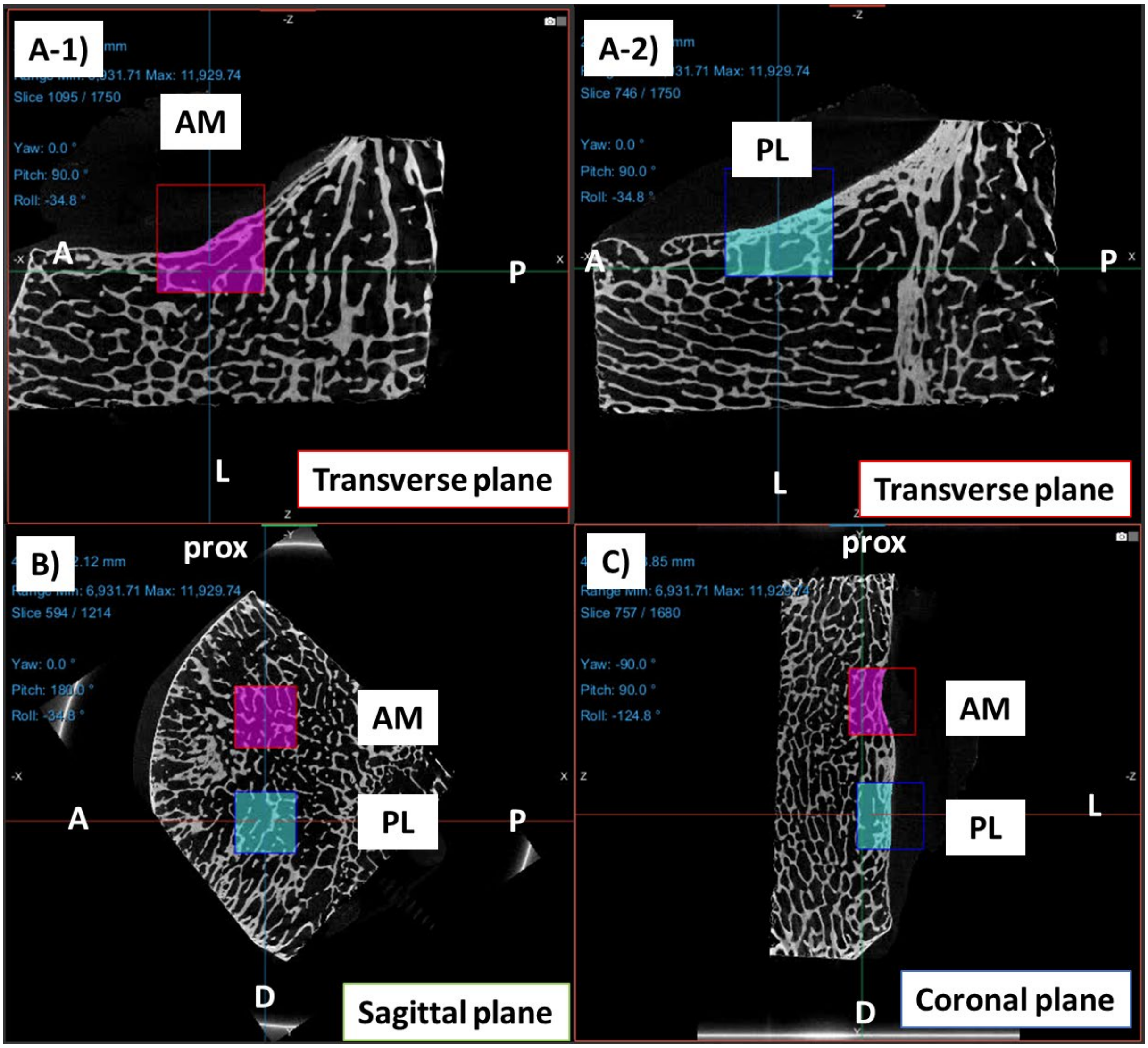

Figure D-5. Sample nano CT image of Specimen P5R. A-1) Transverse plane for AM bundle, A-2) transverse plane for PL bundle, B) sagittal plane, and C) coronal plane

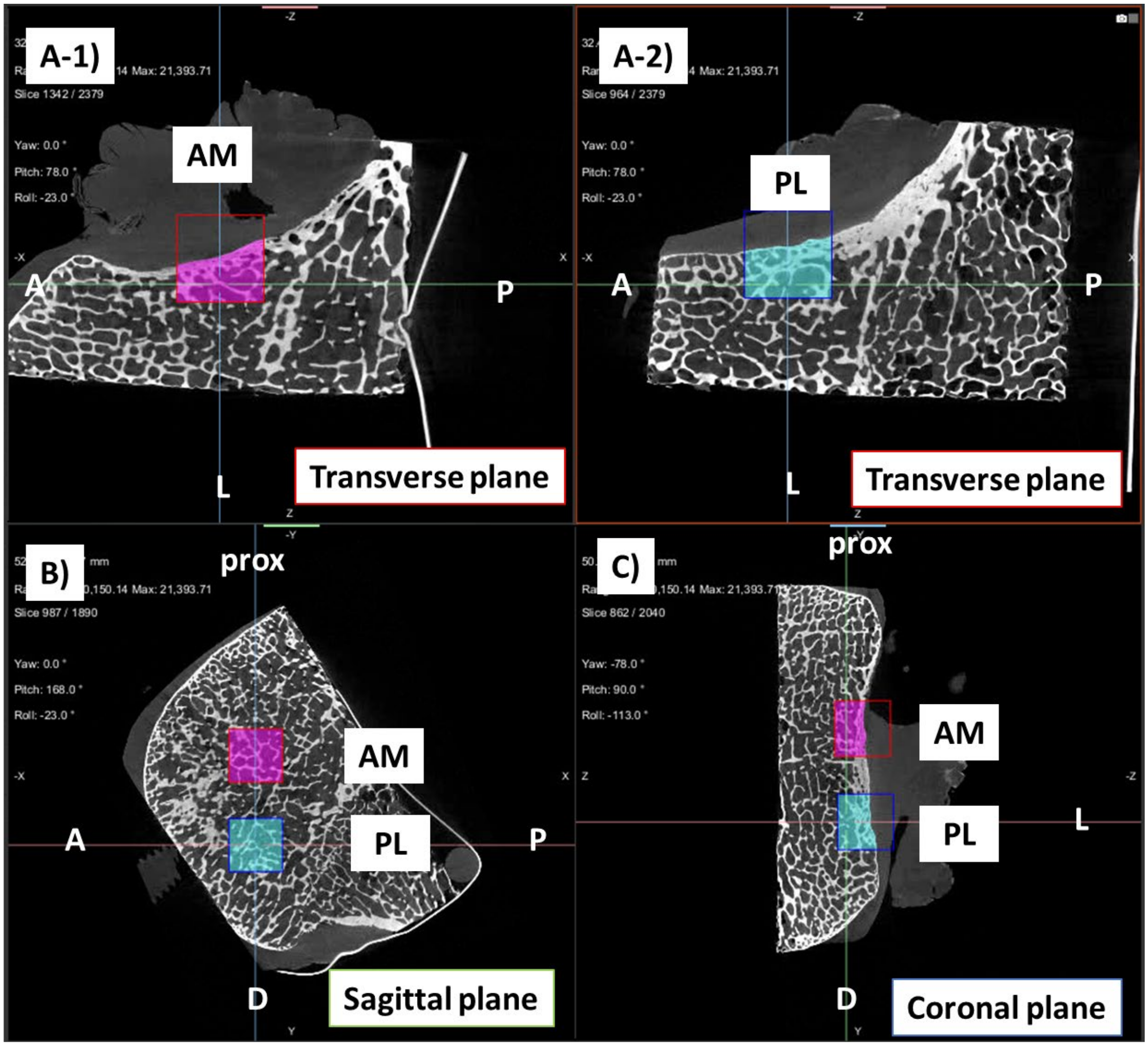

Figure D-6. Sample nano CT image of Specimen P6R. A-1) Transverse plane for AM bundle, A-2) transverse plane for PL bundle, B) sagittal plane, and C) coronal plane

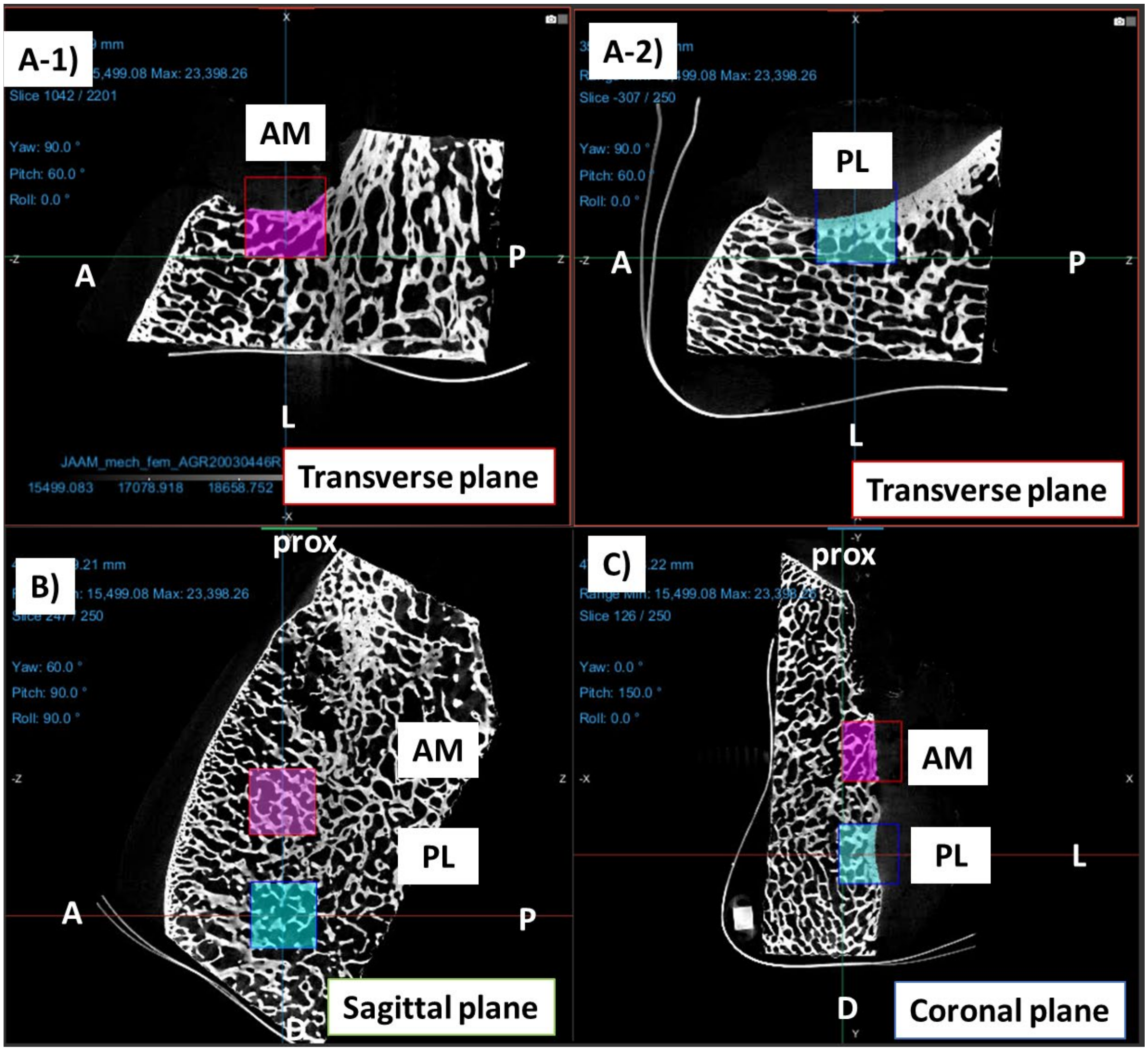

Figure D-7. Sample nano CT image of Specimen P7R. A-1) Transverse plane for AM bundle, A-2) transverse plane for PL bundle, B) sagittal plane, and C) coronal plane

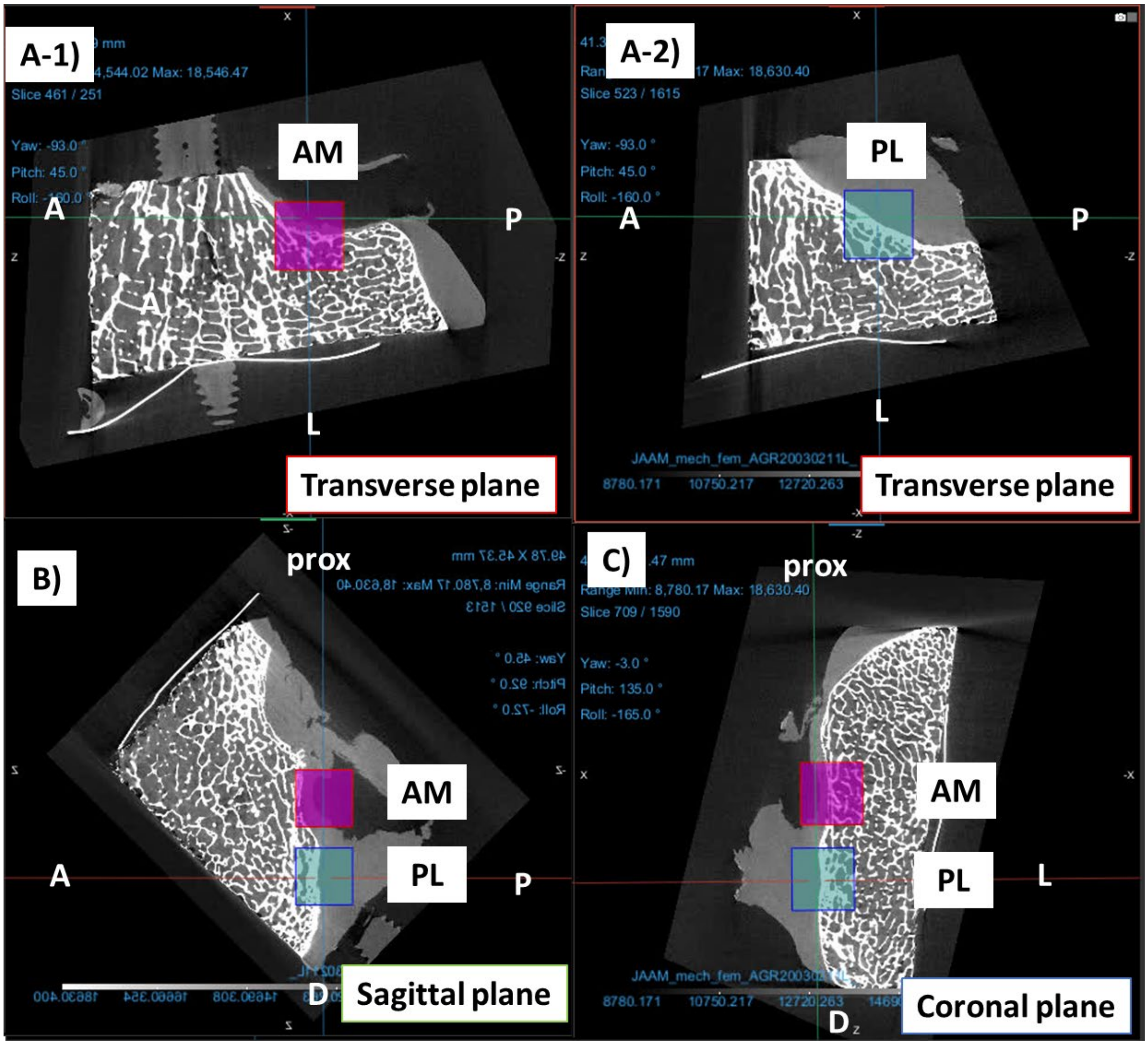

Figure D-8. Sample nano CT image of Specimen P1L. A-1) Transverse plane for AM bundle, A-2) transverse plane for PL bundle, B) sagittal plane, and C) coronal plane

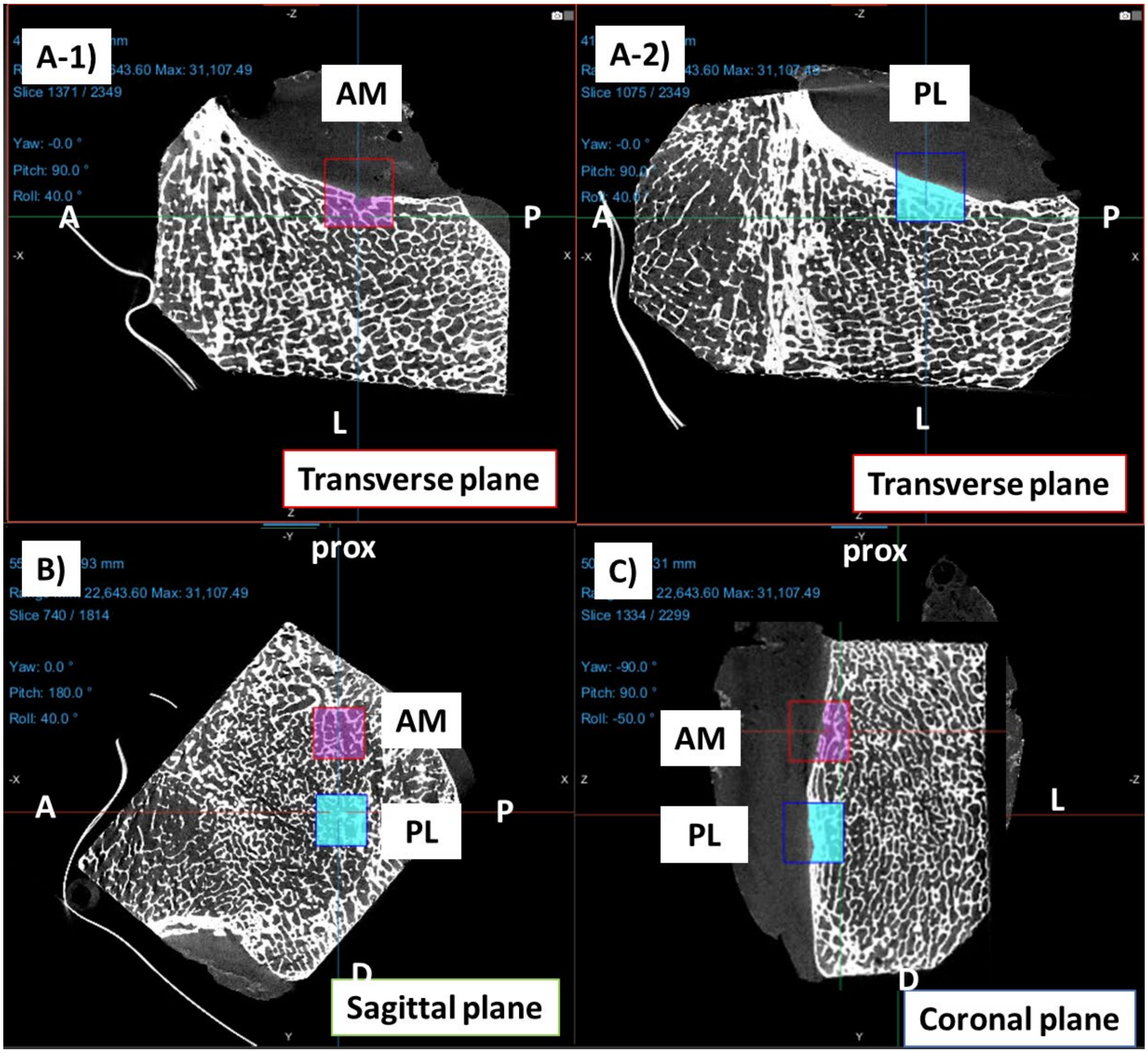

Figure D-9. Sample nano CT image of Specimen P2L. A-1) Transverse plane for AM bundle, A-2) transverse plane for PL bundle, B) sagittal plane, and C) coronal plane

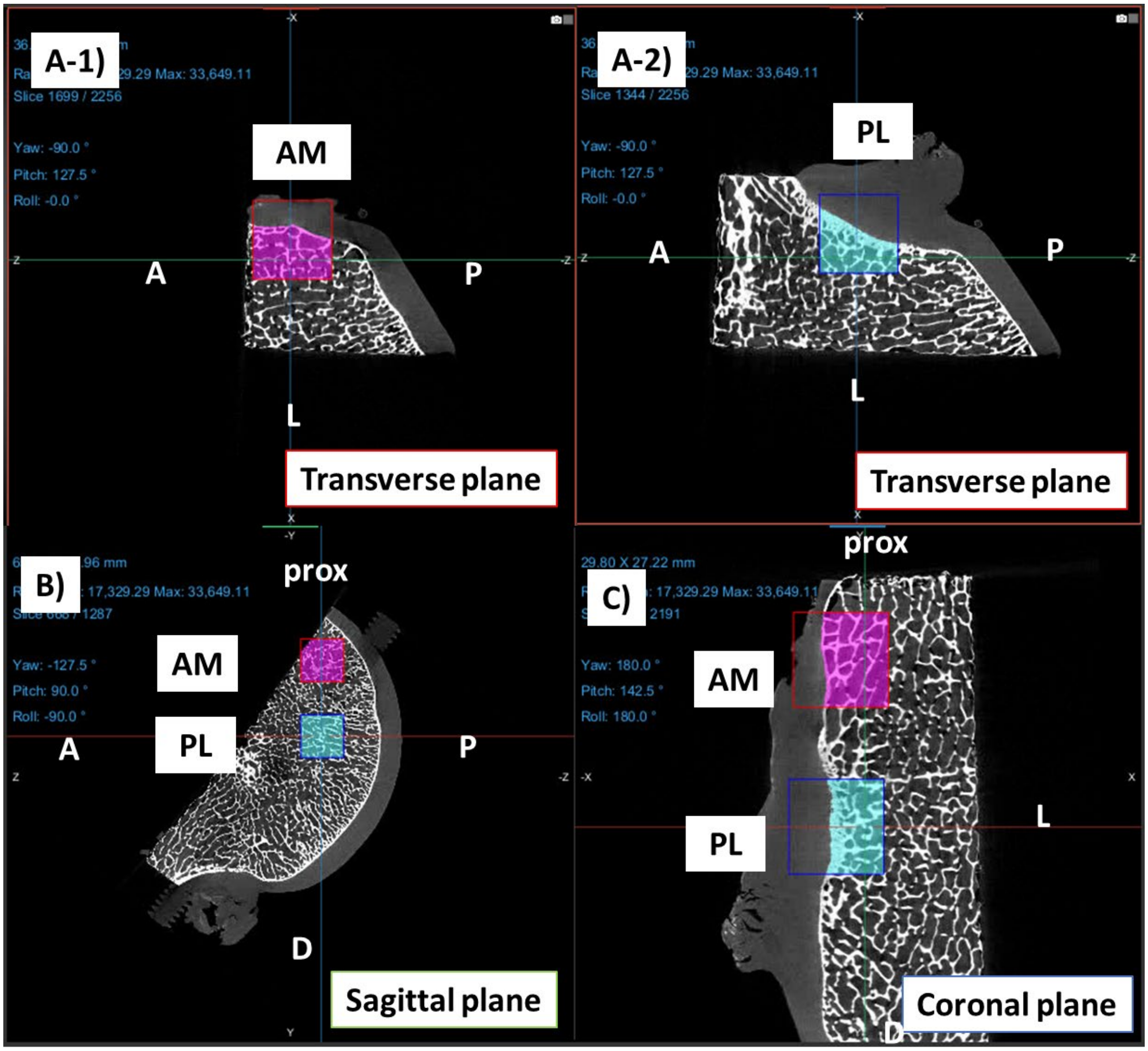

Figure D-10. Sample nano CT image of Specimen P3L. A-1) Transverse plane for AM bundle, A-2) transverse plane for PL bundle, B) sagittal plane, and C) coronal plane

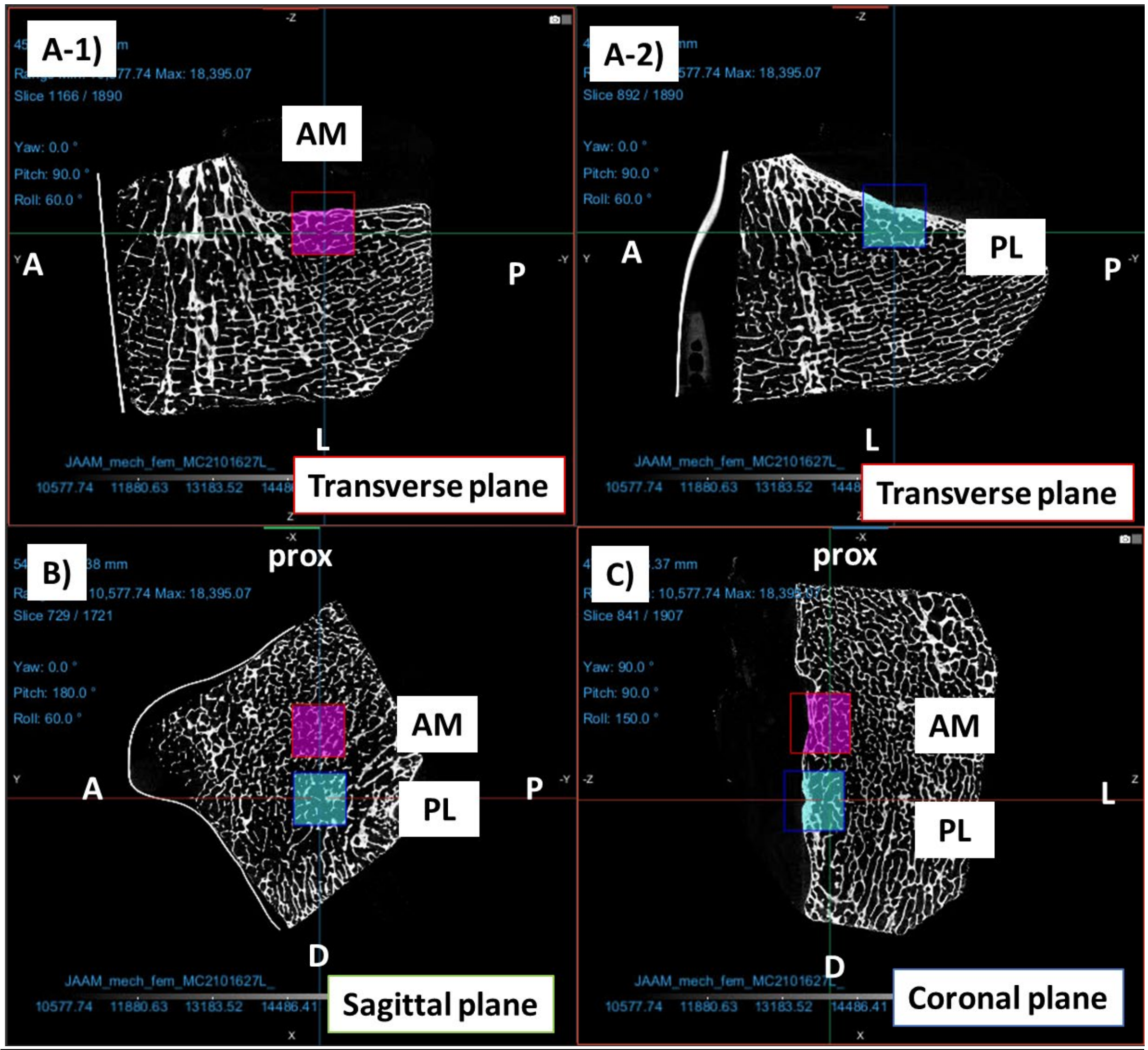

Figure D-11. Sample nano CT image of Specimen P4L. A-1) Transverse plane for AM bundle, A-2) transverse plane for PL bundle, B) sagittal plane, and C) coronal plane

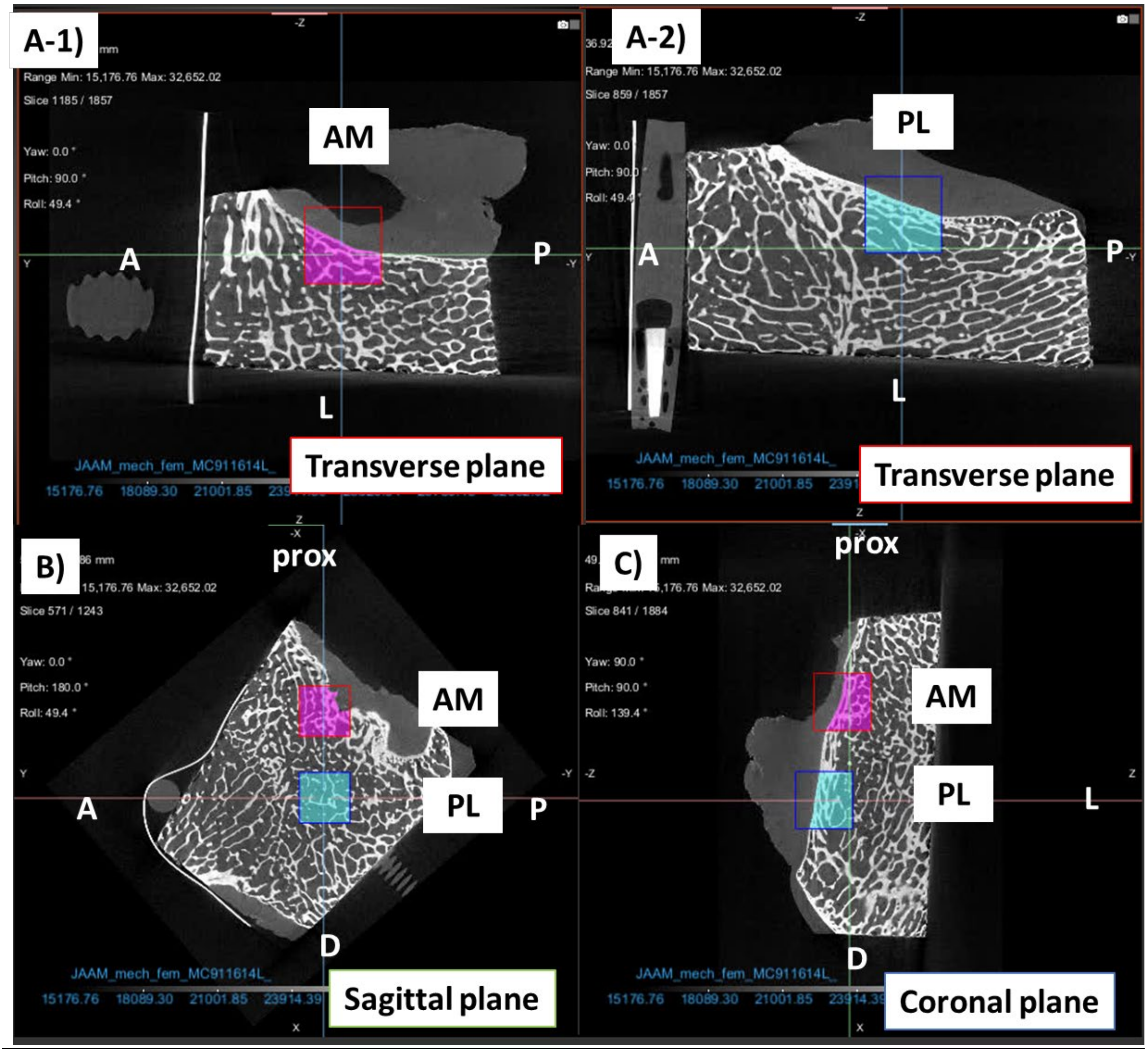

Figure D-12. Sample nano CT image of Specimen P5L. A-1) Transverse plane for AM bundle, A-2) transverse plane for PL bundle, B) sagittal plane, and C) coronal plane

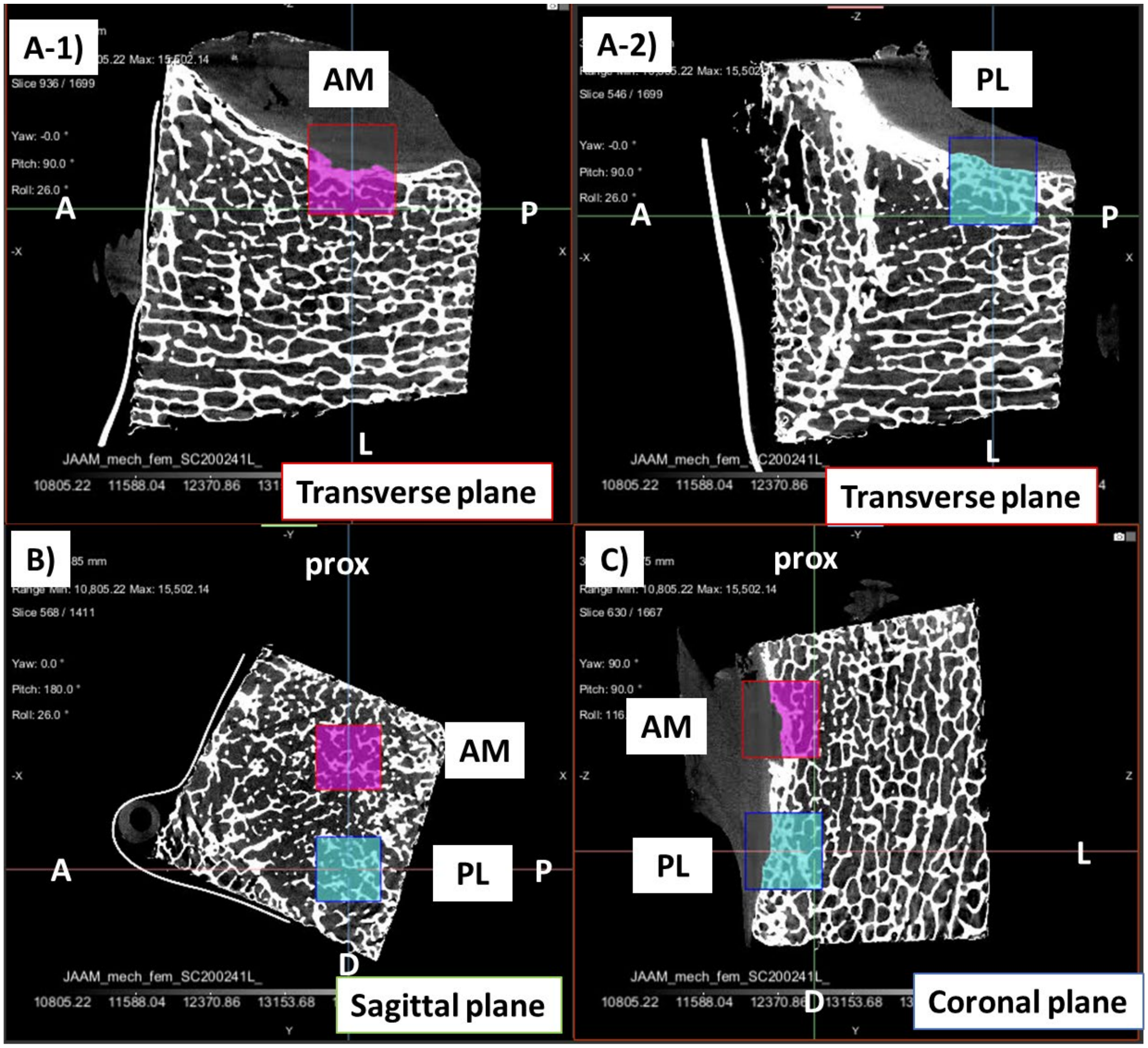

Figure D-13. Sample nano CT image of Specimen P6L. A-1) Transverse plane for AM bundle, A-2) transverse plane for PL bundle, B) sagittal plane, and C) coronal plane

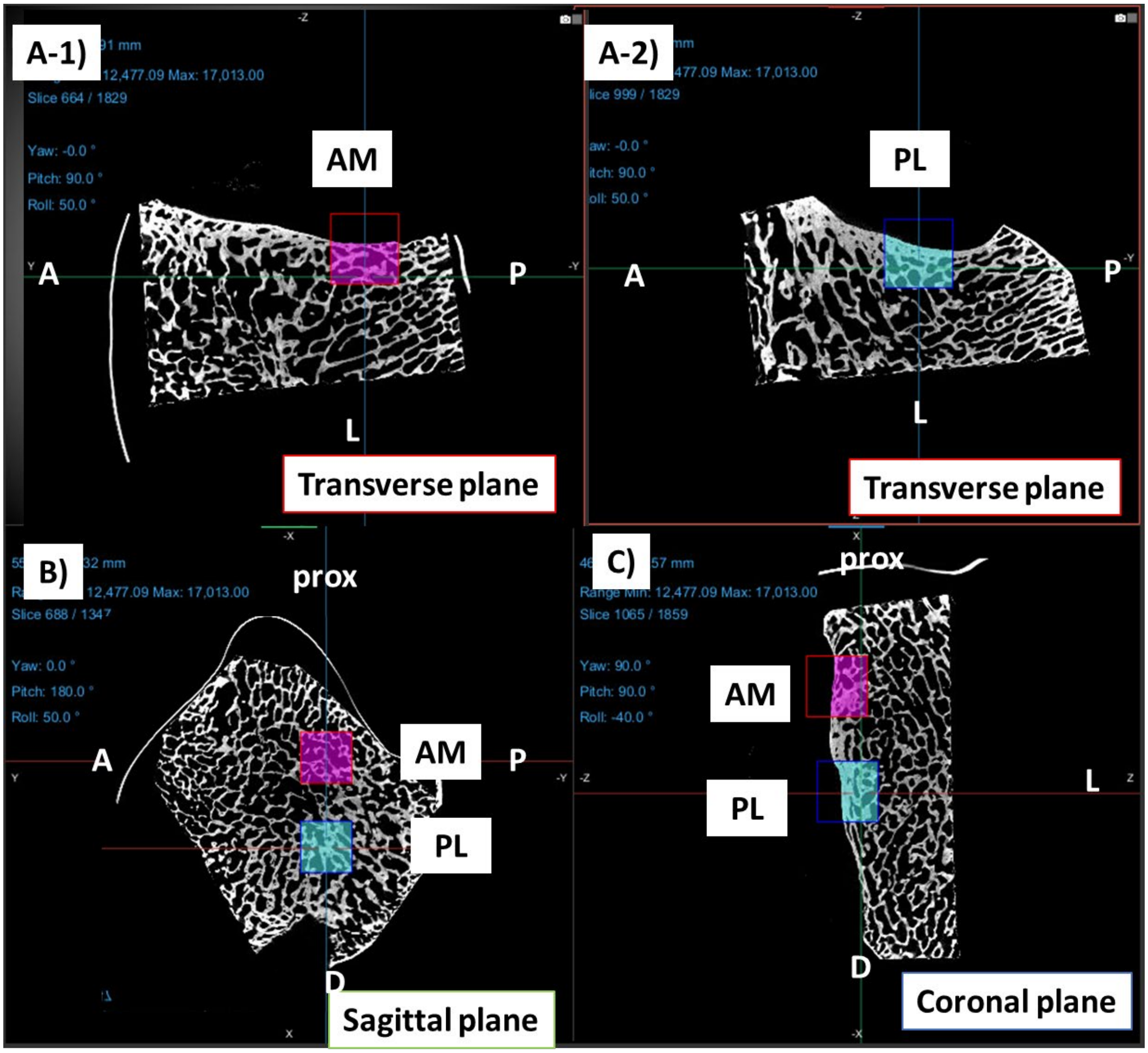

Figure D-14. Sample nano CT image of Specimen P7L. A-1) Transverse plane for AM bundle, A-2) transverse plane for PL bundle, B) sagittal plane, and C) coronal plane

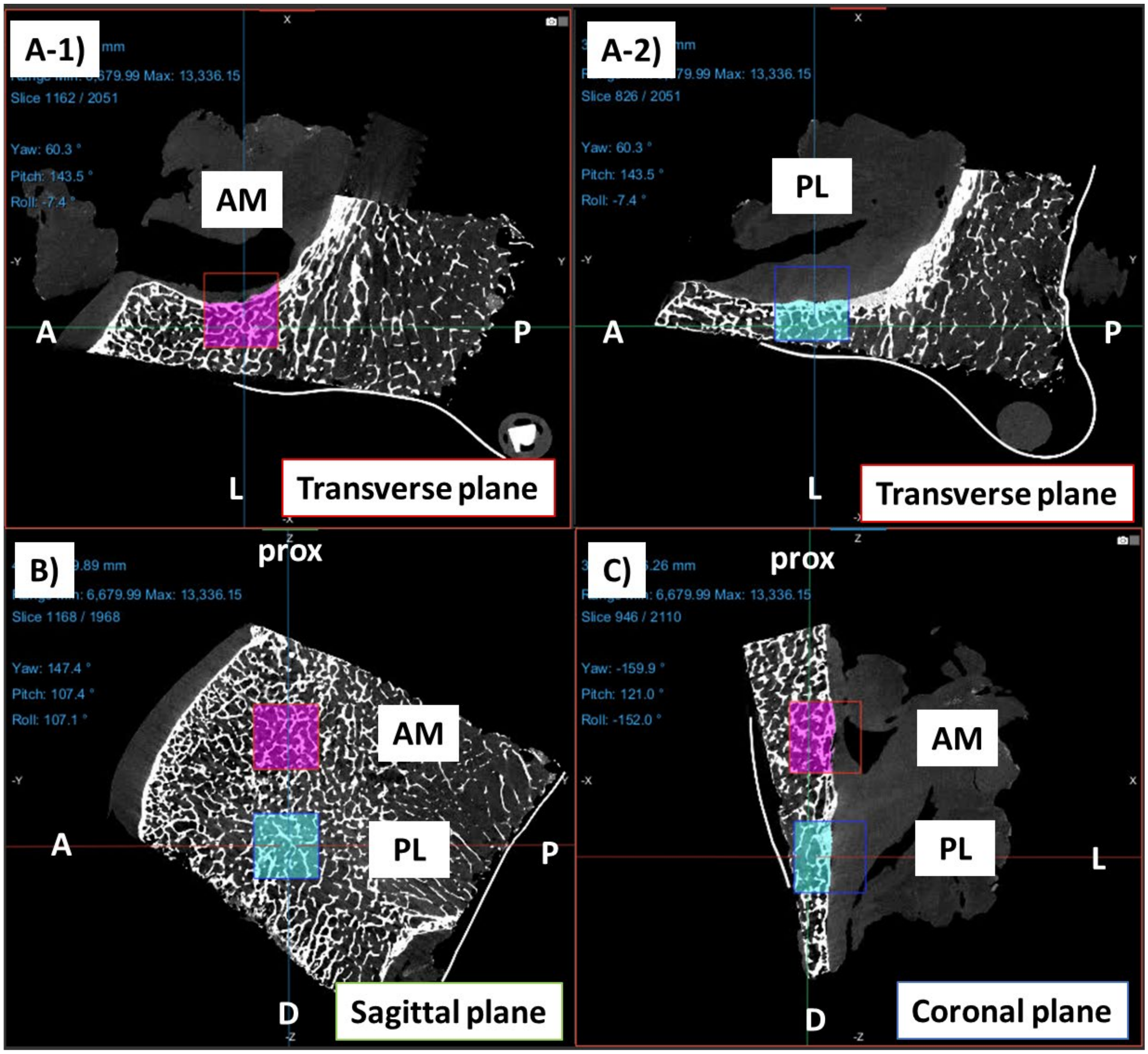

Figure D-15. Sample nano CT image of Specimen S1R. A-1) Transverse plane for AM bundle, A-2) transverse plane for PL bundle, B) sagittal plane, and C) coronal plane

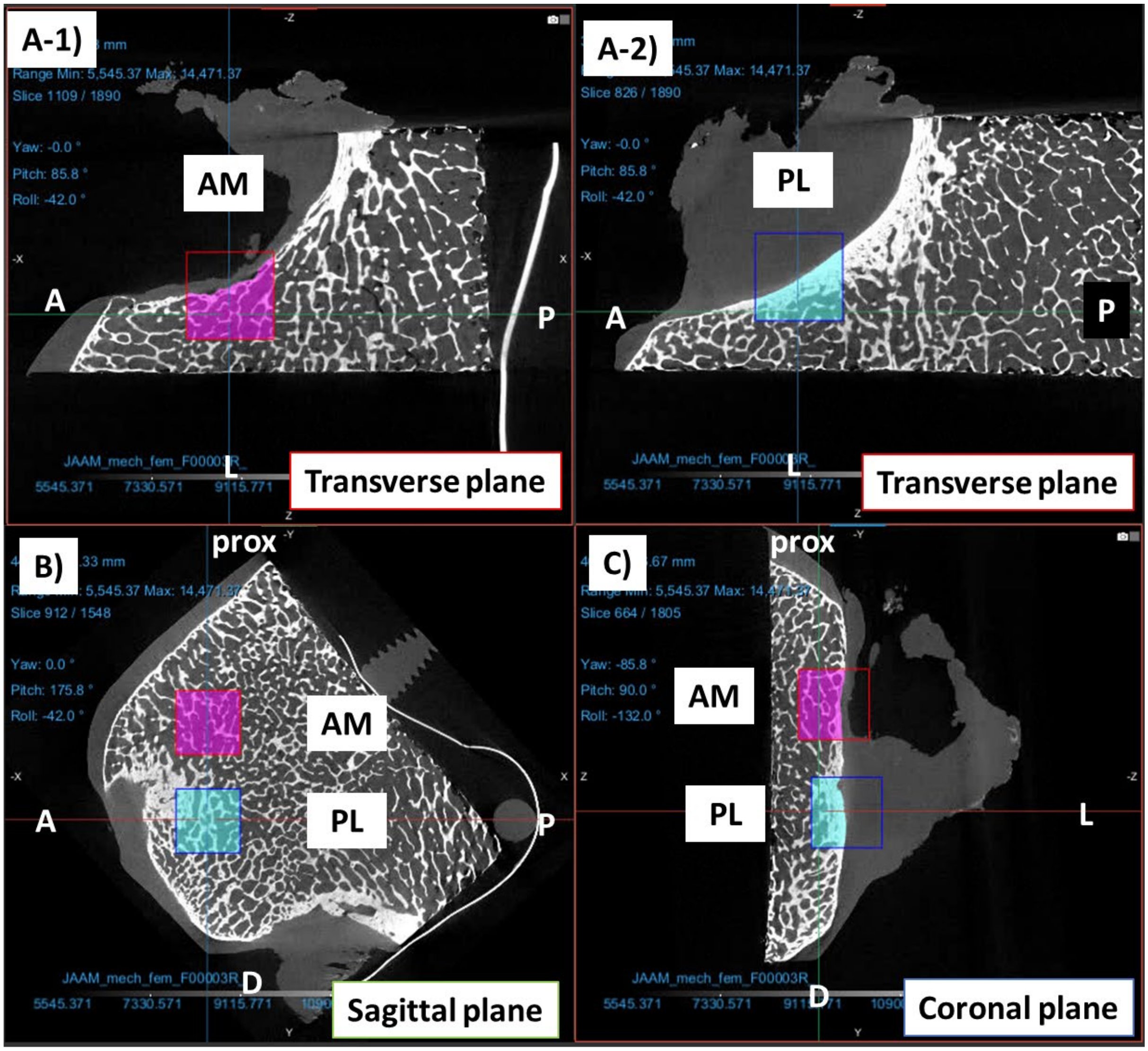

Figure D-16. Sample nano CT image of Specimen S2R. A-1) Transverse plane for AM bundle, A-2) transverse plane for PL bundle, B) sagittal plane, and C) coronal plane

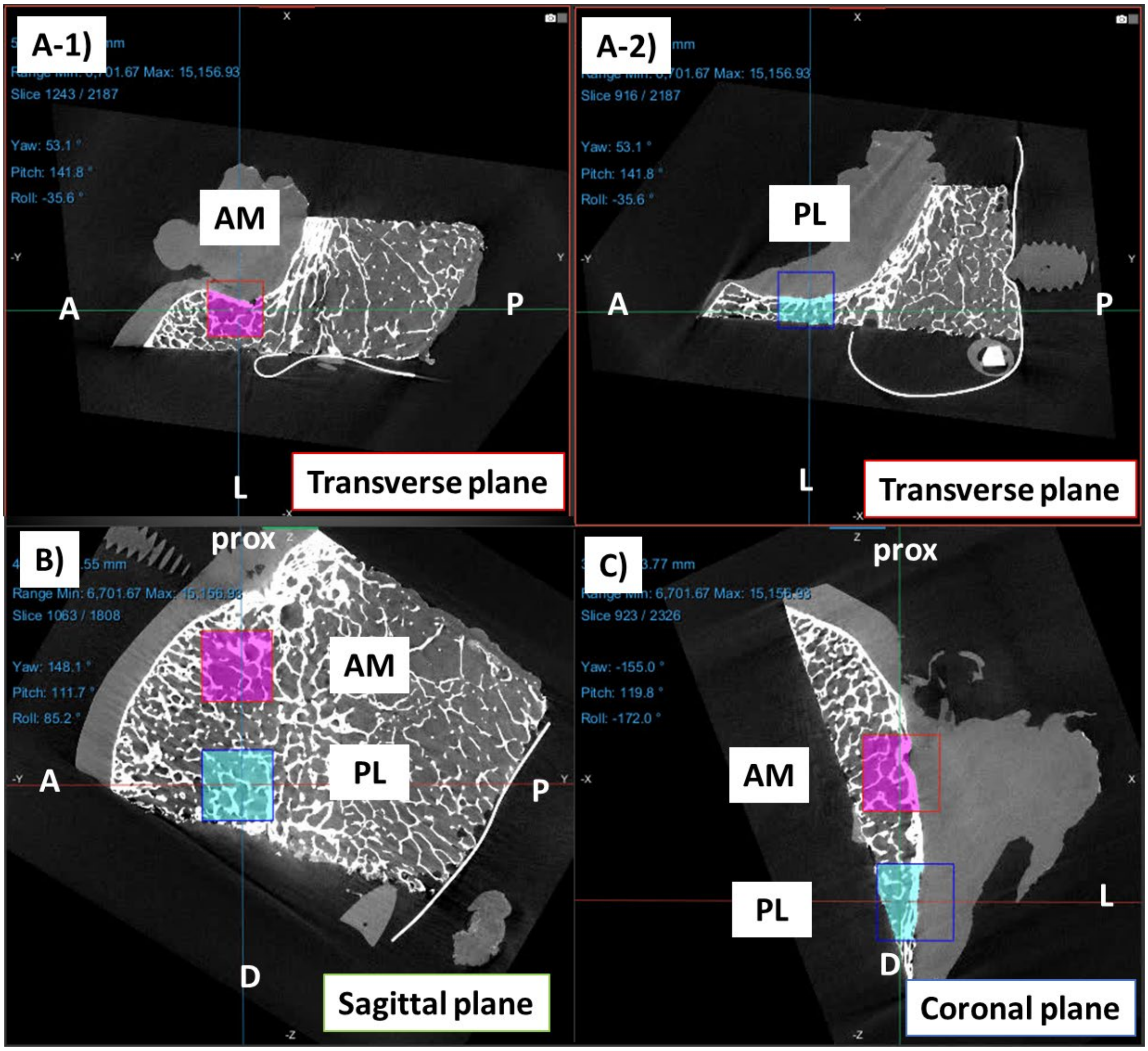

Figure D-17. Sample nano CT image of Specimen S3R. A-1) Transverse plane for AM bundle, A-2) transverse plane for PL bundle, B) sagittal plane, and C) coronal plane

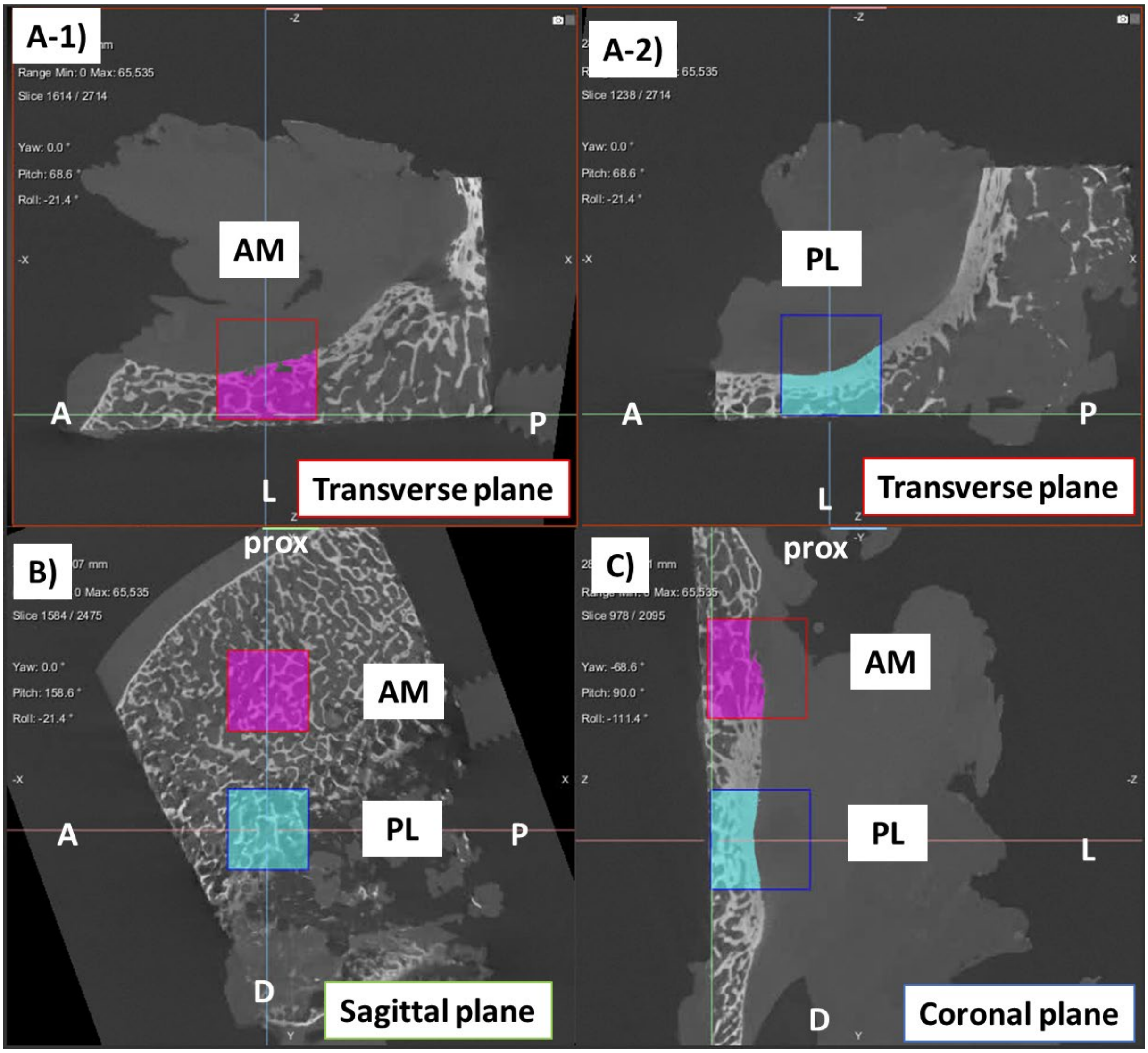

Figure D-18. Sample nano CT image of Specimen S4R. A-1) Transverse plane for AM bundle, A-2) transverse plane for PL bundle, B) sagittal plane, and C) coronal plane

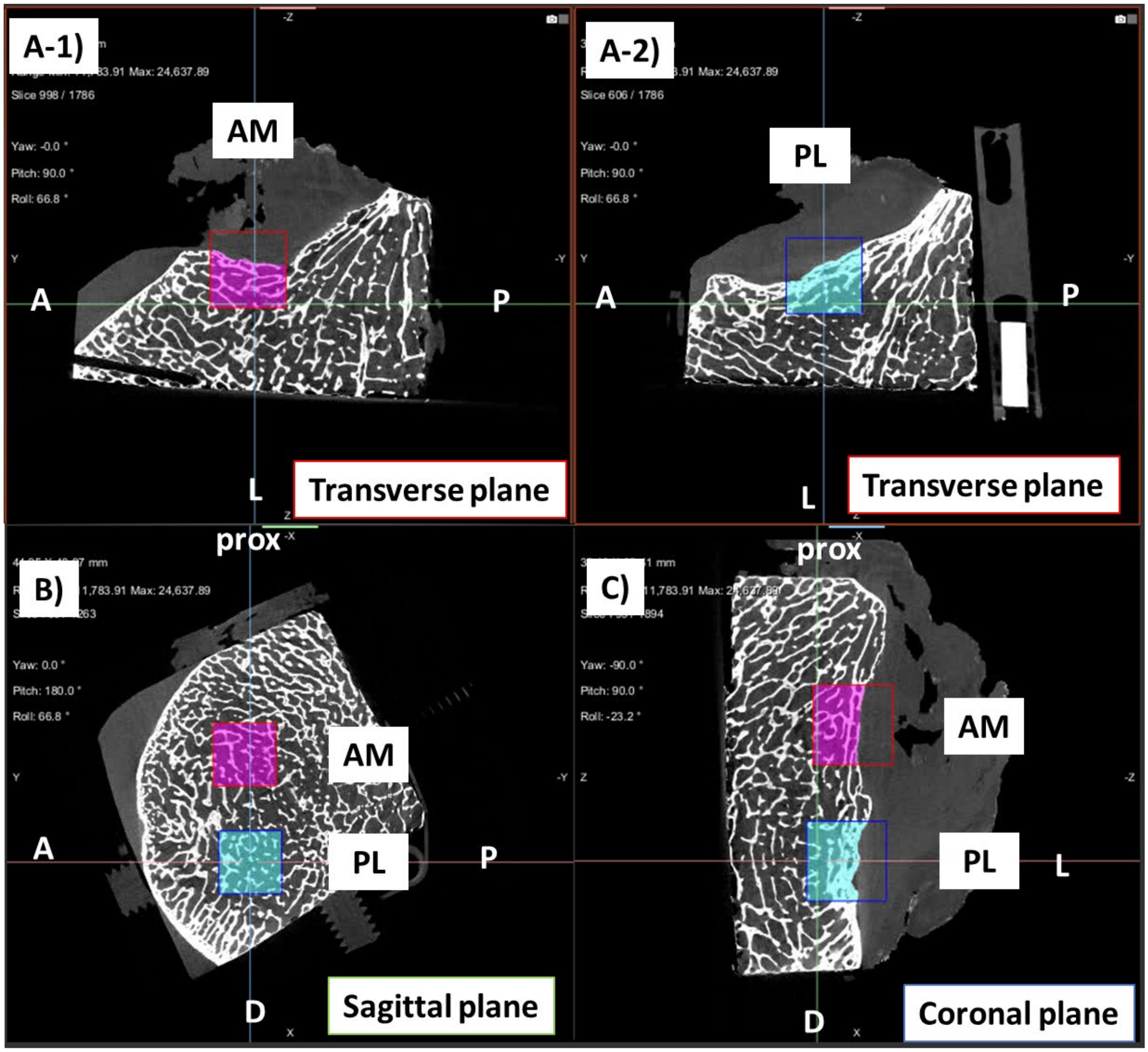

Figure D-19. Sample nano CT image of Specimen S5R. A-1) Transverse plane for AM bundle, A-2) transverse plane for PL bundle, B) sagittal plane, and C) coronal plane

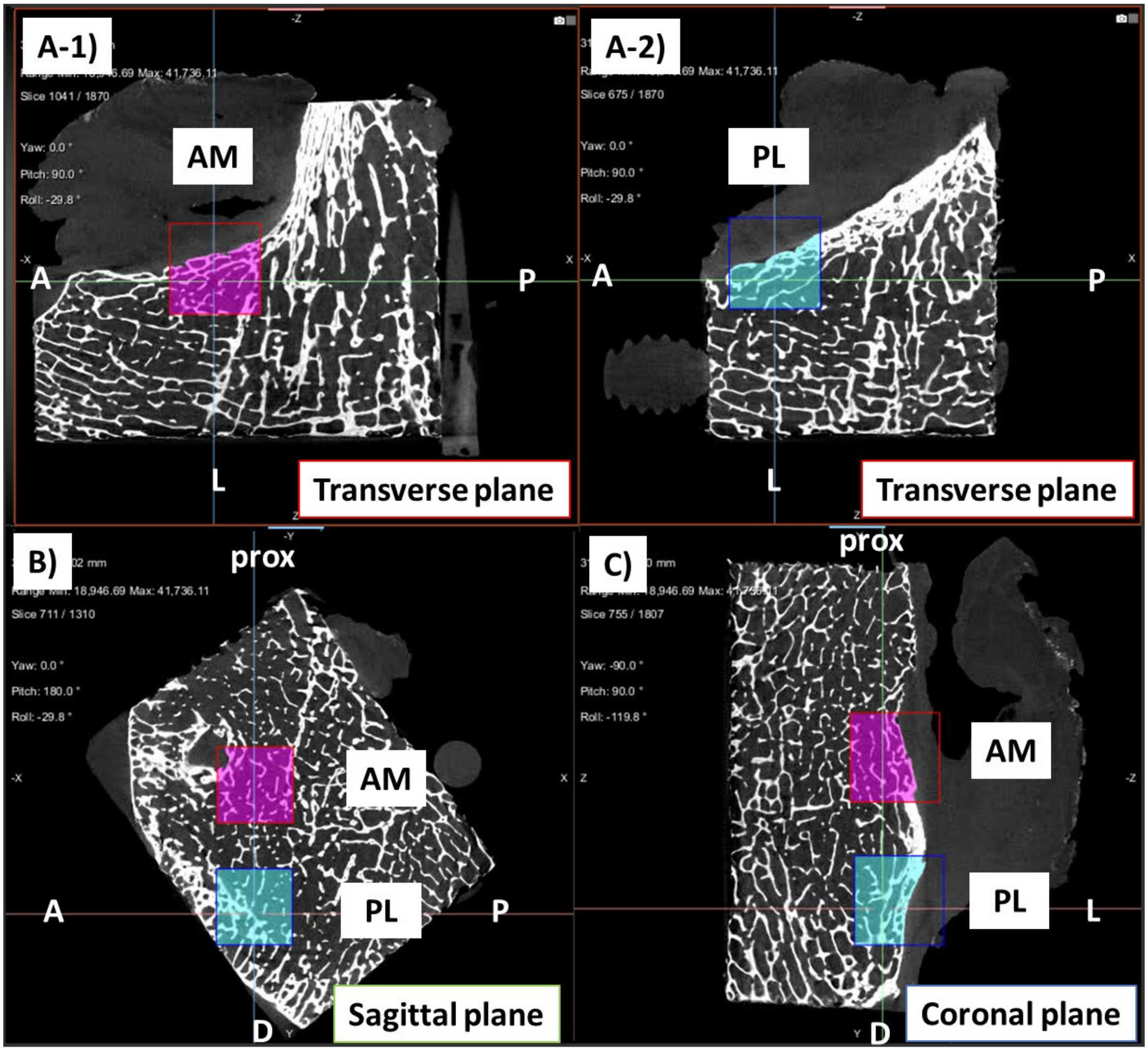

Figure D-20. Sample nano CT image of Specimen S6R. A-1) Transverse plane for AM bundle, A-2) transverse plane for PL bundle, B) sagittal plane, and C) coronal plane

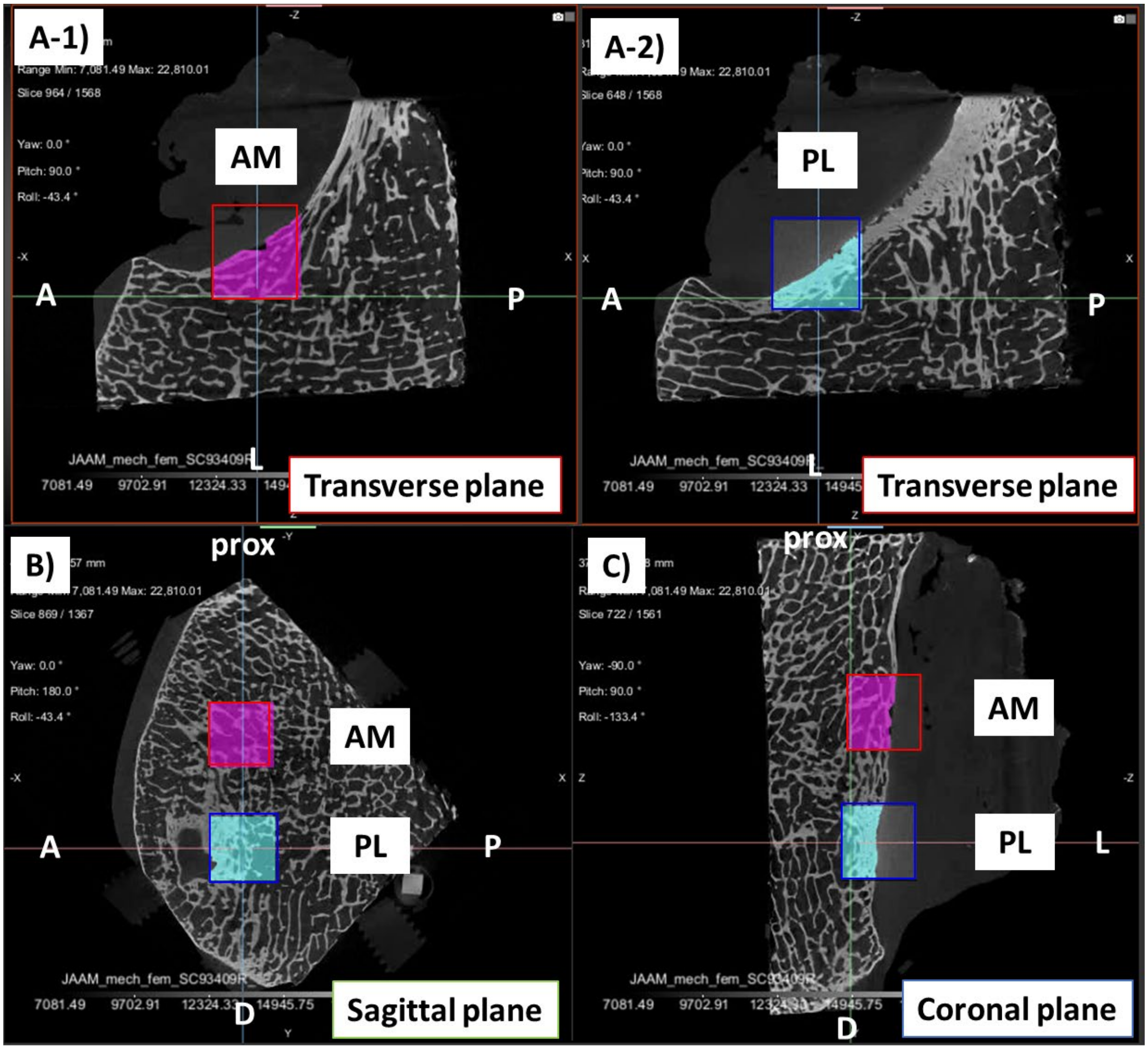

Figure D-21. Sample nano CT image of Specimen S7R. A-1) Transverse plane for AM bundle, A-2) transverse plane for PL bundle, B) sagittal plane, and C) coronal plane

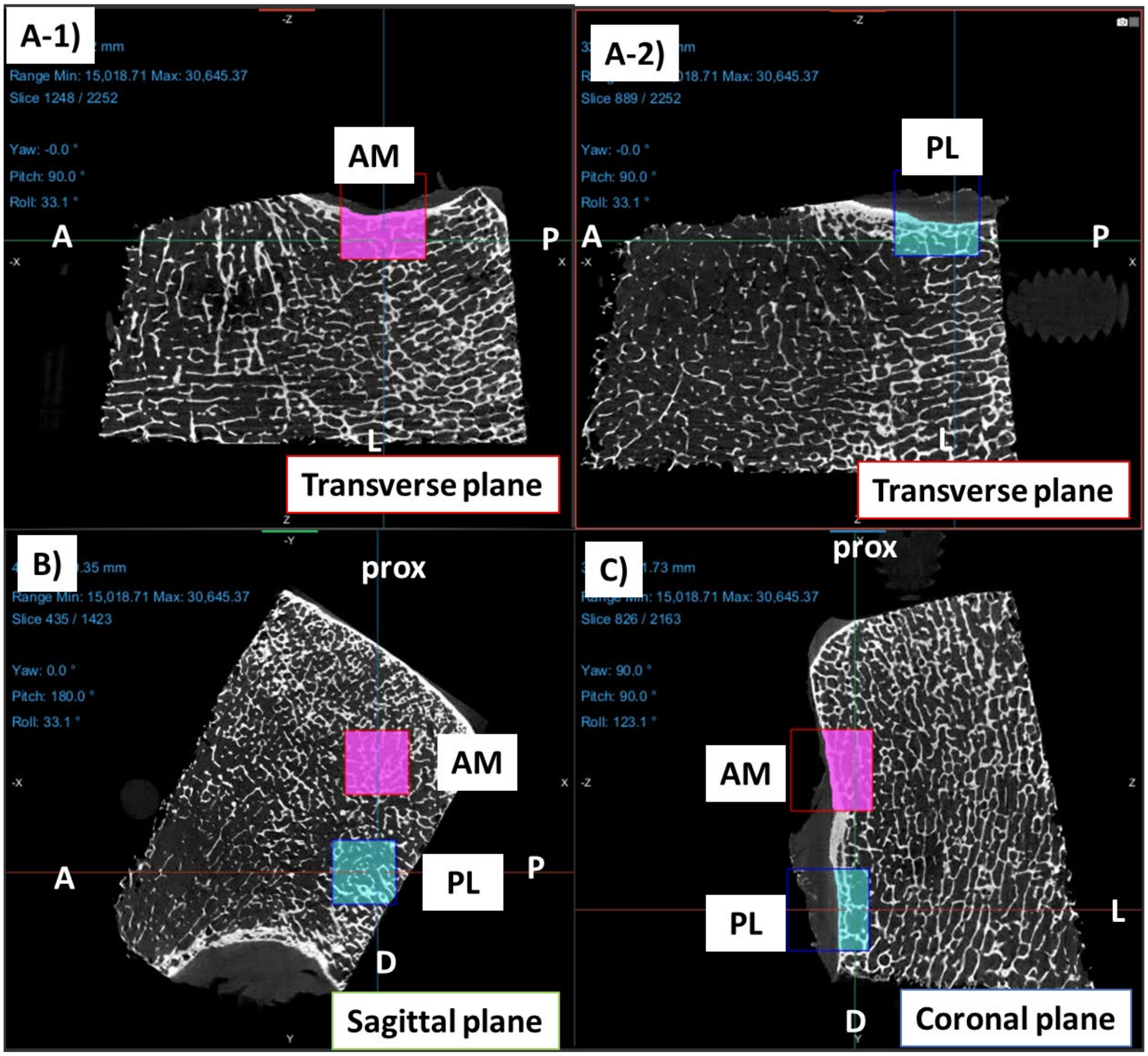

Figure D-22. Sample nano CT image of Specimen S1L. A-1) Transverse plane for AM bundle, A-2) transverse plane for PL bundle, B) sagittal plane, and C) coronal plane

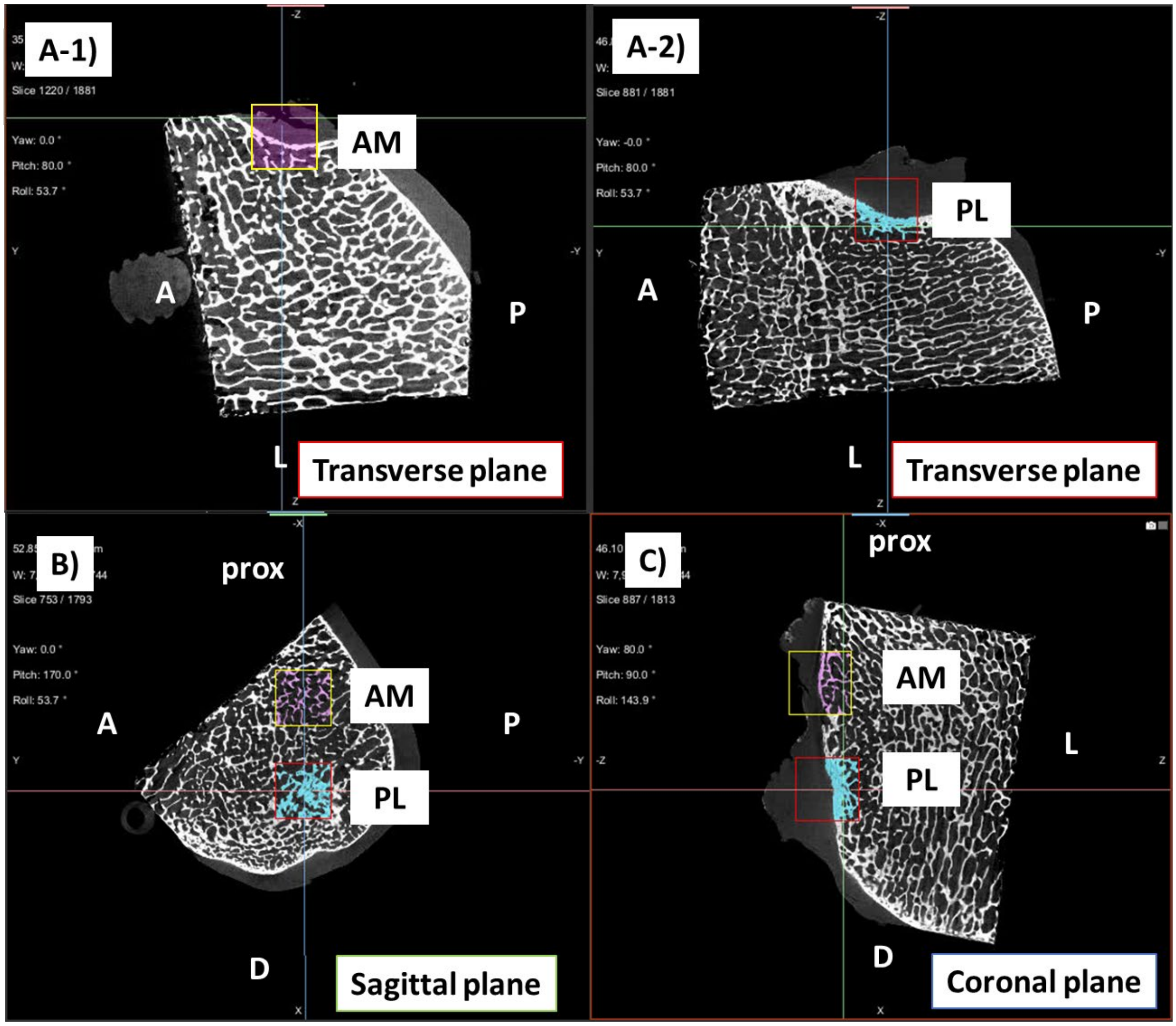

Figure D-23. Sample nano CT image of Specimen S2L. A-1) Transverse plane for AM bundle, A-2) transverse plane for PL bundle, B) sagittal plane, and C) coronal plane

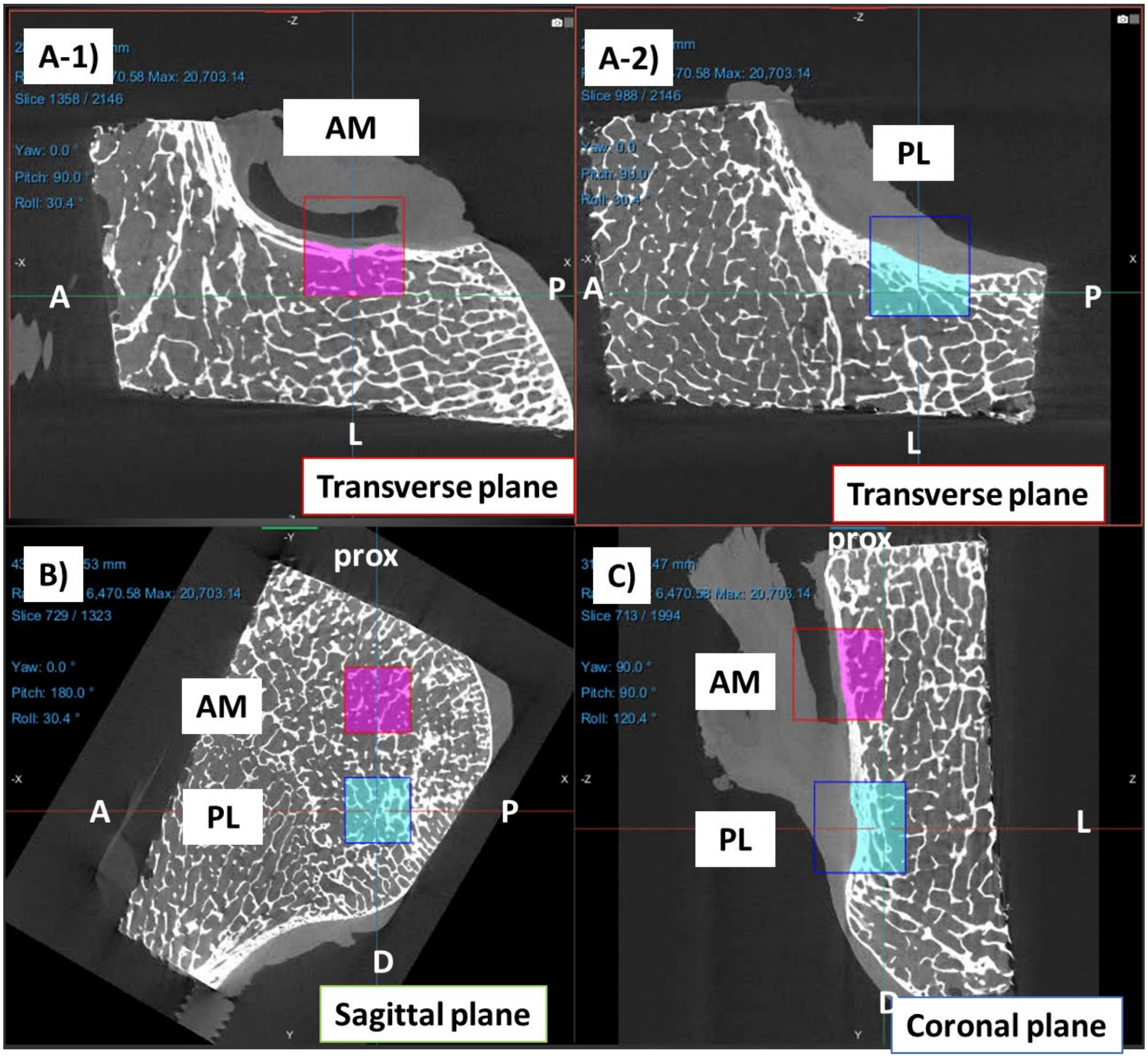

Figure D-24. Sample nano CT image of Specimen S3L. A-1) Transverse plane for AM bundle, A-2) transverse plane for PL bundle, B) sagittal plane, and C) coronal plane

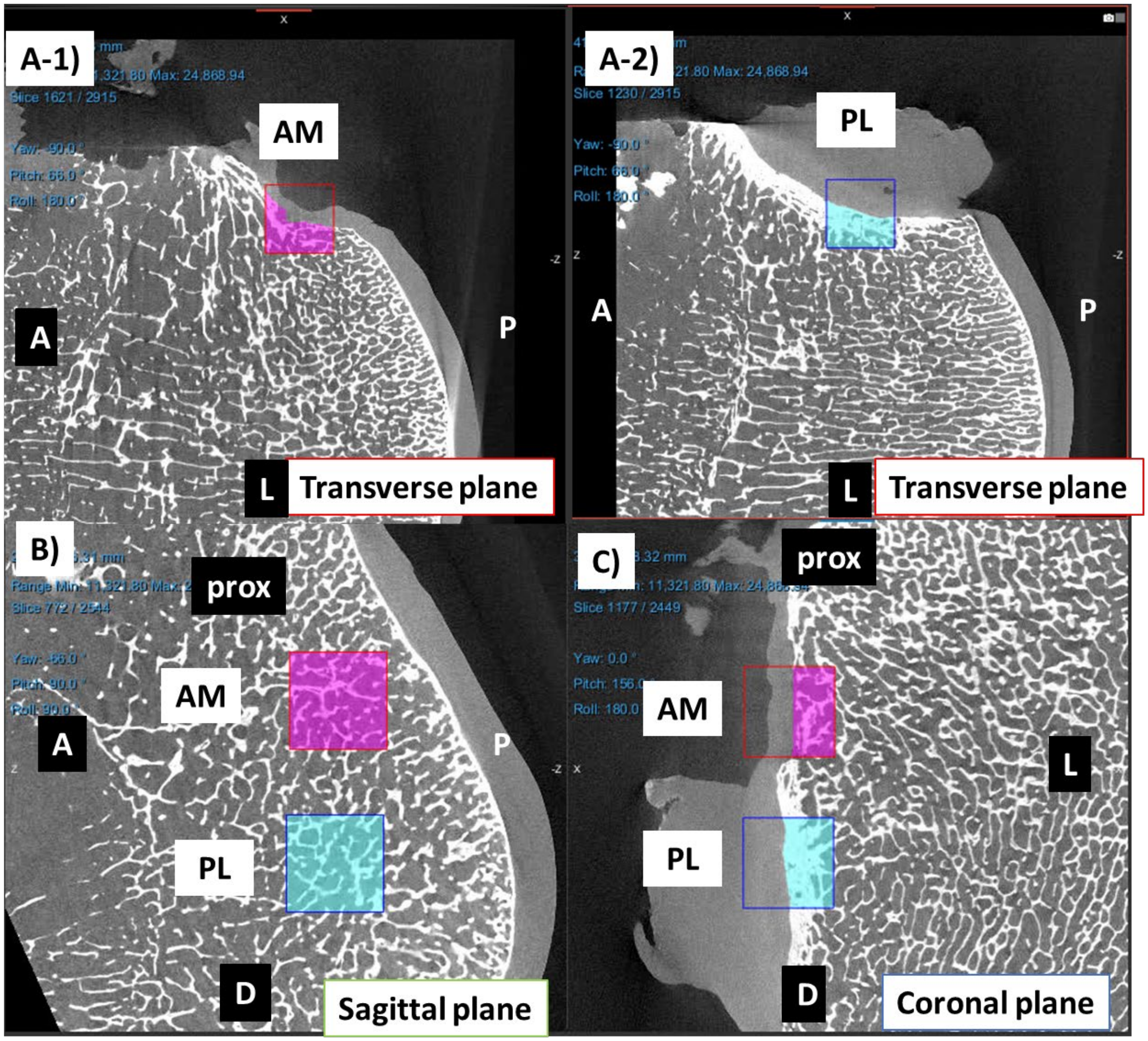

Figure D-25. Sample nano CT image of Specimen S4L. A-1) Transverse plane for AM bundle, A-2) transverse plane for PL bundle, B) sagittal plane, and C) coronal plane

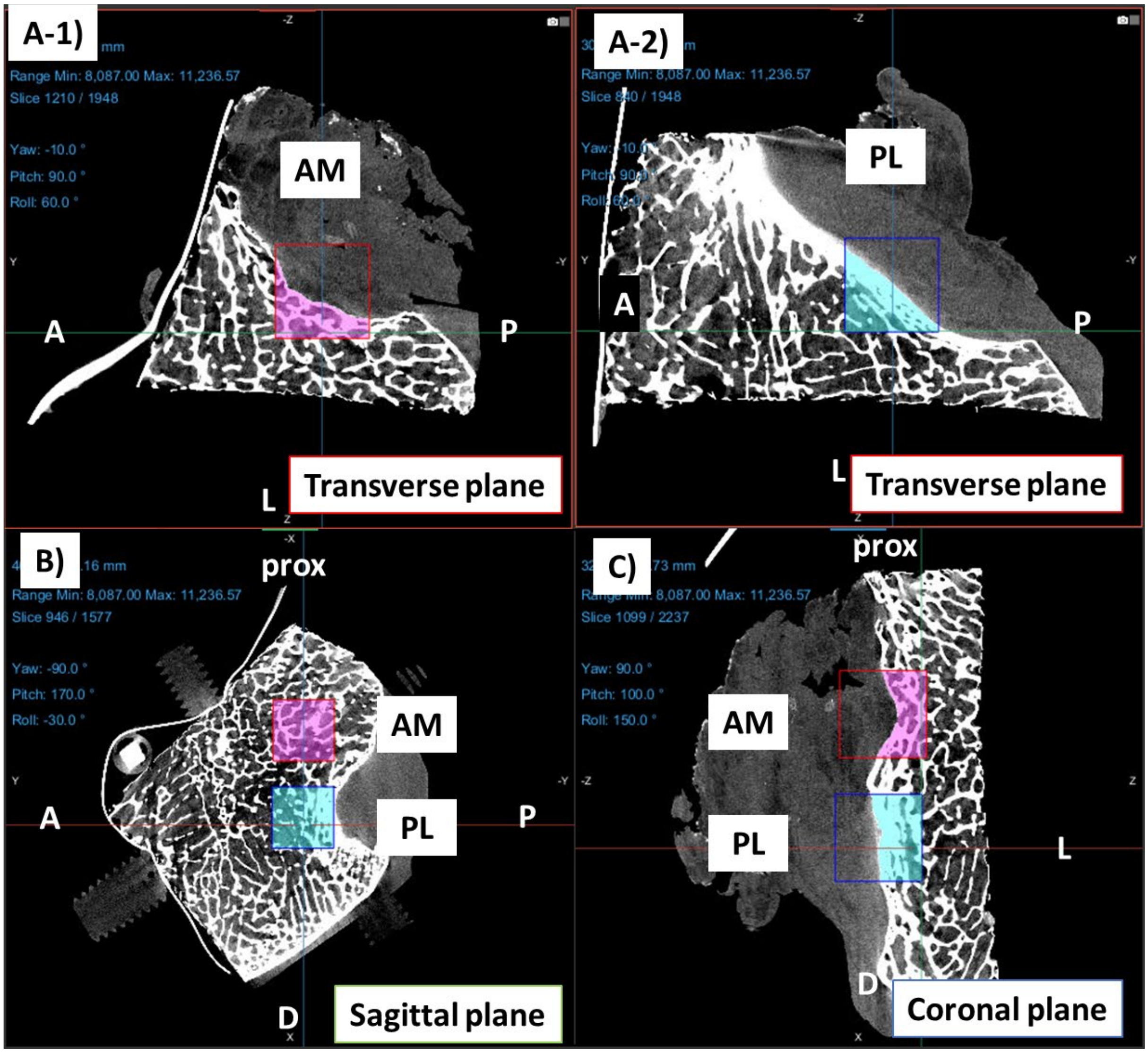

Figure D-26. Sample nano CT image of Specimen S5L. A-1) Transverse plane for AM bundle, A-2) transverse plane for PL bundle, B) sagittal plane, and C) coronal plane

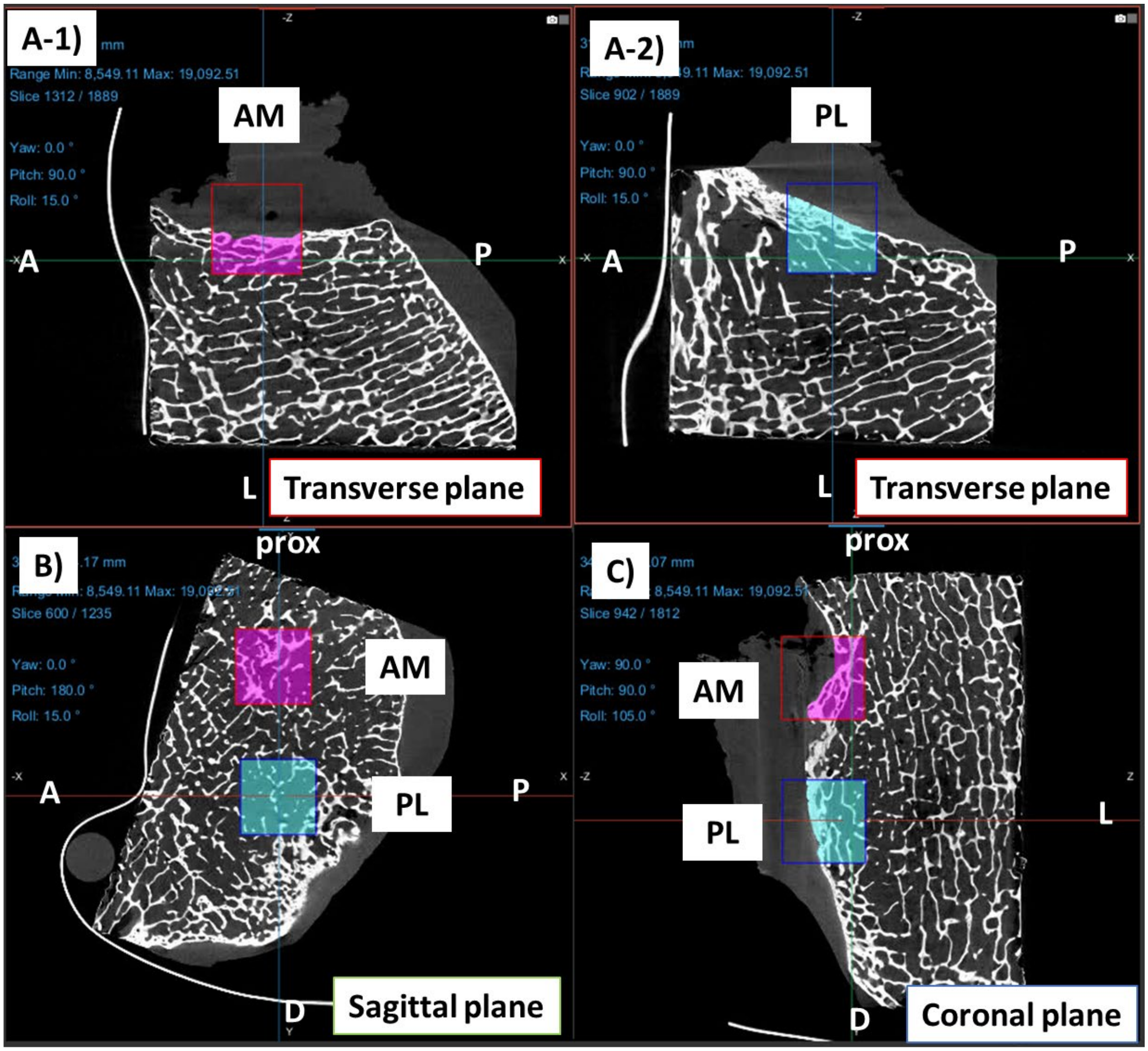

Figure D-27. Sample nano CT image of Specimen S6L. A-1) Transverse plane for AM bundle, A-2) transverse plane for PL bundle, B) sagittal plane, and C) coronal plane

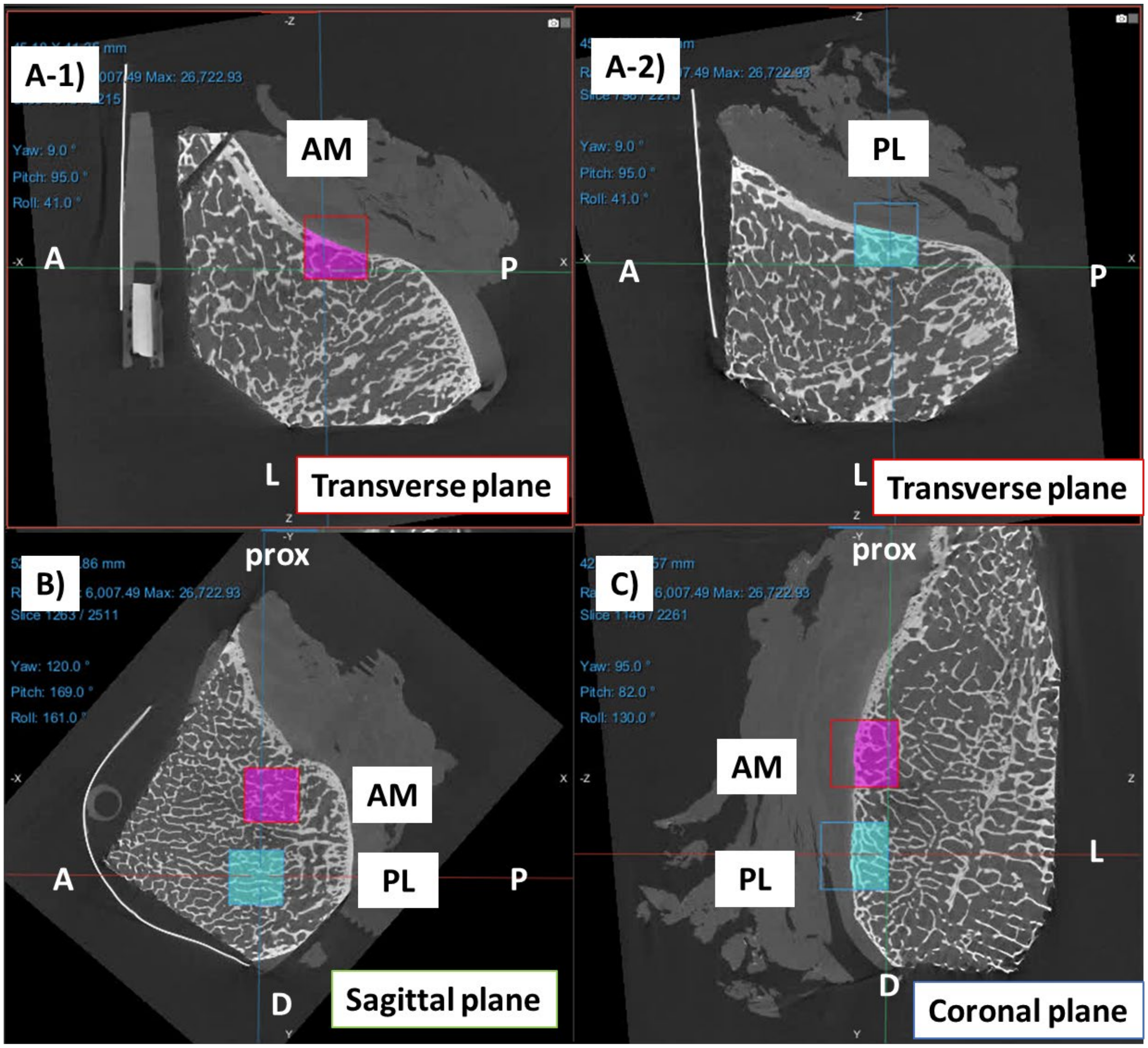

Figure D-28. Sample nano CT image of Specimen S7L. A-1) Transverse plane for AM bundle, A-2) transverse plane for PL bundle, B) sagittal plane, and C) coronal plane

Appendix E: Collection of Directionality Density Plots of All Specimens (Chapter 5 - Aim 3)

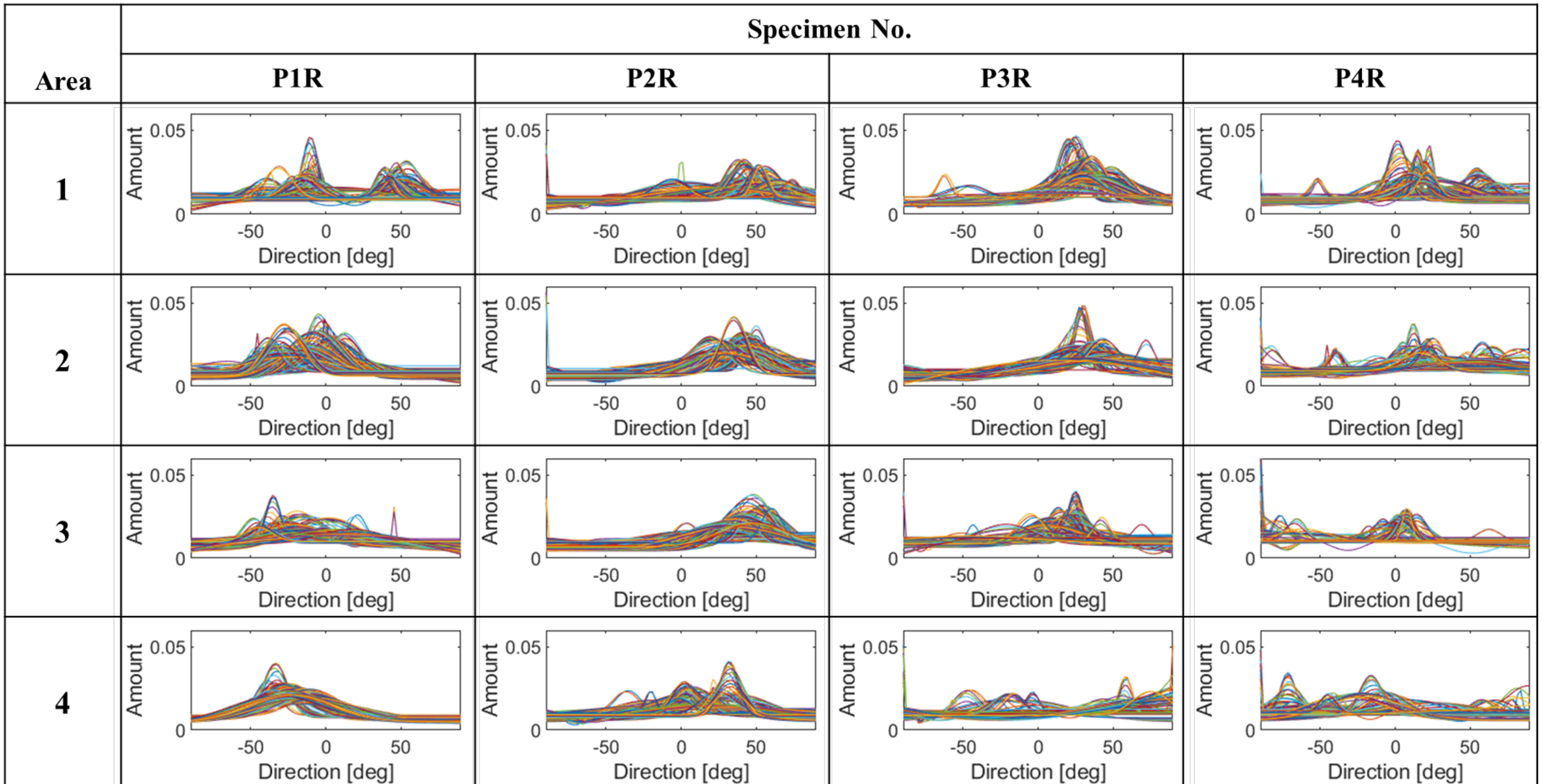

Figure E. Directionality density for Specimens. Figure 5-1-(c) shows the location of measured area (ROI). (Cont.)

Area	Specimen No.			
	P5R	P6R	P7R	
1	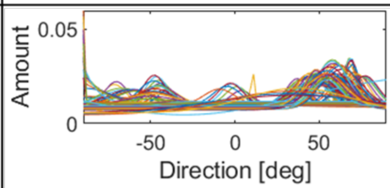	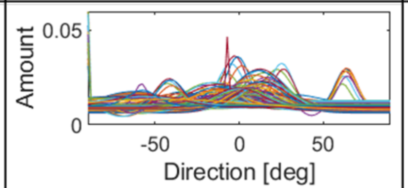	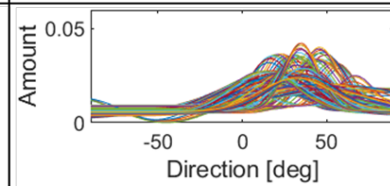	
2	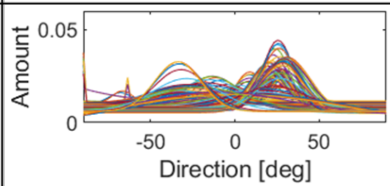	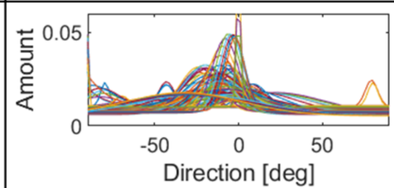	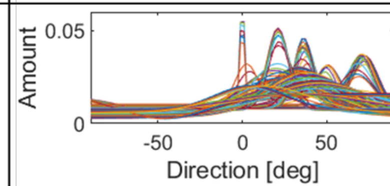	
3	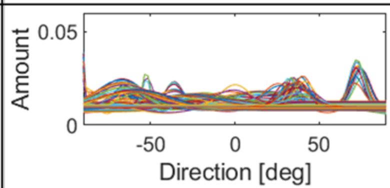	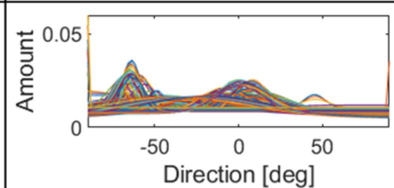	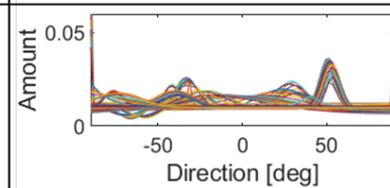	
4	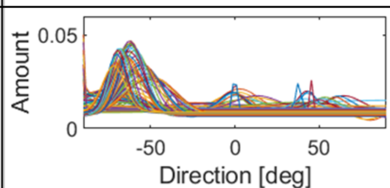	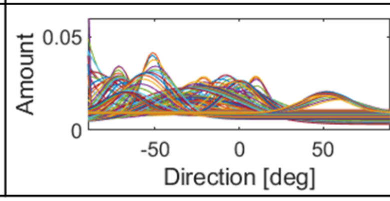	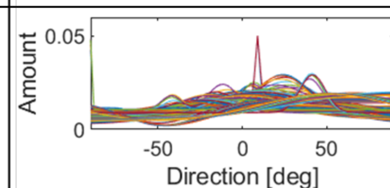	

Figure E. Directionality density for Specimens. Figure 5-1-(c) shows the location of measured area (ROI). (Cont.)

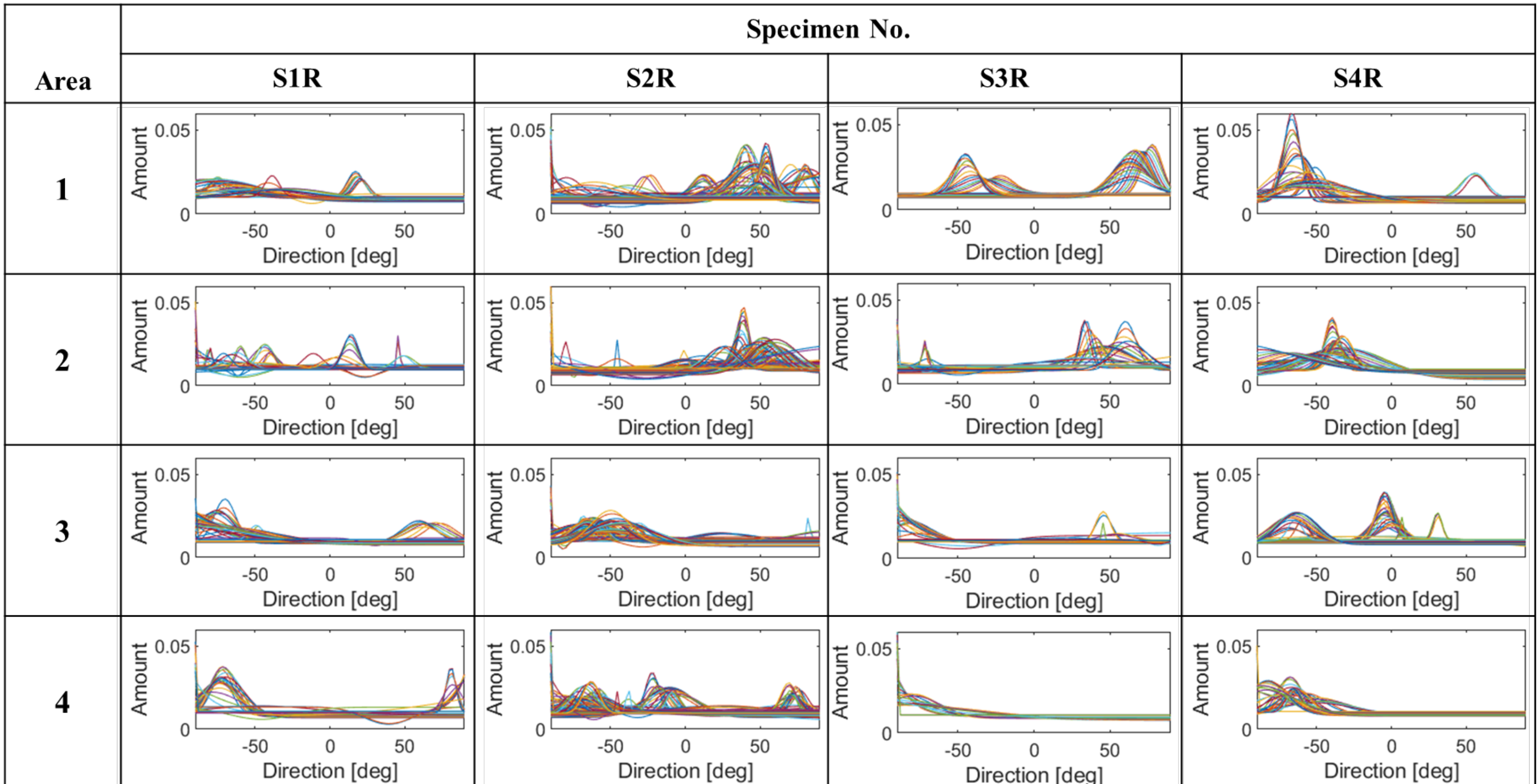

Figure E. Directionality density for Specimens. Figure 5-1-(c) shows the location of measured area (ROI). (Cont.)

Area	Specimen No.			
	S5R	S6R	S7R	
1	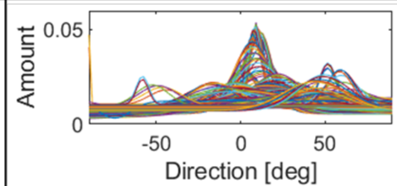	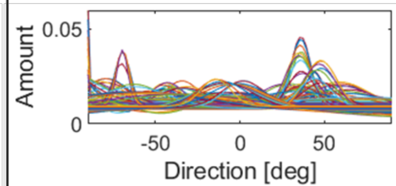	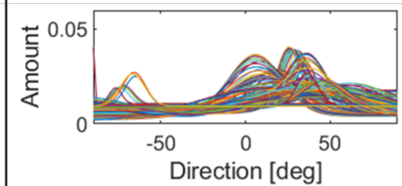	
2	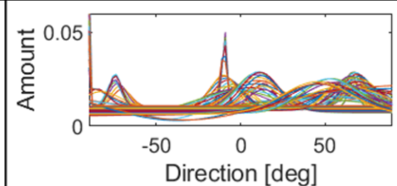	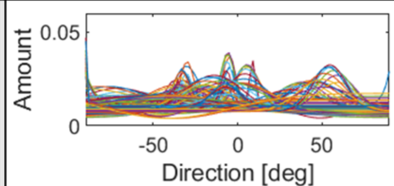	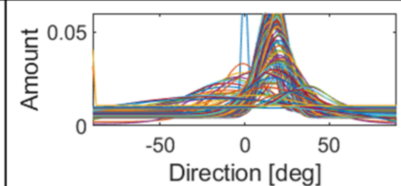	
3	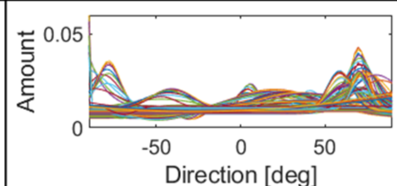	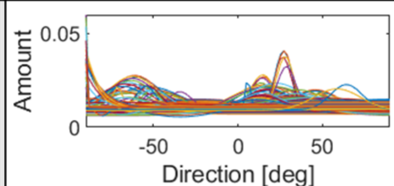	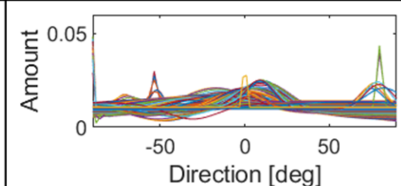	
4	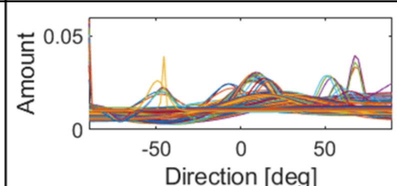	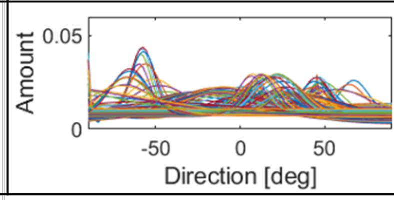	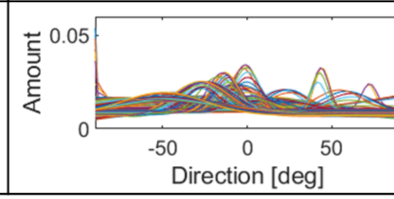	

Figure E. Directionality density for Specimens. Figure 5-1-(c) shows the location of measured area (ROI). (Cont.)

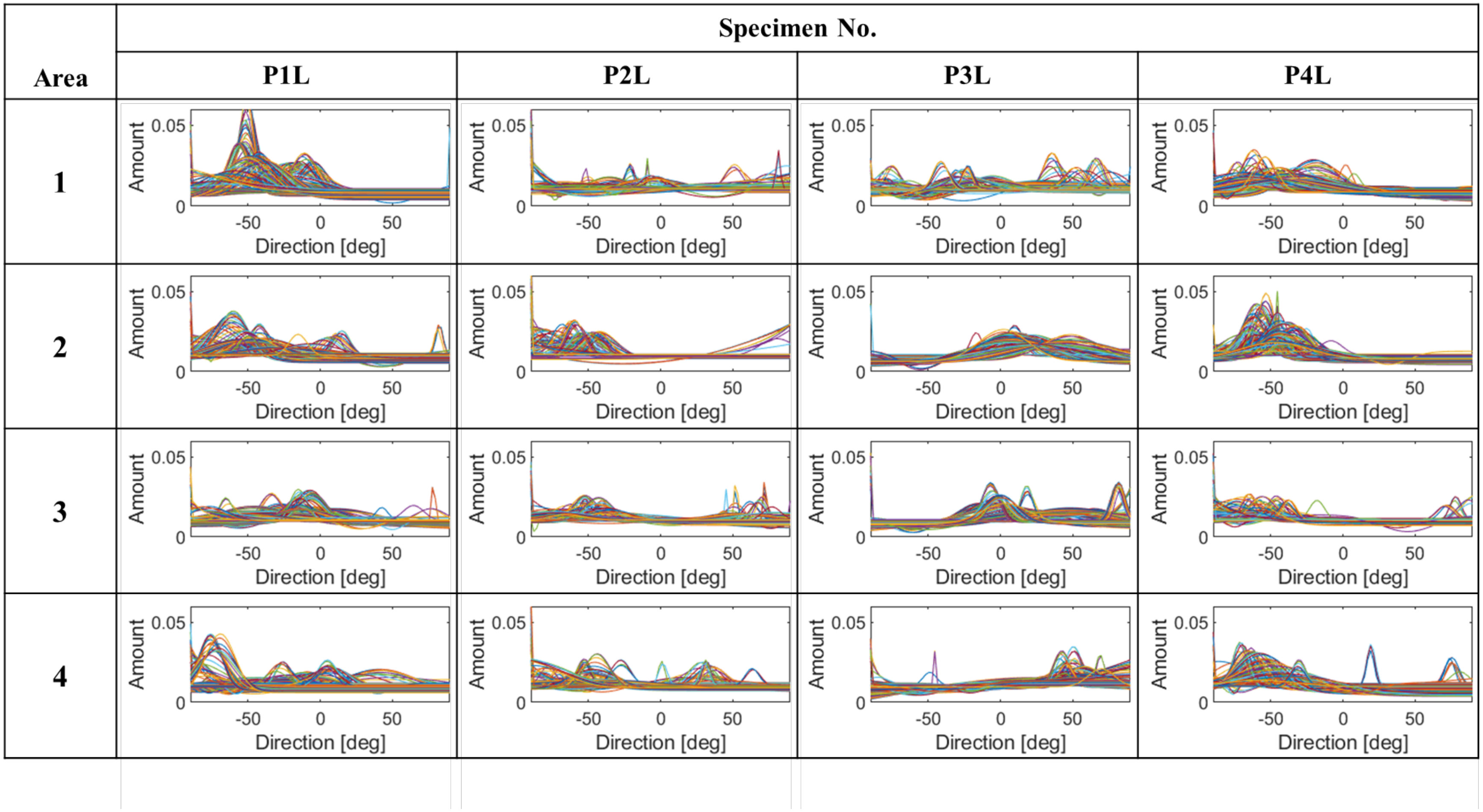

Figure E. Directionality density for Specimens. Figure 5-1-(c) shows the location of measured area (ROI). (Cont.)

Area	Specimen No.			
	P5L	**P6L**	**P7L**	
1	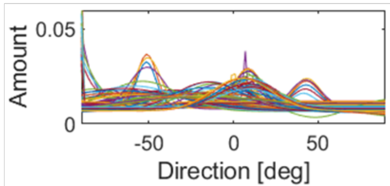	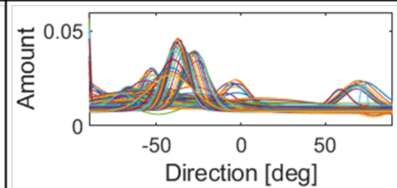	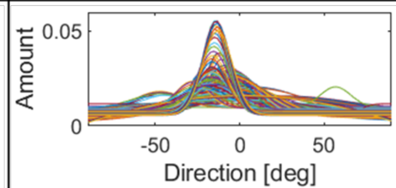	
2	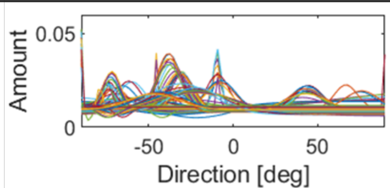	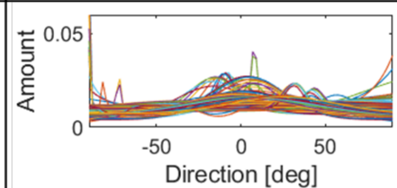	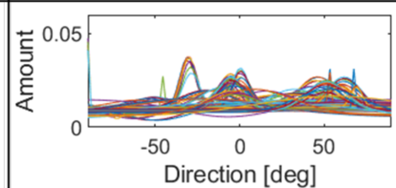	
3	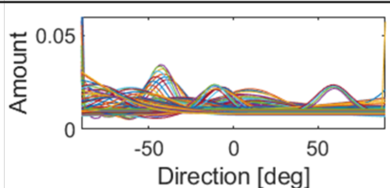	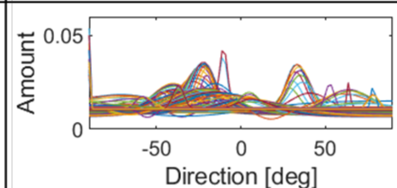	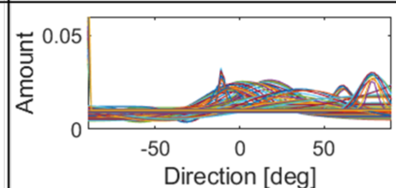	
4	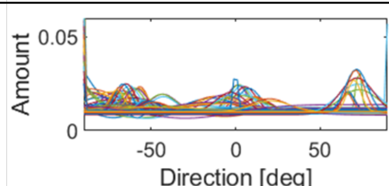	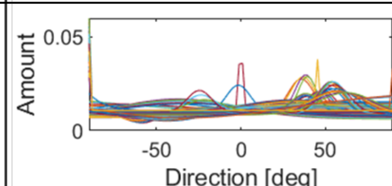	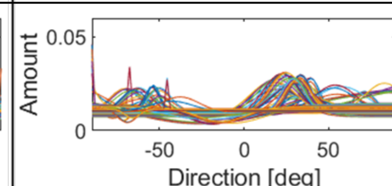	

Figure E. Directionality density for Specimens. Figure 5-1-(c) shows the location of measured area (ROI). (Cont.)

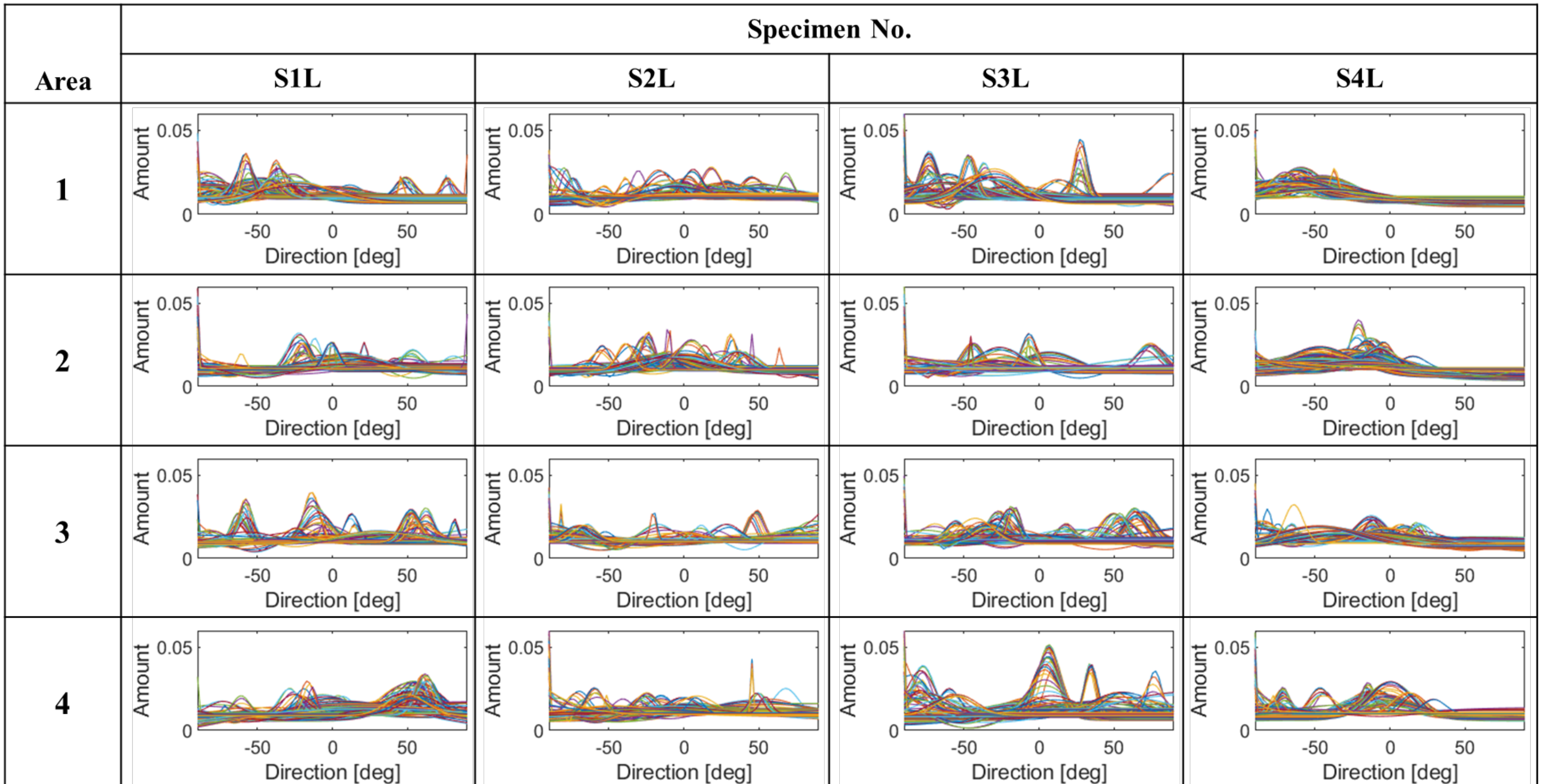

Figure E. Directionality density for Specimens. Figure 5-1-(c) shows the location of measured area (ROI). (Cont.)

Area	Specimen No.			
	S5L	S6L	S7L	S8L
1	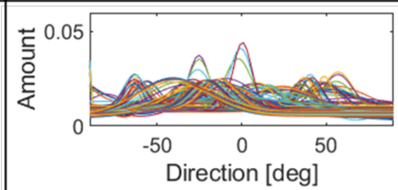	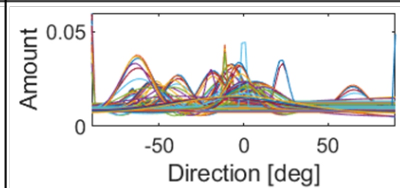	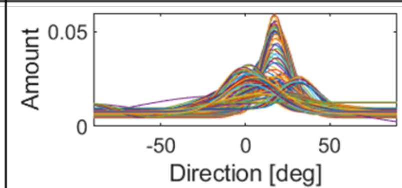	
2	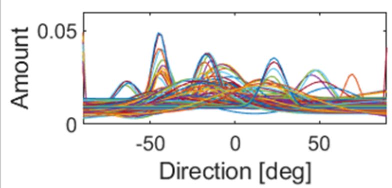	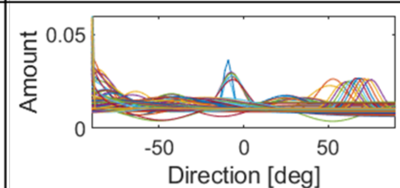	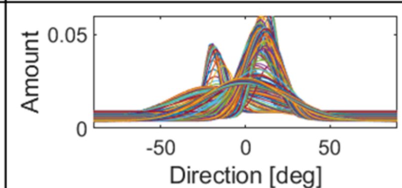	
3	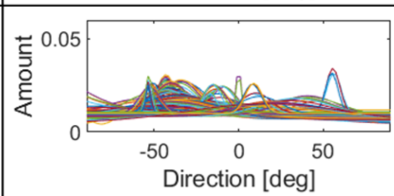	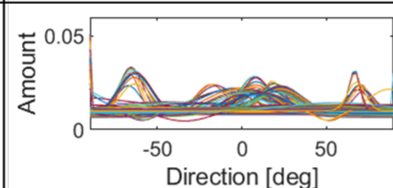	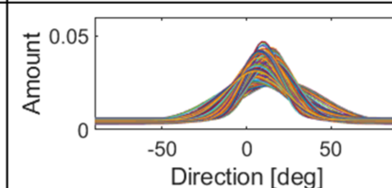	
4	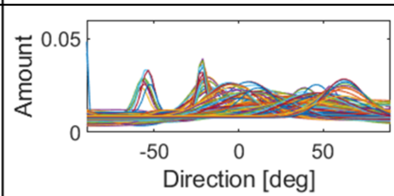	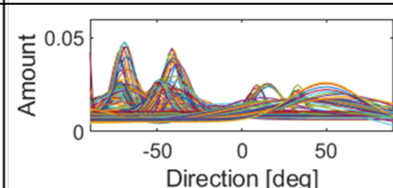	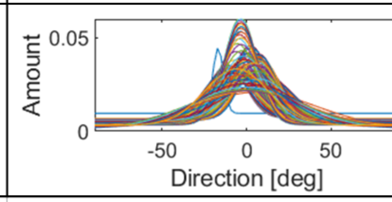	

Figure E. Directionality density for Specimens. Figure 5-1-(c) shows the location of measured area (ROI).